Title: Raman signal enhancement and CARS microscopy

Majid Naji

Thesis submitted to the
Faculty of Graduate and Postdoctoral Studies
in partial fulfillment of the requirements for the Doctorate in Philosophy
degree in Electrical and Computer Engineering

School of Electrical Engineering and Computer Science
Faculty of Engineering
University of Ottawa

To my parents and my sister.

Abstract:

Raman biosensors are appealing for many biomedical applications, due to their accuracy and speed. In addition, Raman microscopy is a non-labeled imaging technique that offers chemical contrast based on Raman vibrational frequencies. However, the weak Raman signal represents a significant obstacle to using Raman in biological applications. The objective of my PhD research, presented in this thesis, is to enhance the Raman signal, thereby enabling it to be used in a wide variety of biomedical applications.

More specifically, the research focuses on two different Raman signal enhancement techniques. The first is to improve the Raman signal using hollow-core photonic crystal fibers; this enhanced the Raman signal of ethanol 40 times. The second approach is by generating a coherent anti-Stokes Raman scattering (CARS) signal.

We demonstrated CARS microscopy of myelin (lipid-rich) structures using a single femtosecond Ti:sapphire laser, and a photonic crystal fiber (PCF) with two closely lying zero dispersion wavelengths (ZDWs). Generating low noise supercontinuum (Stokes beam) out of two closely lying ZDW PCFs, enabled us to perform fast data acquisition (84 μs per pixel) CARS imaging using a homebuilt microscope. However, the application of this fiber is often limited to CARS imaging of molecular species with vibrations at wavenumbers ≥ 2000 cm^{-1} Raman shift. In addition, as it is not a polarization maintaining fiber, it cannot be used for polarization CARS microscopy. A polarization-maintaining PCF with two far-lying zero dispersion wavelengths offers important advantages for polarization CARS microscopy, and for CARS imaging in the fingerprint region. This PCF, though commercially available, has had limited use for CARS microscopy in the C-H bond region. The main problem is that the supercontinuum from this fiber is typically noisier than that from a standard PCF with two closely-lying zero dispersion wavelengths. To overcome this, we determined the optimum operating conditions for generating a low-noise supercontinuum out of a PCF with two far-lying zero dispersion wavelengths, in terms of the input parameters of the excitation pulse. We measured the relative intensity noise (RIN) of the Stokes and the corresponding CARS signal, as a function of the input laser parameters in this fiber. We demonstrated that the results of CARS imaging using this alternate fiber are comparable to those achieved using the standard fiber for

input laser pulse conditions of low average power, narrow pulse width with a slightly positive chirp, and polarization direction parallel to the slow axis of the selected fiber.

Finally, we demonstrated a novel fiber-delivered, portable, multimodal CARS exoscope, for minimally invasive in-vivo imaging of tissues. The device was based on a micro-electromechanical system-scanning mirror and miniaturized optics, and light delivery by photonic crystal fibre. A single Ti:sapphire femtosecond laser approach is used to produce CARS and two photon excitation fluorescent and second harmonic generation images of different samples using the new setup. The high resolution and distortion-free images achieved with various samples, particularly in the reverse direction (epi), successfully demonstrate proof of concept, and paves the way to minimally or non-invasive in vivo imaging. Moreover, combining this novel endoscope with a portable femtosecond fiber laser will accelerate delivering multimodal nonlinear imaging endoscopy/microscopy to clinical bed-side applications.

Acknowledgments

The research and findings presented in this thesis are the result of positive and constructive ideas and collaborations, and the support I received from my supervisor and colleagues during my PhD studies.

I would first like to express special thanks to my supervisor, Dr. Hanan Anis, who I have worked with since 2007. I did my PhD research under her direction and supervision, and I was the beneficiary of many ideas, as well as support and novel experiences. She gave me the opportunity to grow scientifically and personally.

I would also like to thank Dr. Sangeeta Murugkar for her scientific advice and support regarding the CARS microscope and exoscope projects, during the last four years of my PhD.

It was a great experience to work with my friend and colleague, Mr. Altaf Khetani. In addition to our constructive discussions, we shared many ideas and laboratory measurements during my optimization of the Raman setup and explored new ideas for enhancing the Raman signal using HC-PCF. I would like to express my sincere gratitude for his help and input.

During my first year of graduate studies, I had the opportunity to work on CARS microscopy with Dr. Sty's group at the Ottawa Civic Hospital. Dr. Andrew Ridsdale and Craig Brideau provided me with valuable scientific experience, for which I express my sincere thanks.

To acquire and prepare the myelin samples for testing our CARS microscope and exoscope, I received assistance from Dr. H. Ala Yasin and Dr. M. Parsanajat from the Neuroscience Division of the University of Ottawa, for which I am truly grateful.

I also would like to thank my lab colleagues which I had a chance to work with while completing my PhD, particularly Brett Smith, Hossein Khotb, Dr. Vidhu Tawari, Dr. Mohammed Abosafe, Ali Momen Pour and Shiyu Gao.

Table of Contents

List of Figures

List of Acronyms

BP	Band pass (filter)
CARS	Coherent anti-Stokes Raman scattering
CW	Continuous wave
ESA	Electrical spectrum analyzer
ESM	Endlessly single-mode
fs	Femtosecond
FWM	Four-wave mixing
FWHM	Full width half maximum
FT	Fourier transform
GVD	Group velocity dispersion
HC-PCF	Hollow core photonics crystal fiber
KDP	Potassium dihydrogen phosphate
LMA	Large mode area (fiber)
MPEF	Multi-photon excited fluorescence
MI	Modulation instability
MS	Multiple sclerosis
NA	Numerical aperture
NLSE	Nonlinear Schrödinger equation
NIR	Near-infrared
NSR	Non-solitonic radiation
Nd:YAG	Neodymium/yttrium aluminum garnet laser
OPO	Optical parametric oscillator
OSA	Optical spectrum analyzer
PCF	Photonic crystal fiber
PLS	Partial least squares (analysis)
ps	Picoseconds
RIN	Relative intensity noise
SNR	Signal to noise ratio
SCI	Spinal cord injury

SRS	Stimulated Raman scattering
SERS	Surface enhanced Raman scattering
SHG	Second-harmonic generation
SC	Supercontinuum
SMF	Single mode fiber
SPM	Self phase modulation
SVEA	Slowly varying envelope approximation
TIR	Total internal reflection
Ti-sapphire	Titanium-sapphire
THG	Third harmonic generation
TPEF	Two-photon excited fluorescence
XPM	Cross-phase modulation
ZDW	Zero dispersion wavelength

List of Symbols

a	Bore radius of hollow core fiber
$a^{'}$	Perturbation wave amplitude
A_{eff}	Effective cross-sectional area
A_R	Raman scattering cross section constant in non-resonant CARS
A_t	Two-photon absorption cross section constant
c	Speed of light
C	Chirp parameter
d	Beam diameter
E	Electric field
E_0	Amplitude of the electric field of the incident light
E_p	Electric field of the pump light
E_s	Electric field of the Stokes light
f	Focal length of the lens
$g(\Omega^{'})$	Gain spectrum of the MI
g_R	Raman scattering cross section
I	Scattered light intensity/ photon flux
I_0	Incident flux of photons/ incident light intensity
I_p	Pump beam intensity
I_R	Scattered Raman intensity
I_s	Stokes beam intensity
I_{CARS}	CARS signal intensity
$K^{'}$	Wavenumber of the perturbation
k_0	Wave-vector
K_{as}	Wave-vector of the anti-Stokes field
K_p	Wave-vector of the pump field
K_s	Wave-vector of the Stokes field
L_{eff}	Effective length of the pulse propagation
L_{int}	Effective interaction length

L	Interaction length of light(s) with medium
L_c	Coherence length
L_D	Dispersion length
L_{fiss}	Soliton fission length
L_{NL}	Nonlinear length
M	Figure of merit
n	Linear refractive index of the medium
$\tilde{n}$	Refractive index
n_{sil}	Refractive index of the silica (fiber material)
n_a	Refractive index of the analyte
n_{air}	Refractive index of the air
N	Number of scatterer
N'	Soliton order
N''	Molecular density number
NA	Numerical aperture of the lens
n_2	Nonlinear –index coefficient or Kerr index
P_0	(Normalized) incident power
P	Molecular electric dipole momentum
P_{ave}	Pulse average power
$P^{(3)}$	Third order nonlinear polarization
$\bar{q}$	Amplitude of the pulse in the NLSE
R	Distance from the scatterer site
$Sech^2$	Squared hyperbolic secant function pulse shape
T	Time
W_0	Half width of the Gaussian beam at the focus
z	Propagation/ travelling distance of the excitation light inside of the fiber
z_0	Soliton period
Z_R	Rayleigh length
α	Polarizability of the atom or molecule
α_m	mth order of the polarizability at the Stokes frequency band

α'_m	mth order of the polarizability at the anti-Stokes frequency band
α'	Loss coefficient
β_2	Group velocity dispersion parameter
β_3	Third order dispersion parameter (fs3/mm)
β_4	Forth order dispersion parameter
γ	Nonlinear coefficient of medium
$\delta\omega(t)$	Shift from the central frequency ω_0
ΔK	Phase mismatch
$\Delta\beta_{NL}$	Nonlinear contribution of the propagation constant
Γ_R	Half-width at half maximum of the Raman line(s) of the medium
Γ_t	Half-width at half maximum of the two photon electronic transition
ε_0	Vacuum permittivity
η	Coupling efficiency
θ	Angle between the direction of incident light and observer
θ'	The angle between pump and the Stokes beam (phase matching angle)
θ_c	Critical angle
λ	Wavelength of the incident light
λ_0	Original band-gap central wavelength for HC-PCF
λ'	New band-gap shifted wavelength for HC-PCF
λ''	Average wavelength of the pump and the Stokes
$\nu_{anti\text{-}stokes}$	Raman scattered anti-Stokes frequency
ν_{Photon} .	Incident photon frequency
ν_{vib}	Fundamental vibrating frequency of Molecule
ν_{rot}	Fundamental rotational frequency of Molecule
ν_{Stokes}	Raman scattered Stokes frequency
τ	Pulse duration, Temporal pulse width
τ_0	Temporal pulse width of unchirped pulsed
ϕ	Phase of an optical field

ϕ_{Nl}	Nonlinear phase shift
$\chi^{(3)}$	Third order nonlinear optical susceptibility of the medium
$\chi^{(3)}_{nr}$	Non-resonant term of $\chi^{(3)}$
$\mathrm{Re}(\chi) = \chi'$	Real part of the resonant susceptibility
$\mathrm{Im}(\chi) = \chi''$	Imaginary parts of the resonant susceptibility
ω_{as}	Anti-Stokes frequency
ω_I	Idler frequency
ω_p	Pump frequency
ω_s	Stokes frequency
ω_{pr}	Probe frequency
$\Omega = \omega_{vib}$	Vibrational frequency(s) of the medium
Ω'	Perturbation frequency
Ω_c	Critical frequency

Chapter 1

1.1. Introduction

Raman spectroscopy is an effective way to study the vibrational and rotational modes of different materials, as well as a diagnostic technique for qualitative and quantitative chemical analysis and structural analysis of diverse materials and biological samples. Raman can be used to measure blood glucose levels for diabetics, tumor diagnostics, DNA detection and micro-endoscopy imaging.

One of the major limitations of Raman spectroscopy/microscopy is the weak Raman signal, which requires long exposure data acquisition and/or high power sources that could damage samples and limit biological applications.

There are methods to enhance the Raman signal intensity of a sample. These include coherence anti-Stokes Raman scattering (CARS), increasing the interaction length of the laser beam and analyte using hollow core photonics crystal fiber (HC-PCF), stimulated Raman scattering (SRS), and surface-enhanced Raman scattering (SERS) using gold or silver nanoparticles. During my PhD studies, I focused on two techniques to enhance the generated Raman signal of biological/chemical samples: i) enhancing the interaction length of the laser and analyte, and ii) coherence anti-Stokes Raman scattering (CARS).

1.2. Thesis Objectives

The objective of the research in this thesis is to enhance the Raman signal, thereby enabling it to be used in a wide variety of biomedical applications. More specifically, the research focuses on two different Raman signal enhancement techniques. The first uses hollow core photonic crystal fibers, and the second generates a coherent anti-Stokes Raman signal.

1.3. Contributions

My PhD research resulted in five journal articles, five conference proceedings and one awarded patent as follows:

A. Journals

1. Majid Naji, Sangeeta Murugkar, Hanan Anis, "Determining optimum operating conditions of the polarization-maintaining fiber with two far-lying zero dispersion wavelengths for CARS microscopy", Opti. Exp., Vol. 22, No. 9, 10800-10814, 2014.

2. Brett Smith, Majid Naji, Sangeeta Murugkar, Emilio Alarcon, Craig Brideau, Peter Stys, and Hanan Anis, "Portable Miniaturized, fiber delivered multimodal CARS exoscope", Opt. Exp., Vol. 21, Issue 14, 17161-17175, 2013.

3. Sangeeta Murugkar, Brett Smith, Prateek Srivastava, Adrian Moica, Majid Naji, Craig Brideau, Peter K. Stys, and Hanan Anis, "Miniaturized multimodal CARS microscope based on MEMS scanning and a single laser source", Opt. Exp., Vol. 18, No. 23, 23796-23804, 2010

4. François Légaré, Madji Naji, Philippe Lassonde, Daniel Comtois, Vincent Crozatier, Thomas Oksenhendler, Hanan Anis, and Jean-Claude Kieffer, "Pulse compression and shaping of broadband optical parametric amplifier laser source", Opt. Lett., Vol. 33, No. 23, 2824-2826, 2008.

5. Sangeeta Murugkar, Craig Brideau, Andrew Ridsdale, Majid Naji, Peter Stys, Hanan Anis, "Coherent anti-Stokes Raman scattering microscopy using PCF with two closely laying zero dispersion wavelength", Opt. Exp., Vol. 15, No.21, 14028-14038, 2007.

B. Conference proceeding

1. Brett Smith, Majid Naji, Sangeeta Murugkar, Craig Brideau, Peter Stys, Hanan Anis , "A novel multimodal CARS miniaturized microscope", Photonics West, Proc. SPIE 8226, Multiphoton Microscopy in the Biomedical Sciences XII, 822629 , February 9, 2012.

2. Sangeeta Murugkar, Brett Smith, Majid Naji, Craig Brideau, Peter Stys and Hanan Anis, "Development of a micromirror-scanned multimodal CARS miniaturized microscope for the in vivo study of spinal cord disorders, Photonics West, Proc. of SPIE Vol. 7903 79031D-1, 2011.

3. Majid Naji, Sangeeta Murugkar, Kaisar R. Khan, Hanan Anis, "CARS microscopy using photonic crystal fibre (PCF)", Photonics West, Proc. SPIE 7569, Multiphoton Microscopy in the Biomedical Sciences X, 75692S , February 26, 2010.

4. Vidhu Tiwari, Altaf Khetani, Majid Naji, Hanan Anis, "Study of surface enhance Raman scattering with PCF", IEEE Sensors, 978-1-4244-5335-1, New Zealand, 2009.

5. Majid Naji, Altaf Khetani, Neil Lagali, Rejean Munger, Hanan Anis, "A novel method of using hollow core photonic crystal fibre as a Raman biosensor", Photonics West, Proc. SPIE 6865, Nanoscale Imaging, Sensing, and Actuation for Biomedical Applications V, 68650E, February 13, 2008 .

C. Patent:

1. Altaf Khetani, Majid Naji, Neil Lagali, Hanan Anis, Rejean Munger, "Method for using a photonic crystal fibre as a Raman biosensor", US Patent 7,738,097, 2010.

1.4. Thesis outline:

This PhD thesis is written as a thesis by article. I have separated the work into two chapters representing the two enhancement techniques. Chapter 2 focuses on Raman enhancement using hollow core photonics crystal fibers, and Chapter 3 concentrates on CARS.

In Chapter 2, I discuss my motivation and contribution to the field, followed by a literature review and an examination of the background of hollow core photonics crystal fiber Raman enhancement technique. I also present my publications and my contributions to them.

Chapter 3 begins with a short introduction to CARS applications, followed by my motivation and contributions. I then discuss the CARS theory and the literature review. As a lot of my work depends on supercontinuum generation, I briefly assess the related literature and the physical mechanisms involved. I then list my publications and discuss my contributions to each.

Chapter 4 summarizes the main results of the thesis, and presents a future outlook.

Chapter 2

Enhancing the Raman signal using HC-PCF for biosensing

2.1. Introduction and Motivation

Raman spectroscopy is an attractive way to study the vibrational and rotational modes of different materials, as well as a useful diagnostic tool for quantitative and qualitative chemical analysis of diverse materials and biological samples [1]. Raman spectroscopic measurement is minimally invasive, and highly specific at the chemical fingerprint of a material. It can be done very quickly with a minimal amount (~ microliter) of analyte under test, and without specific sample preparation and the water interference/absorption effects which exist in IR spectroscopy. Raman spectroscopy has great potential for many clinical and medical applications, such as detecting and measuring drug concentrations or rapid detection of relevant biomolecules and glucose in blood [2,3]. The example of the Raman clinical applications I explored in my PhD studies was using Raman spectroscopic technique to measure the heparin concentration in blood during open-heart surgery respectively.

One of the main problems during open-heart surgery is the time required to measure the concentration of heparin in the blood. Heparin is an anticoagulant that is injected to a patient's blood during surgery to prevent blood coagulation in the body [4, 5]. With conventional techniques, the heparin concentration is measured using some chemical techniques and processes that typically take three to five minutes [5]. Therefore there is a need for a faster method, one that can measure the heparin concentration of the blood in the operating room in less than a minute. Raman spectroscopy is a promising candidate [6, 7].

The main obstacle to using Raman techniques for such applications is the weak generated Raman signal, particularly at low-level concentrations of the analyte, which is often the case at the clinical level. Therefore, any technique that can enhance the Raman signal of a biological analyte would have many potential applications in medicine and biology.

The initial goal of my thesis was to develop a Raman signal enhancement mechanism that would improve the detection of the Raman signals of biological samples for clinical and medical applications, including monitoring the glucose and heparin concentrations of a blood sample.

2.1.2. Contributions

After joining Dr. Anis's group, I improved the existing Raman setup in order to get clean Raman spectrum of different analytes. Then, in collaboration with Master's student Altaf Khetani, we designed and implemented a Raman set-up using non-selective filling, i.e. filling all channels and the core, of HC-PCF. In our novel approach, a 1550 HC-PCF was non-selectively filled with a liquid analyte (ethanol, $n_a = 1.36$), and the HC-PCF band-gap central wavelength shifted from 1550 nm to 748 nm. We coupled a 785 nm excitation laser to the core of the filled HC-PCF, and then obtained the Raman spectrum of ethanol in the fiber core. Using a relatively short 9.5 cm length of HC-PCF, we achieved a spontaneous Raman signal enhancement factor of 40 over a bulk solution of ethanol [8, 9]. And by combining non-selective filling of HC-PCF and nanoparticles, we further increased the Raman signal enhancement. In our first experiment, we filled a 7.9 cm length HC-PCF fiber with a solution of Rhodamine 6G and silver nanoparticles (for SERS), and were able to demonstrate a 400 times Raman signal enhancement [10]. After this, I concentrated my research on CARS microscopy.

The idea of measuring the heparin concentration in a blood sample was further explored by my colleagues, using non-selective filled HC-PCF. This ultimately resulted in successful detection of the heparin Raman signal of a clinical concentration heparin sample [7].

2.2. Basics of Raman and weak Raman signal problem

When an incident flux of photons (I_0) collides with a molecule, the photons are scattered without changing the molecule's energy if the collisions are perfectly elastic, as in equation (2-1).

$$I = I_0 \ (8 \pi^4 N \alpha^2/R^2\lambda^4) (1+ \cos^2 \theta) \qquad (2\text{-}1)$$

where I is the scattered photon flux, N is the number of the scatterer, α is the polarizability of the atom or molecule, R is the distance from the scatterer site, λ is the wavelength of the incident light, and θ is the angle between the direction of incident light and the observer.

In contrast, if there is an energy exchanged between photons and the molecule, the collision is inelastic. The molecule can gain or lose discrete amounts of energy according to the vibrational or rotational energy levels of its quantum energy level, and the exchanged energy should be equal to a transition between two vibrational or rotational molecular energy levels (Figure 2-1).

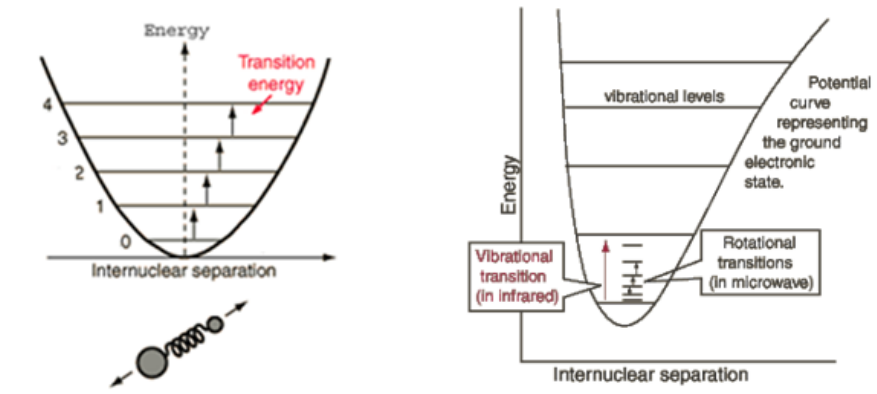

Figure 2-1: A Schematic view of the vibrational and rotational energy levels of a molecule [11].

The induced external molecular electric dipole momentum P can be written as:

$$P = \alpha E \tag{2-2}$$

$$\text{where } E = E_0 \cos(2\pi\nu_{Photon} t), \tag{2-3}$$

E_0 is the amplitude of the electric field of the incident light, ν_{Photon} is the incident photon frequency, and α is the polarizability of the molecule.

For example, a diatomic molecule vibrates at the fundamental frequency of ν_{vib}, so we can write:

$$\alpha = \alpha_0 + \Sigma\, \alpha_m \cos(2\pi m \nu_{vib} t) \qquad m = 1, 2, 3\ldots \tag{2-4}$$

From (2-2), (2-3), and (2-4) we will have:

$$P = \alpha_0 E_0 \cos(2\pi\nu_{Photon} t) + 0.5\, E_0 \sum_m \alpha_m \{\cos[2\pi t(\nu_{Photon} - m\nu_{vib})] + \cos[2\pi t(\nu_{Photon} + m\nu_{vib})]\}$$

$$= \alpha_0 E_0 \cos(2\pi\nu_{Photon} t) + 0.5\, E_0 \{\sum_m \alpha_m \cos[2\pi t(\nu_{Photon} - m\nu_{vib}) + \sum_m \alpha'_m \cos[2\pi t(\nu_{Photon} + m\nu_{vib})]\} \tag{2-5}$$

Where α_m is the mth-order of the polarizability at the Stokes frequency band and a'_m is the mth-order of the polarizability at the anti-Stokes frequency band.

The first term of equation (2-5) shows the elastic scattering and the molecules radiating at the exact frequency of the incident light (Rayleigh scattering).

The second term shows that the molecule will scatter the incident light by frequencies:

$$\nu_{Stokes} = \nu_{Photon} - m\nu_{vib} \qquad m = 1,2,3\ldots \tag{2-6}$$

These new frequencies are called Stokes frequency bands, and are frequencies lower than the incident light frequency.

The last term shows that light can also be scattered at frequencies higher than the incident light frequency:

$$\nu_{\text{anti-stokes}} = \nu_{\text{Photon}} + m\nu_{\text{vib}} \qquad m=1,2,3\ldots \quad (2\text{-}7)$$

This band of frequencies is called the anti-Stokes band. In general $\alpha_m > \alpha'_m$, but both are smaller than α_0 ($\alpha_0 >> \alpha_m > \alpha'_m$) [1].

Thus, with inelastic regime scattering, the scattering site will also scatter the incident light at different discrete frequencies that are lower or higher than the initial frequency of the incident light. However, most of the incident photons will be scattered elastically at the frequency of the incident light.

This type of inelastic scattering is called Raman scattering (or, in general, spontaneous Raman scattering [1]). It is named after C.V. Raman, the Indian scientist who discovered the effect.

The difference between the scattered frequency and the initial frequency of the incident light is different from one molecule to another, as it is proportional to each molecule's unique vibrational frequencies. Therefore, Raman scattering (or spectroscopy) can be used to study the vibrational and rotational states of different molecules (vibrational spectroscopy), and to detect, analyse, image and measure different materials for diverse applications in physics, chemistry, biology, medicine, astrobiology and others, on both laboratorial and industrial scales.

One of the main obstacles in Raman spectroscopy is the extremely weak Raman signal. For example, a chemical sample with a concentration of approximately one millimolar absorbs 90 percent of the incident light over a 1 cm path length, while about 1 in 10^{10} incident photons will experience Raman scattering in this case [1].

The second problem with the Raman technique is background fluorescence. The visible or UV light which was typically used for Raman spectroscopy excites fluorescence of the analyte or impurities more than the recently used near-infrared sources. The fluorescence effect is not a scattering process, and the fluorescence emission spectrum from most liquids and solids does not have the fine vibrational structure observed in the Raman spectrum. However, even a weak fluorescence signal can be much stronger than the Raman signal of the analyte, and easily overwhelm it [1].

These two fundamental problems must be considered in all Raman setups.

2.3. Raman signal enhancement using HC-PCF

Since the generated Raman signal is very weak, it must be enhanced to be useful for many biological/medical applications. Enhancing the Raman signal decreases the need for higher intensity excitation light and/or longer signal acquisition time, both of which limit the biological/clinical applications of Raman spectroscopy/microscopy.

Since the Raman effect was discovered, many methods to enhance the Raman signal of a sample have been suggested and attempted.

During my PhD research, I have focused on increasing the interaction length of the excitation light (laser) with the test analyte, using Hollow Core Photonics Crystal Fiber (HC-PCF) to enhance the Raman signal of the analyte. In the following, I present a literature review regarding enhancing the Raman signal using hollow core fiber followed by the different methods to fill an HC-PCF fiber.

2.3.1. Literature review on increasing the interaction length of excitation light and sample under the test

The most apparent method to enhance the Raman signal is to increase the interaction length of the excitation light and the analyte. The 'figure of merit' is often used to quantify Raman signal enhancement [12]. It is defined as the quantity required to characterize the performance of a new method relative to its alternative conventional method. The Raman figure of merit is expressed as:

$$M = \frac{L_{int}\lambda}{A_{eff}} \tag{2-8}$$

where λ is the excitation light wavelength, L_{int} is the effective constant interaction length, and A_{eff} is the effective cross-sectional area.

As (2-8) shows, the figure of merit can be increased using mirrors and reflectors, or by increasing the intensity of the excitation light with higher focus. However, these techniques do not significantly increase the Raman signal [1].

Using a laser as a source, in conjunction with long hollow core fibers, provides a feasible platform for enhancing the Raman signal of liquid samples, by increasing the interaction length

of the laser and analyte. Figure 2-2 shows one of the first experimental setups using this approach. A 20 meter hollow core quartz fiber with a core diameter of ~75 μm was filled with the benzene and tetrachloroethylene. Due to the internal reflection inside the fiber ($n_{benzene} > n_{quartz}$), the excitation beam was trapped and internally reflected. It then travelled through the core of the filled fiber, which increased the interaction length by 2 to 3 orders of magnitude compared to a conventional Raman signal [13, 14].

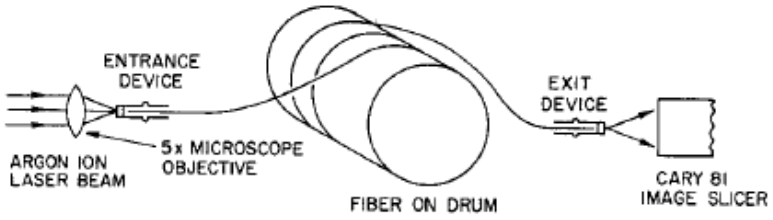

Figure 2-2: Enhancing Raman spectra of benzene using a 20 m filled hollow core benzene filled quartz fiber [13].

However, as the signal is guided by total internal reflection, the refractive index of the analyte being tested must be higher than the refractive index of silica. Thus, as most biological analytes have refractive indexes less than 1.46, it is not possible to use this method to enhance the Raman signal of biological samples.

Photonic Crystal Fibres (PCF) could provide a robust platform for enhancing and measuring the Raman spectra of different analytes [15]. Pristinski et al [16] were the first to show that solid core PCFs could be used as biosensors to measure the Raman spectra of different analytes. They filled the PCF channels with the analyte of interest, and coupled a laser light to the solid core of the fiber. However, as the Raman signal is generated from the interaction of the analyte with the evanescent optical field, the Raman signal enhancement was limited to 4-5 times for a 10 cm length filled PCF [16-17].

The recent advent of hollow-core photonic crystal fibers [15], which consist of a hollow (air-filled) core surrounded by air holes running down the length of the fiber, provides a unique opportunity to enhance the Raman signal. HC-PCF potentially as an efficient biosensor is due to the large overlap between the propagating field and the sample. Moreover, only very small

volume is required to fill the holes of HC-PCF, which is highly advantageous in the case of hazardous or expensive substances.

HC-PCF can be filled selectively or non-selectively. With selective filling, only the hollow core of the fiber is filled with the analyte of interest, while with non-selective filling, both the hollow core and the cladding channels are filled. Several groups have reported selective filling of the HC-PCF core. However, the process is very cumbersome, and restricts the choice of liquid to avoid multimode behaviour [17-18].

The Raman signal can also be enhanced by using a surface-enhanced Raman scattering approach using silver/gold nano-particles [19].

The first SERS example of pyridine adsorbed on a silver surface, that had been roughened by repeated electrochemical oxidation and reduction in chloride solution, was observed by Fleischmann et al [20]. The strong scattering intensity was initially referred to a high microscopic surface area produced by repeated cycling between AgCl and Ag metal. However Jeanmaire and Van Duyne later found that the signal was too strong to be attributed only to chemical surface enhancement, and they proposed electromagnetic enhancement phenomenon [21]. SERS has broad applications due to its high signal enhancement, particularly in medicine, and with biosensors to detect diluted samples or single molecules [1, 22, 23].

Further Raman signal enhancement is achievable by combining the SERS and HC-PCF Raman interaction length enhancement methods, [10, 24, 25] and this is a great opportunity to design a highly sensitive fiber-based Raman biosensor.

2.3.2. Filling an HC-PCF

An HC-PCF can be filled either selectively or non-selectively:

Selective filling: With the selective filling method, only the core of the HC-PCF is filled with the analyte being tested, while sealing off the cladding holes.

There are a few methods to do selective filling [26, 27], but in general selective filling is a time consuming process that requires multiple steps. For example when applying the overhead pressure method for filling an HC-PCF [28], the steps are:

i) Fill HC-PCF with adhesive under pressure and cure with a UV light source, then cleave the fiber at a point where the polymer seals only the center hole;

ii) Fill the cladding holes with adhesive so they are filled more than the core. The fiber is then cured and cleaved so that the core remains empty; then,

iii) Fill the core with the desired analyte. Finally, the fiber is cleaved to remove the polymer region in the cladding holes.

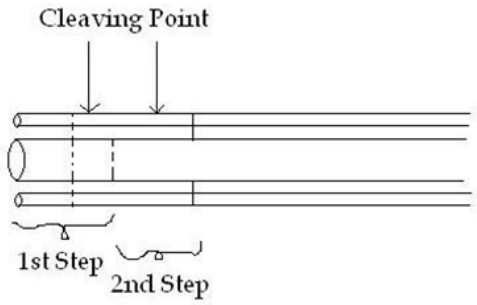

Figure 2-3: The schematic view of 2 steps of selective filling of a HC-PCF [28].

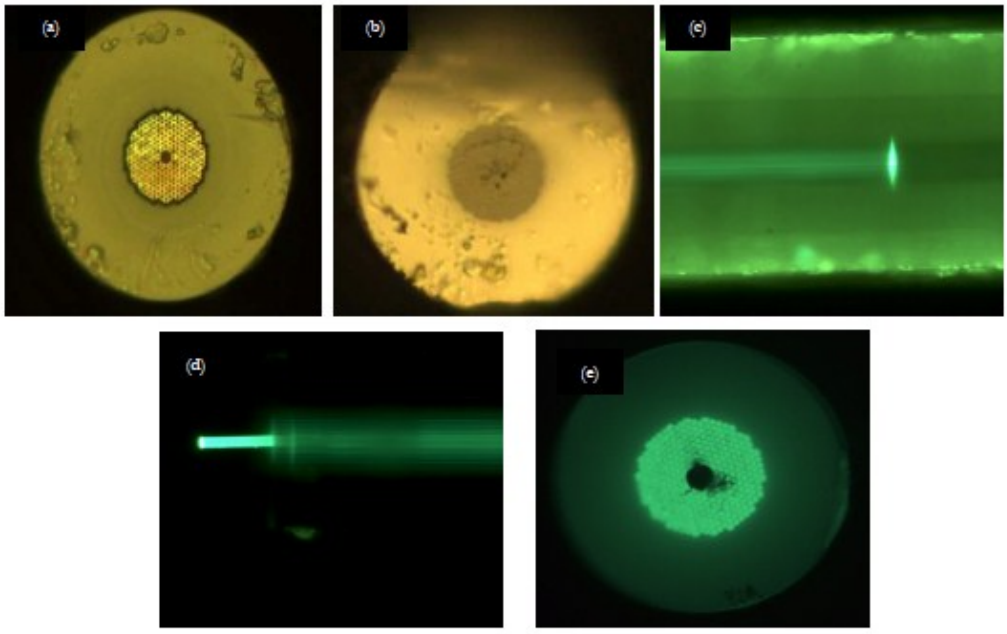

Figure 2-4: Various steps of selective filling of a HC-PCF.
(a) A cross sectional view of an empty HC-PCF. (b) Cross sectional view HC-PCF when all channels and core were filled with adhesive. (c) Traveling UV cured adhesive in the central channel of HC-PCF (d) Vertical view of HC-PCF. (e) Cross sectional view of HC-PCF after second step, showing the empty central core ready to be filled with desired analyte [28].

With selective filling, normal total internal reflection will occur which will result in restriction of the sample choices to avoid highly multimode behavior. In addition, this method is cumbersome and time-consuming, as it involves precise filling of the fiber with adhesives

multiple times, and cleaving at specific locations. This leads to fiber cuts and length limitations. Moreover, the liquid filled in the core tends to evaporate as time goes by, requiring the fiber to be selectively filled again.

Non-selective filling: in non-selective filling of the HC-PCF, the core and cladding holes of the fiber are both filled non-selectively with the sample. In this case, the light is still guided by the band-gap effect, and the fiber transmission wavelength band shifts depend on the refractive index of the sample [29]. The new band-gap shifted wavelength λ' for an HC-PCF filled with an analyte with refractive index n_a is defined as:

$$\lambda' = \lambda_0 \left[\frac{1 - \left(\frac{n_a}{n_{sil}} \right)^2}{1 - \left(\frac{n_{air}}{n_{sil}} \right)^2} \right]^{1/2} \tag{2-9}$$

where λ_0 is the original band-gap central wavelength, n_{sil} is the refractive index of the silica (fiber material), and n_{air} is the refractive index of the air.

This technique is much simpler to implement, and the evaporation problem is addressed by inserting a reservoir filled with the liquid at one end of the fiber.

2.4. Background of the experimental setup and results

When I joined Dr. Anis research group, I first improved an existing Raman setup by finding and eliminating generated background noise sources, developing methods and procedures to acquire forward Raman spectra of many liquid samples. I then began to detect and measure the concentration of glucose and heparin in aquatic samples in order to design a non-invasive Raman biosensor using the improved setup.

Figure 2-5 shows my initial setup, which was used for Raman spectroscopy. For excitation light, I used a multimode 500 mW fiber coupled laser (1) at 784.95 nm and full-width half-maximum (FWHM) of 0.112 nm from BMTEK (BRM-785E). The beam from the laser diode was coupled to a multimode (D = 100 μm, NA. = 0.22) delivery fiber cord (2) guided to the setup. The laser beam out of the fiber was collimated by a short focal length lens (3a), and passed through a 785 nm IRIDIAN band pass filter (4) to remove all the sideband parts of the laser beam and the generated stimulated silica Raman signal of the guiding multimode fiber (Figures

2-6). The collimated, filtered laser beam was focused inside a fused silica cuvette filled with the analyte (5), by means of a short focal length lens (3b). The output beam entered a long pass IRIDIAN PN-ZX000445 785 nm filter (6) to remove most of the excitation laser light at 785 nm. The scattered Raman and Rayleigh signal (6) was collected using a multimode collecting fiber bundle consisting of 39 100 μm core multimode fibers arranged in a circular pattern at the collection end and fixed linearly at the output end (Optical Fiber Systems Inc.) (7). It was then guided to a Kaiser f/1.8 spectrograph (8) with a 785 holographic notch filter (OD = 5) and a TE-cooled Andor CCD camera (9) for detecting the Raman spectra. The output of the CCD detector was sent to a computer for recording and analysing the resulting data.

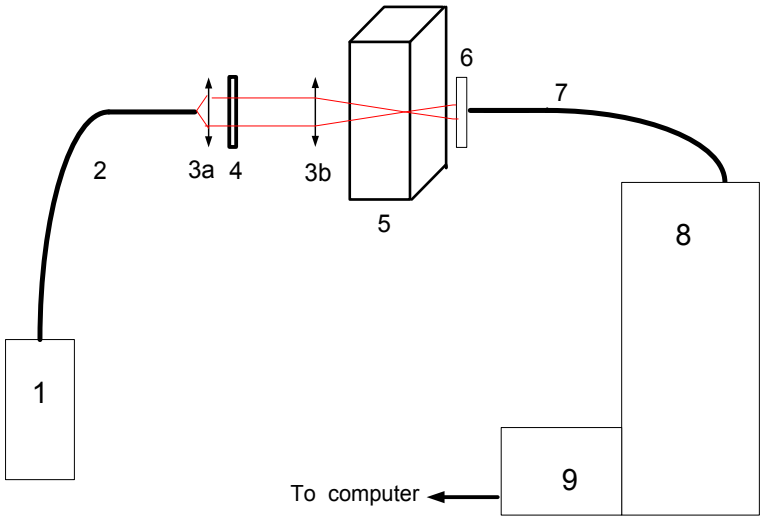

Figure 2-5: The modified initial Raman setup, which I modified and used.

An ethanol sample was used to test and adjust the setup. To acquire a clean ethanol Raman signal, all defined background noises, which included silica Raman spectra, laser sideband and CCD noises, were subtracted from the raw Raman signal of the ethanol. After calculating and estimating the background noise, it was subtracted from the raw spectrum using Andor CCD camera software. Figure 2-7 shows the pure ethanol spectra of the ethanol sample.

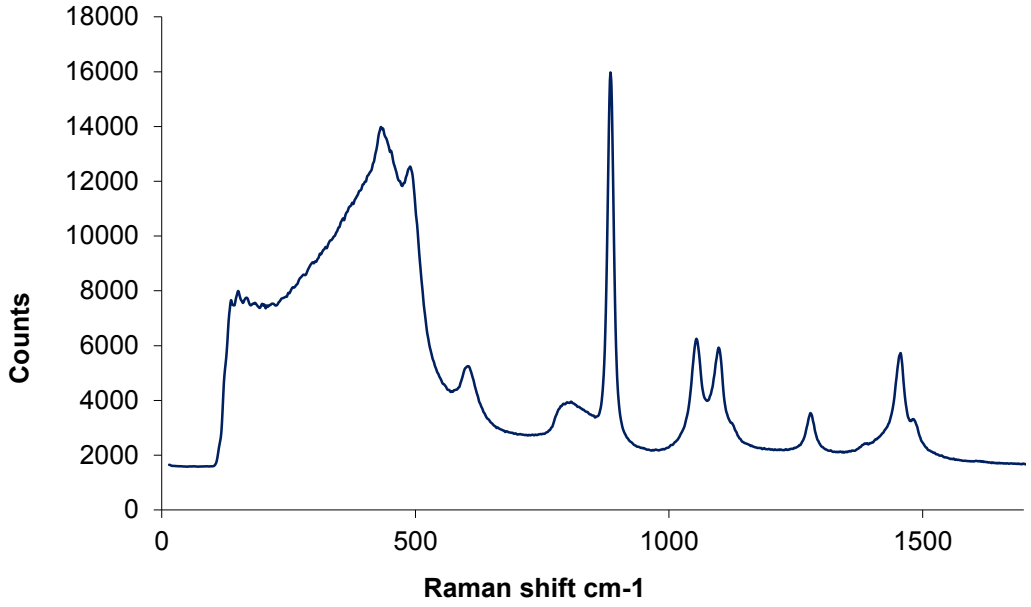

Figure 2-6: The raw Raman spectra of 95% ethanol in the cuvette, plus the background noise of Silica Raman spectra, laser sideband and CCD noise. Laser power of the sample = 253 mW, exposure time = 1s.

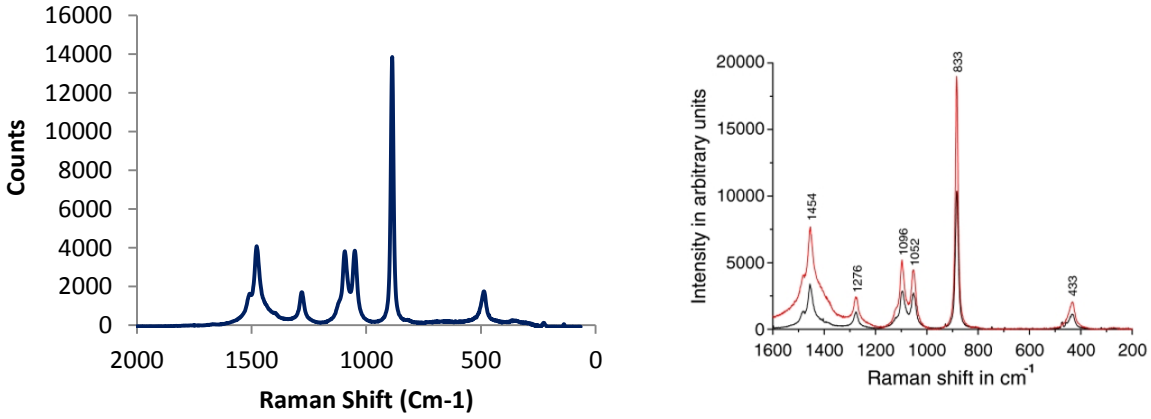

Figure 2-7: Acquired clean Raman Spectra of 95% ethanol sample in the cuvette (left), and reference ethanol Raman spectra (right)[30].

The Raman spectra of concentrated heparin and glucose aquatic samples were then acquired.

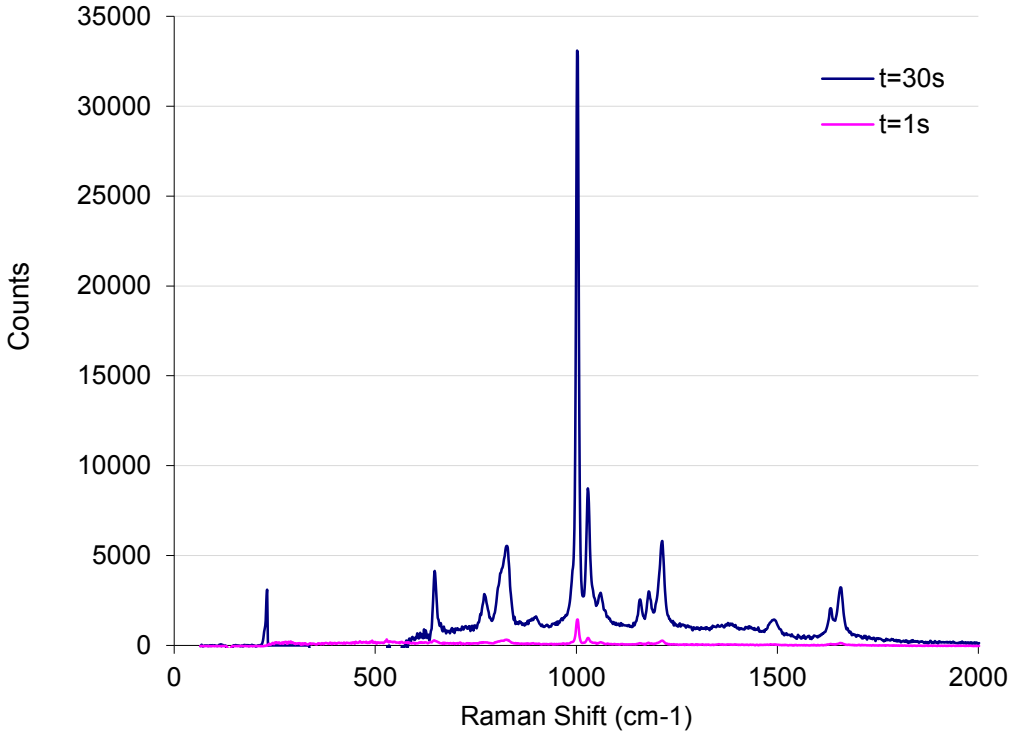

Figure 2-8: The acquired Raman Spectra of the concentrated heparin (>20000 units) for two different acquisition times, 1s and 30 s. CCD temperature T = -70 ºC.

I could not detect and measure the heparin concentration when it was reduced to clinical concentrations levels with our improved conventional Raman setup. Various attempts and measurements were performed, but no results were obtained. Based on this work, it became obvious that there is a need to enhance the Raman signal. So my colleague, Altaf Khetani, and I proposed the idea of using a hollow core photonic crystal fiber (HC-PCF) to enhance the Raman signal of the analyte. Accordingly, the idea of non-selective filling of the HC-PCF for Raman bio-sensor application was developed.

Figure 2-10 shows our experimental setup using HC-PCF to enhance the Raman signal of an ethanol sample. To couple the laser light to the single mode HC-PCF, a single mode 100 mW 14-pin butterfly laser (1) from Innovative Photonic Solutions (I0785SB0100B) was used. The laser beam divergence angle was measured at 0.00098 rad, and was not purely single mode, though most of its energy was in single mode propagation. The beam was reflected by a silver-coated mirror (2), and passed through a 785 nm IRIDIAN band pass filter (3). It was coupled to a filled

ethanol HC-PCF (HC-1550-02, Crystal Fiber Inc.) (5), by means of a 40X Newport microscope objective lens with numerical aperture = 0.65 (4). After passing through a long pass filter (IRIDIAN PN-ZX000445 785 nm) the output beam (6) was collected by a multimode collecting fiber bundle (7), and guided to a Kaiser f/1.8 spectrograph (8) with a TE-cooled Andor CCD camera(9).

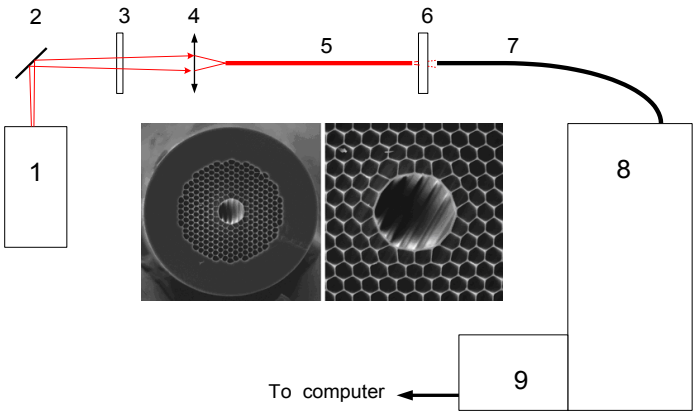

Figure 2-9: Raman signal enhancement using new Raman setup.

Using this new method, Raman measurement of the heparin concentration was done as follows:

First, the HC-PCF was filled with pure water, then the background Raman spectra (containing all attainable background spectra) of the new setup was recorded. The HC-PCF was then filled with a heparin sample (10000 units), and the Raman spectrum of the PCF was recorded. The clean heparin Raman spectra were achieved by subtracting the recorded background Raman spectra from the acquired heparin spectra. Figure 2-11 shows the results:

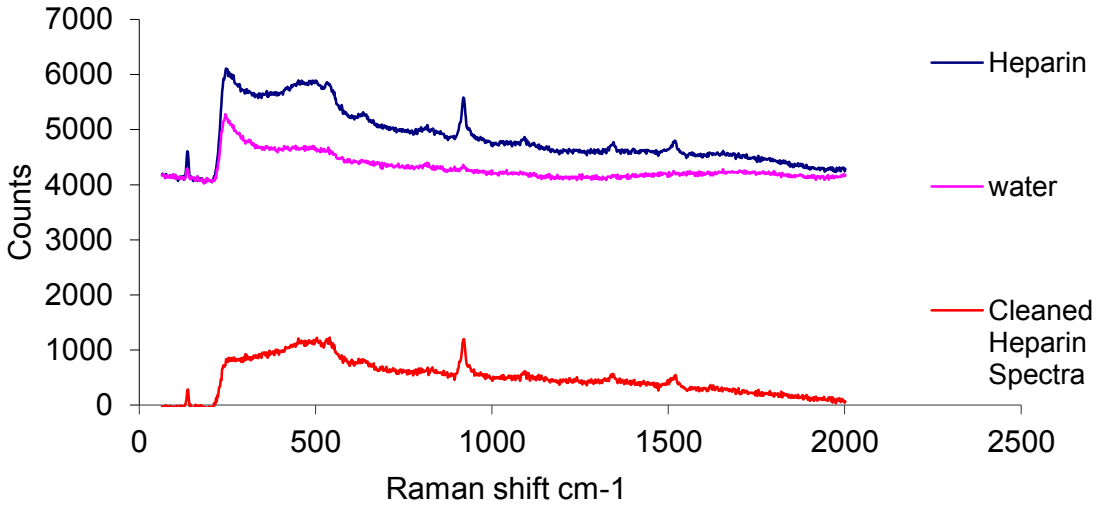

Figure 2-10: The heparin enhanced Raman spectra using HC-PCF.

The clinical heparin dose is approximately 300 units/Kg of the patient's weigh [4]. The blood volume of a male patient is about 5 liters, so injecting a patient weighing 100 kg with 1 millilitre of 30000 units of heparin, will produce an average heparin concentration in the patient's blood of approximately 6 units/cc. To test the new setup, I filled the HC-PCF with a 10 units/cc heparin solution, but I was unable to detect any spectra peaks to measure the heparin concentration, despite many attempts. Therefore, even after enhancing the Raman signal using HC-PCF, my approach was still not sensitive enough to detect a clinical concentration of heparin. However, by applying a backscattering collection method, improving the coupling efficiency of the laser to the HC-PCF, and using partial least squares (PLS) analysis, my colleagues were able to detect clinical heparin concentration in the samples using our modified Raman setup [7].

2.5. Conclusions

Combining a conventional Raman setup with a non-selectively filled HC-PCF setup resulted in a novel HC-PCF based Raman biosensor for enhancing the Raman signal of biological analytes.

Using a 9 cm length of ethanol filled HC-PCF as a Raman platform, and coupling it with a 780 nm laser beam, achieved a 40 times Raman signal enhancement with a forward signal collecting configuration.

The simplicity of this method to achieve a reasonable Raman signal enhancement, combined with the high degree of overlapping of the propagating mode with the analyte and the small sample volumes requirement, make it a promising candidate for a sensitive, low power biosensor for the identification of biological specimens, particularly for clinical applications.

In addition, by using this novel non-selective HC-PCF method, we can overcome the total internal reflection confinement issue of hollow core fibers, and use analytes with refractive indexes less than that of silica.

2.6. Related publications

A. Raman signal enhancement using HC-PCF

2.6.1. Majid Naji, Altaf Khetani, Neil Lagali, Rejean Munger, Hanan Anis, "*A novel method of using hollow core photonic crystal fibre as a Raman biosensor*" Photonics West, Proc. SPIE 6865, Nanoscale Imaging, Sensing, and Actuation for Biomedical Applications V, 68650E, February 13, 2008 .

2.6.2. Altaf Khetani, Majid Naji, Neil Lagali, Rejean Munger, Hanan Anis, "Method for using a photonic crystal fibre as a Raman biosensor" US Patent 7,738,097. 2010

A. Raman signal enhancement using HC-PCF

Novelty

We have demonstrated a novel method to enhance the Raman signal using HC-PCF. A 40 times Raman signal enhancement of ethanol spectra by using a 9 cm filled HC-PCF was achieved. This is a promising approach for enhancing the weak Raman signals of biological samples, since this method needs relatively low laser power (less than 100 mW) as well as small amount of the sample(~microliters).

Contribution

Altaf and I came up with the idea and conducted the experimental measurements based on my modified Raman set-up. Dr. Lagali assisted us with the experiment and through many fruitful discussions.

The results of our idea and experiment were published in a conference paper (Photonics West 2008) and we were awarded a US patent.

2.6.1. A novel method of using hollow-core photonic crystal fiber as a Raman biosensor

Majid Naji [a], Altaf Khetani [a], Neil Lagali [b], Rejean Munger [b], Hanan Anis[a]

[a] Department of Electrical Engineering, School of Information Technology and Engineering, University of Ottawa, Ottawa, Canada
[b] Ottawa Health Research Institute and The Ottawa Hospital, Ottawa, Canada

ABSTRACT

A new method for using a non-selectively filled hollow-core photonic crystal fiber (HC-PCF) as a sensitive Raman spectroscopy platform suitable for biosensing applications is presented. A 1550 HC-PCF was completely filled with ethanol (core and cladding holes). Using a 785 nm excitation laser, the Raman spectrum of ethanol in the fiber core was obtained and compared with the equivalent Raman spectrum of an ethanol-filled cuvette. Using a relatively short 9.5 cm length of HC-PCF, a Raman signal enhancement factor of 40 over a bulk solution of ethanol was observed under the same excitation conditions. The small sample volume utilized and longer interaction length provides the potential for compact, sensitive, and low-power Raman sensing of biological materials

Key words: Hollow-core, photonic crystal fiber, Raman spectroscopy, biosensors, non-selective filling

INTRODUCTION

Raman spectroscopy has been widely used for quantitative concentration measurement of analytes in solid and liquid biological specimens; however, the main drawback is a weak Raman signal, which can be improved by increasing the laser intensity, enhancing the quality of transverse beam profile or increasing the laser beam interaction length in the analyte media. A hollow-core waveguide supporting a single transverse mode with low attenuation losses and long interaction length could simultaneously deliver all the above requirements for enhancing a Raman signal.

The recent advent of hollow-core photonic crystal fibers (HC-PCF), which consist of a hollow (air) core surrounded by air holes running down the length of the fiber, provide a unique opportunity to enhance the Raman signal beyond levels reported in evanescent-type PCF sensors.[1]

HC-PCF has generated a lot of interest as a chemical and biological sensor [2-4]. HC-PCF potential efficiency as a biosensor is due to the large overlap between the propagating field and the sample. Moreover very small volumes are required to fill the holes of HC-PCF, which is highly advantageous in the case of hazardous or expensive substance.

There are two ways to fill HC-PCF and use it as a sensor. The first method is by selective filling of the fiber core with a sample while sealing off the cladding holes. The main drawback of this method is that the process of filling the fiber is cumbersome and restricts the sample choice to avoid highly multimode behavior [5].The other method is to simply fill both the core and cladding holes non-selectively with the sample [6]. In this case, the light remains guided by the bandgap effect and the fiber transmission wavelength band, shifts depending upon the refractive index of the sample.

In this paper, we fill the HC-PCF entirely (non-selectively), as done previously by others [7, 10], however, to our knowledge this is the first report of the acquisition of a spontaneous Raman spectrum in a non-selectively filled HC-PCF. The use of this method of Raman spectroscopy is particularly well-suited for biological sensing applications

where low-power laser irradiation is needed to maintain sample integrity, or where only small sample volumes are available.

METHODS

2.1 Experimental setup

Figure 1, shows the experimental setup. A single mode 100 mW 14 pin butterfly laser (1) from Innovative photonic solutions (I0785SB0100B), reflected by a silver coated mirror (2) and passed through a 785 nm IRIDIAN band pass filter (3).The laser beam was coupled to a filled ethanol HC-PCF (HC-1550-02, Crystal Fiber Inc) (5) by means of a X40 Newport microscope objective lens with Na. =0.65 (4). The output beam after passing a long pass filter, IRIDIAN PN-ZX000445 785 nm, (6) was collected by a multimode collecting fiber bundle (7) and guided to a Kaiser f/1.8 spectrograph (8) with a TE-cooled Andor CCD camera (9).

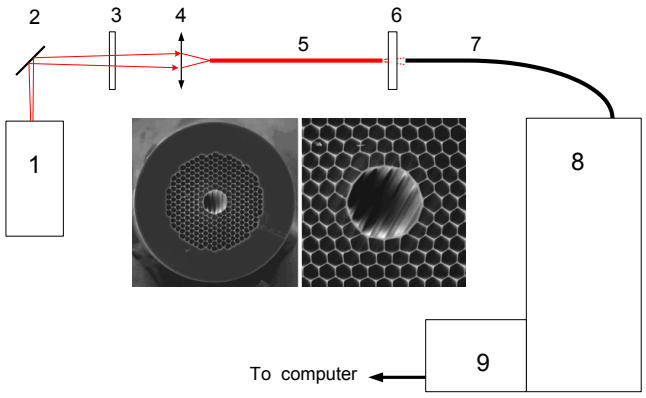

Figure 1: A schematic view of the experimental setup.

2.2 The choice of the HC-PCF:

The guiding property of the HC-PCF changes depending on the refractive index of the sample. In this case, the guiding principle is still due to bandgap effect but the transmission band supported by the fiber is shifted. The shift in wavelength can be determined from the equation given by Russell et al [7, 13, 14], by changing the refractive index n_{air} to the refractive index of the liquid n_{liq} and the shifted wavelength is given by

$$\lambda' = \lambda_0 \left[\frac{1 - \left(\frac{n_{liq}}{n_{sil}} \right)^2}{1 - \left(\frac{n_{air}}{n_{sil}} \right)^2} \right]^{1/2} \quad (1)$$

Where λ_0 is the wavelength at which the bandgap originally occurs, and λ' is the wavelength of the shifted bandgap. Therefore depending on the excitation wavelength, one needs to find a fiber which would guide this wavelength when filled. A list of fibers which would guide when empty and when filled with 3 different liquid is given in Table 1.

In our experiment, the excitation wavelength was 785 nm and HC-PCF was to be filled by ethanol, hence a *HC*-PCF-*1550* was used

Liquid	*Fiber Type* / *Refractive Index*	*HC- 440*	*HC-580*	*HC-633*	*HC-800*	*HC-1060*	*HC-1550*
Empty	n = 1	440(410-470) nm	*580* (515-595) nm	*633* (570-690) nm	*-800* (795-880) nm	*1060* (990-1150) nm	*1550*(1450-1650) nm
Water	n = 1.33	249(232-266) nm	328(291-336) nm	358(322-390) nm	452(450-498) nm	600(560-651) nm	877(820-934) nm
Acetonitryl	n = 1.34	236(220-252) nm	311(276-319) nm	339(306-370) nm	429(426-472) nm	569(531-617) nm	832(778-886) nm
Ethanol	n = 1.36	212(198-227) nm	280(248-287) nm	305(275-333) nm	386(384-425) nm	512(478-555) nm	748(700-797) nm

Table1: Band-gap shift of different HC-PCF fibers for three different liquid (all values are in nm). Numbers in parenthesis are the calculated shifted bandgap (according to Eq. 1)

2.3 Non-selective filling of HC-PCF with lower refractive index material:

In this method HC-PCF's core as well as the cladding channels are filled with the material to be sensed. This technique is much simpler to implement and the problem of evaporation is addressed by inserting a reservoir filled with the liquid at one end of the fiber. The reservoir is shown in Figure 2, and uses a syringe needle whose broader end is filled with liquid and glued with a glass cover slip, while the fiber is inserted into the other end. The reservoir ensures that the liquid is continuously supplied inside the fiber channels to replenish any evaporated liquid.

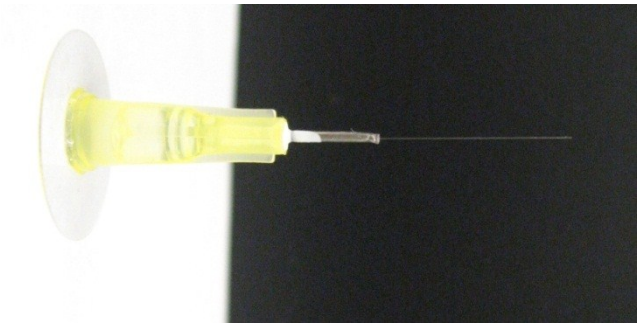

Figure 2: Reservoir (syringe needle) in nonselective filling HC-PCF method.

2.4 Coupling laser light to filled PCF

Filling an HC-PCF non-selectively with 99% pure ethanol (n = 1.36) results in a blue-shift of 765nm in the central bandgap wavelength [12] .For an excitation laser wavelength of 785nm, we therefore chose an HC-PCF designed for

use at 1550nm (HC-1550-02, Crystal Fiber Inc.). Using a finite-element model of this HC-PCF (developed with COMSOL Multiphysics version 3.1and Matlab R13); single-mode operation of the ethanol-filled fiber was confirmed at 785nm and persisted to a wavelength of 890nm (Figure 3). This result predicts the guidance of Raman-shifted light in a range up to 1500cm^{-1}, which is sufficient for spontaneous Raman spectroscopic fingerprinting of a wide range of materials.

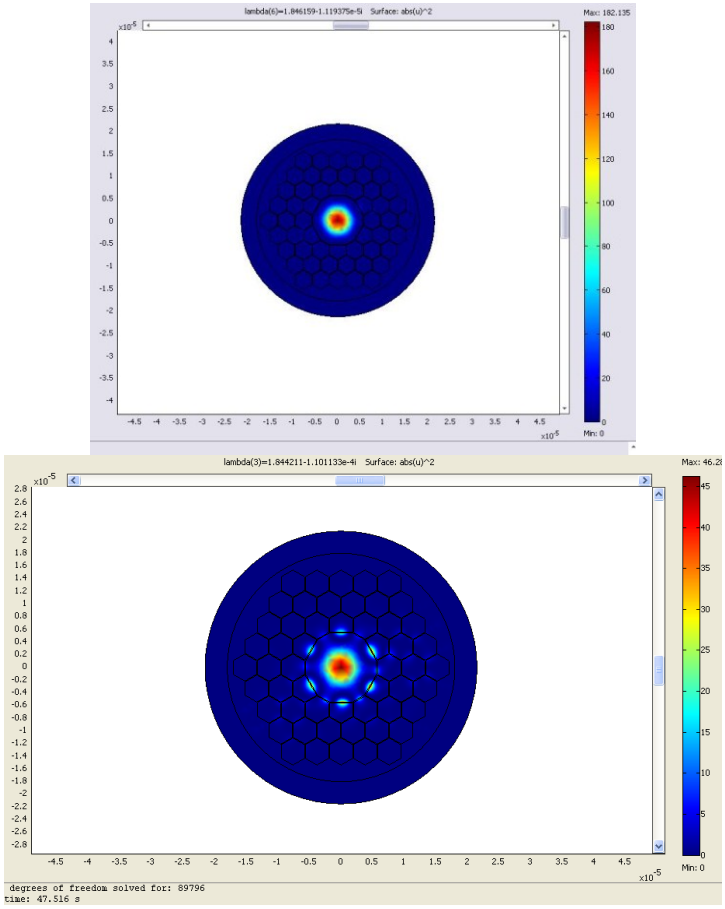

Figure 3: Simulatated mode field intensity in HC-1550-02 PCF filled with ethanol at 785 nm (top) and 890nm (bottom).

A 100 mW single-mode laser emitting at 785 nm was used as our excitation source. The beam divergence angle of the laser was 0.00098 *rad* and the beam consisted of mostly single and first-order modes (Figure 4).

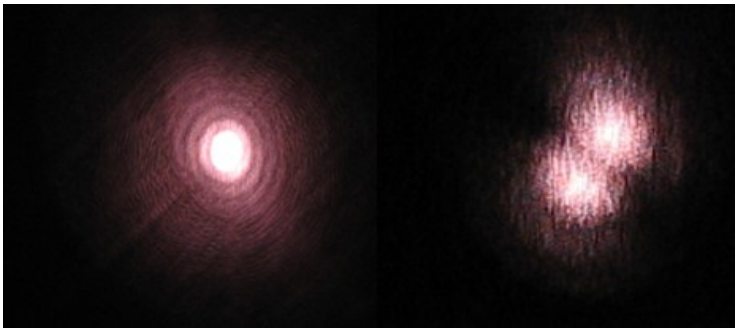

Figure 4: Laser beam was consisted of mostly single and partially second mode.

The laser light after passing a 785 nm band pass filter was coupled to the filled PCF via a X40 microscope objective lens. Coupling laser light to an Ethanol filled Hc-PCF was sensitive, and spurious coupling effects had to be avoided, as they caused a tremendous reduction in Raman generated signal. Therefore the near field laser beam pattern out of the HC-PCF was checked to ensure that the output beam came from the core and not the fiber cladding or jacket (Figure 5).

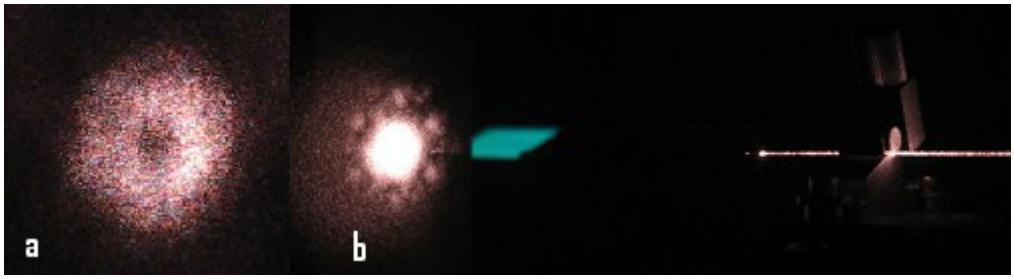

Figure 5: The near field laser beam pattern out of HC-PCF, a) when light came from cladding and jacket b) when it came from core, true coupling

Another effect observed was a change in coupling of the filled fiber over time, originating at the input side of the fiber. Over a few hours, coupling usually became weaker or was lost completely. The exact reason for this is unclear however, we hypothesize that local heating of the fiber tip may have displaced or deformed the fiber over time.

2.5 Measuring the Raman spectra

Light at the output of the non-selectively filled HC-PCF was long-pass filtered to reduce the excitation light and then directly coupled to a collecting fiber bundle consisting of 39 100 μm multimode fibers arranged in a circular pattern at the collection end and stacked in a linear fashion at the output end (Optical Fiber Systems Inc.). The setup of long-pass filtering and then coupling to the fiber bundle proved cumbersome, so it was decided to exclude the long-pass filter and instead record the silica Raman background noise generated in the fiber bundle by the excitation light, and subtract this from each recorded ethanol spectrum (Figure 6).

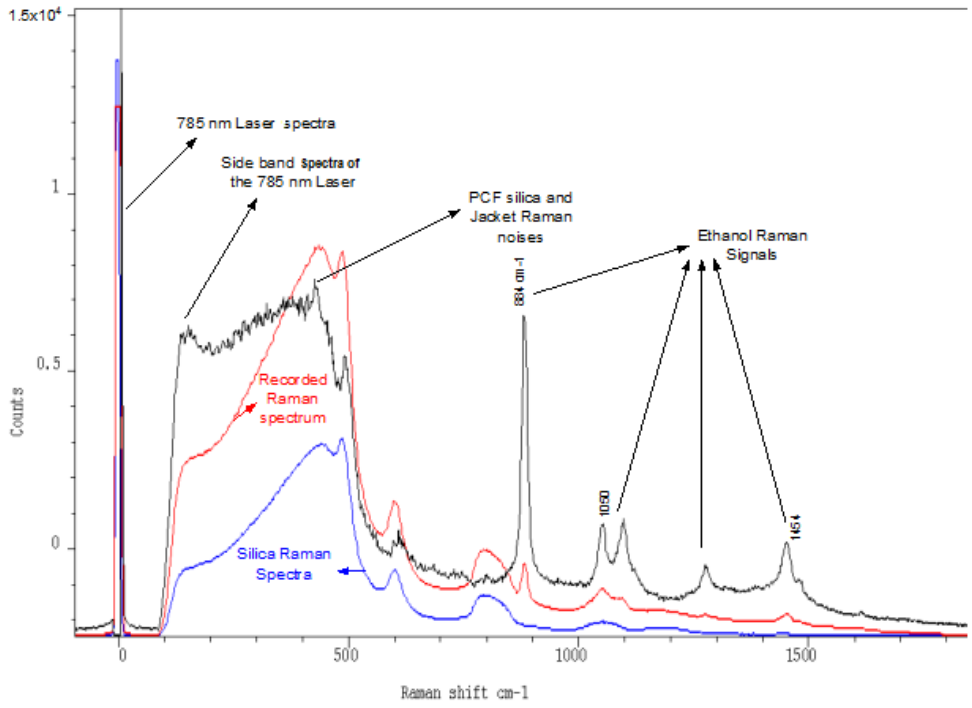

Figure 6: The silica (SiO_2) Raman spectra of the collecting fiber bundle (blue spectra) was subtracted from the recorded Raman spectrum of the ethanol-filled HC- PCF with collecting fiber bundle (red spectrum), to give the pure ethanol Raman spectrum (black spectrum). Because of the785 nm laser side band and spectra generated by the PCF cladding and jacket, the acquired spectra were not completely clean. Note that the black spectrum does not have the same Raman signal count scale, but is expanded for clarity.

3. Results

To derive a Raman signal enhancement factor from the non-selectively filled HC-PCF, the ethanol spectra from 3, 5, 7, and 9.5 cm of filled PCF were acquired and compared with the Raman spectrum from a 1 cm path-length ethanol-filled quartz cuvette. (Figure 7) Using the 885 cm^{-1} ethanol peak from each spectrum, ratios of peak heights were used to determine the enhancement at each HC-PCF length.

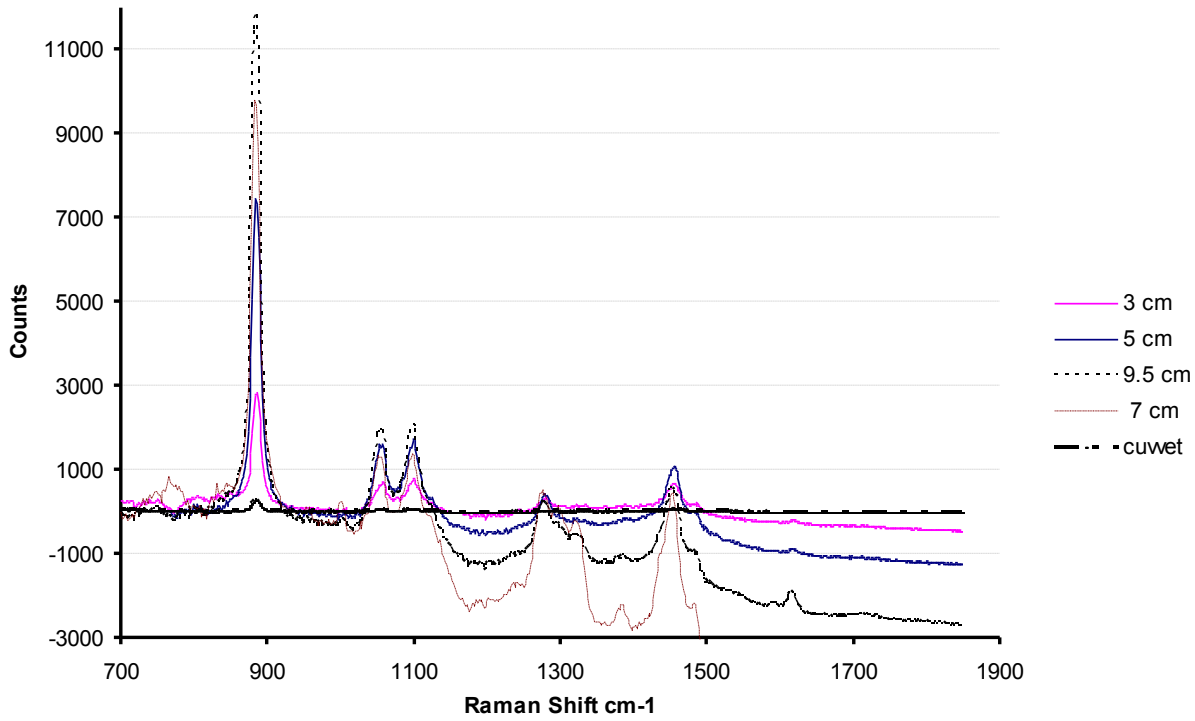

Figure 7: The background-subtracted Raman spectra of ethanol from 3, 5, 7 and 9.5 cm lengths of non-selectively filled PCF, and a 1cm path length quartz cuvette. Because the HC-PCF guiding loss increases by increasing Raman shift of spectrum, spectrum lines with higher Raman shift attenuated more, this attenuation is proportional to the fiber length, therefore here this non-uniformity oin HC- PCF attenuation as a function of Raman shift and HC-PCF length can be easily seen.

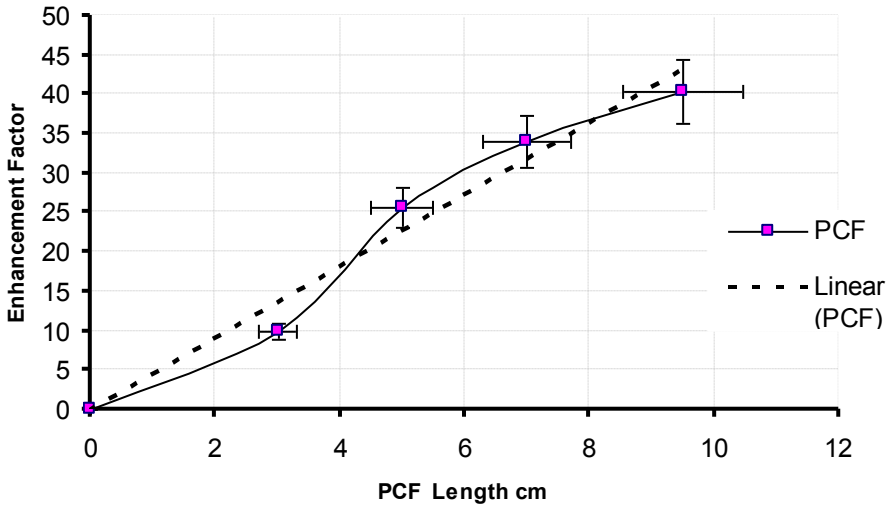

Figure 8: Relative enhancement factor for different HC-PCF length compare to the 1cm path length quartz Cuvette.The bar lines are 10% error bars.

Figure 8 shows the enhancement factor measurements in non-selective ethanol filled HC-PCF as a function of HC-PCF length. In theory for spontaneous Raman we expect a linear relation, by ignoring fiber loss for short fiber lengths, between the interaction length and Raman enhancement factor ^{2}, (black dashed line in figure 8), and so a good correlation between the theory and our measurements was observed.

4. CONCLUSION

In conclusion, we demonstrated a novel Raman spectroscopy platform by filling HC-PCF non-selectively. The simplicity of this method, having reasonable Raman signal enhancement combined with the high degree of overlap of the propagating mode with the analyte and small sample volumes required make it a promising candidate for sensitive, low-power identification of biological specimens.

REFERENCES

1. D. Pristinski , H. Du, "Solid-core photonic crystal fiber as a Raman spectroscopy platform with a silica core as an internal reference", Opt. Lett , **31**, 22, 3246(2006)
2. F. Benabid, J. C. Knight, G. Antonopoulos, P. St. J. Russell , "Stimulated Raman Scattering in Hydrogen-Filled Hollow-Core Photonic Crystal Fiber" , Science , Vol. **298**, 399 (2002)
3. Kristian Nielsen et al, "Selective filling of photonic crystal fibers", J. Opt. A: Pure Appl. Opt. 7**,** L13 (2005)
4. G.E. Walrafen, J. Stone, "Intensification of Spontaneous Raman Spectra by Use of Liquid Core Optical Fibers" Appl. Spectrosc, **26**, 6, 585(1972)
5. R. Altkorn et al, "Low-loss liquid-core optical fiber for low-refractive-index liquids: fabrication characterization, and application in Raman spectroscopy ", Appl. Opt, **36**, 34, 8992 (1997)
6. Y. Zhang et al, "Liquid core photonic crystal fiber sensor based on surface enhanced Raman scattering", Appl. Phys. Lett., **90**, 193504 (2007)
7. G. Antonopoulos, F. Benabid, T. A. Birks, D. M. Bird, J. C. Knight and P. St. J. Russell "Experimental demonstration of the frequency shift of bandgaps in photonic crystal fibers due to refractive index scaling", Optics Express, Vol. **14** No.7, 2006, 3000-3006
8. H. Yan et al, "Hollow core photonic crystal fiber surface-enhanced Raman probe", Appl. Phys. Lett, **89**, 204101 (2006)
9. S. Yiou et al, "Stimulated Raman scattering in an ethanol core microstructured optical fiber", Opt. Express, **13**, 12, 4786 (2005)
10. S. Lebrun et al., "High-efficiency single-mode Raman generation in a liquid-filled photonic bandgap fiber", Opt. Lett., **32**(4), 337 (2007).
11 C. M. B. Cordeiro, E. M. dos Santos, C. H. Brito Cruz, C. J. de Matos, D. S. Ferreiira, "Lateral access to the holes of photonic crystal fibers – selective filling and sensing applications", Opt. Express **14**, 8403-8412 (2006)
12 L. Xiao, W. Jin, M. Demokan, H. Ho, Y. Hoo, C. Zhao, "Fabrication of selective injection microstructured optical fibers with a conventional fusion splicer", Opt. Express **13**, 9014-9022 (2005)
13. T A. Birks, D M. Bird, T D. Hedley, J M. Pottage, P St J. Russell "Scaling laws and vector effects in bandgap-guiding fibers", Opt. *Express,* **12,** 69-74 2004
14. F. M. Cox, A. Argyros, M. C. J. Large, "Liquid-filled hollow core microstructured polymer optical fiber", Opt. Express **14**, 4135-4140 (2006)

US007738097B2

(12) **United States Patent**
Khetani et al.

(10) **Patent No.: US 7,738,097 B2**
(45) **Date of Patent: Jun. 15, 2010**

(54) **METHOD FOR USING A PHOTONIC CRYSTAL FIBER AS A RAMAN BIOSENSOR**

(75) Inventors: **Altaf Khetani**, Kanata (CA); **Majid Naji**, Ottawa (CA); **Neil Lagali**, Ottawa (CA); **Hanan Anis**, Ottawa (CA); **Rejean Munger**, Ottawa (CA)

(73) Assignee: **University of Ottawa**, Ottawa, Ontario (CA)

(*) Notice: Subject to any disclaimer, the term of this patent is extended or adjusted under 35 U.S.C. 154(b) by 160 days.

(21) Appl. No.: **12/174,313**

(22) Filed: **Jul. 16, 2008**

(65) **Prior Publication Data**

US 2010/0014077 A1 Jan. 21, 2010

(51) **Int. Cl.**
G01J 3/44 (2006.01)
G01N 21/65 (2006.01)
G02B 6/32 (2006.01)

(52) **U.S. Cl.** **356/301**; 385/125

(58) **Field of Classification Search** 356/301; 385/125

See application file for complete search history.

(56) **References Cited**

U.S. PATENT DOCUMENTS

7,595,882 B1 * 9/2009 Chen et al. 356/437
2007/0020144 A1 * 1/2007 Du et al. 422/58

OTHER PUBLICATIONS

Yan et al., "Hollow core photonic crystal fiber surface-enhanced Raman probe", Applied Physics Letters, 89, 204101, Nov. 15, 2006.*

Zhang et al., "Liquid core photonic crystal fiber sensor based on surface enhanced Raman scattering", Applied Physics Letters, 90, 193504, May 8, 2007.*

Danny Noordegraaf, et al., "Electrically and mechanically induced long period gratings in liquid crystal photonic bandgap fibers." Optics Express Jun. 25, 2007/ vol. 15, No. 13.

F.M.Cox et al., "Liquid-filled hollow core microstructured polymer optical fiber." Optics Express May 1, 2006/vol. 14, No. 9.

T. A. Birks, et al., "Scaling laws and vector effects in bandgap-guiding fibres." Optics Express Jan. 12, 2004/vol. 12, No. 1.

Sylvie Lebrun et al., "High-efficiency signle-mode Raman generation in a liquid-filled photoic bandgap fiber." 2007 Optical Society of America.

G. Antonopoulos, et al. "Experimental demonstration of the frequency shift of bandgaps in photonic crystal fibers due to refractive index scaling." Optics Express Apr. 3, 2006/vol. 14, No. 7.

* cited by examiner

Primary Examiner—F. L Evans
(74) *Attorney, Agent, or Firm*—Harness, Dickey & Pierce PLC

(57) **ABSTRACT**

A method is provided for biosensing using a photonic crystal fiber having a hollow core. The method includes: designating an analyte of interest; determining a wavelength for an excitation light source which generates a Raman spectrum when incident upon the analyte of interest; selecting a photonic crystal fiber that would guide the light when the fiber is non-selectively filled with a solvent hosting the analyte of interest; non-selectively filling a photonic crystal fiber with the solvent hosting the analyte of interest; interrogating the analyte of interest by coupling light from the light source to the photonic crystal fiber; and analyzing the light output from the photonic crystal fiber for Raman fingerprints.

16 Claims, 6 Drawing Sheets

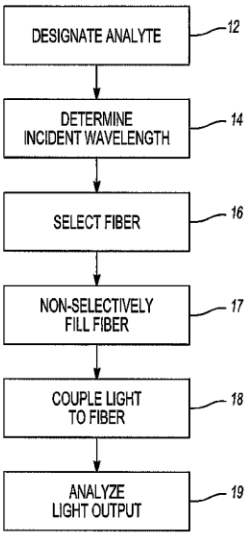

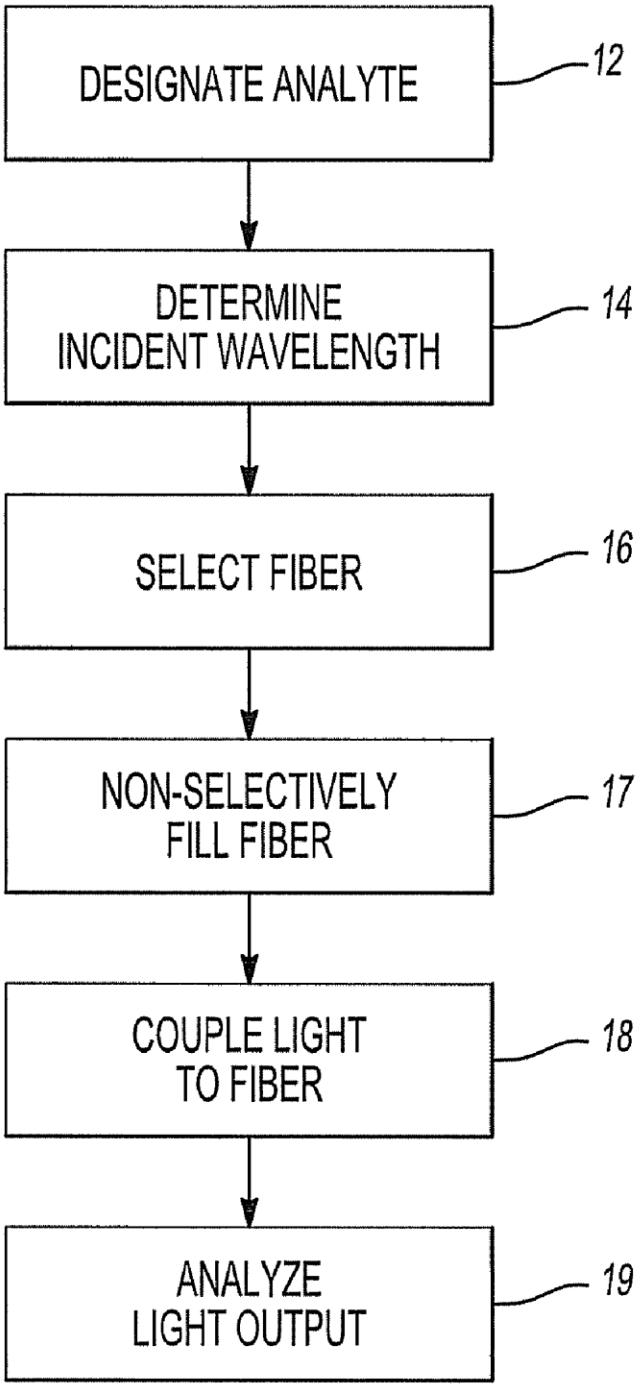
DESIGNATE ANALYTE
12
DETERMINE INCIDENT WAVELENGTH
14
SELECT FIBER
16
NON-SELECTIVELY FILL FIBER
17
COUPLE LIGHT TO FIBER
18
ANALYZE LIGHT OUTPUT
19

Fig-1

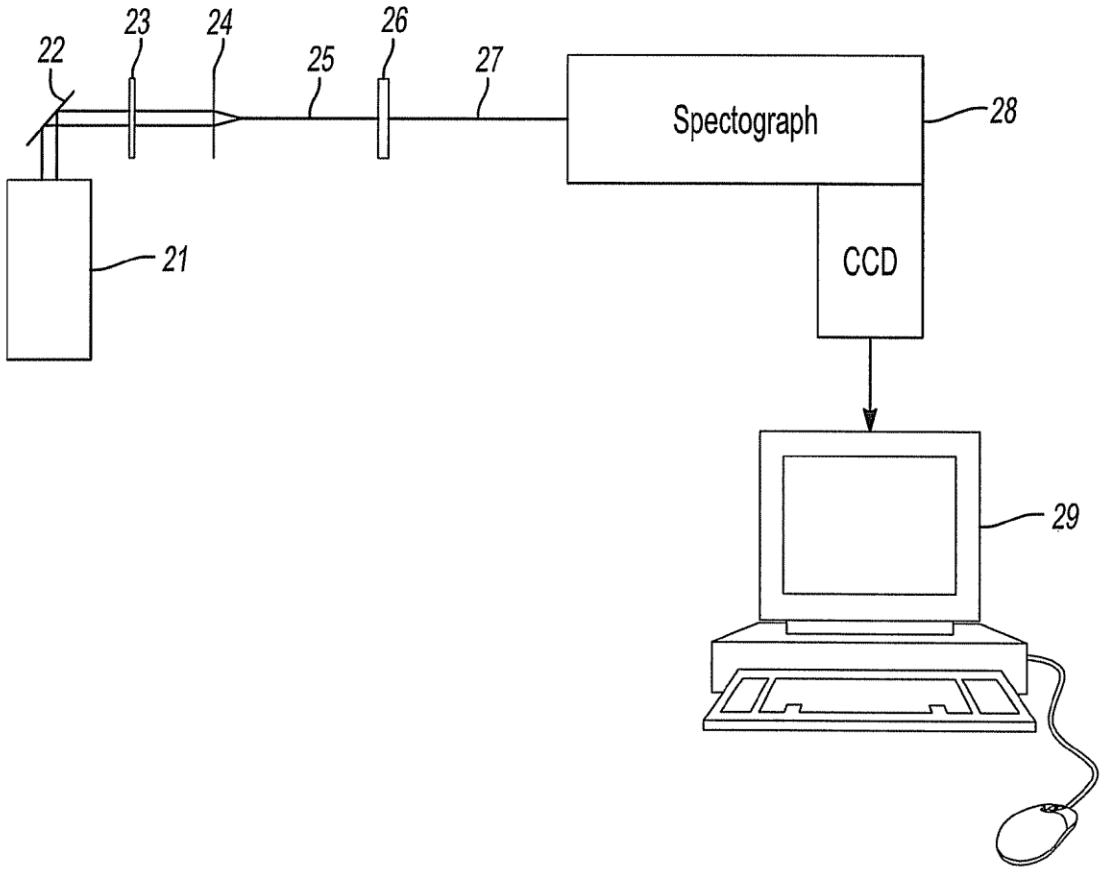

Fig-2

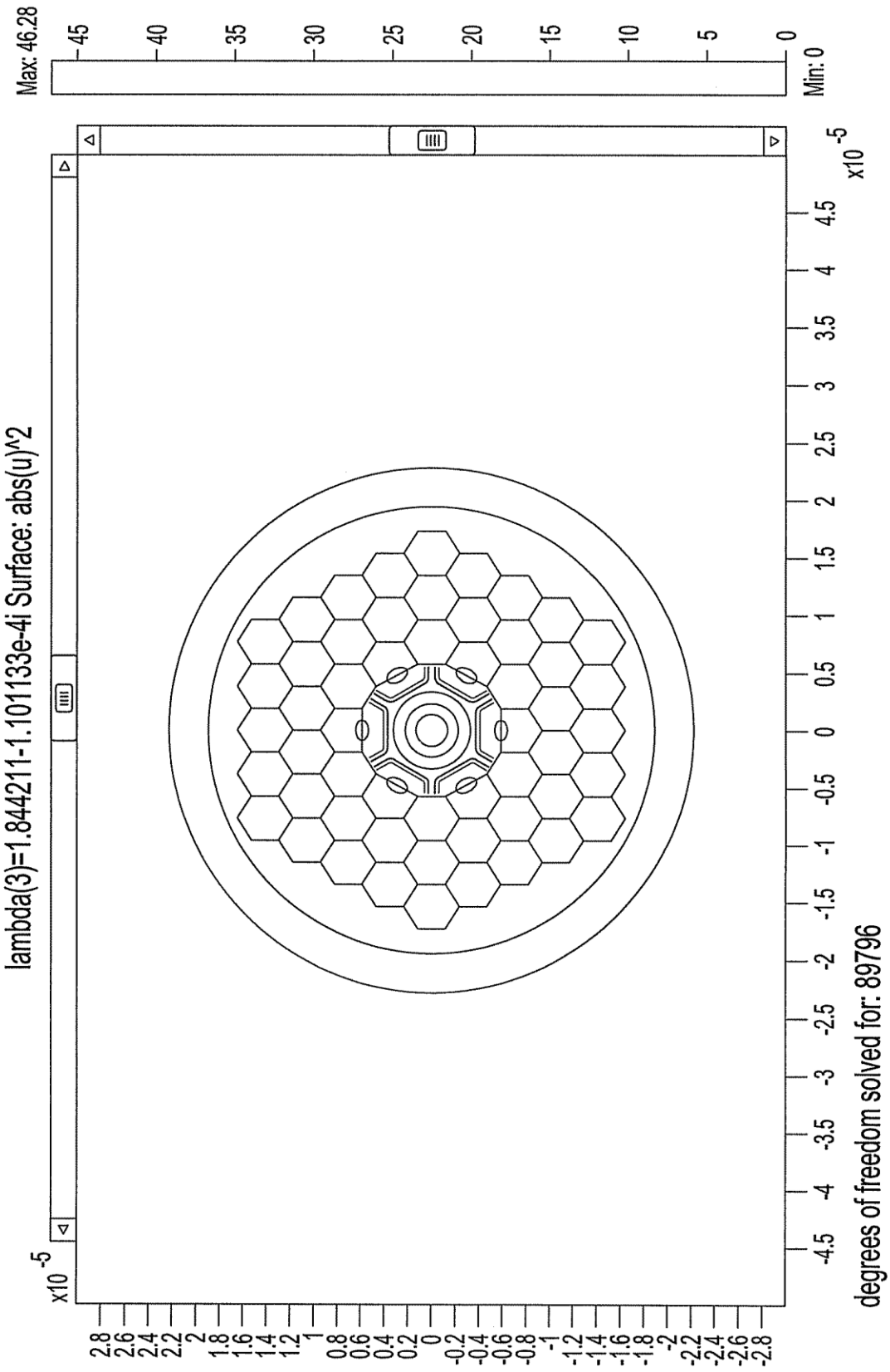
lambda(3)=1.844211-1.101133e-4i Surface: abs(u)^2
Max: 46.28
Min: 0
x10^-5
x10^-5
degrees of freedom solved for: 89796
time: 47.516 s

Fig-3B

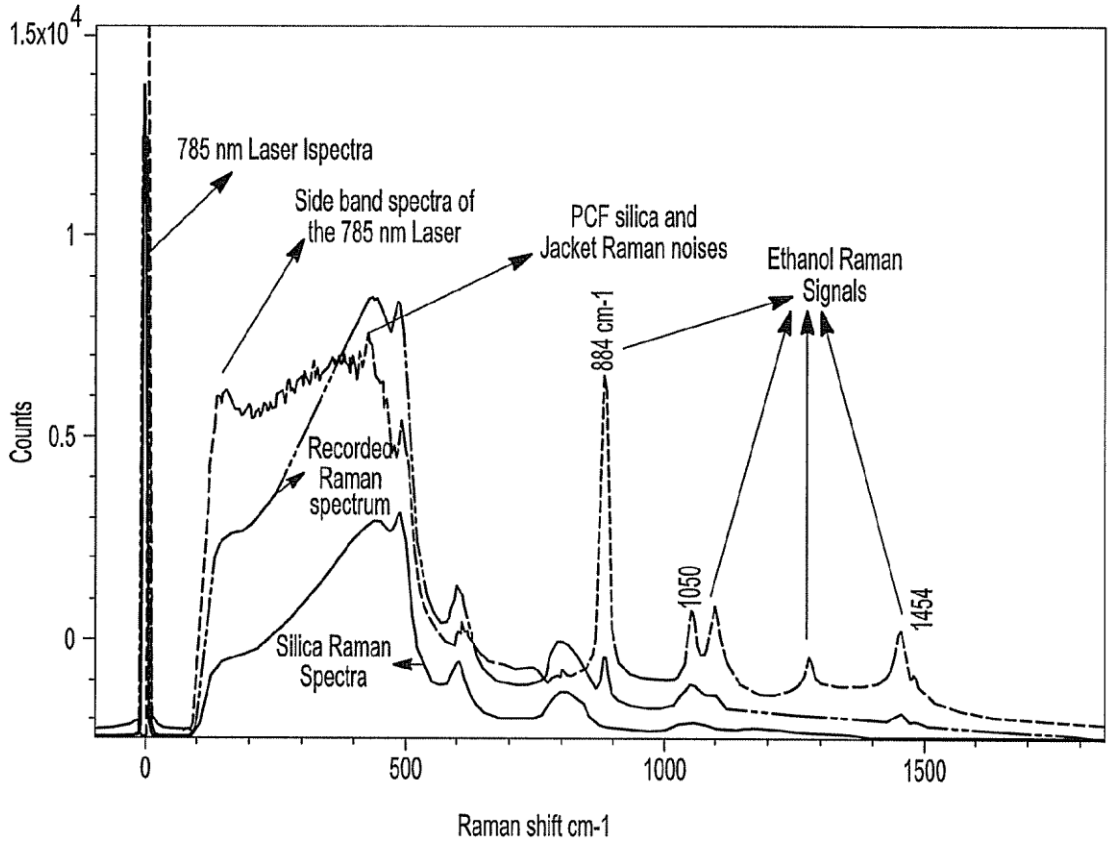
1.5x10^4
1
0.5
0
Counts
785 nm Laser Ispectra
Side band spectra of the 785 nm Laser
PCF silica and Jacket Raman noises
Ethanol Raman Signals
884 cm-1
1050
1454
Recorded Raman spectrum
Silica Raman Spectra
0
500
1000
1500
Raman shift cm-1

Fig-4

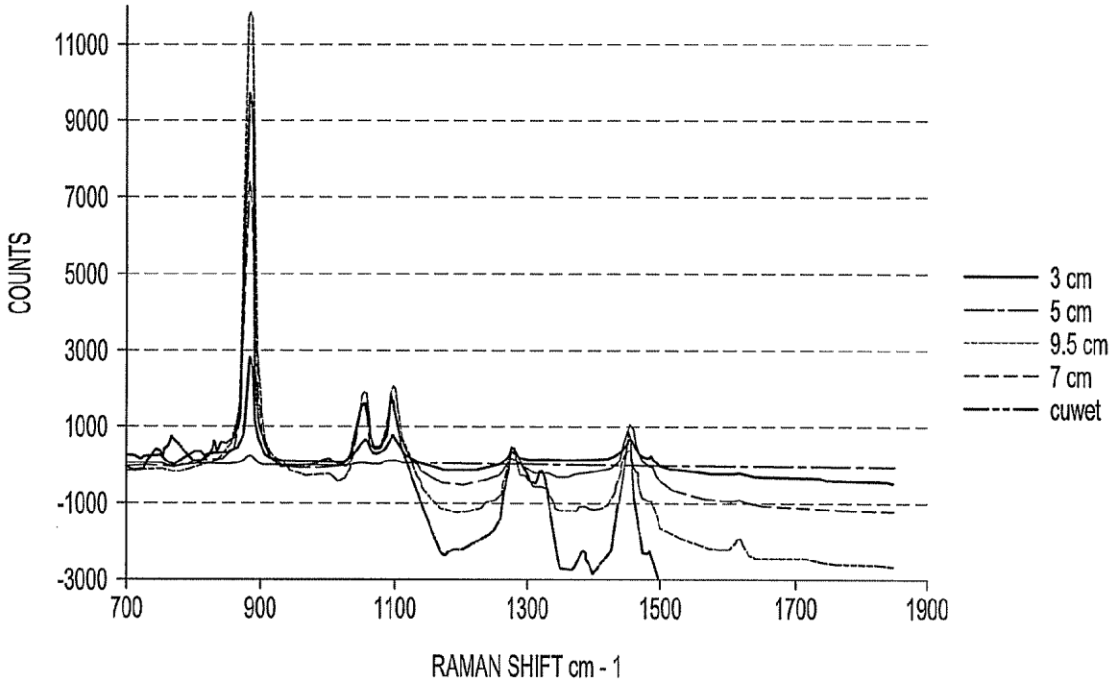
11000
9000
7000
5000
3000
1000
-1000
-3000
COUNTS
700
900
1100
1300
1500
1700
1900
RAMAN SHIFT cm - 1
3 cm
5 cm
9.5 cm
7 cm
cuwet

Fig-5

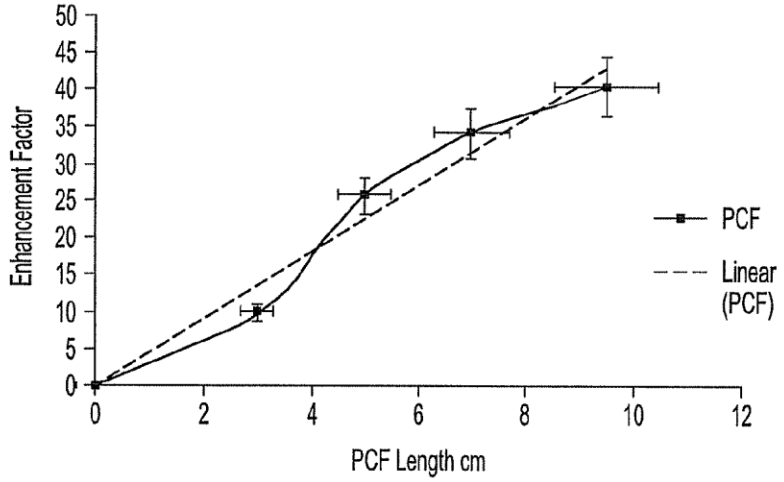
50
45
40
35
30
25
20
15
10
5
0
Enhancement Factor
0
2
4
6
8
10
12
PCF Length cm
PCF
Linear (PCF)

Fig-6

METHOD FOR USING A PHOTONIC CRYSTAL FIBER AS A RAMAN BIOSENSOR

FIELD

The present disclosure relates to a system and method for using a photonic crystal fiber as a Raman spectroscopy platform suitable for biosensing applications.

BACKGROUND

Optical techniques have played an important role in instrumentation and sensor applications especially in non-contact measurements. It is well established that the detection and identification of bacteria, protein and pathogens as infectious agents in people, environment and food sample is very important and has been the prime focus of interest. In recent years, the advancement in optical technologies has surged in the field of sensors. Most optical based sensors are spectroscopic techniques involving fluorescence or absorbance. Although these techniques are very popular and effective they require, for instance in fluorescence, labeling of the molecule which can lead to alterations in target-receptor interactions caused by conformational changes. This has led to considerable effort investigating other alternatives.

Raman spectroscopy is a compelling technique. It provides an optical fingerprint of chemicals and biomolecules corresponding to the vibrational frequencies of molecular bonds. Therefore, this label-free optical sensing technique has the ability to quantify molecules attached to the sensing surface, which should improve the well known problem of non-specific binding in all solid surface sensing systems. Additionally, it is desirable to have a small, rapid assays that use small sample volumes and capable of detecting several compounds of species in parallel. This is significant because in many cases, sample collection is limited and sample processing also requires time. All of these factors point toward being able to detect multiple agents in parallel using small sample volumes.

One of the principle drawbacks of Raman spectroscopy is a weak Raman signal. Signal strength may be improved by increasing laser intensity, enhancing the quality of transverse beam profile or increasing the laser beam interaction length in the analyte media. A hollow-core waveguide that supports a single transverse mode with low attenuation losses and long interaction length might meet the requirements for enhancing a Raman signal. This disclosure is the first to contemplate non-selectively filling a hollow-core photonic crystal fiber for biosensing applications. Photonic crystal fiber offers a medium with long interaction lengths which enhance the Raman signal, thereby enabling the use of low-cost, low-power lasers and detectors. Thus, non-selectively filled photonic crystal fibers can provide an improved platform for performing Raman spectroscopy.

The statements in this section merely provide background information related to the present disclosure and may not constitute prior art.

SUMMARY

A method is provided for biosensing using a photonic crystal fiber having a hollow core. The method includes: designating an analyte of interest; determining a wavelength for an excitation light source which generates a Raman spectrum when incident upon the analyte of interest; selecting a photonic crystal fiber that would guide the light when the fiber is non-selectively filled with a solvent hosting the analyte of interest; non-selectively filling a photonic crystal fiber with the solvent; interrogating the analyte of interest by coupling light from the light source to the photonic crystal fiber; and analyzing the light output from the photonic crystal fiber for a Raman effect.

Further areas of applicability will become apparent from the description provided herein. It should be understood that the description and specific examples are intended for purposes of illustration only and are not intended to limit the scope of the present disclosure.

DRAWINGS

FIG. **1** is a flowchart illustrating a method for using a photonic crystal fiber as a Raman spectroscopy platform;

FIG. **2** is a diagram depicting an exemplary embodiment for a biosensor in accordance with the present disclosure;

FIGS. **3**A and **3**B illustrate the simulated mode field intensity of light in a photonic crystal fiber at 785 nm and 890 nm, respectively;

FIG. **4** illustrates the Raman spectra for pure ethanol determined by subtracting the Raman spectra of the collecting fiber bundle from the measured Raman spectrum of an ethanol-filled photonic crystal fiber;

FIG. **5** illustrates the Raman spectra for pure ethanol determined with photonic crystal fiber having different lengths; and

FIG. **6** illustrates a relative enhancement factor for different length fibers as compared to a 1 cm length quartz cuvette.

The drawings described herein are for illustration purposes only and are not intended to limit the scope of the present disclosure in any way.

DETAILED DESCRIPTION

Raman spectroscopy is based on a light scattering phenomenon known as "Raman effect". When a monochromatic light is incident on an atom or molecule, a fraction of light is scattered and other is absorbed. Most of the scattered light is elastically scattered known as Rayleigh scattering, which has same wavelength and frequency as the incident light. However, a small fraction (1 in 1 million) of photons is scattered at different frequency, usually lower than the incident light. The amount of energy corresponding to shift in wavelength is due to the vibrational and rotational energy level of the molecules of the sample. The spectrum caused due to shift in frequency is known as Raman Spectrum and the phenomenon is called the Raman effect. Raman spectra usually contain many sharp peaks corresponding to the specific molecular vibrational frequencies and thus give a clear signature of the presence of specific molecules in the sample. Raman spectra can therefore be used to discriminate between several chemical species in materials for qualitative and quantitative analysis.

Photonic crystal fibers have unique properties which appear to provide a promising platform for Raman spectroscopy. A hollow-core photonic crystal fiber (HC-PCF) is comprised of an air core surrounded by a cladding consisting of a periodic array of air holes. The periodic cladding structure prevents light in a range of wavelengths from propagating. As a result, the hollow core guides and confines the range of wavelengths. Various types of hollow-core photonic crystal fibers are readily known in the art.

FIG. **1** illustrates a technique for using a hollow-core photonic crystal fiber as a Raman spectroscopy platform suitable for biosensing applications. To use as a sensor, the fiber will be filled with a sample to be analyzed. However, the guiding property of the fiber changes depending on the refractive index of the sample. Therefore, it is first necessary to determine the analyte of interest at **12**, including the solvent or host for analyzing the analyte.

In an exemplary experiment, zinc oxide nanoparticles are the analyte of interest and ethanol is used as a solvent for

analyzing the particles. The host of the analyte of interest is referred to herein as the sample being analyzed. Given an analyte of interest, a preferred wavelength for incident light which creates a Raman effect may be readily determined at **14** for the analyte. For zinc oxide nanoparticles, incident light having a 765 nm wavelength is preferred. While the description below makes reference to this particular experiment, it is readily understood that other types of analytes and solvent materials are within the scope of the present disclosure.

Depending upon the excitation wavelength, a fiber can be selected at **16** that would guide this wavelength when the fiber is filled with the sample. Since the bandgap of a sample filled photonic crystal fiber will shift, the fiber selection must account for this bandgap shift. The shift in bandgap can be determined using the refractive scaling laws. More specifically, the shifted wavelength is given by:

$$\lambda' = \lambda_0 \left[\frac{1 - \left(\frac{\eta_{liq}}{\eta_{sil}}\right)^2}{1 - \left(\frac{\eta_{air}}{\eta_{sil}}\right)^2} \right]^{1/2}$$

where λ_o is the central wavelength of the bandgap of an empty photonic crystal fiber, λ' is the central wavelength of the shifted bandgap of the sample filled fiber; η_{liq} is the refractive index for the liquid sample, η_{air} is the refractive index for air and η_{sil} is the refractive index for silica. Knowing the sample used to fill the fiber (and thus a refractive index for the same), the bandgap shift for a sample filled fiber may be computed in accordance with the refractive scaling law. Further information regarding the refractive scaling law applied herein may be found in an article by Birks et. al. entitled "Scaling laws and vector effects in bandgap-guiding fibres", Opt. Express, 12, 69-74 (2004).

To guide light having a 765 wavelength through an ethanol filled photonic crystal fiber, a hollow core photonic crystal fiber (i.e., HC-1550) with 1550 nm original central bandgap must be selected. For illustration purposes, a table of exemplary types of fibers is provided below.

Liquid	Refractive Index	Fiber Type HC-440	HC-580	HC-633	HC-800	HC-1060	HC-1550
Empty	n = 1	440 (410-470) nm	580 (515-595) nm	633 (570-690) nm	−800 (795-880) nm	1060 (990-1150) nm	1550 (1450-1650) nm
Water	n = 1.33	249 (232-266) nm	328 (291-336) nm	358 (322-390) nm	452 (450-498) nm	600 (560-651) nm	877 (820-934) nm
Acetonitryl	n = 1.34	236 (220-252) nm	311 (276-319) nm	339 (306-370) nm	429 (426-472) nm	569 (531-617) nm	832 (778-886) nm
Ethanol	n = 1.36	212 (198-227) nm	280 (248-287) nm	305 (275-333) nm	386 (384-425) nm	512 (478-555) nm	748 (700-797) nm

Entries in the table provide shifted central wavelength and the wavelength range (in parenthesis) supported by the photonic crystal fiber when empty or filled with various solvents. It is readily understood that other types of fibers may be selected.

The selected fiber may then be filled at **17** with a sample to be analyzed. More specifically, the fiber is non-selectively filled. In other words, both the hollow core and all of the cladding holes (or channels) are filled with the sample to be analyzed. The problem of evaporation may be addressed by inserting a reservoir filled with the sample at one end of the fiber. The reservoir may use a syringe needle whose broader end is filled with the sample and glued with a glass cover slip, while the fiber is inserted at the other end. The reservoir ensures that the liquid is continuously supplied inside the fiber to replenish any evaporated liquid. Alternatively, evaporation may be circumvented by confining the sample within the fiber through pressure or by sealing the fiber ends.

Raman spectroscopy may now be carried out by coupling excitation light of the excitation light source to the photonic crystal fiber as indicated at **18**. By analyzing Raman spectrum of the light output from the photonic crystal fiber at **19**, the presence of an analyte of interest may be determined. In particular, we are interested in a spectrum of spontaneously scattered Raman-shift light. Different techniques for analyzing the light output are readily known in the art and may be applied to interrogate the sample contained in the fiber.

A basic construct for a biosensor suitable for implementing this technique is set forth below. The biosensor includes a coherent excitation light source, a photonic crystal fiber having a hollow core, and a light detector. The excitation light source is optically coupled to an inlet of the photonic crystal fiber and the light detector is optically coupled to an outlet of the photonic crystal fiber. The fiber is non-selectively filled with a sample to be analyzed. In operation, light from the light source is projected through the fiber. The light detector detects a Raman shift experienced by the light received from the filled photonic crystal fiber. It is to be understood that only the required components are discussed above, but that other optical components may be used to implement the biosensor.

FIG. **2** depicts an exemplary embodiment for a biosensor **20** in accordance with the present disclosure. In the exemplary embodiment, the excitation light source **21** projects monochromatic light having a 785 nm wavelength. The light source **21** may be implemented with a single mode 100 mW, 14 pin butterfly laser commercially available from Innovative Photonic Solutions. The laser beam from the light source **21** is directed through a silver coated mirror **22** and then passed through a band pass filter **23** (e.g., a 785 nm band pass filter commercially available from Iridian). Light passing through the filter **23** is coupled to a photonic crystal fiber **25** using an objective lens **24** (e.g., a 40× Newport microscope objective lens with NA.=0.65). Coupling laser light to a filled fiber was sensitive and spurious coupling effects had to be avoided as they caused a tremendous reduction in Raman generated signal. Accordingly, the near field laser beam pattern out of the fiber was checked to ensure that the output beam came from the core and not the fiber cladding. Other optical arrangements for coupling the light to the fiber are contemplated by this disclosure.

A fiber which would guide light having a 785 nm wavelength when filled with ethanol was selected in the manner described above. Simulation was done using a commercial software COMSOL Multiphysics version 3.1 to check guidance at 785 nm as well as to see whether the Raman shift at 890 nm is supported. This result predicts the guidance of

Raman-shifted light in a range up to 1500 cm^{-1}, which is sufficient for spontaneous Raman spectroscopic fingerprinting of a wide range of materials which can be seen from FIGS. **3**A and **3**B.

Light at the output of the fiber **25** was passed through a long-pass filter **26**, to reduce the excitation light and then directly coupled to a collecting fiber bundle **27** consisting of 30-100 μm multimode fibers arranged in a circular pattern at the collection end and stacked in a linear fashion at the output end. Such fiber bundle is commercially available from Fiber Optic Systems Inc. The multimode fiber bundle **27** is in turn coupled into a spectrograph **28** (e.g., Kaiser f/18 spectrograph, which had a TE-cooled Andor CCD camera). The spectrometer is equipped with a noth or edge filter to reject the elastically scattered photons (Rayleigh photons) which have the same energy as the laser photons. Data processing may be performed with a computer **29** in data communication with the CCD of the spectrograph **28**.

The setup with a long-pass filter and then a coupling into the fiber bundle proved cumbersome, so in one exemplary implementation the long-pass filter was excluded and instead the silica Raman background noise generated in the fiber bundle by the excitation light was recorded. Because of the 785 nm laser side band and Raman spectra generated by the PCF cladding jacket and the fiber bundle, the acquired spectra were not completely clean. Therefore, the silica Raman spectra of the collecting fiber bundle was subtracted from the recorded Raman spectrum of the ethanol-filled fiber with collecting fiber bundle, to give the pure ethanol Raman spectrum as shown in FIG. **4**. Note that in FIG. **4** the pure ethanol Raman spectrum does not have the same Raman signal count scale, but is expanded for clarity.

To derive a Raman signal enhancement factor from the non-selectively filled PCF, the ethanol spectra from 3, 5, 7, and 9.5 cm of filled PCF were acquired and compared with the Raman spectrum from a 1 cm path-length ethanol-filled quartz cuvette as shown in FIG. **5**. Using the 885 cm^{-1} ethanol peak from each spectrum, ratios of peak heights were used to determine the enhancement at each PCF length. Because the PCF guiding loss increases by increasing Raman shift of spectrum, the spectrum lines with higher Raman shift attenuated more, this attenuation is proportion to the fiber length. Therefore, this non-uniformity of PCF attenuation as a function of Raman shift and PCF length can be easily seen.

FIG. **6** shows the enhancement factor measurements in non-selective ethanol filled PCF as a function of PCF length. In theory, for spontaneous Raman spectrum we expect a linear relation, by ignoring fiber loss for short fiber lengths between the interaction length and Raman enhancement factor (dashed line in FIG. **6**). Therefore, a good correlation between the theory and our measurements was observed. Thus, a novel Raman spectroscopy platform is provided by filling HC-PCF non-selectively. The simplicity of this method, having reasonable Raman signal enhancement combined with the high degree of overlap of the propagating mode with the analyte and small sample volumes required, makes it a promising candidate for sensitive and low-power identification of biological specimens.

Furthermore, large enhancement can be obtained through surface enhanced Raman spectroscopy. In surface enhanced Raman spectroscopy, an analyte is chosen that will adsorb (attract) to surface of metal nanoparticle (e.g., having a size of 20-100 nm) and will result in electromagnetic and chemical enhancement. The metal nanoparticles can be deposited on the inner walls of the cladding channels or merely contained in the solvent with the analyte of interest; otherwise, the method for using a photonic crystal fiber for biosensing is as described above.

An exemplary application for the Raman spectroscopy platform described above is the measurement of heparin or other blood parameters. As optical methods are well-suited for measurement of relative changes in blood parameters, they are ideal for monitoring changes in blood resulting from large administered doses of heparin during heart surgery. If heparin can be accurately monitored optically, continuous readout could be made available during surgery, resulting in improved and early detection of potentially life-threatening blood clotting events. By filling a photonic crystal fiber with blood, it can serve a dual purpose. The first is as a Raman enhancer as light interacts with matter for longer interaction length as well as a nano container.

In an exemplary arrangement, the fiber is configured as an interchangeable sample container (e.g., a test tube). For example, the fiber may be contained in a small needle like container with a small opening lid on the top to insert blood samples for testing. In order to measure heparin content the only thing to be done is to fill the fiber with blood and place it in a space provided in the apparatus for heparin measurement. The light is coupled into the filled fiber, after passing long pass filter the output light is collected by a detector and processed through a processor for determining the concentration of heparin in blood. Other applications for the Raman spectroscopy platform described herein are also contemplated by this disclosure.

The above description is merely exemplary in nature and is not intended to limit the present disclosure, application, or uses.

What is claimed is:

1. A method of biosensing using a photonic crystal fiber having a hollow core surrounded by a cladding with a plurality of channels, comprising:

designating an analyte of interest;

determining a wavelength for an excitation light source which generates a Raman spectrum when incident upon the analyte of interest;

selecting a photonic crystal fiber which accounts for a bandgap shift when the photonic crystal fiber is filled with a solvent hosting the analyte of interest;

filling the hollow core and the entirety of the cladding channels of the photonic crystal fiber with the solvent; and

interrogating the analyte of interest by coupling light from the light source to the photonic crystal fiber.

2. The method of claim **1** further comprises analyzing the light output from the photonic crystal fiber for a spectrum of spontaneously scattered Raman-shift light.

3. The method of claim **1** further comprises evaluating the analyte of interest based upon Raman spectrum experienced by the light output from the photonic crystal fiber.

4. The method of claim **1** wherein selecting a photonic crystal fiber further comprises:

determining a refractive index for the solvent used to fill the photonic crystal fiber; and

computing a bandgap shift caused by non-selectively filling of the photonic crystal fiber using refractive index scaling laws.

5. The method of claim **4** wherein computing a bandgap shift is determined in accordance with

$$\lambda' = \lambda_0 \left[\frac{1 - \left(\frac{\eta_{liq}}{\eta_{sil}}\right)^2}{1 - \left(\frac{\eta_{air}}{\eta_{sil}}\right)^2} \right]^{1/2}$$

where λ_o is a central wavelength of the bandgap of the photonic crystal fiber with an empty core; λ' is a central wavelength of a shifted bandgap of the filled photonic crystal fiber;

η_{liq} is a refractive index of the liquid sample, η_{air} is a refractive index of air and η_{sil} is a refractive index of silica.

6. The method of claim **1** further comprises enhancing the Raman signal experienced by the light output from the photonic crystal fiber by increasing length of the photonic crystal fiber.

7. A method of biosensing using a photonic crystal fiber having a hollow core, comprising:

designating an analyte of interest;

determining a wavelength of light that generates a Raman spectrum when incident upon the analyte of interest;

determining a refractive index of a solvent used to host the analyte of interest;

selecting a photonic crystal fiber that would guide the light when the fiber is non-selectively filled with the solvent using refractive index scaling laws;

filling the selected photonic crystal fiber non-selectively with the solvent having the analyte of interest;

coupling light from a light source to the photonic crystal fiber; and

evaluating the analyte of interest by analyzing the light output from the photonic crystal fiber.

8. The method of claim **7** further comprises analyzing the light output from the photonic crystal fiber for a spectrum of spontaneously scattered Raman-shift light.

9. The method of claim **7** further comprises analyzing the light output from the photonic crystal fiber for a Raman spectrum and evaluating the analyte of interest based upon the Raman spectrum experienced by the light output from the photonic crystal fiber.

10. A biosensor comprising:

a photonic crystal fiber having a hollow core surrounded by a porous cladding, where core and cladding of the photonic crystal fiber is filled with a sample having an analyte of interest;

an excitation light source optically coupled to an input of the photonic crystal fiber; and

a light detector optically coupled to an output of the photonic crystal fiber and configured to detect a spectrum of spontaneously scattered Raman-shift light received from the photonic crystal fiber.

11. The biosensor of claim **10** further comprises an objective lens that optically couples the light source to the photonic crystal fiber.

12. The biosensor of claim **11** further comprises a band pass filter arranged to pass light from the light source to the objective lens.

13. The biosensor of claim **10** further comprises a multimode fiber bundle arranged to collect light output from the photonic crystal fiber.

14. The biosensor of claim **10** further comprises a long pass filter arranged to pass light output from the photonic crystal fiber to the light detector.

15. The biosensor of claim **10** wherein the light detector is further defined as a spectrograph.

16. A method of biosensing using a photonic crystal fiber having a hollow core surrounded by a cladding with a plurality of channels, comprising:

designating a metal nanoparticle that will be deposited on inner walls of the cladding channels;

designating an analyte of interest that will be adsorbed to the metal nanoparticles;

determining a wavelength of light that generates a Raman spectrum when incident upon the analyte of interest;

selecting a photonic crystal fiber that would guide the light when the fiber is non-selectively filled with a solvent using refractive index scaling laws;

filling the selected photonic crystal fiber non-selectively with the solvent having the analyte of interest and the designated metal nanoparticles;

coupling light from a light source to the photonic crystal fiber; and

evaluating the analyte of interest by analyzing the light output from the photonic crystal fiber.

* * * * *

Chapter 3.

Coherent Anti-Stokes Raman scattering microscopy/ endoscopy imaging using photonic crystal fibers

3.1 Introduction

CARS microscopy is a powerful tool for non-invasive chemical imaging of biological samples. A CARS signal is generated when the frequency difference between the pump and the Stokes incident in a sample is in resonance with the sample's molecular vibration frequency. The CARS signal is directional, due to its coherent nature and nonlinear dependence on the excitation intensity, and it is only generated at the focal volume of the objective lens of the microscope. This gives CARS microscopy imaging a relatively fast data acquisition time, and inherent 3-dimensional sectioning capability. In addition, as CARS relies on molecular vibrations, there is no need for samples to be labeled. Moreover, when CARS is combined with other nonlinear imaging and spectroscopic techniques, such as two photon excitation fluorescence (TPEF) and second harmonic generation (SHG), the utility of the acquired images is greatly increased, and considerable chemical information can be extracted from biological tissues.

While CARS microscopy has been demonstrated by preliminary research in many fields (e.g. cancer identification, drug therapy selection, biological lipid droplet imaging, myelinated axon structure, spinal cord injuries and demyelination, arterial atherosclerosis detection, determination of hepatic fat content of liver tissue [33]), the significant costs for equipment and highly qualified operational personnel have limited its entry into mainstream medicine [34]. One of the primary reasons for this complexity and expense is the light sources that generate the pump and Stokes beams. An optimal CARS setup requires expensive and bulky light sources, ranging from two synchronized picosecond lasers [35], to the current state-of-the-art synchronously pumped optical parametric oscillators (OPO) system [36]. A fiber-based approach, using a single broadband laser source and photonic crystal fiber to generate both the pump and Stokes pulses, would be a compact and cost effective multimodal CARS microscope. While imaging tissues ex-vivo is useful, making nonlinear imaging practical for clinical use requires endoscopic variants of current microscopes. Extensive research has been performed on integrating fibre-delivered

SHG and TPEF probes, but fiber-delivered CARS endoscopic research has been limited. The difficulty with CARS as an imaging modality is that it is absolutely critical that the pump and Stokes beams overlap temporally and spatially at the sample. Without this temporal and spatial overlap, no vibrational resonance is created within the bonds of the molecule being probed, as the pump and Stokes photons cannot interact in tandem with the molecule [35].

3.2 Motivation and contribution in CARS microscopy/endoscopy

Our research group's interest in CARS microscopy was motivated by our collaborator, Dr. Peter Stys, and his interest in multiple sclerosis (MS) [37]. In 2010, the number of people with MS worldwide was 2 to 2.5 million (approximately 30 per 100,000), and Canada has one of the highest rates of MS, with three people diagnosed daily. Women are three times more likely to develop MS than men [38].

MS is caused by damage to the myelin surrounding the axon of a neuron (Figure 3-1). Understanding the demyelination mechanism would be a great help to neurologists and physicians who are working to determine what can be done to reverse the effects of demyelination, or to prevent it entirely. A 3D, in-vivo, label free imaging method, capable of differentiating between different cellular myelin layer and structures, would significantly enhance this research. Since the myelin consists of lipid structures, and the CARS signal of the C-H bonds is broad and strong, a CARS multimodal nonlinear microscope is the perfect tool for such an investigation [39].

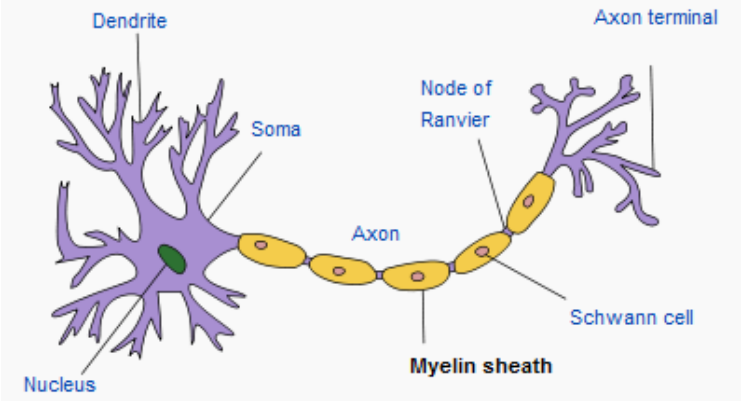

Figure 3-1: Neuron typical structure [37].

However, despite its acknowledged power and usefulness, CARS microscopy is not yet a widely adopted, commercially available biomedical imaging tool. This is largely due to the technological complexity, the high cost of light sources required to generate the pump and Stokes beams, and the size and lack of portability. A current CARS setup is usually bulky and complex, and requires a lot of free space beam and path alignments [40].

Thus, there is an established need for an approach that can reduce the complexity, size and cost of the setup, and addressing this was the main motivation and goal of my PhD studies. I have worked on three interrelated projects: 1) developing a CARS setup that uses one light (single femtosecond laser) source rather than two; 2) extending the single fs laser approach to perform CARS imaging in the fingerprint region; and 3) developing a portable CARS imaging setup (endoscope) for in-vivo applications.

3.2.1. Developing CARS setup using just one light source

While working on the Raman setup, I also helped develop a CARS setup at the Ottawa Civic Hospital. This was a joint project by my supervisor, Dr. Anis, and Dr. Stys (neuroscientist). I worked on beam manipulation, including a dispersion compensation strategy and supercontinuum generation and characterization. The result of our novel approach was published in Optics Express 2007 [40].

When Dr. Stys moved to Calgary in 2008 we had to develop a new set-up in our lab, and due to my experience at the Civic I assumed a leading role in this work. I ordered and bought parts, and redesigned and assembled the second CARS setup, with the help of Dr. Murugkar. Once the set-up was complete, we demonstrated TPEF and SHG imaging. I then obtained the CARS signal of an oil sample, by finely realigning the pump and Stokes paths and adjusting the delay lines to accomplish CARS imaging at the C-H bond region, i.e. region around 2800 cm^{-1} Raman shift. I further improved the alignment of our microscope, and developed a method to reduce aberration and increase the Stokes beam signal quality, to enhance the overall CARS image quality. Once I was able to reproduce the results we achieved at the Civic, I focused on extending the approach to include CARS imaging in the fingerprint region. The fingerprint region for organic/chemical molecules in Raman spectroscopy is the region with the wavenumber range from ~500 cm^{-1} to ~2000 cm^{-1}.

3.2.2. Extending the approach to include CARS imaging in the fingerprint region

The two closely lying zero dispersion wavelengths (ZDWs) PCFs used in our setup are suitable for generating a CARS signal in the C-H bond region. However, due to the limited spectral density at 850-950 nm, and the lack of linear polarization of the generated SC from this fiber, it cannot be used to perform CARS imaging/spectroscopy in the fingerprint region, or polarization CARS. The alternative is to use another high nonlinear polarization maintaining PCF. I led this effort, and found a PCF that could produce SC with significant spectra density in the 850-950 nm regions. I then developed an approach to compare the CARS image quality of the new fiber with the fiber typically used to generate a Stokes beam in a CARS set-up. This work demonstrated that it is possible to use two far-lying ZDWs fiber [41] to achieve high contrast CARS imaging of lipid rich samples at ~ 2850 cm^{-1}. Once the parameters of the input laser beam were properly adjusted, the CARS image quality was comparable to the images produced using a standard two closely lying ZDWs fibers [40, 42]. As the two far-lying ZDW fibers have a large spectral density in the region of 850-950 nm (corresponding to Raman shifts in the fingerprint region), it is possible to use this fiber to carry out CARS spectroscopy and microscopy in the fingerprint region. Performing Raman imaging in the finger print region can open the door to imaging of protein rich samples in the region between 500 cm^{-1} -2000 cm^{-1} Raman shift.

3.2.3. Developing a portable CARS imaging setup (endoscope) for in-vivo applications

I was also involved in the development of a miniaturized, handheld multimodal CARS exoscope/endoscope, which was prompted by the need to image disease progression in the same animal over time. While animal models of MS are well developed, experimental treatment and time-driven imaging of tissue changes in the same animal are limited, due to the size and lack of portability of existing multimodal CARS setups [43]. There is a clear need for a relatively non-invasive, in vivo CARS setup capable of examining the spinal tissue of live animals (e.g. mice) over time, with reasonable microscopic resolution [44]. A multimodal, nonlinear miniaturized endoscope that combines CARS, TPEF and SHG microscopy was required.

To achieve this goal, we designed, developed and tested a miniaturized endoscope/exoscope in the Innovation Lab of Photonics at the University of Ottawa. My role in this work was to test the endoscope design and perform any required modifications. For example, in the first endoscope design we attempted to use a double-core PCF to deliver the pump and Stokes beams. Through a series of measurements, I demonstrated the complexity and difficulty of the double-core PCF approach and, instead, we used a large core mode area (LMA) for the pump and Stokes beams delivery.

I worked with Dr. Murugkar and a Master student Brett Smith to test the endoscope barrel, and then the full-assembled endoscope. I developed protocols, and prepared samples for CARS, TPEF and SHG imaging using the new multimodal endoscope. I also mentored Brett, and helped him obtain 2 photon fluorescence, second harmonic and CARS images of different samples, and measure the aberration, axial resolution and collecting efficiency of the endoscope.

Finally, I investigated the possibility of using the new endoscope set-up with the 2 far-lying ZDW fibers to perform CARS microscopy in the fingerprint region. As a proof of concept, I demonstrated the CARS spectra of nitrobenzene and toluene in the fingerprint region. This enables the investigation of samples in the fingerprint region using the new fiber, and suggests the possibility of a number of new applications.

3.3. Coherent anti-Stokes Raman scattering

3.3.1. CARS theory

CARS is a four-wave mixing (FWM) process related to the third order susceptibility tensor of the medium. In the CARS process a pump, a Stokes and a probe field, with frequencies of ω_p, ω_s and ω_{pr} respectively, induce a third order nonlinear polarization $P^{(3)}$ in the sample, which generates an anti-stokes Raman signal of the frequency [35]:

$$\omega_{as} = \omega_p + \omega_{pr} - \omega_s \tag{3-1}$$

In practice, to reduce the complexity of the CARS setup, the pump and the probe photons are obtained from the same laser ($\omega_p = \omega_{pr}$). The magnitude of the 3rd order nonlinear polarization $P^{(3)}$ is determined by the field strength of the excitation electric fields E, and the nonlinear optical susceptibility of the medium, $\chi^{(3)}$, as in:

$$P^{(3)} = \chi^{(3)} E_p E_p E_s \tag{3-2}$$

Where E_p is the electric field of the pump light and E_s is the electric field of the Stokes light. By assuming pump and Stokes plane waves, the time averaged CARS signal intensity can be written as [45]:

$$I_{CARS} = \frac{\omega_{as}^2 N''^2}{16\varepsilon_0^2 c^4}[\chi^{(3)}(\omega_p - \omega_s)]^2 I_p^2 I_s L^2 [\frac{Sin\ (\Delta KL/2)}{(\Delta KL/2)}]^2 \tag{3-3}$$

where I_p and I_s are the pump and Stokes beam intensities, L is the interaction length of the pump and Stokes with the medium, N'' is the molecular density number, c is the speed of light, ε_0 is the vacuum permittivity, $\chi^{(3)}(\omega_p - \omega_s)$ is the medium susceptibility at the frequency $\omega_p - \omega_s$, and ΔK is the phase mismatch, which is defined as:

$$\Delta K = K_{as} - (2K_p - K_s) \tag{3-4}$$

where $K_{as}, K_p and\ K_s$ are the wave vectors of the anti-Stokes, pump and Stokes field respectively.

If a well phased matching ΔK = 0 is achieved, the CARS intensity varies quadratically with the interaction length. ΔK = 0 typically occurs only in the gas medium; in solid and liquid media ΔK will not equal zero due to media dispersion. In this case, phase matching is achieved if the pump and the Stokes beams are crossed (the non-collinear geometry) at angle θ', the phase matching angle (Figure 3-2a). Here, the interaction length of the beams is limited by the beam walk-off. While θ' is usually small (~1° for benzene at 992 cm^{-1}), it increases with the Raman shift [45]. Figure 3-2 shows the different practical phase-matching schemes in CARS microscopy processes.

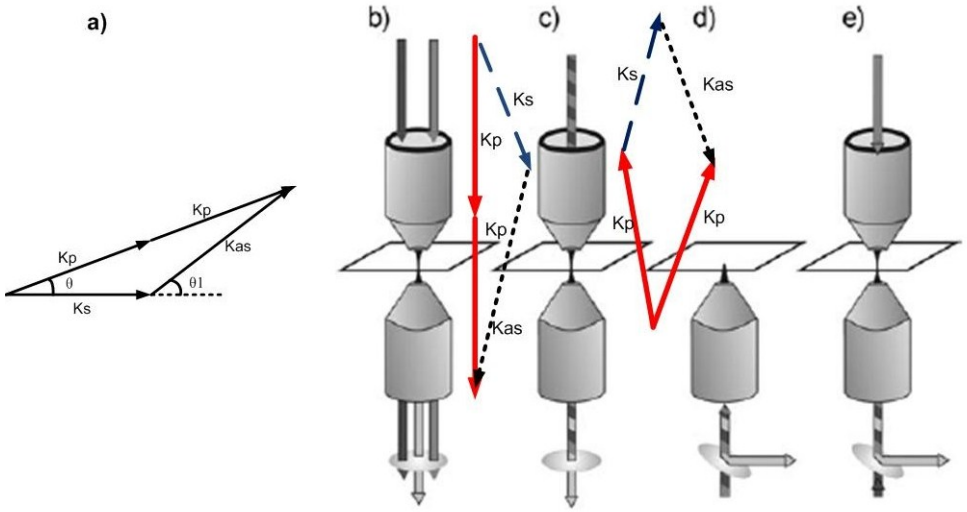

Figure 3-2: Wave vector diagram for phase matching a) in the case of existing dispersion in the medium, b) phase-matched excitation, c) collinear excitation in Box CARS, d) epi-detection, and e) counter-propagating [35].

In the case of $\Delta K \neq 0$, if the beams are not crossed the CARS signal intensity shows sinusoidal variations with the path length, as in equation (3-3). The coherence length L_c is defined as the path length which gives the maximum CARS conversion efficiency. This occurs when

$$\frac{\Delta K \, L_c}{2} = \frac{\pi}{2} \tag{3-5}$$

and, therefore, L_c is defined as:

$$L_c = \frac{\pi}{\Delta K} \tag{3-6}$$

In the case of Box CARS; that is, when the input Gaussian Stokes and pump beams illuminate in a crossbeam configuration using a high numerical aperture lens (Figure 3-2c and d), the CARS signal intensity in the focussing volume will be proportional to [39]:

$$I_{CARS} \propto \left|\chi^{(3)}\right|^2 [2\tan^{-1}(\frac{2L\pi d^2}{8\lambda'' f^2})]^2 = \left|\chi^{(3)}\right|^2 [2\tan^{-1}(\frac{L\pi NA^2}{\lambda'' n^2})]^2 \tag{3-7}$$

Where, f is the focal length of the lens, d is the beam diameter, NA is the numerical aperture of the lens when the back aperture is completely filled with the incident beams, λ'' is the average wavelength of the pump and the Stokes, and n is the refractive index of the medium.

Equation (3-7) shows that approximately 71% of the maximum CARS generation takes place over length L when it equals $\frac{32\lambda''}{\pi NA^2}$, which suggests using a very high numerical aperture lens when doing CARS microscopy in this manner.

The nonlinear optical susceptibility in equation (3-7) has two terms of non-resonant and resonant, as follows [33]:

$$\chi^{(3)} = \frac{A_R}{\Omega - (\omega_p - \omega_s) - i\Gamma_R} + \left(\frac{A_t}{\omega_t - 2\omega_p - i\Gamma_t} + \chi_{nr}^{(3)}\right) \tag{3-8}$$

where Ω is the vibrational frequency(ies) of the medium, Γ_R is the half-width at half maximum of the Raman line(s) of the medium, and Γ_t is the half-width at half maximum of the two photon electronic transition of the medium. A_R and A_t are Raman scattering and the two-photon absorption cross section constant, respectively.

The first term in equation (3-8) is the vibrational resonant contribution of $\chi^{(3)}$ (Figure 3-3A). The second term in parentheses is the non-resonant term of $\chi^{(3)}$, which includes an enhanced non-resonant term due to the two-photon electronic resonance (Figure 3-3C), and an independent Raman shift non-resonant term (Figure 3-3B).

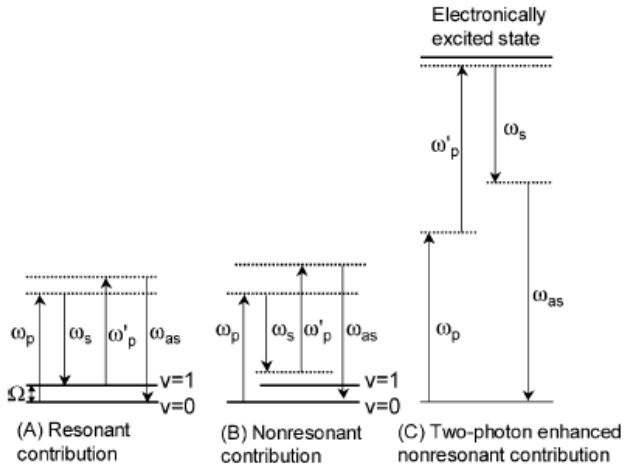

Figure 3-3: Energy diagram of CARS signal generation. (A) Resonant CARS ($\Omega = \omega_{vib}$); (B) Non-resonant CARS generated by an electronic contribution; (C) Non-resonant CARS caused by a two-photon resonance of the pump beam associated with excited electronic states. (Dotted lines indicate virtual states) [35].

The resonant susceptibility has real (Re(χ) or χ') and imaginary (Im(χ) or χ'') elements. The real element has a dispersive line shape related to the nonlinear refractive index of the medium, and the imaginary element, which mirrors the spontaneous Raman line, has a Lorentzian shape (Figure 3-4).

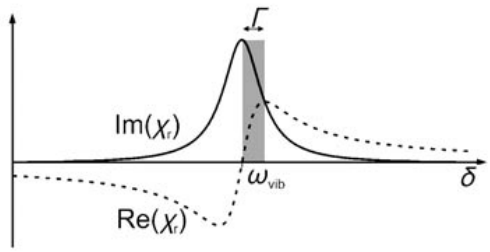

Figure 3-4: Real (Re (χ)) and imaginary (Im (χ)) contributions of resonant susceptibility of the Raman line with a line width of Γ [35].

The intensity of the CARS signal is proportional to the square modulus of the induced polarization $P^{(3)}$ and we can write:

$$I_{CARS} \propto \left|P^{(3)}\right|^2 \propto \left|\chi^{(3)}\right|^2 = (\chi' + \chi_{nr}^{(3)})^2 + (\chi'')^2 = (\chi')^2 + 2\chi'\chi_{nr}^{(3)} + (\chi_{nr}^{(3)})^2 + (\chi'')^2 \qquad (3\text{-}9)$$

The mixing of non-resonant and resonant susceptibility from the cross term $2\chi'\chi_{nr}^{(3)}$ adds an asymmetric shape to the CARS spectrum. Figure 3-5 shows CARS intensity versus frequency for a resonance frequency of 1 cm^{-1} and a line width of 1 cm^{-1}, for varying concentrations of a resonant material to obtain a constant non-resonant susceptibility of 1.0. By decreasing the concentration of the resonant medium, the maximum peak of the CARS spectrum shifts slightly.

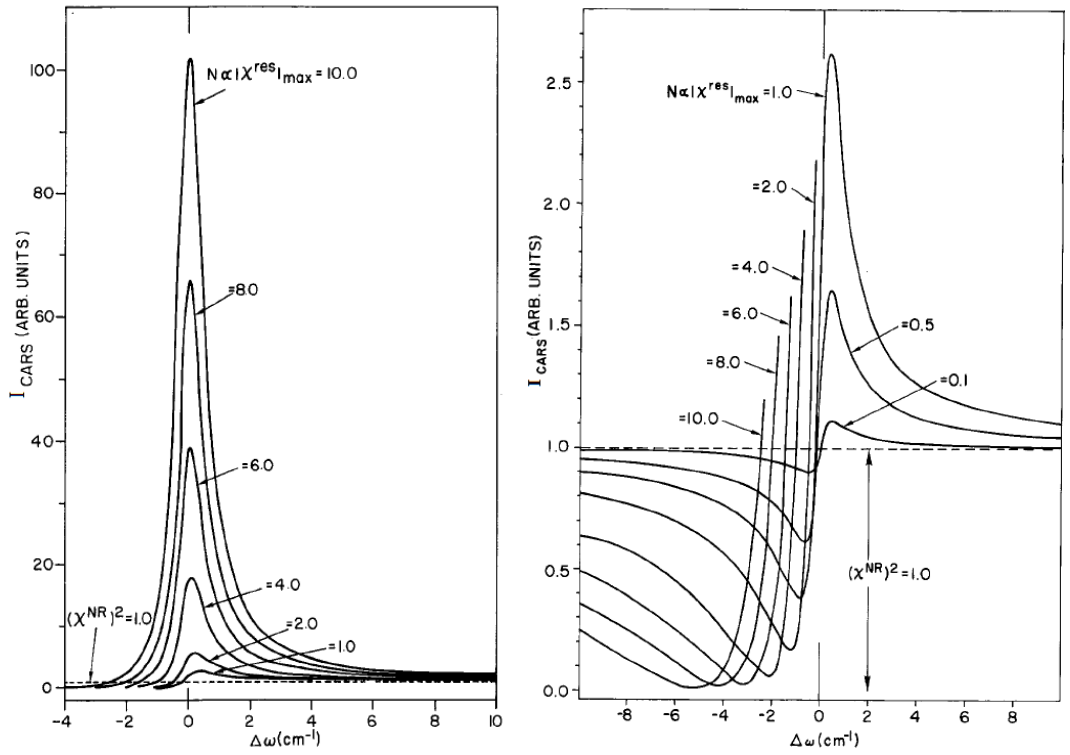

Figure 3-5 CARS signal intensity versus frequency for a resonant frequency of 1 cm^{-1} for a medium with a non-resonant susceptibility of 1, for different density numbers of the resonant material. The graph on the right shows more details for low density numbers of the resonant material [45].

In the case of using the same pump and probe field to achieve the maximum third order resonant susceptibility (Eq. 3-8), the frequency difference between the two beams should be equal to the vibrational frequency(ies) of the medium of interest.

$$\omega_{vib} = \Omega = \omega_p - \omega_s \tag{3-10}$$

The pump and Stokes beams should overlap, so the wave vector mismatch confinement (Equation 3-4) is fulfilled. Due to the use of high peak power pulsed laser sources, to obtain the spatial overlap requirement of the pump and the Stokes beams (pulses) the two laser sources must be synchronized, and the beam paths of the pump and the Stokes must be the same.

From a light source perspective, CARS spectroscopy/microscopy can be performed using three different approaches:

i) In the first approach, two synchronized picosecond lasers provide the pump and Stokes beams for CARS [39]. Though this method provides high quality images, synchronizing

the two systems is difficult, and the cost associated with acquiring two sources is a major disadvantage.

ii) With the second approach, a synchronously pumped optical parametric oscillator (OPO) system is used to generate both the pump and Stokes beams [36]. This approach provides similar signal quality as the first, and has the same cost and complexity issues.

iii) The third approach uses a single femto-second laser to generate both the pump and Stokes pulses, by generating a supercontinuum using a tapered fiber [46] or a high nonlinear PCF [47], and a portion of the pump fs laser beam. The Stokes beam is usually obtained by filtering the IR portion of the generated SC. The advantages of this approach are its simplicity compared to the two previous methods, reduced costs and compact setup; the main disadvantage is the decreased image quality.

3.3.2. Literature review on CARS

In 1982, Duncan et al. [48] built the first CARS microscope, using picosecond visible dye lasers as the light source. They employed non-collinear excitation geometry, similar to the phase-matching condition in conventional CARS spectroscopy. However, regardless of the microscope geometry, the main problem with their CARS signal was the non-resonant CARS background signal, which overwhelmed the CARS image contrast.

In 1999, Zumbusch et al [49] explored collinear phase matching in order to avoid many of the limitations encountered earlier. They overlapped two pump and Stokes beams, then focused them tightly on the sample up to two micrometers from the focal point of a high NA microscope objective lens, where the CARS signal was generated due to the high density of both beams. They also employed near-infrared light sources for CARS imaging, which enabled them to reduce the non-resonant CARS signal background, and achieve higher penetration depths for 3D imaging of the biological samples.

Cheng et al. used two synchronized 2-3 picosecond (ps) near-infrared laser sources, and obtained a much higher signal-to-background ratio of the CARS signal by reducing the non-resonant background. Using ps laser pulses, they reduced the spectral widths of the pump and Stokes beams and got closer to the Raman bandwidths of the sample, to avoid more independent Raman shift non-resonant background excitation (Figure 3-3 (B))[33]. At the same time, Paulsen et al. demonstrated the potential of using only one femtosecond (fs) laser source, and a photonics

crystal fiber to generate a supercontinuum (SC) as the second source [50]. They utilized a photonic crystal fiber to generate a frequency-shifted beam SC as the pump beam in the CARS process. They used the soliton decay peak at 643 nm of generated SC as the pump beam, and mixed it collinearly and spatially with the fundamental 795 nm femtosecond laser beam as Stokes beam, to generate the CARS signal [50].

Using photonic crystal fiber eliminated the need for more-complex laser systems, and for the first time demonstrated the possibility of performing CARS microscopy with a photonic crystal fiber based light source as the pump [50]. They showed the applicability of their setup by CARS imaging of micrometer-sized polystyrene beads [50]. However, the generated pump beam quality was lower than an OPO beam, due to the coherence degradation and amplitude fluctuations of the generated SC[51].

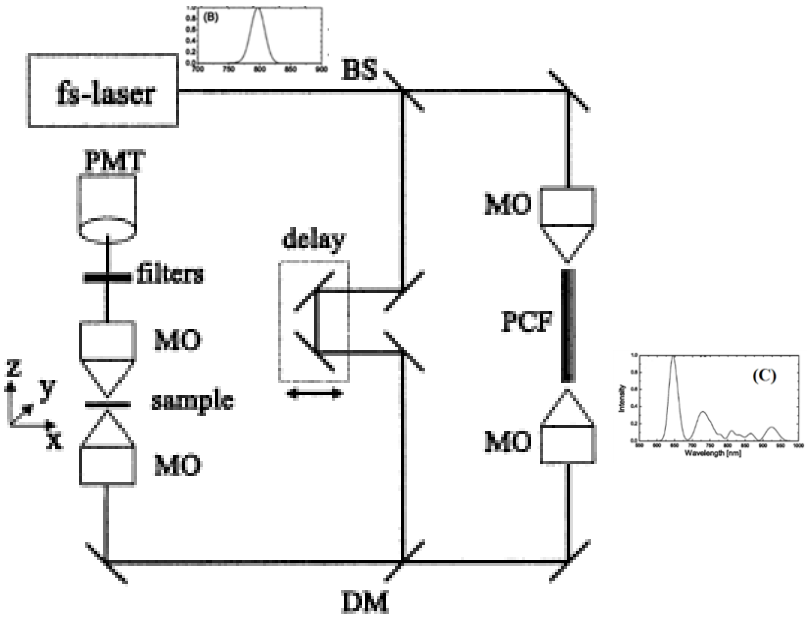

Figure 3-6: (A) Schematic overview of H. N. Paulsen's setup: BS denotes the beam splitter, DM the dichroic mirror, MOs the microscope objectives, PCF the photonic crystal fiber, and PMT the photomultiplier tube. (B) The spectra of the fs laser beam coupled to PCF is used as Stokes beam (C) output of the photonic crystal fiber [46].

In another approach, H. Kano and H. Hamaguchi [52] used 100 fs laser pulses at 801 nm from a Ti-sapphire laser to generate SC out of a 2 far-lying ZDWs PCF (crystal fiber NL-1.7-690). In their CARS setup, the near-infrared (NIR) portion of the SC spectrum was used as the

Stokes beam. The balance of the fs laser beam was spectrally filtered with a narrow-band pass filter, then used as the pump beam to generate the CARS signal and conduct CARS imaging of the polystyrene beads and living yeast cells in the C-H stretching vibrational region. Later, K.M. Hilligsøe et al. [53] showed that a 2 closely-lying ZDW photonics crystal fiber can generate a less noisy supercontinuum that is not as dependent on the input laser beam parameters, and proposed that it could be used for CARS imaging applications. Our group demonstrated [54] fast data acquisition CARS microscopy imaging of lipid rich biological samples, using low noise SC from 12 cm of a two closely lying ZDW PCF. However using a 2 closely-lying ZDW fiber in a single fs laser CARS approach can limit the capability to perform CARS imaging/spectroscopy in the fingerprint region, as there is not enough spectral density in the generated SC out of a 2 closely lying ZDW PCF between 850 and 950 nm (when using an 800 nm pump laser). We then demonstrated that using a polarization maintaining PCF with two far-lying ZDWs could provide a CARS signal in the fingerprint region. In addition, B. V. Vacano, et al. [55] showed the potential of performing broadband CARS imaging/spectroscopy of polymer samples using a single fs laser setup, and applying a 2 far-lying ZDWs PCF to generate a broad continuous CARS spectrum.

A main technical problem with the single fs laser CARS approach is the non-resonant background, which is due to the spectrally broad fs pump beam. This can be particularly significant in the fingerprint region when the resonant vibrational band is very narrow and causes overlapping of the resonant and non-resonant signals. Adrian F. Pegoraro, et al. demonstrated that by using the spectral focusing method, and introducing a large amount of chirp to the pump and Stokes beams before focusing on the sample, it is possible to reduce the non-resonant background intensity and achieve better CARS imaging quality in the fingerprint region [56,57].

Finally, imaging tissues ex-vivo is useful, but a CARS endoscope is required to make nonlinear imaging practical for clinical use. A number of groups have attempted to develop a miniaturized portable CARS microscope. F. Légaré, et al. [58] demonstrated a proof-of-principle of a CARS endoscope (Figure 3-7). A passively mode-locked 10W Nd:YVO4 laser, operating at 1064 nm with 7 ps pulses, was used to synchronously pump an OPO to generate a 5 ps pulse train with broad tuning range of 780 to 920 nm. A portion of the 1064nm output of the Nd:YVO4 laser was used as a Stokes beam, and the tunable output of the OPO provided the

required pump beam. The spatially and temporally overlapped pump and Stokes beams were coupled to a single mode fiber, then focused on the sample by focusing lenses to generate the CARS signal. The generated epi CARS signal was collected by the same fiber, and separated from the pump and Stokes beams using a dichroic mirror. To perform 3-D imaging, the sample was raster scanned by a three-dimensional piezo stage, with respect to the fixed fiber assembly. This was the first demonstration of a fiber delivered miniaturized microscope, and it enabled them to perform CARS imaging of 0.75 um and 5 um bead samples. However, the scanning mechanism was external, and the quality was not adequate to image tissue samples.

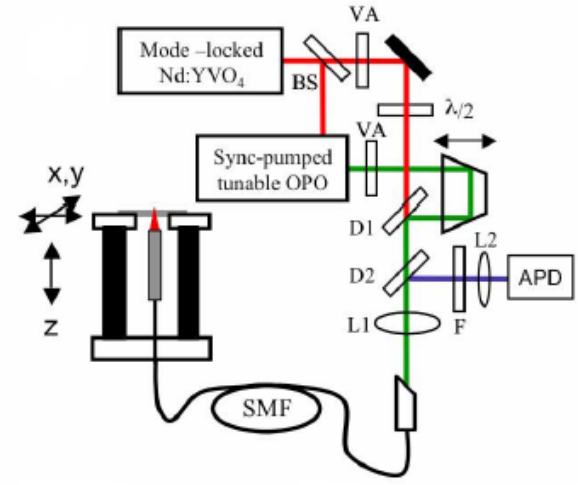

Figure 3.-7 : F. Légaré et al CARS endoscope setup [58].

Parallel work with shorter pulse widths was performed by Wang, et al. at Purdue University, who investigated the differences between SMF and PCF delivery. Specifically, they attempted to quantify the SPM and GVD effects generated by the propagation of the shorter pulses through the different delivery fibres. Their laser system consisted of two Ti-sapphire lasers with outputs of 2 ps and 3 ps pulses for the pump and the Stokes beams respectively. The trials were performed on two 1m long fibres: an SMF (NA = 0.13) and a PCF (NA = 0.05). While the 2 and 3 ps pulses suffered very little SPM and GVD while propagating through the PCF (<1% pulse broadening), a 200 fs pulse had significant spectral broadening, from 5 to 12 nm. Based on this, it is clear that using femtosecond pulses requires pre-compensation to counteract fibre generated nonlinearities. The SMF fibre also induced significant spectral broadening of the 2 ps pump pulse. Additional wings produced in the autocorrelation trace corresponded to a pulse width of 3.1 ps. When the pump and Stokes beams were delivered by the SMF, the CARS intensity was

only half of the PCF delivered light [59]. Though this is not surprising, quantifying the reduction in CARS intensity was an important step in understanding the benefits of using PCFs as a photon delivery method. The use of PCFs in conjunction with picosecond pulses (with macro optics) allowed Wang et al. to obtain the epi images.

More recently, B. G. Saar et al. [60] developed a coherent Raman scanning fiber endoscope for label-free imaging of biological tissues, using a miniaturized fiber scanner and an optical parametric oscillator (OPO) to generate the pump and Stokes beams. In this approach, the pump and the Stokes beams scanned the sample, which facilitated performing CARS imaging in situ. They used green lenses to focus the excitation light at the sample, and to overcome the inherent chromatic aberrations of a single green lens system, the objective lens was made up of two GRIN lenses with a diffractive optic between them [60]. Since they mounted the optical detector on the tip of the CARS probe, the large size of the endoscope made it virtually impossible to insert the scanning fibre endoscope into a small cavity to perform CARS imaging.

Our group [61] has demonstrated a novel, portable, miniaturized, fibre delivered multimodal CARS exoscope/endoscope. It uses a single fs laser and a short length two closely lying ZDWs PCF to generate the pump and the Stokes beams respectively. It is capable of performing SHG, TPEF and CARS imaging of biological samples.

3.4. Supercontinuum generation

Supercontinuum generation is a key element in single fs laser-based CARS microscopy. Therefore, if we better understand the various mechanisms that contribute to supercontinuum generation, as well as its dependency on the input parameters, we can enhance the quality of generated CARS images. The following presents a literature review and short theoretical discussions about the main nonlinear optical processes involved in supercontinuum generation.

3.4.1. Supercontinuum generation literature review

Supercontinuum generation is the formation of continuous broadband optical spectra by propagating a very high power laser pulse through nonlinear media. This effect was first observed and reported by Alfano and Shapiro in 1970 [62, 63].

Further studies of launching short laser pulses (10 ps to 10 ns) to a single mode fiber demonstrated the roles of self-phase modulation (SPM), cross-phase modulation (XPM), soliton fission, stimulated Raman scattering, and a variety of four-wave mixing (FWM) optical processes, in the generation of new frequencies to produce a spectrally smooth SC [64,65]. It was found that when laser pulses are pumped at the normal GVD region of the fiber (medium), the SPM, FWM and stimulated Raman broadening mechanism are dominant during SC generation, while when pumping in the anomalous GVD region of the fiber, the spectral broadening during SC generation is mainly due to soliton fission processes [66, 67]. In addition, as input parameters such as power, pulse duration and wavelength change, the impact of the different physical mechanisms also change. Moreover, the dispersion profile and length of the PCF have strong impact on the shape of the spectrum and the dominant mechanism [68]. By changing the distance between the two zero dispersion wavelength points and the value of the dispersion magnitude of a PCF, the supercontinuum mechanism and SC spectrum out of a PCF can be manipulated by controlling the balance between the SPM and the dispersion mechanism.

This can be achieved by modifying the ratio of fiber pitch to air hole size of the PCF structure, which results in a changed ZDW location and dispersion value (Figure 3-8).

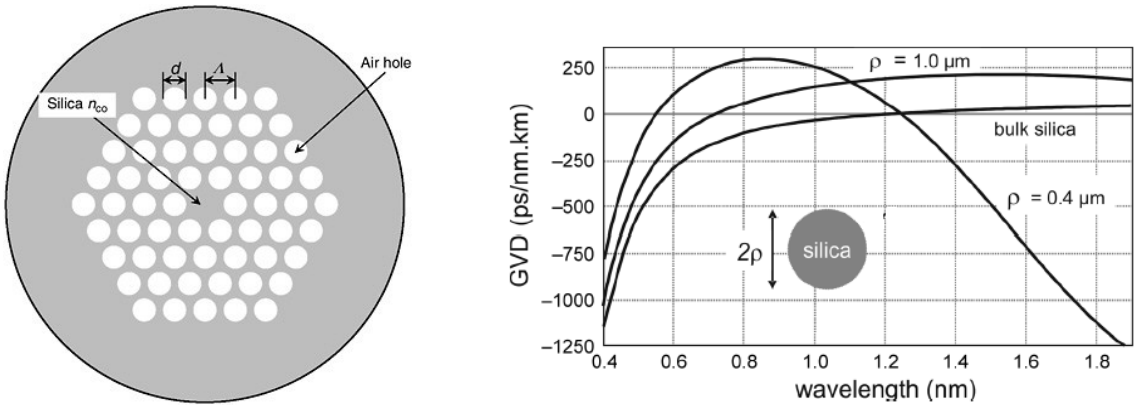

Figure 3-8: Left: Structure of a solid core photonics crystal fiber with d=hole diameters and Λ= pitch and hole to hole spacing. Right: Group velocity dispersion curve of two engineered GVD PCFs with core diameters (ρ) of 0.4 μm and 1.0 μm and bulk silica (material dispersion). The ZDW of pure silica is approximately 1.3 μm [69].

Figure 3-9 presents the group velocity dispersion parameter (β_2) of the two PCFs used in all our experiments and the CARS setup. As shown, by changing the structure of the PCF, the location of the ZDWs and the β_2 value can be changed hundreds to thousands of times, resulting in different SC generation mechanisms and SC spectrums in each fiber.

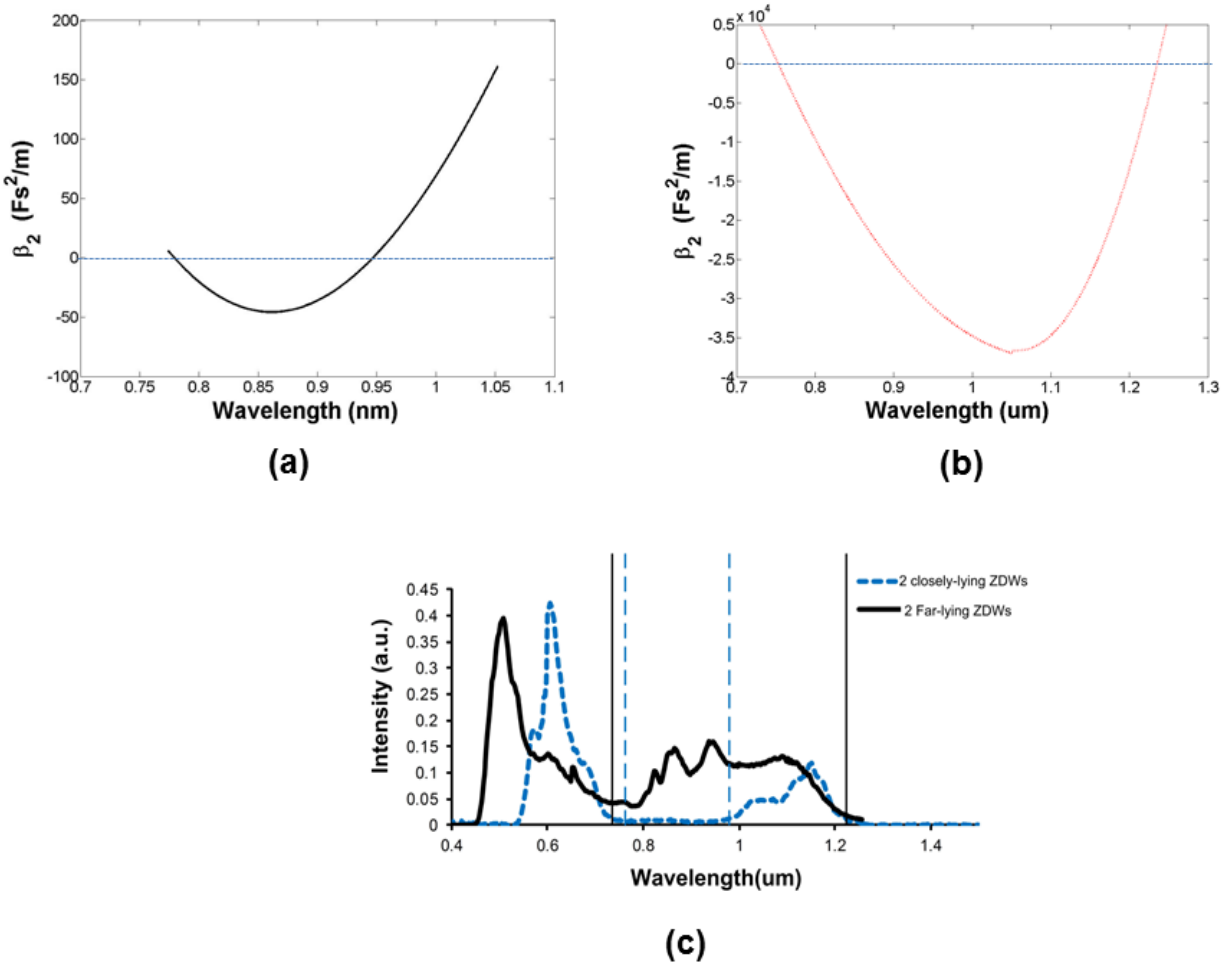

Figure 3-9: (a) group velocity dispersion parameter (β_2) of PCF with two closely-lying ZDWs (Fiber A); (b) PCF with 2 far-lying ZDWs (Fiber B), with dashed lines indicating the zero dispersion (courtesy of Crystal Fiber Inc.); (c) the supercontinuum spectra out of two far-lying ZDWs (black line) and two closely-lying ZDWs (blue dotted line) fibers for the same input power of 530 mW and pulse duration of ~100 fs. Vertical lines indicate the positions of the ZDWs. The intensity scales of the two SCs are not exactly the same.

Before PCF, laser sources with pulse energies at micro-Joule levels were required to generate SC in bulk materials. However, the development of dispersion-engineered PCF with blue shifted ZDW of approximately 800 nm and high nonlinearity allows the use of less powerful lasers. In addition, the broadband single-mode guidance property of the endlessly single-mode PCF resulted in retention of the uniform spatial profile generated SC out of the PCF. These advantages enabled PCF to be used in many applications, including metrology, spectroscopy [70], optical coherence tomography [71], and Coherence anti-Stokes Raman scattering (CARS) microscopy [50].

3.4.2. Major physical processes contributing to supercontinuum generation

In the following, the main nonlinear processes that contribute to generating a broad spectrum SC inside the core of a PCF are discussed.

3.4.2.1. Self-phase modulation and spectral broadening

Most of the nonlinear optical phenomena in PCFs are a result of the Kerr effect, or the nonlinear refractive index changes of the medium caused by changing the propagating pulse intensity.

$$\tilde{n}(\omega, I) = n(\omega) + n_2|\mathrm{I}| \qquad (3-11)$$

where $\tilde{n}(\omega, I)$ is the refractive index, n(ω) is the linear part of the refractive index, I is the optical intensity inside the fiber, and n_2 is the nonlinear index coefficient, or Kerr index. The phase of an optical field propagating inside the fiber can be written as:

$$\phi = \tilde{n} k_0 L = n k_0 L + n_2 I k_0 L \qquad (3-12)$$

where $k_0 = \frac{2\pi}{\lambda}$, λ is the wavelength of the optical pulse, and L is the propagation length.

Temporally varying the phase of the optical field of a temporal intensity varying pulse generates instantaneous optical frequency broadening, with a $\delta\omega(t)$ shift from the central frequency ω_0. Using a squared hyperbolic secant beam from a mode locked fs laser as an example, a closed form is shown to be given by [72]:

$$\delta\omega(t) = -\frac{d\phi_{nl}}{dt} = -\frac{L_{eff}}{L_{NL}}[\frac{\partial}{\partial t} I(0,t)] = \frac{L_{eff}}{L_{NL}} \tanh(\frac{t}{\tau}) Sech^2(\frac{t}{\tau}) \qquad (3-13)$$

where L_{eff} is the effective length of the pulse propagation, $L_{NL} = (\gamma P_0)^{-1}$ is the nonlinear length, P_0 is the peak power, τ is the pulse duration, and γ is the nonlinear coefficient of the core medium.

Figure 3-10 presents the experimental spectral broadening inside a PCF with two closely-lying wavelengths at 775 nm and 945 nm, as a function of the average laser input power. As shown, increasing the average laser input power will reduce the fiber nonlinear length, and based on equation (3-13) the SPM spectral broadening ($\delta\omega$) will increase.

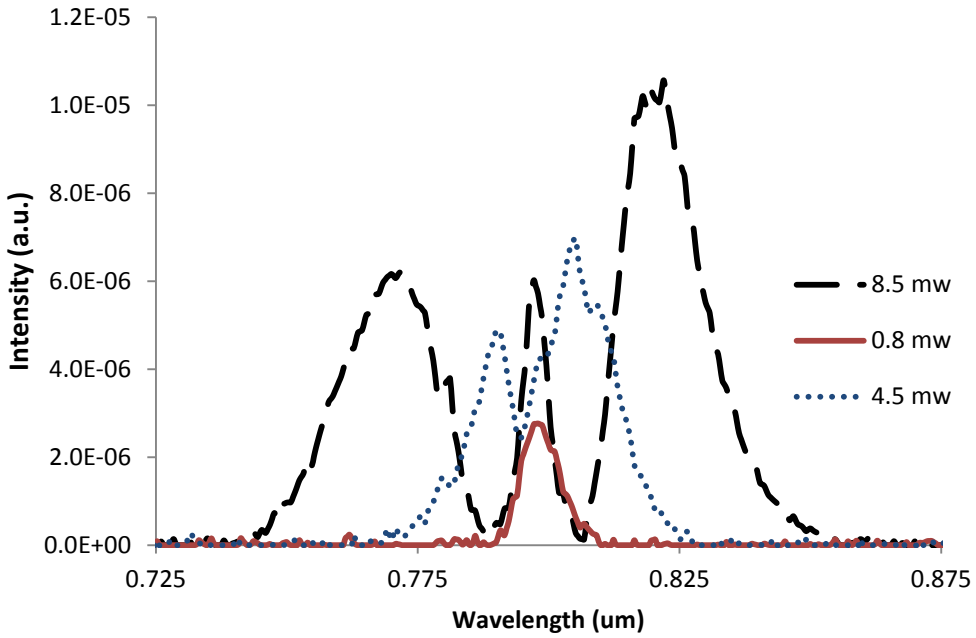

Figure 3-10: Experimentally observed spectral broadening (largely due to SMP) of fs laser pulses (FWHM=100 fs) at 0.8 μm coupled to a 2 closely lying ZDWs fiber with 12 cm length, for different average power laser pulses.

3.4.2.2. Soliton formation and fission

An optical pulse that can propagate inside the fiber core without distortion, and follows a periodic evolution pattern, is known as an 'optical soliton'.

If a high power laser beam is coupled to the anomalous dispersion region of an optical fiber, the effects of the nonlinear positive chirp induced by the SPM and the linear negative chirp from GVD can be balanced, which leads to the formation of solitons. The soliton order (N') of an input ultra-fast pulse is determined by both the pulse and fibre parameters, as follows [72]:

$$N' = \sqrt{\frac{L_D}{L_{NL}}} = \sqrt{\frac{\gamma P_0 \tau^2}{|\beta_2|}} \qquad (3-14)$$

Where $L_D = \tau^2 |\beta_2|^{-1}$ is the dispersion length, β_2 group velocity dispersion parameter and L_{NL} is the nonlinear length.

The fundamental soliton is defined by $N' = 1$, and in this case both the spectral and temporal profiles of the input pulse will remain unchanged during the propagation of the pulse through the fiber core.

As shown in Figure 3-11, higher-order solitons exhibit periodic spectral and temporal evolution with propagation, as a function of the soliton period.

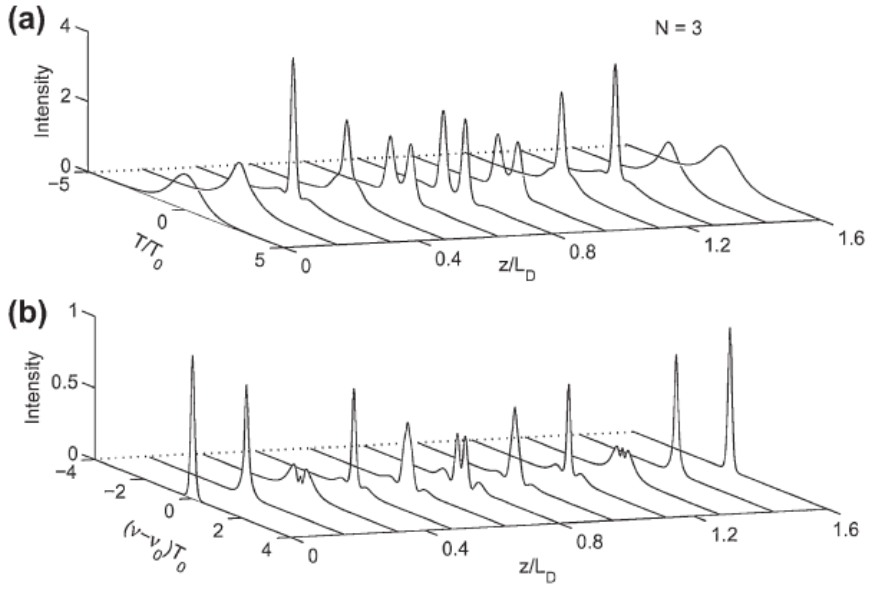

Figure 3-11: (a) Temporal and (b) spectral evolution of a third-order soliton as a function of traveling distance, z [72].

The soliton period z_0 is the distance after which a higher order soliton returns to its original spectral and temporal shape. The distance is defined as:

$$z_0 = \frac{\pi}{2} L_D = \frac{\pi \tau^2}{2|\beta_2|} \tag{3-15}$$

This temporal and spectral periodic pattern change is repeated over each propagation distance of length z_0. However, the propagation behaviour of the higher ordered solitons will be different in the vicinity of a zero dispersion wavelength with a highly positive magnitude of third order dispersion and a self-steepening effect [66, 67, 72]. After a short propagation distance of L_{fiss}, a higher order soliton with number N will split into N constituent one-soliton pulses, with different red-shifted central frequencies and group velocities [67]. Here, L_{fiss} is the soliton fission length, and is defined as:

$$L_{fiss} \approx \frac{L_D}{N'} = \sqrt{L_D L_{NL}} \tag{3-16}$$

As shown in Figure 3-12, increasing the pulse power inside a two far-lying ZDWs fiber core rapidly decreases the soliton fission length, while increasing the laser pulse width coupled to the

fiber increases the soliton fission length. Thus, by controlling the pulse power and pulse temporal duration of a fs laser pulse coupled to a PCF, we can control both the soliton fission length and the soliton number.

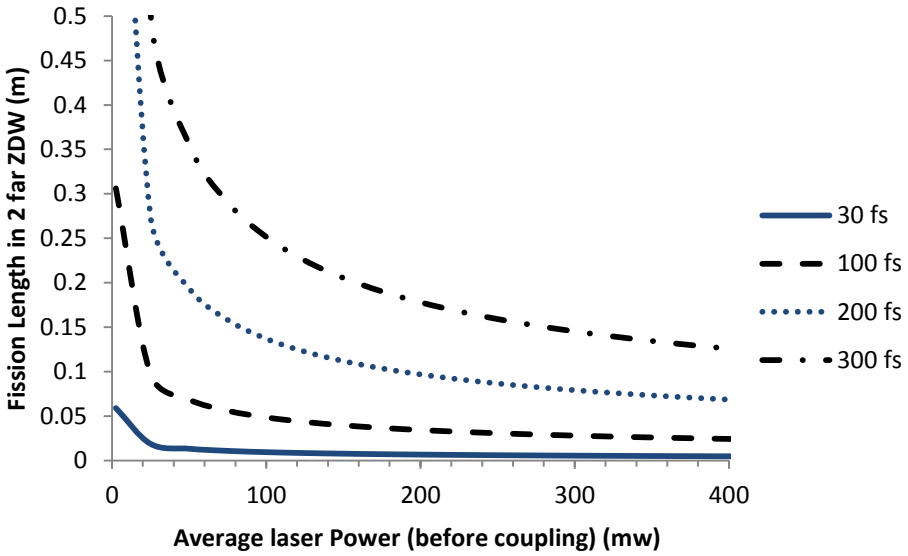

Figure 3-12: Soliton fission length in a 2 far–lying ZWDs fiber vs. laser average power coupled to the PCF.

Moreover, during a soliton fission process, each soliton pulse will lose energy by emitting nonsolitonic, blue-shifted radiation that is phase-matched to the corresponding pulse, while simultaneously moving to the IR region [66, 67].

In a higher order soliton fission process, the fact that there are several solitons with different red shifted frequencies causes a broad spectrum in the blue spectral region of the generated SC, due to the presence of corresponding blue-shifted nonsolitonic radiation for each soliton. The intermediate region in the SC spectrum rises during SC generation, due to four wave mixing between the solitons and their corresponding blue-shifted nonsolitonic continuums [67].

As shown in Figure 3-13, a 3rd order soliton pulse (red) split into three fundamental red shifted solitons (green), and their corresponding phase-matched blue-shifted nonsolitonic radiation (NSR) pulses (blue), generates a broad spectrum supercontinuum of at least six peaks.

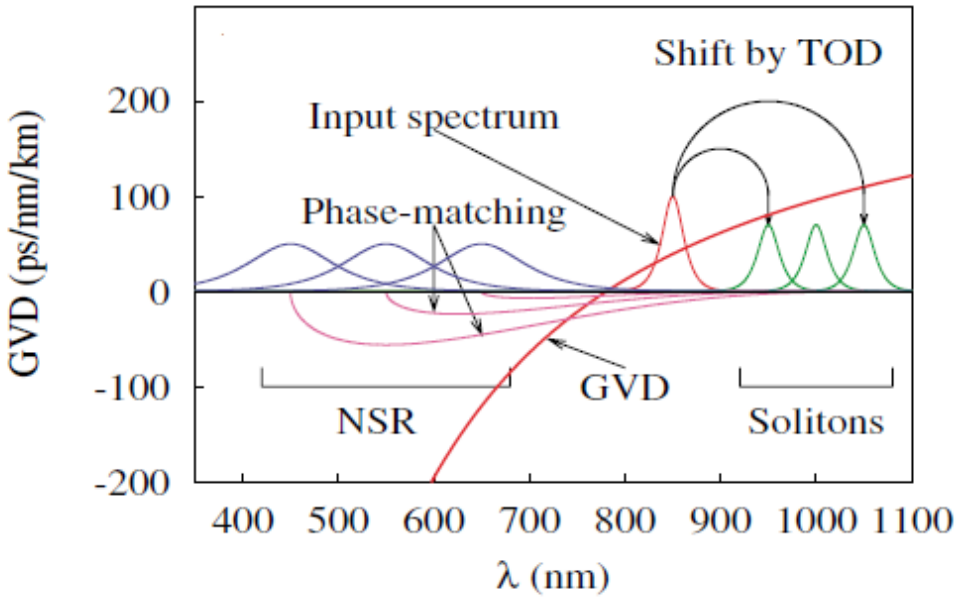

Figure 3-13: Schematic of a soliton fission mechanism for a third order soliton (red pulse), propagating in the vicinity of the zero dispersion wavelength of a PCF [67].

3.4.2.3. Modulation instability and pulse broadening

Modulation instability (MI) is modulation of the steady state of a continuous wave (CW), or a quasi-CW in the case of slowly varying envelope approximation, propagating radiation inside a fiber core due to the interplay between the nonlinear and dispersive effects in the time domain in the core [72, 73].

By solving the NLSE (nonlinear Schrödinger equation) in the presence of the SPM, we have:

$$\bar{q} = \sqrt{P_0}\exp(i\phi_{Nl}) \tag{3-17}$$

where P_0 is the incident power, $\phi_{Nl} = \gamma P_0 z$ and "z" is propagation distance is the nonlinear phase shift induced by the SPM.

In the presence of a small perturbation of amplitude "$a^{'}$", equation (3-17) will become:

$$\bar{q} = (\sqrt{P_0} + a^{'})\exp(i\phi_{Nl}) \tag{3-18}$$

As with the presence of the SPM, by substituting (3-18) in the NLSE and solving it, the perturbation term $a^{'}(z,T)$ of the initial pulse as a function of pulse width and propagation distance, can be obtained[72]:

$$a^{'}(z,T) = a^{'}_1 \exp[i(K^{'}z - \Omega^{'}T)] + a^{'}_2 \exp[-i(K^{'}z - \Omega^{'}T)] \tag{3-19}$$

where Ω' and K' are the frequency and wavenumber of the perturbation respectively, and a'_1 and a'_2 are arbitrary amplitudes of the two propagating perturbation waves. Here, K' is defined as:

$$K' = \pm 0.5\left|\beta_2 \Omega'\right|[\Omega'^2 + sign(\beta_2)\Omega_c^2]^{0.5} \tag{3-20}$$

where $sign(\beta_2)$ is the sign of β_2, and $\Omega_c^2 = \frac{4}{|\beta_2| L_{NL}}$.

K is real in a normal GVD region with $\beta_2 > 0$, thus for all values of Ω' the steady state of the propagating light will be stable, regardless of small power perturbations. However, in the case of anomalous GVD with $\beta_2 < 0$, K' becomes imaginary for all frequencies (Ω') smaller than Ω_c. In this case, the perturbation term ($a'(z,T)$) will grow exponentially with z, as shown in equation (3-19). In this situation, the gain spectrum of the MI is defined as:

$$g(\Omega') = \left|\beta_2 \Omega'\right|(\Omega_c^2 - \Omega'^2)^{0.5} \tag{3-21}$$

Figure 3-14 shows the gain spectrum of the MI in the two different PCFs with different β_2, as a function of the frequency shift Ω' from the central frequency and the average laser power coupled to the fibers. As shown, the MI effect is much more pronounced in the 2 far-lying ZDWs fiber, due to the higher absolute value of β_2.

In the presence of higher terms of β, dispersion parameter, (β_4 fourth order dispersion parameter) the MI spectra gain can be written as [74]:

$$g(\Omega') = \mathrm{Im}[(\frac{\beta_2 \Omega'^2}{2} + \frac{\beta_4 \Omega'^4}{24})(2\gamma P_0 + \frac{\beta_2 \Omega'^2}{2} + \frac{\beta_4 \Omega'^4}{24})]^{0.5} \tag{3-22}$$

and the MI gain can appear even in the normal dispersion region.

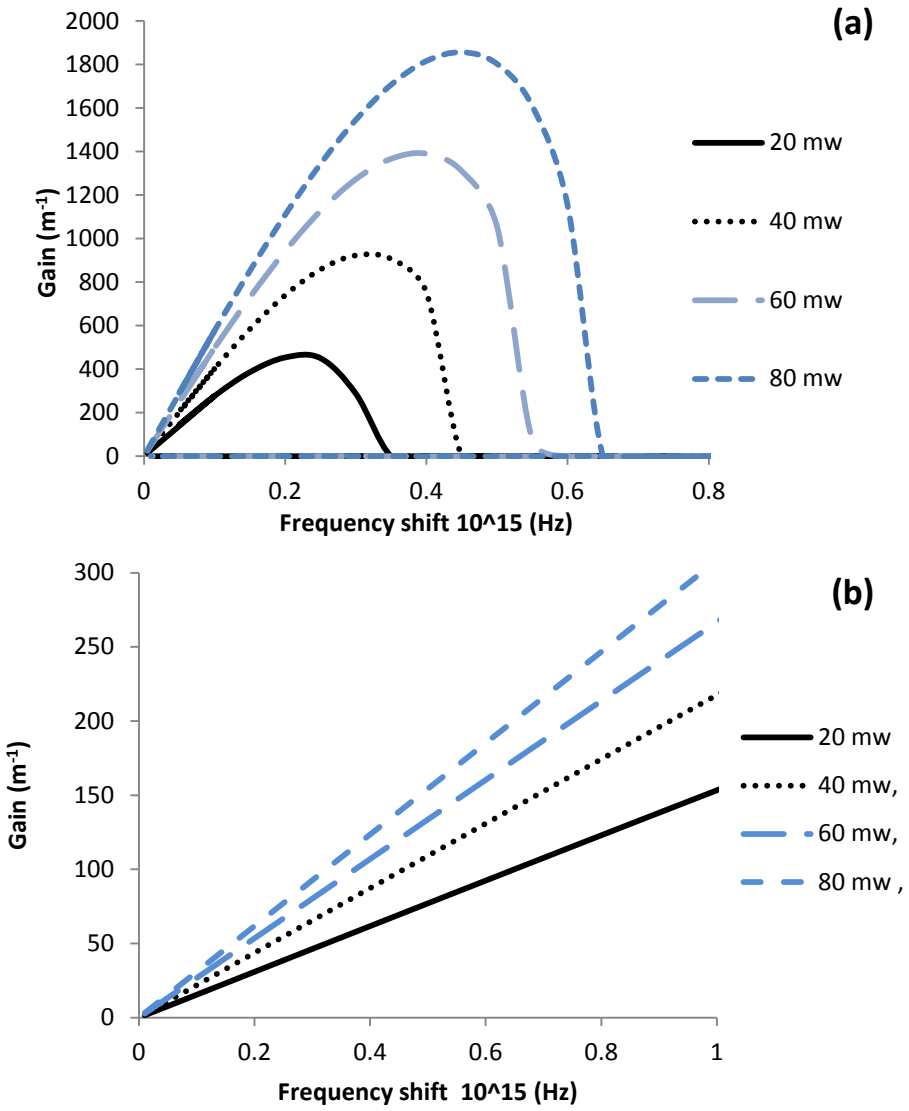

Figure 3-14: Gain spectra of modulation instability for four power levels of a 100 fs laser pulses at 800 nm coupled to a 12 cm length of (a) two far-lying ZDWs PCF, and (b) two closely lying ZDWs PCF. Due to the lower value of β_2 for the two closely lying ZDWs fiber, the maximum MI gain is at the higher frequency shifts.

Figure 3-15 shows the MI gain at a frequency shift of 110 THz in a 2 far-lying ZDWs PCF, as a function of the pulse width and average power of the fs laser coupled to the PCF. The MI gain increases as the average power is increased. As shown in Figures 3-15 and 3-16, in the absence of other nonlinear optical processes, the MI gain is enhanced by decreasing the fs laser pulse width. However, due to the presence of the SPM or soliton fission, the MI contribution (different from MI gain) in distortion of the propagating pulse will actually decrease by reducing the fs laser pulse width [51, 74].

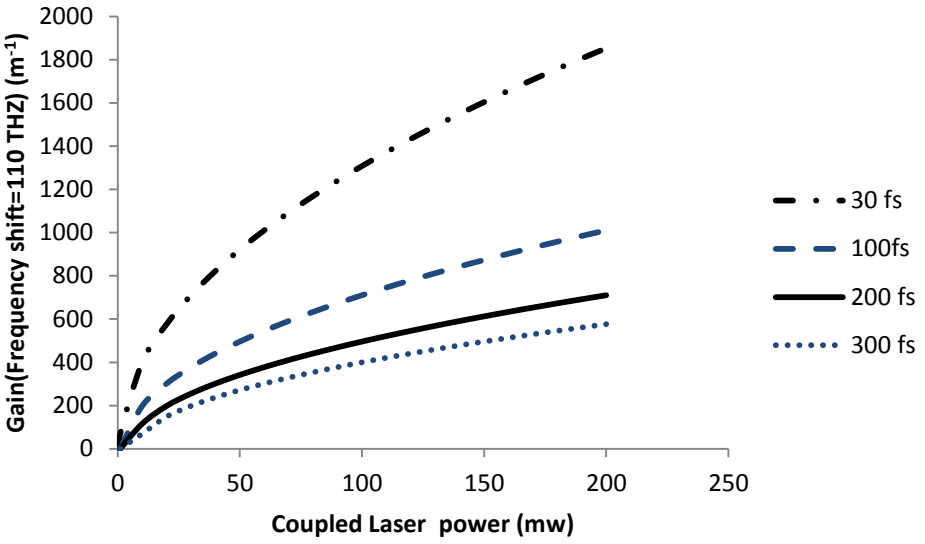

Figure 3-15: Modulation instability gain at a frequency shift of 110 THz (around 1040 nm) from the 800 nm fs laser input pulse for four different pulse widths, versus different average power of coupled fs lasers. (Fiber length =12 cm)

MI plays an important role in the initial spectrum/temporal broadening of a short pulse propagating inside a fibre core when dealing with high peak power laser pulses or pulses with temporal widths longer than ($\tau > 500 fs$). However, in the case of shorter laser pulses ($\tau < 500 fs$), the interplay between the soliton fission and MI/FWM is important in SC generation inside the core of a high nonlinear PCF [74].

As shown in Figure 3-16, due to the smaller soliton fission length for shorter fs laser pulses (Figure 3-12), the product of the multiplication of the MI gain to the soliton fission length is reduced significantly by decreasing the pulse width of the coupled fs laser to the fiber. Here, it is assumed that the MI cannot have a major impact after soliton fission occurs, since the peak pulse power significantly decreases after soliton fission, and the soliton fission length is picked up as the effective MI propagation length.

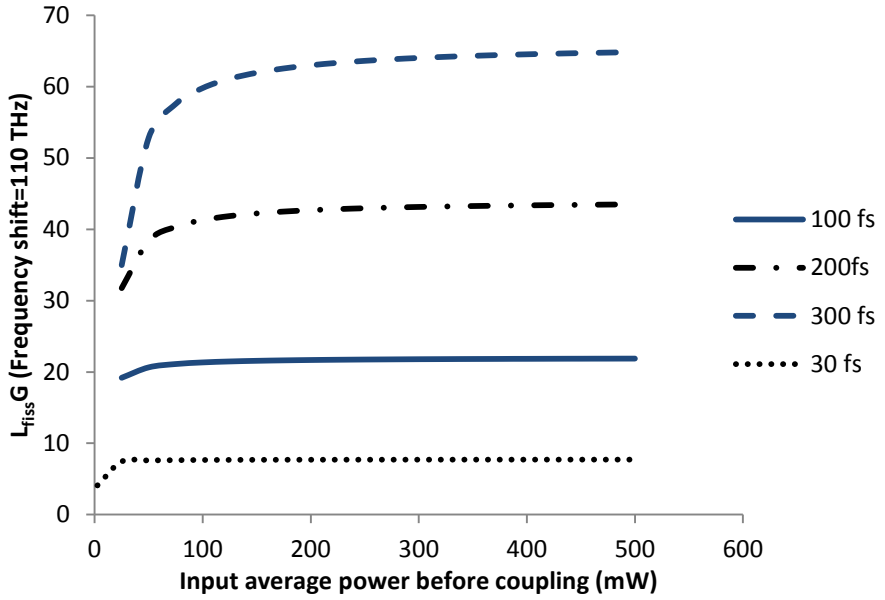

Figure 3-16: The multiplication of modulation instability gain (G) at a frequency shift of 110 THz by the soliton fission length(L_{fiss}) for a 12 cm length of 2 far-lying ZDW PCF, versus the average fs input laser power for four different fs laser pulses widths.

Figure 3-17 shows the MI role for two different fs laser pulse widths propagating inside a 2 far-lying ZDW PCF when the soliton fission process is occurring. As the MI function is increased exponentially by the product of the MI gain and the propagation length, and the effective propagation length of the MI is confined by the soliton fission (approximately zero MI after soliton fission), the MI role can be raised exponentially by increasing the average laser pulse power for the 100 fs laser pulses (as expected), while it is negligible for 30 fs laser pulses compared to the 100 fs pulses.

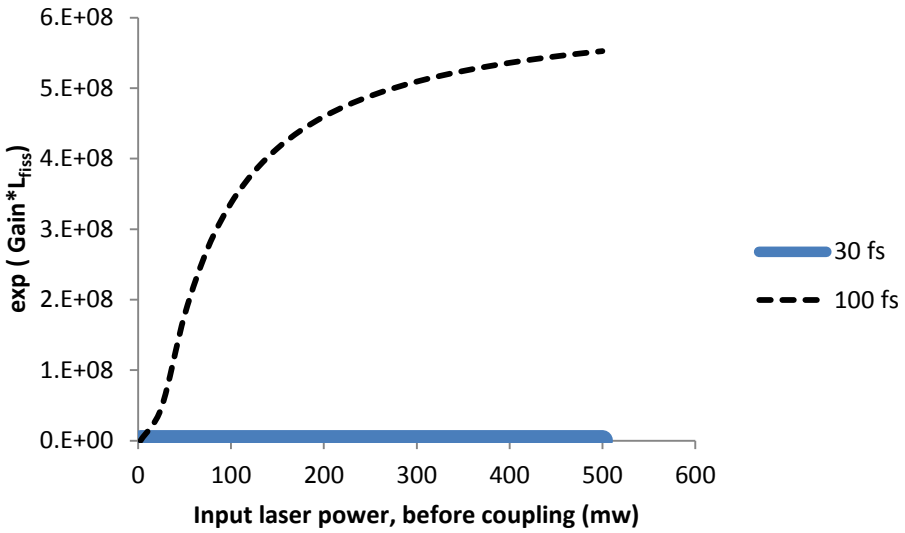

Figure 3-17: The exponential value of the modulation instability gain at a frequency shift of 110 THz multiplied by the soliton fission length, versus the average fs input laser power for two different fs laser pulse widths.

3.4.2.4. Four wave mixing and phase matching condition

In the absence of the soliton fission process (e.g. when the L_{fiss} is longer than the length of the fiber when using a 12 cm length of 2 closely lying ZDWs PCF), FWM will play an important role in generating a broadband supercontinuum and determining the coherence of the SCG.

In this case, degenerate FWM produces two photons from a pump beam with frequency ω_p which are then converted into a signal photon with frequency ω_s and an idler photon with frequency ω_I. Phase-matching is achieved when both the energy (equation 3-23) and the momentum (equation 3-24) are conserved [53, 72] :

$$\omega_s + \omega_I - 2\,\omega_p = 0 \qquad (3\text{-}23)$$

$$\beta(\omega_s) + \beta(\omega_I) - 2\beta(\omega_p) + \Delta\beta_{NL} = 0 \qquad (3\text{-}24)$$

where $\Delta\beta_{NL}$ is the nonlinear contribution to the propagation constant that originates from the self-phase and cross-phase modulation. By integrating the measured dispersion of the fiber core (propagating medium) and solving equation (3-23) and (3-24), the phase-match conditions can be determined, as shown in the figure 3-18 [53].

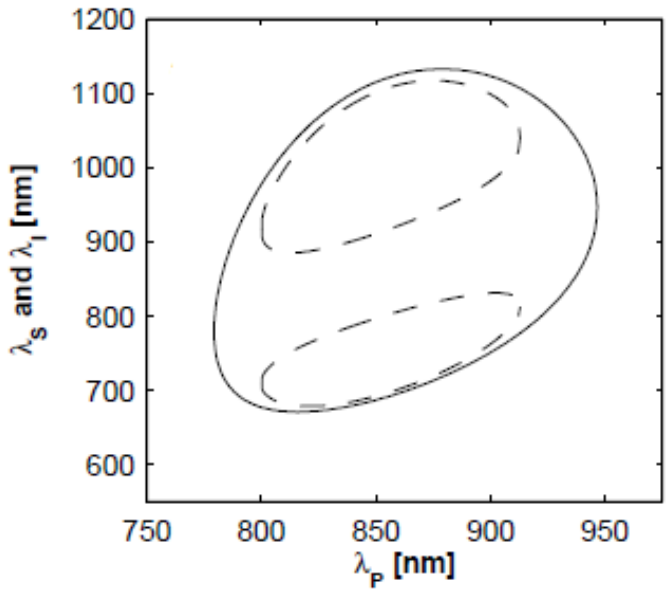

Figure 3-18: Phase-matching curves for four-wave mixing in two closely lying ZDWs fibers (fiber A). The full curve depicts the phase-matching curve without a power-dependent term, and the dashed curves show the phase matching with an input power of 300 W in the presence of the SPM [53].

The existence of the degenerate FWM causes major spectral density depletion in the generated SC out of 2 closely-lying ZDWs PCF between the two zero dispersion wavelengths. This creates two big continuum peaks out of the ZDWs region in the generated SC out of this fiber. (Dashed line in Figure 3-9 (c)).

3.5. Related Publications

A. CARS microscopy using PCF with two far-lying ZDW

3.5.1. Majid Naji, Sangeeta Murugkar and Hanan Anis, *"Determining optimum operating conditions of the polarization-maintaining fiber with two far-lying zero dispersion wavelengths for CARS microscopy",* Optics Express, Vol 22, No. 9, 10800-10814, 2014.

3.5.2. Majid Naji, Sangeeta Murugkar, Kaisar R. Khan and Hanan Anis, "*CARS microscopy using photonic crystal fibre (PCF)",* Photonics West, Proc. SPIE 7569, Multiphoton Microscopy in the Biomedical Sciences X, 75692S , February 26, 2010.

B. CARS microscopy using PCF with 2 closely lying ZDWs

3.5.3. Sangeeta Murugkar, Carig Brideau, Andrew Ridsdale, Majid Naji, Peter Stys and Hanan Anis ,"*Coherent anti-Stokes Raman scattering microscopy using PCF with two closely laying zero dispersion wavelength*", Optics Express, Vol. 15, No. 21, 14028-14038, 2007.

C. Portable miniaturized fiber deliverd Exoscope

3.5.4. Sangeeta Murugkar, Brett Smith, Prateek Srivastava, Adrian Moica, Majid Naji, Craig Brideau, Peter K. Stys, and Hanan Anis, "*Miniaturized multimodal CARS microscope based on MEMS scanning and a single laser source*", Optics Express, Vol. 18, No. 23, 23796-23804, 2010.

3.5.5. Sangeeta Murugkar, Brett Smith, Majid Naji, Craig Brideau, Peter Stys and Hanan Anis ,*"Development of a micromirror-scanned multimodal CARS miniaturized microscope for the in vivo study of spinal cord disorders*., Photonics west, Proc. of SPIE Vol. 7903 79031D-1, 2011.

3.5.6. Brett Smith, Majid Naji, Sangeeta Murugkar, Craig Brideau, Peter Stysa and Hanan Anis , "*A novel multimodal CARS miniaturized microscope*", Photonics West, Proc. SPIE 8226, Multiphoton Microscopy in the Biomedical Sciences XII, 822629 , February 9, 2012.

3.5.7. Brett Smith, Majid Naji, Sangeeta Murugkar, Emilio Alarcon, Craig Brideau, Peter Stys and Hanan Anis, *" Portable Miniaturized, fibre delivered multimodal CARS exoscope*," Optics Express, Vol. 21, No. 14, 17161-17175, 2013.

D. Fs laser pulse compressing

3.5.8. François Légaré, Madji Naji, Philippe Lassonde, Daniel Comtois, Vincent Crozatier,Thomas Oksenhendler, Hanan Anis and Jean-Claude Kieffer, "*Pulse compression and shaping of broadband optical parametric amplifier laser source*", Optics Letters, Vol. 33, No. 23, 2824-2826, 2008.

A. CARS microscopy using PCFs

Novelty:

I demonstrated the importance of the relative intensity noise (RIN) measurements of the generated Stokes beam (the IR portion of the generated supercontinuum) and the corresponding CARS signal of a standard oil sample, using a high nonlinear PCF to determine the optimum operation point, and selecting a PCF to perform single fs CARS microscopy. By doing a series of RIN measurements of the Stokes beam and the corresponding CARS signal of a sample as a function of the fs laser beam parameters coupled to the fiber, the optimum operation point of the two far/closely lying ZDWs PCFs for CARS imaging in the C-H bond region was determined. It was found that the two far lying ZDWs PCF can generate CARS image quality that is as high as the standard two closely-lying ZDWs PCF, when the input laser parameters were carefully selected. In addition, the potential for two far-lying ZDWs fiber for performing CARS imaging/spectroscopy in the fingerprint region using the spectra focusing method was demonstrated.

Contribution:

I have designed the experiment and performed all the required measurements and analysis. I have benefitted from many discussions related to the analysis with my supervisor Dr. H. Anis, Dr. S. Murugkar and Dr. Khan, the two postdoctoral researchers in our CARS research group.

The first results of my measurements and analysis were published in the proceedings of Photonics West Conference of 2010, while more comprehensive results and analysis were published in Optics Express Journal 2014 (article 3-4-1).

3.5.1. Determining optimum operating conditions of the polarization-maintaining fiber with two far-lying zero dispersion wavelengths for CARS microscopy

Majid Naji,, * Sangeeta Murugkar,[2] and Hanan Anis[1]

1 School of Electrical Engineering and Computer Science, University of Ottawa, Ottawa, K1N 6N5, Canada
2 Department of Physics, Carleton University, Ottawa, K1S 5B6, Canada

Abstract: Single femtosecond laser-based coherent anti-Stokes Raman scattering (CARS) microscopy, using a photonic crystal fiber (PCF) pumped in the near-IR to generate a supercontinuum for the Stokes source, is rapidly being adopted as a cost-effective approach. A PCF with two closely-lying zero dispersion wavelengths is a popular choice for the Stokes source, but it is often limited to imaging lipids. A polarization-maintaining PCF with two far-lying zero dispersion wavelengths offers important advantages for polarization CARS microscopy, and for CARS imaging in the fingerprint region. This PCF fiber, though commercially available, has limited use for CARS microscopy in the C-H bond region. The main problem is that the supercontinuum from this fiber is typically noisier than that from a standard PCF with two closely-lying zero dispersion wavelengths. To overcome this, we determined the optimum operating conditions for generating a low-noise supercontinuum out of a PCF with two far-lying zero dispersion wavelengths, in terms of the input parameters of the excitation pulse. We measured the relative intensity noise (RIN) of the Stokes and the corresponding CARS signal as a function of the input laser parameters in this fiber. We showed that the results of CARS imaging using this alternate fiber are comparable to those achieved using the standard fiber, for input laser pulse conditions of low average power, narrow pulse width with slightly positive chirp, and polarization direction parallel to the slow axis of the selected fiber.

OCIS codes: (060.5295) Photonic crystal fibers; (320.6629) Supercontinuum generation; (180.4315) Nonlinear microscopy; (300.6230) Spectroscopy; coherent anti-Stokes Raman scattering.

References and links

1. H. N. Paulsen, K. M. Hilligsøe, J. Thøgersen, S. R. Keiding, and J. J. Larsen, "Coherent anti-Stokes Raman scattering microscopy with a photonic crystal fiber based light source," Opt. Lett. **28**(13),1123-1125 (2003).
2. S. Murugkar, C. Brideau, A. Ridsdale, M. Naji, P. K. Stys, and H. Anis, "Coherent anti-stokes Raman scattering microscopy using photonics crystal fiber with two closely laying Zero dispersion wavelengths," Opt. Express **15**(21), 14028-14037 (2007).
3. A. F. Pegoraro, A. D. Slepkov, A. Ridsdale, J. P. Pezacki, and A. Stolow, "Single laser source for a multimodal coherent anti-Stokes Raman scattering microscopy," Appl. Opt. **49**(25), F10-F17 (2010).
4. T. Lee, R. P. Trivedi, and I. I. Smalyukh, "Multimodal nonlinear optical polarizing microscopy of long-range molecular order in liquid crystals," Opt. Lett. **35**(20), 3447-3449 (2010).
5. A. D. Slepkov, A. Ridsdale, H.N. Wan, M.H. Wang, A. F. Pegoraro, D. J. Moffatt, J. P. Pezacki, F.J. Kao, and A. Stolow, "Forward-collected simultaneous fluorescence lifetime imaging and coherent anti-Stokes Raman scattering microscopy," J. Biomed. Opt. **16**, 021103 (2011).
6. J. Yuan, G. Zhou, H. Liu, C. Xia, X. Sang, Q. Wu, C. Yu, K. Wang, B. Yan, Y. Han, G. Farrel, and L. Hou, "Coherent anti-Stokes Raman scattering microscopy by dispersive wave generations in a polarization maintaining photonic crystal fiber," Prog. in Electromagnetics Res. **141**(65), 659-670 (2013).
7. B.C. Chen, J. Sung, X. Wu, and S. H. Lim, "Chemical imaging and microspectroscopy with spectral focusing coherent anti-Stokes Raman scattering," J. Biomed. Opt. **16,** 021112 (2011).
8. A. F. Pegoraro, A. D. Slepkov, A. Ridsdale, D. J. Moffatt, and A. Stolow, "Hyperspectral multimodal CARS microscopy in the fingerprint region," J. Biophotonics **7(**1–2), 49–58 (2014).
9. B. G. Saar, R. S. Johnston, C. W. Freudiger, X. S. Xie, and E. J. Seibel, "Coherent Raman scanning fiber endoscopy," Opt. Lett. **36**(13), 2396 (2011).
10. B. Smith, M. Naji, S. Murugkar, E. Alarcon, C. Brideau, P. Stys, and H. Anis, "Portable, miniaturized, fibre delivered, multimodal CARS exoscope," Opt. Express **14**, 17161-17175 (2013).

11. H. Tu and S. A. Boppart, "Coherent anti-Stokes Raman scattering microscopy: overcoming technical barriers for clinical translation," J. Biophotonics, **7**(1–2), 9–22 (2014).
12. A. F. Pegoraro, A. Ridsdale, D. J. Moffatt, J. P. Pezacki, B. K. Thomas, L. Fu, L. Dong, M. E. Fermann, and A. Stolow, "All-fiber CARS microscopy of live cells," Opt. Express **17**, 20700-20706, (2009).
13. T. Gottschall, M. Baumgartl, A. Sagnier, J. Rothhardt, C. Jauregui, J. Limpert, and A. Tünnermann, "Fiber-based source for multiplex-CARS microscopy based on degenerate four-wave mixing," Opt. Express **20,** 12004-12013 (2012).
14. NKT, "Femtowhite CARS, Supercontinuum Device for Coherent Anti-Stokes Raman Scattering Applications," www.nktphotonics.com/files/files/femtoWHITE-CARS.pdf.
15. NKT, "NL-PM-750, Nonlinear Photonic Crystal Fiber," http://www.nktphotonics.com/files/files/NL-PM-750-090612.pdf.
16. C. Pohling, T. Buckup, and M. Motzkus, "Hyperspectral data processing for chemoselective multiplex coherent anti-Stokes Raman scattering microscopy of unknown samples," J. Biomed. Opt. **16**(2), 021105 (2011).
17. K. Shi, P. Li, and Z. Liua, "Broadband coherent anti-Stokes Raman scattering spectroscopy in supercontinuum optical trap," Appl. Phy. Lett. **90**, 141116 (2007).
18. H. Kano and H. Hamaguchi, "Vibrationally resonant imaging of a single living cell by supercontinuum-based multiplex coherent anti-Stokes Raman scattering microspectroscopy," Opt. Express **13**(4), 1322-1327 (2005).
19. P. Groß , L. Kleinschmidt , S. Beer , C. Cleff, and C. Fallnich, "Single-laser light source for CARS microscopy based on soliton self-frequency shift in a microstructured fiber," Appl. Phys. B **101**(1),167-172 (2010).
20. P. Klarskov, A. Isomäki, K. P. Hansen, and P. E. Andersen, "Supercontinuum generation for coherent anti-Stokes Raman scattering microscopy with photonic crystal fibers," Opt. Express **19**(27), 26672-26683 (2011).
21. K. Hilligsoe, T. Andersen, H. Paulsen, C. Nielsen, K. Molmer, S. Keiding, R. Kristiansen, K. Hansen, and J. Larsen, "Supercontinuum generation in a photonic crystal fiber with two zero dispersion wavelengths," Opt. Express **12**(6), 1045-1054 (2004).
22. J. M. Dudley, G. Genty, and S. Coen, "Supercontinuum generation in photonic crystal fiber," Rev. Mod. Phys. **78**(4),1135–1184 (2006).
23. M. H. Frosz, P. Falk, and O. Bang, "The role of the second zero-dispersion wavelength in generation of supercontinuum and bright-bright soliton-pairs across the zero-dispersion wavelength," Opt. Express **13**, 6181-6192 (2005).
24. A.V. Husalou and J. Herrmann, "Supercontinuum generation of higher-order solitons by fission in photonics crystal fibers," Phys. Rev. Lett. **l87**(20), 203901-4 (2000).
25. J. Herrmann, U. Griebner, N. Zhavoronkov, A. Husakou, D. Nickel, J. C. Knight, W. J. Wadsworth, P. St. J. Russell, and G. Korn, "Experimental evidence for supercontinuum generation by fission of higher-order solitons in photonics fiber," Phys. Rev. Lett. **l88**(17), 173901-4 (2002).
26. G. P Agrawal, "*Nonlinear Fiber Optics*," fifth edition, Academic press, NY. (2013).
27. K. L. Corwin, N. R. Newbury, J. M. Dudley, S. Coen, S. A. Diddams, K. Weber, and R. S. Windeler, "Fundamental Noise Limitations to Supercontinuum Generation in Microstructure Fiber," Phys. Rev. Lett. **90**, 113904 (2003).
28. J.M. Dudly, S. Coen, "Coherence properties of supercontinuum spectra generated in photonic crystal and tapered optical fibers," Opt. Lett. **27**(13),1180-1182 (2002).
29. M. Naji, S. Murugkar, K. Khan, and H. Anis, "Coherent anti-Stokes Raman scattering microscopy using photonic crystal fibers," Proc. SPIE, **7569**, 75692S-75692S-6 (2010).
30. A. Demircan and U. Bandelow, "Analysis of the interplay between soliton fission and modulation instability in supercontinuum generation," Appl. Phys. B **86**, 31-39 (2007).
31. Z. Zhu and T. G. Brown, "Polarization properties of supercontinuum spectra generated in birefringent photonic crystal fiber," J. Opt. Soc. Am. B **21**(2), 249-257 (2004).
32. C. L. Evans and X. S. Xie, "Coherent Anti-Stokes Raman Scattering Microscopy: Chemical imaging for biology and Medicine," Annu. Rev. Anal. Chem. **1**, 883-909 (2008).

1.0 Introduction

Coherent anti-Stokes Raman scattering (CARS) microscopy, using a single femtosecond (fs) laser for both the pump and the Stokes beams, has been gaining popularity [1-6]. In this approach, a portion of the fs laser is used as the pump beam, while the Stokes beam is obtained by generating a supercontinuum (SC) by coupling the rest of the fs laser beam to a photonic crystal fiber (PCF), followed by a band-pass filter to select the desired Stokes wavelength.

This single fs-laser approach reduces the complexity of the CARS setup and results in a more compact and cost-effective system. Moreover, the narrowband imaging approach enables fast acquisition time CARS imaging of biological samples at a fixed Raman shift. By combining the spectral focusing technique with the single femtosecond (fs) laser CARS approach, the rapid scanning Raman shift CARS microscopy in the C-H bond and fingerprint regions becomes feasible [7,8]. Moreover, by combining this technique with an endoscope/exoscope, the development of a cost-effective, miniaturized, portable multimodal CARS imaging platform for in-vivo and bed-side clinical applications becomes more feasible [9-11].

One of the important issues with the single fs-laser approach, particularly if a fs fiber laser is used, is to find a PCF that can generate a stable, low noise, broad supercontinuum spectrum with low average power from the laser source [12-13].

In our earlier work, we successfully demonstrated the use of a 12 cm PCF with two closely-lying zero dispersion wavelengths (ZDWs) at 775 nm and 945 nm, (NL-1.4-775-945 Crystal Fiber), housed in a hermetically sealed package (FemtoWhite CARS, NKT Photonics), for single fs laser CARS microscopy of lipid-rich biological

specimens [2]. This PCF resulted in a highly stable supercontinuum which was used as the Stokes beam in a CARS imaging setup, and subsequently became the standard fiber for performing CARS at the C-H bond region [14]. However, the application of this fiber is often limited to CARS imaging of molecular species with vibration at wavenumbers $\geq$ 2000 cm^{-1} Raman shift, and an appropriate choice of pump wavelength around 800 nm [2]. In addition, as it is not a polarization maintaining fiber, it cannot be used for polarization CARS microscopy. Thus, a polarization maintaining PCF that can provide a wider range of Stokes wavelengths to reach the lower Raman shifts in the fingerprint region (~ 800 cm^{-1}-1800 cm^{-1}), with comparable quality (low noise and high coherence), is highly desirable.

An available fiber that can satisfy these requirements would be a polarization maintaining PCF, NL-PM-750 (NKT Photonics, Denmark), with the two far-lying ZDWs at 750 nm and 1260 nm (Fig.1(b)). The fiber is available in a compact module, FemtoWhite 800 (NKT Photonics) with a mark that indicates the direction of the slow polarization axis of the fiber module [15]. Moreover, the hermetically sealed module FemtoWhite 800 provides a convenient and robust solution for fiber handling, as well as coupling excitation light into the PCF with two far-lying ZDWs. A number of groups have successfully used the two far-lying ZDWs fiber to perform narrow band and broadband multiplex CARS imaging in both C-H and fingerprint regions. However, they did not examine the quality of the generated supercontinuum out of the fibre systematically [6, 14, 15-19]. Klarskov et al. [20] investigated the different PCF designs with two ZDWs, to determine the best PCF design for generating the Stokes beam for the CARS microscopy. They did this by comparing the spectral density of the generated SC around 648 nm and 1027 nm of each PCF with an existing standard PCF (NL-1.4-775-945 Crystal Fiber) for CARS microscopy [20]. In their measurements, they assumed that the best fiber is the one that can generate the highest amount of spectral density of polarization maintained SC around 648 nm and 1027 nm to generate CARS signal, while they ignored the amplitude noise and stability of the generated SC in their measurements. Since CARS is a nonlinear four-wave mixing process, it does not depend only on the intensity of the pump and the Stokes beams, but also on their quality in terms of coherence, polarization and intensity stability. As the pump is of high quality, the intensity and relative intensity noise (RIN) of the generated CARS signal can be used to determine the quality of supercontinuum generation.

Previous work did not examine the signal quality of the generated Stokes and CARS signal from the FemtoWhite 800 module, nor did it compare the quality of the generated images with those obtained with the FemtoWhite CARS module containing the PCF with two closely-lying ZDWs. Consequently, the FemtoWhite 800 module was not used at its optimal point to generate the highest possible CARS signal intensity with the minimum noise value, in order to obtain high contrast CARS images with short acquisition times for studying dynamic living systems. We determined the optimal operating parameters for the fiber with two far-lying ZDWs (NL-PM-750) inside a FemtoWhite-800 module [15] for CARS microscopy, corresponding to the C-H vibration band at ~ 2850 cm^{-1}. We also took relative intensity noise (RIN) measurements of the generated Stokes beam and its corresponding CARS signal of an oil sample, and compared the results with those obtained from the standard fiber module containing the PCF with two closely-lying ZDWs [15].

In this paper, after a short introduction on SC generation and the noise amplification mechanism in both fibers, the experimental setup and results are presented. The relative intensity noise (RIN) of the SC out of the two far-lying ZDW fibers and two closely-lying ZDW fibers, and the RIN of the generated CARS signals of a bulk oil sample for different input laser conditions, are demonstrated. Based on the RIN of the Stokes and CARS signals, as well as the CARS signal intensity, the optimum conditions for implementing the two far-lying ZDWs PCF are shown. Finally, to compare the performance of the two fibers for CARS microscopy, the CARS images of a standard 4.5 μm polystyrene bead sample using both fibers are presented.

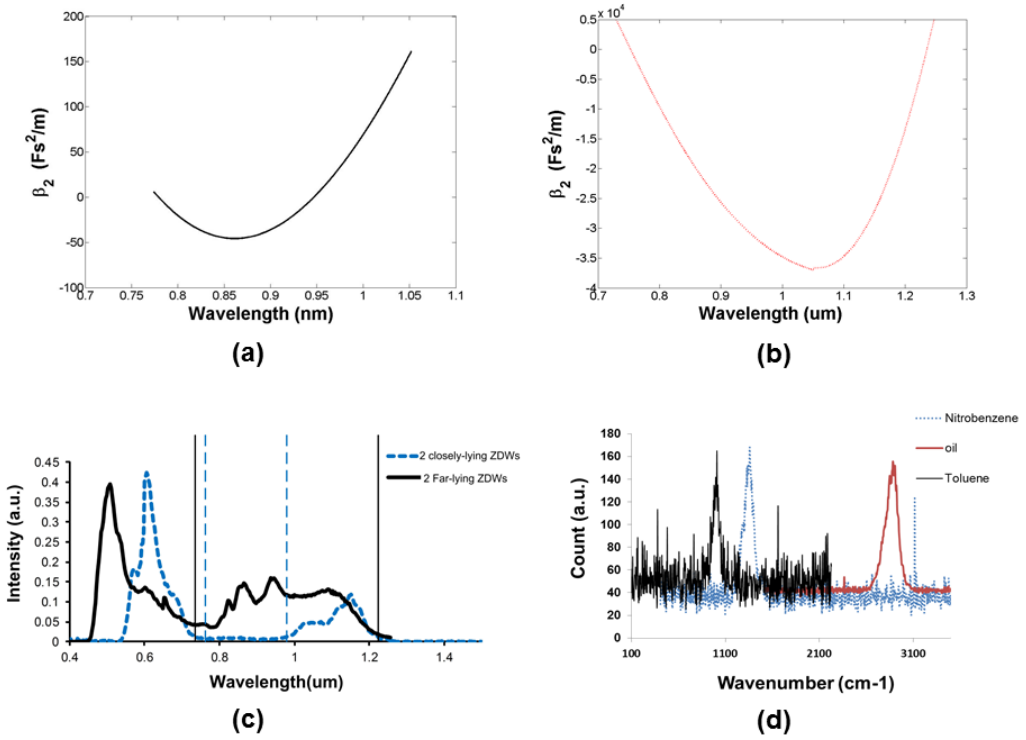

Fig. 1. (a) Group velocity dispersion parameter (β_2) of PCF with two closely-lying ZDWs and (b) PCF with two far-lying ZDWs (Courtesy of Crystal Fiber Inc.), (c) The supercontinuum spectra out of two far ZDWs (black line) and two closely-lying ZDWs(blue dotted line) fibers for a same input power of 530 mW and pulse duration of ~100 fs. Vertical lines indicate the position of two ZDWs. (Intensity scales of two SCs are not exactly the same). (d) CARS spectrum of Oil, ~2850 cm^{-1}, Nitrobenzene, ~1350 cm^{-1}, and Toluene, ~990 cm^{-1}, using the spectral focusing technique, our existing miniaturized fiber delivered CARS exoscope and the two far-lying ZDWs fiber to generate SC. (The exposure times of each CARS spectra were 0.1s, 5s and 1s respectively.)

2.0 Spectral Features of pulse in PCFs with closely-lying and far-lying ZDWs

The supercontinuum generation mechanisms in the PCF with two closely-lying ZDWs and the PCF with two far-lying ZDWs are not the same due to the difference in their dispersion profiles (Fig. 1(a) and 1(b)). This difference in dispersion plays a significant role in the phase matching conditions during the SC generation. When an 800 nm wavelength, low power femtosecond laser pulse propagates a short distance (~12 cm) through the fiber with two closely-lying ZDWs, the supercontinuum is generated by self-phase modulation (SPM) and phase-matched four-wave mixing (FWM) [21]. In this case, the supercontinuum is more independent of the input pulse parameters and is coherent through its entire spectrum. The phase-matched FWM mechanism causes a significant depletion in the anomalous region between the two zeros during the SC propagation in the fiber, causing a very low spectral density between the two ZDWs (Fig. 1(c)).

In the PCF with two far-lying ZDWs, because of the higher magnitude of β_2, (group velocity dispersion parameter) in the anomalous dispersion region, and the less phase-matched FWM, the supercontinuum generation is mostly dominated by higher-order noise sensitive soliton fission [21-23]. Moreover, the modulation instability (MI) gain in the anomalous dispersion region is bigger due to the higher value of β_2 and consequently, the generated SC out of this fiber is more sensitive to the input pulse parameters and noises. Thus, controlling those parameters can have a significant effect on the quality of the produced SC [22, 24-27].

The balance between group velocity dispersion in the anomalous region and SPM leads to the formation of solitons in two far-lying ZDWs fiber. At higher amplitudes of the input fs pulse, a high-order soliton with a soliton number of N is formed. Higher-order solitons of the nonlinear Schrödinger equation show periodic changes with propagation, although, in vicinity of the zero dispersion wavelengths with a big positive magnitude of third order dispersion and self-steepening effect, the propagation behaviour of the higher ordered solitons will be different. In this situation, a higher-order soliton pulse will split into N pulses after a short propagation distance of L_{fiss}, and

generates N different red-shifted soliton pulses with different group velocities [22-26]. Here L_{fiss} is the soliton fission length and is defined as:

$$L_{fiss} \approx \sqrt{L_D L_{NL}} = \sqrt{\frac{T_0^2}{\gamma P_0 |\beta_2|}} \quad (1)$$

Where $L_{NL} = (\gamma P_0)^{-1}$ and $L_D = T_0^2 |\beta_2|^{-1}$

L_D is the dispersion length, T_0 is the temporal width of the input pulse, L_{NL} is the nonlinear length, P_0 is the peak power, and γ is the nonlinear coefficient of the core.

Figure 2 shows the generated supercontinuum spectrum out of two far-lying ZDWs fiber, as the input power increases from 28 mW to 319 mW. It can be seen that as the input power to the fiber increases, each generated soliton pulse loses energy by emitting non-solitonic, blue-shifted radiation that is phase-matched to the corresponding pulse, while simultaneously moving to the IR region until reaching stability.

In the case of higher input average power (P_0 > 160 mW) there will be higher order soliton fission processes due to the presence of several solitons with different red shifted frequencies. In addition, there is a broad-spectrum peak in the blue spectral region of the generated SC as a result of the presence of corresponding blue-shifted non-solitonic radiation for each soliton. The intermediate region in the SC spectrum arises because of four wave mixing between the solitons and their corresponding blue-shifted non-solitonic continuum during the SC generation [24, 25] (fig. 2).

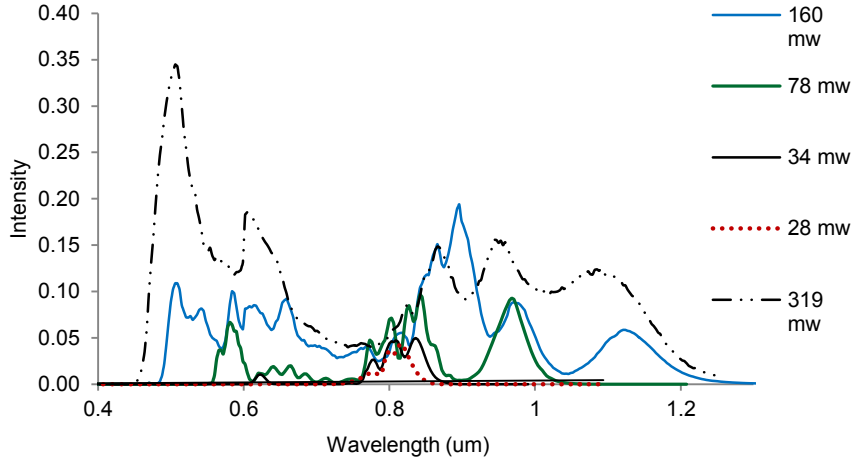

Fig. 2. The measured SC spectrum out of the PCF with two far-lying ZDWs , for low input average laser power. As it is shown, the soliton fission mechanism happens around 34 mW of input power, generating a red-shifted soliton around 830 nm and corresponding blue-shifted non-solitonic peak around 620 nm. At the higher input average power, the presence of several solitons with different red shifted frequencies causes a broad spectrum in the blue and red spectral regions of the generated SC at the input powers more than 160 mW. (Average coupling efficiency, η =40%)

Figure 3 shows the soliton fission length in both fibers as a function of input average power for a 100 fs pulse (input pulse width). As two closely-lying ZDWs fiber has a smaller β_2 value compared to two far-lying ZDWs fiber, the soliton fission length is much longer for two closely-lying ZDWs fiber. In fact, at the nominal average power of 300mW and for a fiber length of 12 cm, L_{fiss} is much shorter than the fiber length for the case of two far-lying ZDWs fiber and much longer than 12 cm for the case of two closely-lying ZDWs fiber. This indicates that the soliton fission mechanism cannot occur in the implemented two closely-lying ZDWs fiber (the fiber with two closely-lying ZDWs) at 300 mW input laser power during the SC generation for the chosen fiber length. Therefore, SPM and phase-matched FWM mechanism are dominant in SC generation in this fiber, leading to a less noisy and more coherent SC [21].

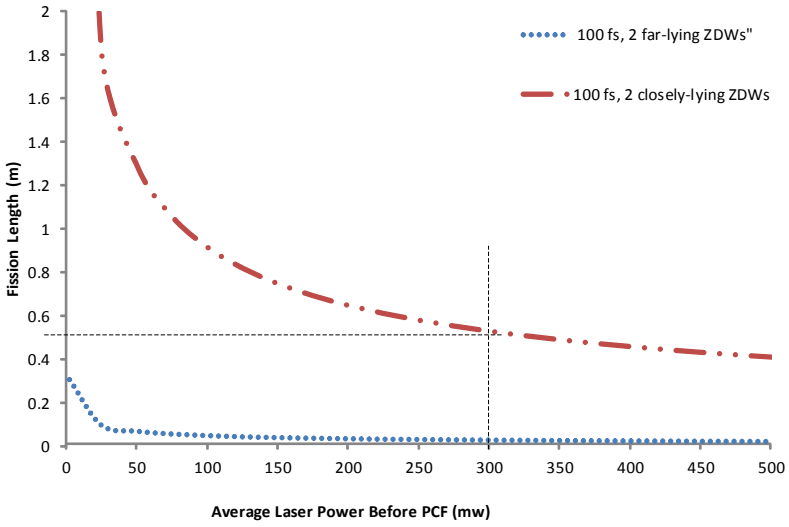

Fig. 3. Soliton fission length vs. input average power before coupling to the fiber. The intersection of vertical dotted line at 300 mW and soliton fission length (L_{fiss}) curve indicates the value of the fission length for each fiber type. (Coupling efficiency=40%, laser pulse width =100 fs)

3.0 Method: RIN Measurements and CARS Imaging

3.1 RIN Measurement

In order to measure the stability of intensity, polarization and coherence of the Stokes beam, the RIN of the Stokes beam and the CARS signal of an oil sample were measured.

Here we define the stability of polarization as the stability of the linear polarization direction of the Stokes beam and the coherence stability as the phase degradation and timing jitter of the generated Stokes pulses [28].

As the CARS mechanism is coherent and nonlinear, and as the RIN of the Ti-sapphire laser beam (-113 dB/Hz) is much lower than the RIN of the Stokes beam (range between ~ -97 dB/Hz and ~ -79 dB/Hz), the measured RIN of the CARS signal is a good indicator of the coherence, polarization and intensity stability of the Stokes beam. The RIN of the Stokes beam was measured by Fourier-analysis of the electrical signal from a photodetector using an electrical spectrum analyser (ESA) in the range of 0-81 MHz with a resolution bandwidth of 1 KHz and 100 Hz [27]. For each measurement, the signal power at 80 MHz was compared to the noise figure at a fixed point in the frequency range. For the RIN measurement of the CARS signal, the beam-scanning mirror was turned off. Then the CARS signal, generated by temporally and spatially overlapped Stokes and pump beams from a very small volume focused inside a drop of an oil sample, was collected and sent to the Photomultiplier tube (PMT, Hamamatsu H7422P-40). The corresponding electrical signal out of the PMT was amplified and sent to the ESA for RIN analysis.

3.2 CARS imaging

The pump and Stokes wavelengths were selected for CARS imaging of the lipid density corresponding to the molecular vibrations of C-H bonds in the range of 2800-3000 cm^{-1} Raman shift. The input pulse at 800 nm after adjusting power, chirp and polarization direction was coupled to the PCF with two far/closely-lying ZDWs to generate the Stokes beam. The pump and Stokes beams were collinearly combined and spatio-temporally overlapped inside the sample by using a dichroic mirror, delay line and our home-built scanning microscope [2]. The average powers (measured by optical power meter) of the pump and the Stokes beams at the sample were about 11 mW and ~2 mW respectively.

3.3 Experimental setup

To measure the relative intensity noise (RIN) of the generated supercontinuum around 1040 nm and RIN of the generated CARS signal using the IR portion of SC, Stokes beam, (λ_C = 1040 nm, full width at half maximum,

FWHM, = 60 nm) as well as to obtain the CARS image of the lipid rich biological samples, the following setup was used (Fig. 4).

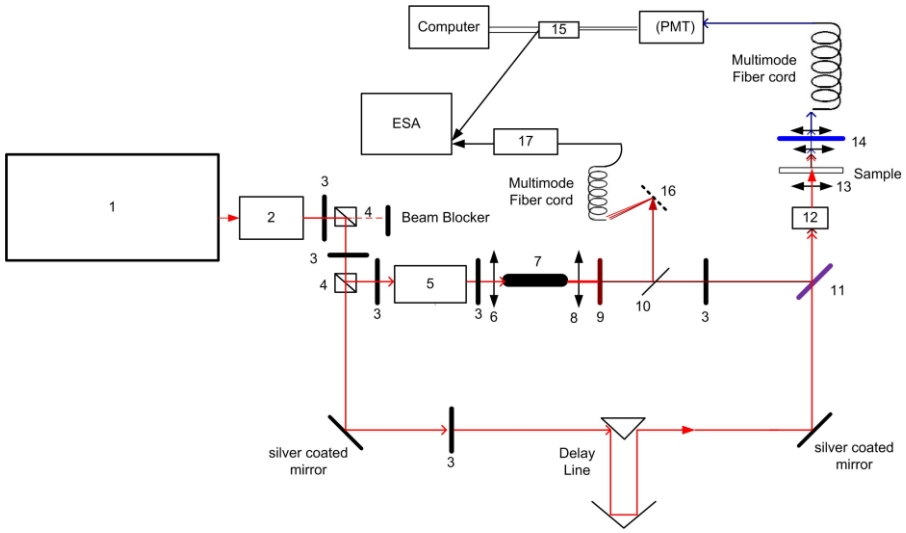

Fig. 4. Experimental setup: (1) Ti:sapphire laser, (2) Faraday isolator, (3) half wave plate, (4) beam splitter, (5) prism compressor, (6) microscope objective lens (40x), (7) PCF with two far/closely ZDWs, (8) collimating aspheric lens of 5mm focal length, (9) band pass filter, (10) flip mirror for routing to RIN measurement setup, (11) dichroic mirror for overlapping Stokes beam on the pump beam, (12) X-Y scanning mirrors, (13) focusing objective lens, (14) short pass filter, (15) PMT amplifier and discriminator, (16) diffraction grating mirror and (17) fast photodetector.

By using a double path prism compressor, the chirp and pulse temporal width of fs laser pulses in the Stokes arm were adjusted. An intensity autocorrelator was used to measure the pulse width of the fs laser pulse before coupling to the PCF fiber(s). By using a half wave plate before the coupling lens (6), the direction of the polarization of the laser beam was controlled. This light was coupled into a module, FemtoWhite 800 (FemtoWhite CARS) containing two far-lying ZDWs fiber (two closely-lying ZDWs fiber).

The generated SC out of each module (two closely/far-lying ZDWs fibers) was collimated and passed to a band pass filter (Chroma, central wavelength 1040 nm, FWHM = 60 nm). The filtered SC (here called "Stokes beam") was directed toward a grating mirror to have a narrower bandwidth Stokes beam (FWHM = 10 nm) for RIN measurement. The RIN of narrower bandwidth Stokes was measured by using a fast photodetector (Newport, 818-BB-21A) and an electrical spectrum analyser (ESA, Agilent E4411B).

4.0 Results

4.1 Comparing the RIN of two far-lying and two closely-lying ZDWs PCF

In order to compare coherence, intensity and polarization stability of the SC generated by the two far-lying ZDWs fiber with that of the SC of two closely-lying ZDWs fiber the RIN of the Stokes beams, and corresponding CARS signals of an oil sample, from both modules were measured.

MI process and higher–ordered soliton fission mechanism are the two main sources of instabilities during the SC generation in the two far-lying ZDWs fiber [21, 22 and 26]. Consequently, by reducing the impact of MI and higher–ordered soliton fission, a more stable generated SC can be achieved. Fig. 5 depicts the RIN of Stokes beam as a function of input fs laser pulse width for both fiber types. The positive pulse width means positive chirp while negative pulse width means negative chirp. The input average power was 300 mW with an average coupling efficiency ~40%. As fig. 5 shows, the Stokes beam of two far-lying ZDWs fiber has a minimum RIN of ~ -95 dB/Hz at around +100 fs input pulse width, which is 10 dB less than its value at 200 fs. This is mainly due to the shorter soliton fission length, for a 100 fs pulse compared to the longer input pulses. This reduces the MI process chance to play a significant role in perturbing the pulse break up process during the supercontinuum generation, leading to higher intensity stability (less RIN) [26].

In addition, by decreasing the pulse width of the input laser, the number of the noise sensitive higher–ordered soliton fission will decrease, resulting in a less noisy supercontinuum [26].

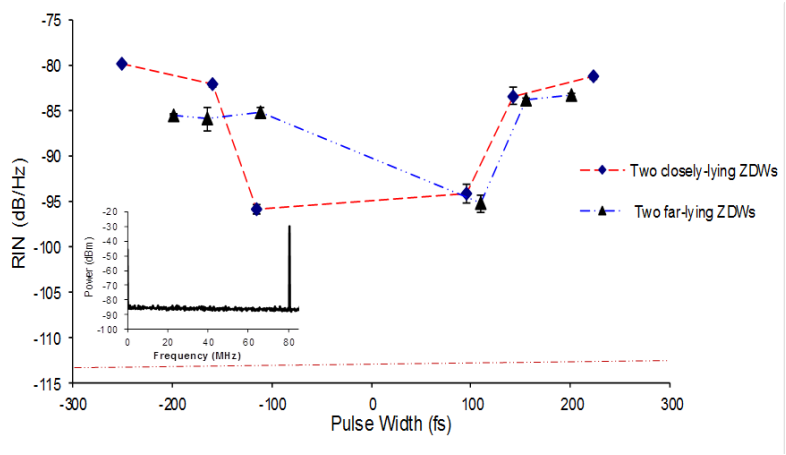

Fig. 5. The RIN of the Stokes beam, using fibers with two far and two closely-lying ZDWs. The error bars are the variance of the RIN values at each pulse width. The input average power was 300 mW with an average coupling efficiency 40%. The red dashed line shows the value of the RIN of fs laser beam at the 100 fs, which is taken as the minimum theoretical RIN of the generated Stokes beam out of the both fibers. Lower left Corner: the RF power spectrum of the Stokes beam out of two far-lying ZDWs PCF (Resolution bandwidth=1000 Hz).

As Fig. 5 shows, the RIN value of the Stokes beam out of two closely-lying ZDWs fiber is minimal when the fs laser pulse is close to transform limited. In two closely-lying ZDWs fiber, for short transform-limited pulses, or pulses with a small positive chirp that undergo initial compression, the spectral broadening due to self-phase modulation (SPM) is more rapid than for pulses with a large negative/positive chirp [27]. This leads to an overall reduction in noise amplification for transformed limited pulses because of rapid falling of the pulse peak power inside the fiber core, causing a reduced total RIN value [27]. In other words for the short transform-limited pulses, the spectral broadening due to SPM will happen earlier, giving less chance for MI amplification during the pulse propagation in the fiber core.

To determine the polarization noise (instability) as well as the coherence of the Stokes beam out of both fibers, the RIN of the generated CARS signals from both fibers were measured. Fig. 6 shows the RIN of CARS signals for a 300 mW average power laser coupled to both PCF fibers as a function of pulse width.

As Fig. 6 depicts, the RIN value of CARS of the two closely-lying ZDWs fiber is less than that of the two far-lying ZDWs fiber around 100 fs, which indicates that the Stokes beam of the two closely-lying ZDWs fiber is still less noisy at 300 mW. This result is in line with that of Hilligsoe et al. [21].

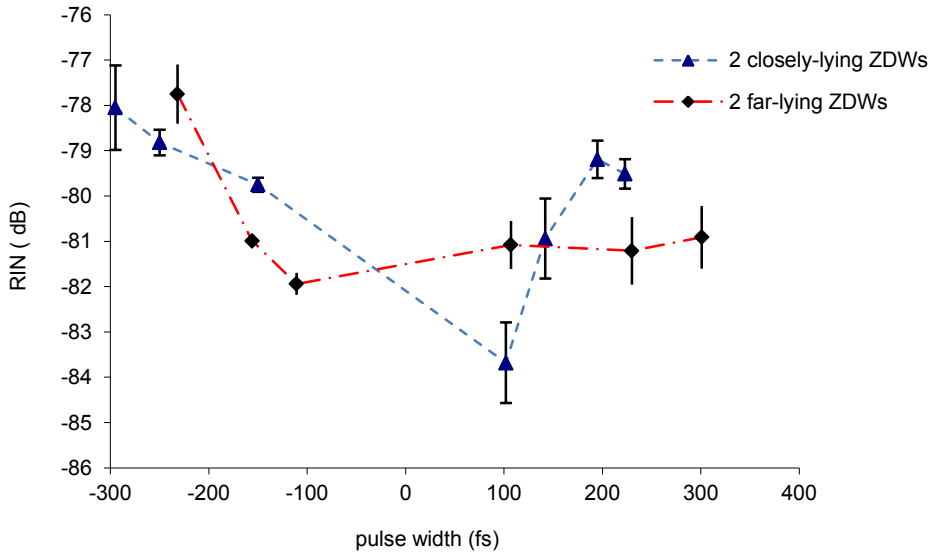

Fig. 6. The RIN of the CARS signal of an oil sample, using fibers with two far and two closely lying ZDWs for 300 mW average power of the laser coupled to both PCF fibers. The error bars are the variance of the RIN values at each pulse width (Negative sign indicate the negative chirp).

4.2 Determining the optimum operating point for the fiber with two far- lying ZDWs

In order to reduce the total RIN of the Stokes beam out of two far-lying ZDWs fiber, the average input power of the fs laser beam coupled to the fiber was reduced [27]. By reducing the average power of the coupled fs laser to two far-lying ZDWs fiber, the average power of the generated Stokes beam will be generally reduced. However its stability will increase because of the reduction in noise amplification during the SC generation [27-31]. Therefore, there will be a point of optimum fs laser average power, coupled to two far-lying ZDWs fiber that can generate the highest stable CARS signal intensity with a minimum RIN value.

The polarization direction of the coupled laser beam can also play an important role in the polarization stability of the generated SC and consequently the Stokes beam [31]. Since the intensity of a CARS signal depends on the polarization direction of the Stokes and the pump beam, the polarization direction of the laser beam at 800 nm with slightly positively chirped ~100 fs pulses coupled to the fiber was also considered to find the optimum operation point for this fiber. The average power of the input laser was changed for two different polarization angle (direction) states: one in parallel with slow axis of two far-lying ZDWs fiber (0 ° angle) and the other with a 45º angle with respect to the slow axis of the fiber (45º angle).

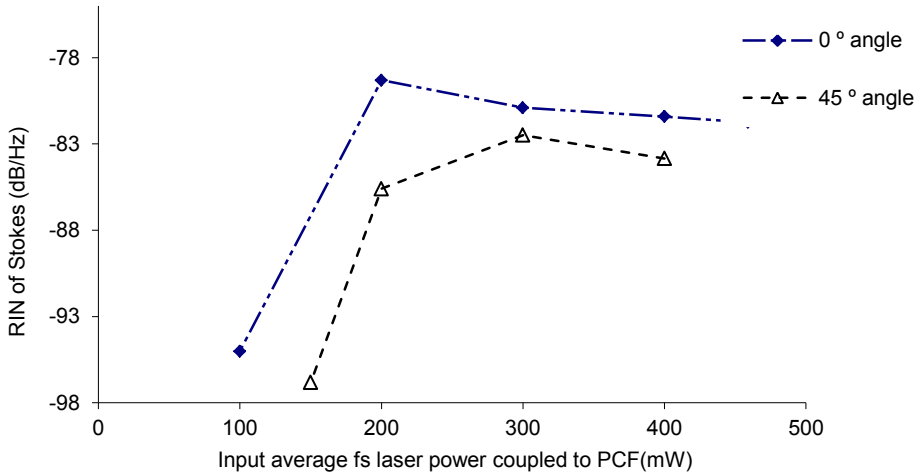

Fig. 7. The RIN of the Stokes beams generated by two different polarization angles of fs laser beam vs. input average power of the fs laser coupled to the PCF with two far-lying ZDWs, with a constant pulse width of ~100 fs. Error bars were negligible compared to the size of data points.

Figure 7 shows the RIN of the Stokes beam out of two far-lying ZDWs fiber as a function of input laser average power before coupling to the PCF, for two different polarization states of the input laser. As Fig. 7 shows, the RIN of the 0º and 45º angles Stokes beams do not change much between an input average power range of 500 mW to 200 mW. However, they experience a significant reduction for input powers less than 200 mW, mostly because of exponential reduction of the MI process by reducing the input power [26]. This reduction seems more prominent for the 45º angle. Launching at 0º means that all the power is in the "x" direction of the fiber rather than divided between the "x" and the "y" as in the case of the 45º launching angle. This will result in higher order noise sensitive soliton fission and slightly more intensity RIN [26].

The RIN of the CARS captures the intensity stability, the polarization stability and the coherence of the Stokes beam. To separate the various effects we measure the RIN of the Stokes and generated CARS signal.

The RIN of the Stokes is a good indicator of the intensity stability of the Stokes beam. Since the fast photodetector is blind to the polarization variation of the Stokes beam, to detect the polarization instability of the 45º angle Stokes beam, compared to the slow axis direction of the two far ZDWs PCF, the RIN of the 45º angle Stokes beam was measured once with a polarizer in front of the photodetector (Fig.4 (#17)) and once without the polarizer. The RIN difference in the two measurements shows the polarization instability of the 45º angle Stokes beam. As it is shown in the Fig. 8, the RIN of 45º angle Stokes beam increases by about 4 dB/Hz when the polarization instability of the 45º angle Stokes beam is considered.

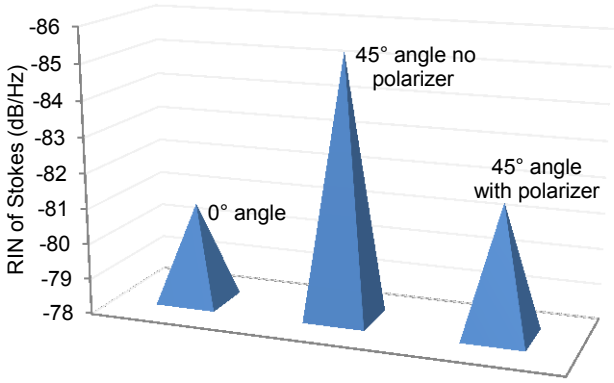

Fig. 8. The RIN of the Stokes beams generated by two different polarization angles of 45º and 0º angles of fs laser coupled to the two far-lying ZDWs fiber, (The measured RIN value variance was ~ +/- 0.54 dB/Hz)

Figure 9 shows the RIN of the CARS signal generated by the Stokes beam as a function of the average input laser power. As it is demonstrated, the RIN of the CARS signal generated by the Stokes beam produced by a 45º angle input laser beam (here it is called "45º Stokes") was constant for all average input powers. This indicates that despite the significant reduction in the RIN intensity of the Stokes beam around 100-200 mW average input laser power as seen in Fig. 7, the 45º Stokes beam is still noisy and its polarization stability does not improve. However, for the Stokes beam generated by 0º input laser polarization direction (here it is called "0º Stokes") there is a significant reduction in its intensity, coherence and polarization noises (RIN) for input laser average powers less than 200 mW. This can be explained as follows. At a 45º angle and in the absence of cross-phase modulation (XPM), the two polarization components in the "x" (slow axis of the fiber) and "y" (fast axis of the fiber) directions evolve very independently and separately from each other due to their different group velocities [26]. Nevertheless during the SC generation in the early stage, the "x" component gets more energy and compresses more than the "y" component because of interplay between SPM and XPM. With further propagation of a pulse in the "x" direction, the higher-order soliton fission happens earlier because of having a larger β_2. This process also happens in the "y" direction, but in a more dramatic way, causing the polarization state of the SC out of the two far-lying ZDWs fiber becomes less stable [31]. Consequently, the 45º angle Stokes beam has less polarization stability.

In Fig. 9, the ~ -85 dB/Hz RIN of the CARS signal with an average power of 100 mW is comparable with the RIN of the CARS signal (~ -84 dB) generated by the Stokes beam out of two closely-lying ZDWs fiber with an average power of 300 mW, which was selected as our standard CARS signal in all our measurements (Fig. 6). This indicates an intensity and polarization-stable Stokes beam out of two far-lying ZDWs fiber at this selected operating condition. In summary, launching a low power fs pulse at 0º will generate a more stable polarized SC, although it has a slightly more intensity RIN value compared to the 45º angle scenario for the same input power laser pulse.

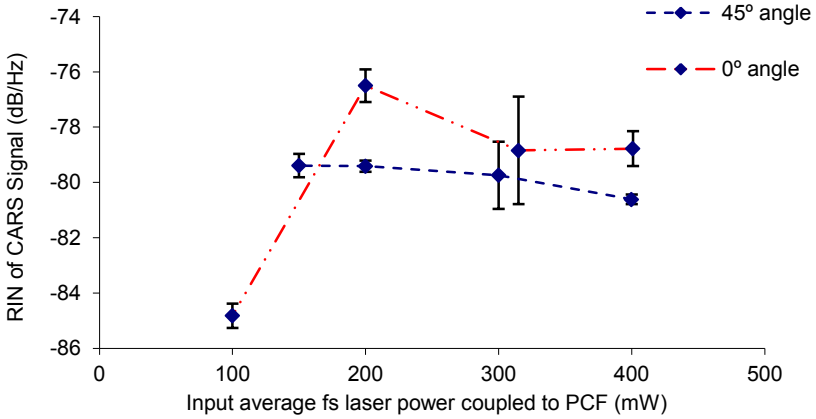

Fig. 9. The RIN of the CARS signal using PCF with two far-lying ZDWs, generated by two different Stokes beams of two different input laser polarization angles (0º and 45º to the slow axis of the PCF). Average input laser power was ~ 100 mW and pulse width is 100 fs.

The CARS intensity is proportional to the Stokes intensity, I_{Stokes}, multiplied by the square of the intensity of the pump, I_{Pump}, (Equation 2 below). As CARS is a nonlinear process, it also depends on the polarization and coherence of both the pump and the Stokes beams [32]. Because the CARS signal intensity strongly depends on the polarization direction of the Stokes beam (ideally it should be parallel to the pump polarization direction), any polarization instability in the Stokes beam will generate less CARS signal and more noise that leads to an enhancement in the RIN value of the generated CARS signal (Fig. 9).

$$I_{CARS} \propto I_{Stokes} I_{Pump}^2 \tag{2}$$

Figure 10 shows a comparison between the CARS signal intensity of an oil sample at 0º Stokes input angle for different average input powers. All the measured polarization, intensity and pulse width of the pump beam at the sample were constant since we used the same portion of the fs laser beam as our pump. As we have a constant and stable pump and identical experimental setup during all measurements, any changes in the intensity of the CARS signal can be attributed to either the power or quality (i.e. coherence, phase and polarization stability) of the Stokes beam at the sample. By comparing the intensity of the CARS signal and its corresponding Stokes beam power at the sample, we can determine the quality of the Stokes beam.

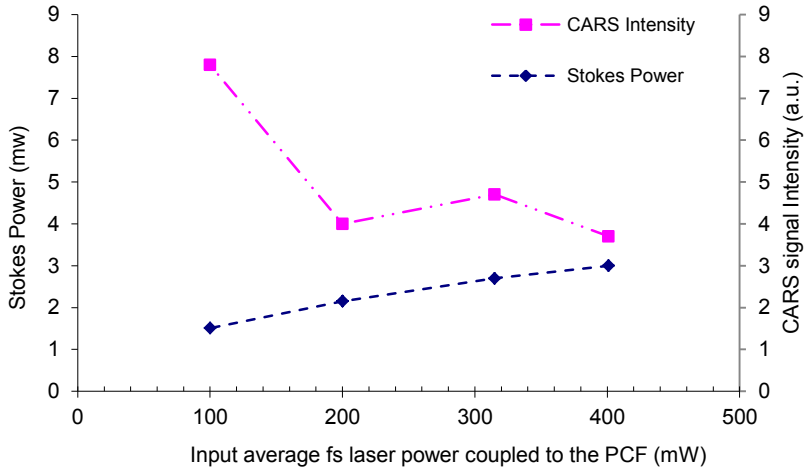

Fig. 10. The 0º Stokes power (~100 fs pulse width) at the focal point of the CARS microscope, at the oil sample, and the intensity of its generated CARS signal, as a function of the average laser power coupled to the PCF with two far-lying ZDWs. The averaged coupling efficiency=40% (measurement error was less than 5%).

As shown in Fig. 10, by increasing the average input power (P_0) coupled to two far-lying ZDWs fiber, the Stokes power at the sample increases. However, the CARS signal intensity does not follow a similar trend especially with low power, because of a substantial improvement of the Stokes signal quality by reducing the input laser power (P_0) coupled to two far-lying ZDWs fiber. For example at P_0 = 100 mW the Stokes power at the sample was half of the value of the Stokes power at P_0 = 400 mW, while its corresponding CARS signal intensity was double, i.e. the Stokes quality was much better at P_0 = 100 mW compared to 400 mW despite a 50% reduction in the Stokes power intensity at the sample. Unfortunately, it was found that by reducing P_0 to values less than 100 mW, the Stokes power reduced significantly and rapidly, therefore, it was not sufficient to generate a strong and detectable CARS signal for performing CARS imaging of the biological samples. Consequently the P_0=100 mW, with 0º polarization direction and ~100 fs pulse width with slightly positively chirped pulses, was chosen as the optimum operation point for using two far-lying ZDWs fiber to perform CARS imaging of lipid rich biological samples.

5. CARS imaging results

In order to show the impact of the optimization of the parameters of the laser input coupled to the two far-lying ZDWs fiber, CARS images of the 4.5 μm polystyrene beads sample were obtained (Fig. 11) under the same imaging conditions but at two different (optimized and non-optimized) input conditions for the fiber. As seen in Fig. 11 (b), at the condition of 230 fs pulse width and average input power of ~300 mW coupled into the two far-lying ZDWs fiber, the CARS image is more pixelated. This is attributed to an increase of the RIN of the CARS signal and is

consistent with the ~ 3.6 dB/Hz worsening of the RIN seen earlier in figures 6 and 9, going from the optimized to non-optimized input condition for the two far-lying ZDWs fiber.

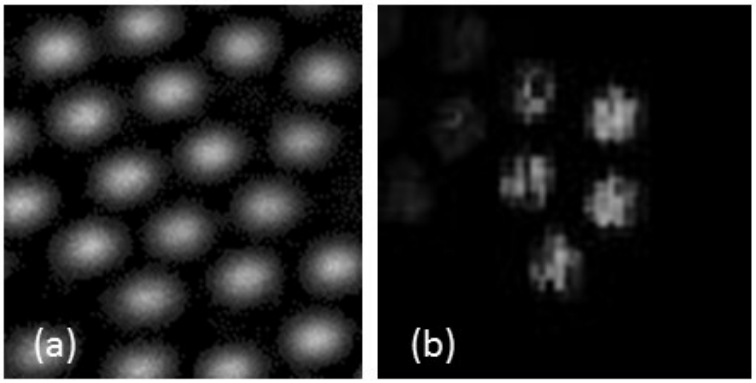

Fig. 11. The CARS image of the 4.5 μm polystyrene bead sample using two far-lying ZDWs fiber under similar imaging conditions, but with optimized (a) and non-optimized (b) input conditions of the fiber. (a) Pumping the PCF with 100 fs laser and average input power ~100 mW and (b) pumping the PCF with a 230 fs laser beam and average input power ~300 mW coupled into the fiber. Frame size is 256x 256 pixels with ~5.5 s acquisition time per frame.

To demonstrate the ability of using two far-lying ZDWs fiber at optimum operating conditions to perform high contrast and low noise CARS imaging of lipid density of biological samples, we performed CARS imaging of myelin structures of a fixed nerve sample (Fig. 12).

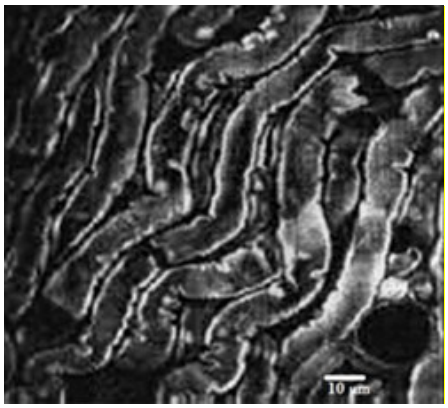

Fig. 12. CARS images (256 x 256 pixels) of myelin from fixed unstained mouse nerve using two far-lying ZDWs fiber module under optimum operating condition.

To compare the performance of two far-lying ZDWs fiber with the standard two closely-lying ZDWs fiber, the CARS image of a 4.5 μm polystyrene beads (with a strong Raman peak at 3070 cm^{-1}) sample was performed.

Two far-lying ZDWs fiber was operated at its optimum operation condition (average power 100 mW, 100 fs pulse width and 0º polarization direction) while input fs laser beam parameters to the two closely-lying ZDWs fiber was 300 mW, 100 fs pulse width and 0º polarization direction. As it is shown in Fig. 13, there is no significant difference between the CARS image of the 4.5 μm bead sample using either fiber.

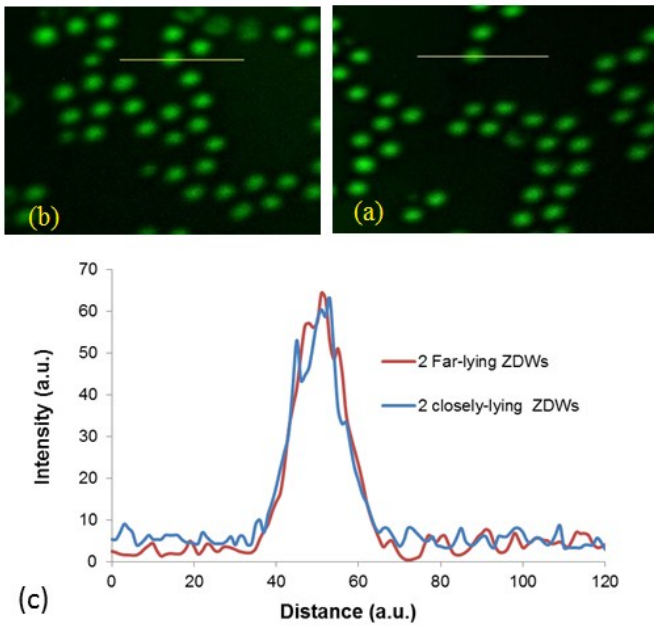

Fig. 13. (Above) (a) CARS images of 4.5 μm polystyrene bead sample using two far-lying ZDWs fiber operating at its optimum point and (b) two closely-lying ZDWs fiber operating at 300 mW average power input fs laser using our existing miniaturized fiber delivered CARS exoscope. (Below) (c) The intensity profile of a selected bead image, in above images ((a) and (b)), using both fibers.

6. Conclusion

In this paper, we investigated the conditions under which a module consisting of 12 cm of polarization-maintaining PCF with two far-lying ZDWs, can be used to perform a high quality and stable polarization CARS imaging of lipid rich density biological samples. The RIN of Stokes and CARS signals were measured as functions of the chirp, temporal duration, polarization and average power of the input femtosecond laser coupled to the PCF with two far-lying ZDWs. We showed that the generated Stokes from the PCF with two far-lying ZDWs often has a higher RIN and lower quality than the Stokes beam obtained from the module consisting of 12 cm of a PCF with two closely-lying ZDWs. However, a comparable high quality CARS signal is obtained from the fiber with two far-lying ZDWs, when the coupled laser has pulse duration around 100 fs, a slightly positive chirp and minimum possible average power (around 100 mW), as well as a polarization direction parallel to the slow axis of the PCF. The low fs laser power requirement for the two far-lying ZDWs (100 mW versus 300 mW) provides the opportunity to use this fiber with low power sources, such as femtosecond fiber lasers, to perform single fs laser CARS microscopy/endoscopy.

To demonstrate that the quality of the CARS signal using both fibers is comparable at optimal conditions, a CARS imaging of a 4.5 μm polystyrene bead sample was performed using both fibers. This work could be extended to determine the optimum operating conditions for CARS microscopy in the fingerprint region.

Acknowledgments

We express our special thanks to Dr. K. Khan, who read the first manuscript very thoroughly and gave us his valuable feedbacks and Dr. Hossein Aleyasin for helping in the preparation of mouse nerve biological samples.

3.5.2. Coherent anti-Stokes Raman scattering microscopy using photonic crystal fibers

Majid Naji, Sangeeta Murugkar, Kaisar R. Khan, Hanan Anis

School of information Technology and Engineering (SITE), University of Ottawa, Ottawa, Ontario, K1N 6N5

Abstract

The performance of two different photonic crystal fibers (PCF) of identical lengths for implementation of the Stokes source in a multimodal microscopy (CARS) and spectroscopy setup is compared. RIN measurements are performed to determine the noise in the supercontinuum from the two fibers as well as in the CARS signal under similar excitation conditions of the input pulse into the PCF. Results indicate a correlation between the spacing of the two zero dispersion points of the PCF and the RIN of the CARS signal.

Key words: CARS imaging, Photonic crystal fiber, Supercontinuum spectrum, RIN

1. Introduction

Broadband multiplex coherent anti-Stokes Raman scattering (CARS) microscopy using a single femtosecond laser (pump beam) and a supercontinuum (Stokes beam) generated in a photonic crystal fiber (PCF) by the femtosecond laser, has been recently gaining popularity.[1,2] An ideal Stokes beam derived from the PCF would provide sufficient power and broad tunability in order to access the molecular vibrations associated with the fingerprint region (800 – 1800 cm^{-1}) as well as the vibrations due to lipid and water molecules.

In our earlier work, we successfully demonstrated the use of a PCF with two closely lying zero dispersion wavelengths (ZDW) for CARS microscopy of lipid-rich biological specimen [1]. The PCF used was NL-1.4-775-945 (Crystal Fiber, Denmark and named Fiber 1 in the following), with two ZDW at 775 nm and 945 nm. It produces a highly stable SC that is used as the Stokes beam in the CARS imaging setup. Its application is however limited to CARS imaging of molecular species whose vibration is at ~ 1200 cm^{-1} Raman shift, with appropriate choice of pump wavelength [1]. A PCF that can provide a wider range of Stokes wavelengths to reach the lower Raman shifts (~ 800 cm^{-1}) in the fingerprint region is highly desirable. With this as our objective, we perform a comparative investigation of the SC properties of another type of PCF, NL-PM-750 (Crystal Fiber, Denmark and named Fiber 2 in the following) with two widely lying ZDW at 759nm and 1260 nm [3] for implementation in a CARS microscopy setup.

Here we compare the performance of the two fibers, Fiber 1 and Fiber 2, for CARS imaging of C-H bonds of lipid-rich samples such as myelin. We measure the relative intensity noise (RIN) of the Stokes beam [4,5] and of the CARS signal of a bulk oil sample. Simulations are employed to understand the physical process underlying the experiments.

2. Methodology

2.1: Experimental setup

The experimental setup is shown in Fig.1 and is very similar to the one described in Ref 1.

The two beams are spatially and temporally overlapped and focused at the sample. The CARS signal is collected in the forward direction by a long working distance air objective (Mitutoya, X20) or a water immersion objective (Olympus, X40). The filtered CARS signal is then coupled to a photomultiplier tube (PMT, Hamamatsu H7422P-

40) for imaging or routed (15 in Fig. 1) to the electrical spectrum analyzer (ESA, Agilent E4411B) for RIN measurement.
For measuring the RIN of the Stokes beam, the Stokes beam was spectrally dispersed by a grating (16 in Fig.1). A spectrally narrow portion (FWHM ~7 nm), centered at 1040 nm was coupled to a multimode fiber and then sent to an amplified fast photodetector (Newport, 818-BB-21A and 17 in Fig. 1). The corresponding electrical signal was sent to the ESA for RIN analysis.

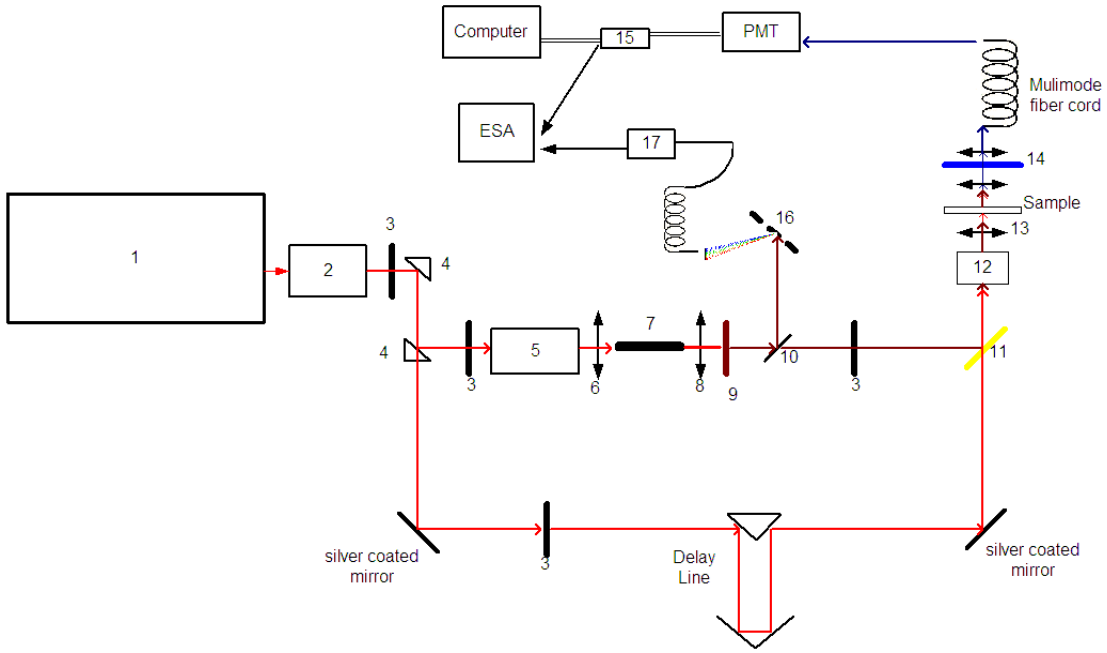

Figure 1: Experimental setup: (1) Ti:sapphire laser (2) Faraday isolator (3) half wave plate (4) beam splitter (5) prism compressor (6) microscope objective lens (40x) (7) PCF (8) collimating aspheric lens of 5mm focal length (9) band pass filter with 1040 nm central wavelength and 60 nm FWHM (10) flip mirror for routing to RIN measurement setup. (11) dichroic mirror for overlapping Stokes beam on the pump beam (12) X-Y scanning mirrors and (13) focusing objective lens **13, 14**…

2.2: Supercontinuum spectra

Figure 2 shows the experimentally obtained supercontinuum (SC) spectra out of Fiber 1 (Fig. 2a) and Fiber 2 (Fig. 2b). The generation of the SC is simulated in both fibers using the generalized nonlinear Schrödinger equation (GNLSE) [6 – 9] and corresponding results are also plotted in Fig. 2a and 2b for the case when average input power is 300 mW and pulse width of 280 fs. It is evident that very good agreement between the experimental and simulated spectra is observed.

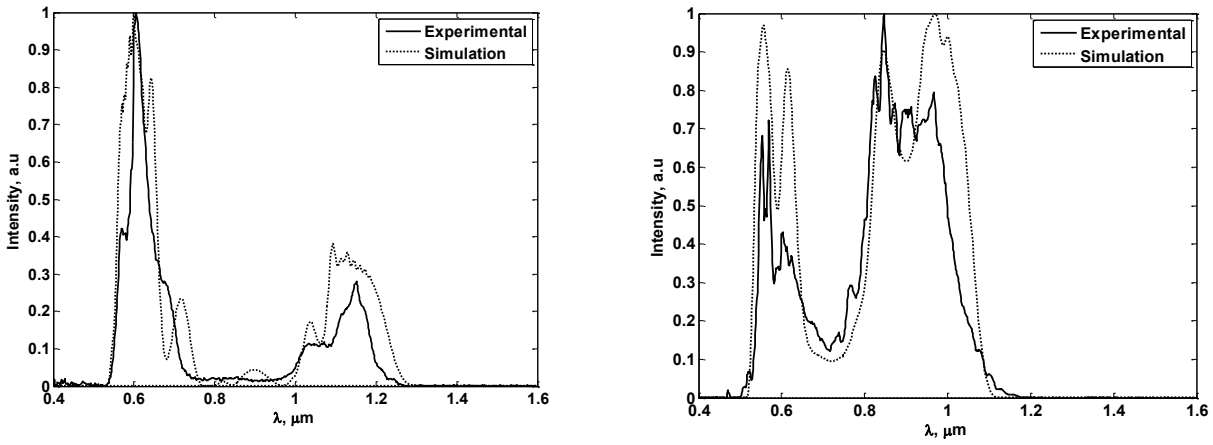

Figure 2 Experimental and simulated spectral profile of 280 fs, 300 mW input power pulses propagating through two different PCF with (a) two closely separated ZDW (Fiber 1) and (b) two widely separated ZDW (Fiber 2)

2.3. RIN measurement

In order to measure the RIN of the Stokes beam the corresponding electrical signal out of fast photodetector (Figure 1) was Fourier-analysed by ESA in a range of 0-81 MHz with a resolution band width of the 1 kHz and 100 Hz [4]. For each measurement the signal power at 80 MHz was compared to the noise figure at a fixed point in the frequency range. For the RIN measurement of the CARS signal, the beam scanning was turned off and the CARS signal from a single point focus inside a drop of oil was collected and sent to the PMT. The corresponding electrical signal out of the PMT was sent to the ESA for RIN analysis.

.

2.4. CARS imaging

The pump and Stokes wavelengths were selected for CARS imaging of the lipid density corresponding to molecular vibrations at 2800-3000 cm^{-1} Raman shift. The input pulse at 800 nm, 300 mW average power and varying pulse temporal duration and chirp was coupled to Fiber 1 or Fiber 2 of identical length of 12.5 cm, to generate, on average, more than 5 mW in the 60 nm wide band making up the Stokes beam.The pump and Stokes beams were collinearly combined and spatio-temporally overlapped inside the sample by using a dichroic mirror, delay line and our home build scanning microscope. The average power of pump and Stokes beams at the sample was 28 mW and 2.5 mW, respectively.

.

3. Results

3.1 RIN of Stokes using both fibers

Fig 3 shows a comparison of the RIN of the Stokes from Fiber 1 and Fiber 2. It can be seen that both fibers have a lower RIN value by as much as 10 dB when the pulse is close to the transform limited. This observation is consistent with noise measurements reported earlier for another type of PCF with a single ZDW [4]. It can be explained by the fact that for short transform-limited pulses or pulses with a small positive chirp, which undergo initial compression, the spectral broadening due to self phase modulation (SPM) is more rapid than for pulses with a large negative chirp. The more rapidly the spectrum broadens, the more rapidly the pulse will spread temporally through fiber dispersion, leading to a reduced overall noise amplification (akin to modulation instability gain), and therefore a reduced overall RIN [4]. In our experiments, we had technical difficulty in implementing and measuring the positive and negative chirp for pulse duration below 100 fs (transform limited is ~ 76 fs). The different shapes for the curves

for the RIN for both fibers for these values of chirp is thus attributed to the lack of sufficient data. However, we expect them to be similar for both fibers.

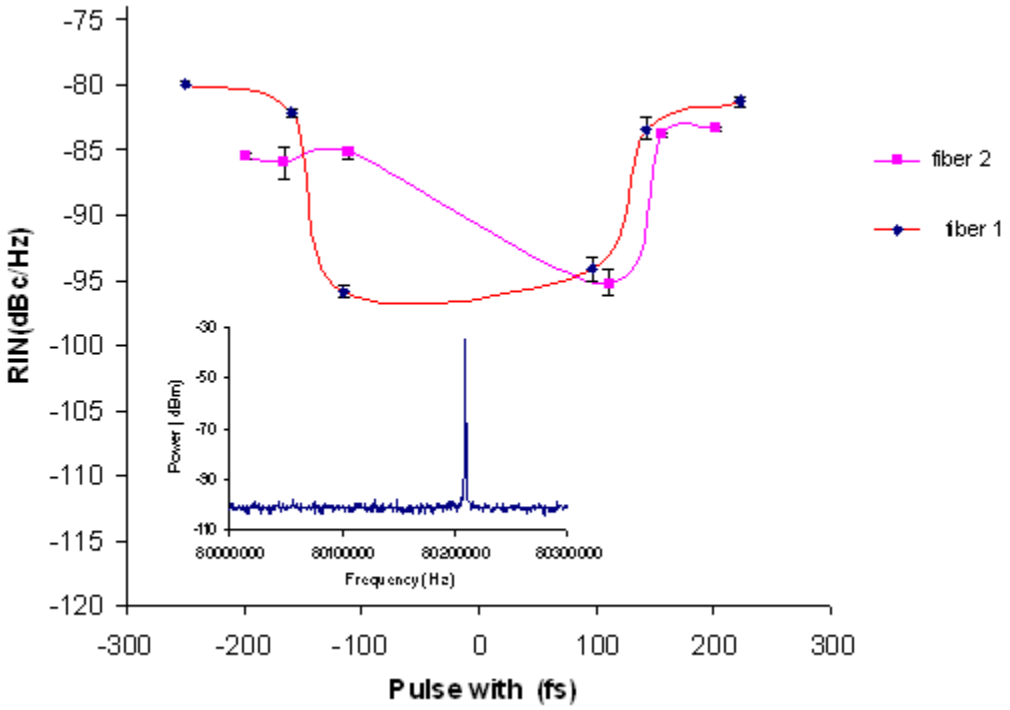

Figure 3: RIN of Stokes beam, using PCF NL-1.4-775-945 (Fiber 1) and PCF NL-PM-750 (Fiber 2) . The error bars are the variance of the RIN values at each pulse width. Lower left Corner: the rf power spectrum of Stokes beam out of PCF. (RBW = 100Hz)

3.2 RIN of CARS using both fibers

The RIN of the CARS signal from an oil sample was obtained as described earlier using the Stokes from either fiber and is shown in Figure 4. A comparison of the RIN values from Fig. 3 and Fig.4, reveals that the RIN of the CARS signal is higher than the RIN of the corresponding Stokes signal, in both Fiber 1 and Fiber 2. This is expected because CARS generation is a coherent process. Any incoherent noise of laser or Stokes signal causes an additional noise, resulting in increased RIN value of the CARS signal compared to the Stokes signal. It is also seen from Fig. 4 that RIN of the CARS signal from Fiber 1 is lower than the corresponding value at 100 fs duration (both positive and negative chirp). Our simulations suggest that the phase of the Stokes signal around 1040 nm for fiber 1 is closer to the pump signal compared to that of Fiber 2. This could be a possible explanation for the lower RIN for CARS in Fiber 1.

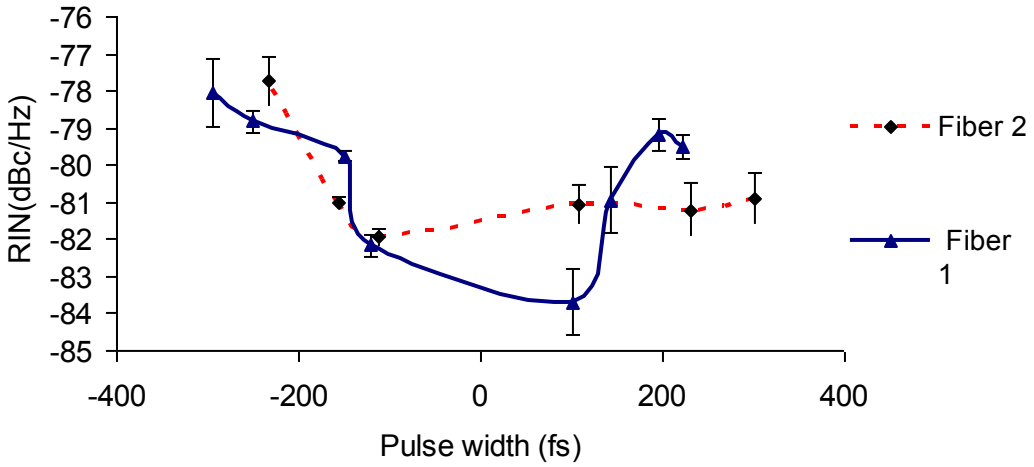

Figure 4: The RIN of CARS of oil, using PCF NL-1.4-775-945 (Fiber 1) and PCF NL-PM-750 (Fiber 2). The error bars are the variance of the RIN values at each pulse width.

3.3 CARS imaging of lipid density with Fiber 2

Since the RIN measurements of CARS signals from both fibers are very similar (Fig. 4), we anticipated that CARS imaging of lipid density using Fiber 2, should also be possible. This is indeed the case as can be seen from the CARS image of fixed unstained myelin from mouse nerve in Fig. 5.

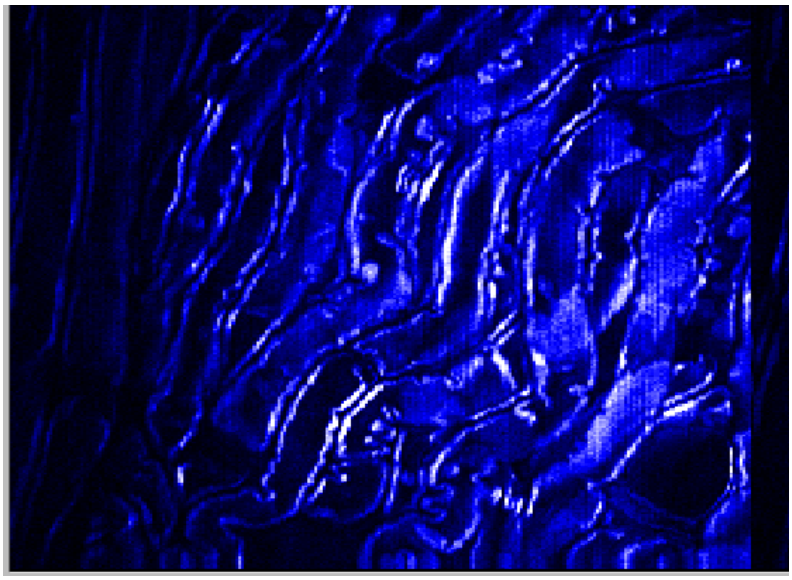

Figure 5: CARS image (256 x 256 pixels) of myelin from fixed unstained mouse nerve using Fiber 2 (PCF NL-PM-750) (pulse width in Stokes arm =225 fs)

4. Conclusion

In this paper, we have compared the performance of two PCFs with different separation of the 2 ZDWs, as Stokes sources for CARS microscopy. The broadband noise in the SC from both fibers is quantified as a RIN value. This is measured as a function of the chirp and duration of the input pulse going into the PCF. It is found

that lowest RIN values for Stokes beam from both fibers are obtained at close to transform limited pulse durations. The RIN values for Stokes beams from both fibers are very similar within the technical limitations of our measurement setup. As anticipate, the RIN of the CARS signal is found to be higher than the RIN of the corresponding Stokes signal, in both Fiber 1 and Fiber 2. In confirmation with these results for the RIN of the Stokes and CARS using both fibers, we found that fiber 2 can also be used for imaging lipid density in myelin with vibrations of C-H bonds at ~ 2850 cm^{-1}. Moreover, since this fiber has a large spectral density in the region of 855 nm - 950 nm corresponding to Raman shifts in the fingerprint region; it is a promising candidate for implementing CARS microscopy or spectroscopy in this same region. This will be confirmed in future experiments with this fiber. Our simulation model for Stokes from both fibers demonstrates close agreement with the experimental results. More simulation studies are underway in order to confirm the coherence properties of the Stokes spectra from both fibers and to explain some of the experimental results.

Reference

1. Sangeeta Murugkar et al "Coherent anti-stokes Raman scattering microscopy using photonics crystal fiber with two closely laying Zero dispersion wavelengths", Opt Express, Vol. 15, Issue 21, 14028, 2007

2. Hideak Kano, Hiro-o Hamaguchi, " Characterization of a supercontinuum generated from a photonics crystal fiber and its application to coherent Raman spectroscopy, Opt. lett. Vol.28, No.23, 2360, 2003

3. Kim P Hansen, R. E. Kristiansen, "Application Note: Supercontinuum Generation in Photonic Crystal Fiber", http://www.nktphotonics.com/

4. K.L.Corwin et al, " Fundamental Noise Limitations to Spercontinuum Generation in Microstructure Fiber", Phys. Rev. Lett., Vol 90, No.11,113904, 2003

5. D. Dimitropoulos et al, "Noise figure and photon statistics in coherent anti-Stokes Raman scattering", Opt. Express, Vol. 14, No. 23, 11418, 2006

6. J. M. Dudley, G. Genty, S. Coen, "Supercontinuum generation in photonic crystal fiber," Rev. Mod. Phys **78**, 1135 – 1184 (2006).

7. K. Hilligsoe, T. Andersen, H. Paulsen, C. Nielsen, K. Molmer, S. Keiding, R. Kristiansen, K. Hansen and J. Larsen, "Supercontinuum generation in a photonic crystal fiber with two zero dispersion wavelengths," Opt. Express **12**, 1045 - 1054 (2004).

8. M. H. Frosz, P. Falk, and O. Bang, "The role of the second zero-dispersion wavelength in generation of supercontinua and bright-bright soliton-pairs across the zero-dispersion wavelength," Opt. Express **13**, 6181-6192 (2005).

9. G. P Agrawal, "Nonlinear Fiber Optics, 3rd edition", Academic press, (2001).

B. CARS microscopy using PCF with two closely lying ZDWs

Novelty:

In this work, we demonstrated for the first time that using a PCF module that has a 12 cm two closely lying ZDWs PCF, enables the generation of a strong, low noise CARS signal, suitable for fast imaging of biological samples. We measured the spectral density of the generated SC for different input laser pulse widths and central wavelengths for different average laser input power, coupled to the PCF to characterize the SC spectrum for performing C-H bond region CARS microscopy imaging.

Contribution:

The fs pulse compressor and PCF parts of the CARS setup for the measurements in the article were installed, calibrated and optimized by C. Brideau and myself, and all the spectrum measurements were done by Dr. Murugkar and myself. Dr. Ridsdale prepared the biological samples and performed the imaging, and Dr. Murugkar was the main author of the article. The article was based on my research work at the Ottawa Civic Hospital as a new member of their CARS research group. I subsequently created a similar CARS setup in our lab at the University of Ottawa.

3.5.3. Coherent anti-Stokes Raman scattering microscopy using photonic crystal fiber with two closely lying zero dispersion wavelengths

Sangeeta Murugkar[1*], Craig Brideau[2], Andrew Ridsdale[2], Majid Naji[1], Peter K. Stys[3], Hanan Anis[1]

[1]*School of Information Technology and Engineering (SITE), University of Ottawa 800 King Edward, P.O. Box 450, Stn A, Ottawa, Ontario, K1N 6N5 , Canada*
[2]*Division of Neuroscience, Ottawa Health Research Institute, University of Ottawa, 725 Parkdale Ave. Ottawa ON K1Y 4E9, Canada*
[3]*Department of Clinical Neurosciences, Hotchkiss Brain Institute, University of Calgary, AB, T2N 4N1, Canada*

Abstract: We demonstrate coherent anti-Stokes Raman scattering (CARS) microscopy of lipid-rich structures using a single unamplified femtosecond Ti:sapphire laser and a photonic crystal fiber (PCF) with two closely lying zero dispersion wavelengths (ZDW) for the Stokes source. The primary enabling factor for the fast data acquisition (84 μ s per pixel) in the proof-of- principle CARS images, is the low noise supercontinuum (SC) generated in this type of PCF, in contrast to SC generated in a PCF with one ZDW. The dependence of the Stokes pulse on average input power, pump wavelength, pulse duration and polarization is experimentally characterized. We show that it is possible to control the spectral shape of the SC by tuning the pump wavelength of the input pulse and the consequence for CARS microscopy is discussed.

OCIS codes: (180.4315) Nonlinear microscopy; (300.6230) Spectroscopy, coherent anti-Stokes Raman scattering; (190.4370) Nonlinear optics, fibers.

References and links

1. J. X. Cheng and X. S. Xie, " Coherent anti-Stokes Raman scattering microscopy: Instrumentation, Theory, and applications," J. Phys. Chem B **108**, 827-840 (2004).
2. F. Ganikhanov, S. Carrasco, X. S. Xie, M. Katz, W. Seitz and D. Kopf, "Broadly tunable dual-wavelength light source for coherent anti-Stokes Raman scattering microscopy," Opt. Lett. **31**, 1292-1294 (2006).
3. C. L. Evans, E. O. ,Potma, M Puoris'haag., D. Côté, C. P. Lin, and S. Xie, "Chemical imaging of tissue in vivo with video-rate coherent anti-Stokes Raman scattering microscopy,". Proc. Natl. Acad. Sci. USA **102**, 16807–16812 (2005).
4. T. Kee and M. T. Cicerone, "Simple approach to one-laser, broadband coherent anti-Stokes Raman scattering microscopy," Opt. Lett. **29**, 2701 – 2703 (2004).
5. H. Kano and H. Hamaguchi, "Vibrationally resonant imaging of a single living cell by supercontinuum- based multiplex coherent anti-Stokes Raman scattering microspectroscopy," Opt. Express, **13**, 1322-1327 (2005).
6. E. R. Andresen, H. N. Paulsen, V. Birkedal, J. Thogersen and S. R. Keiding, "Broadband multiplex coherent anti-Stokes Raman scattering microscopy employing photonic crystal fibers," J. Opt. Soc. Am. B **22**, 1934 – 1938 (2005).
7. E. R. Andresen , C. K. Nielsen, J. Thøgersen and S. R. Keiding "Fiber laser-based light source for coherent anti-Stokes Raman scattering microspectroscopy," Opt. Express **15**, 4848 – 4856 (2007).
8. N. R. Newbury, B. R. Washburn, K. L. Corwin, and R. S. Windeler, "Noise amplification during supercontinuum generation in microstructure fiber," Opt. Lett. **28**, 944 - 946 (2003).
9. K. L. Corwin, N. R. Newbury, J. M. Dudley, S. Coen, S. A. Diddams, K. Weber, and R. S. Windeler, "Fundamental Noise Limitations to Supercontinuum Generation in Microstructure Fiber," Phys. Rev. Lett. **90**, 113904 (2003).
10. J. M. Dudley, G. Genty, S. Coen, "Supercontinuum generation in photonic crystal fiber," Rev. Mod. Phys **78**, 1135 – 1184 (2006).
11. K. Hilligsoe, T. Andersen, H. Paulsen, C.Nielsen, K. Molmer, S. Keiding, R. Kristiansen, K. Hansen and J.Larsen, "Supercontinuum generation in a photonic crystal fiber with two zero dispersion wavelengths," Opt. Express **12**, 1045 - 1054 (2004).
12. A. Aguirre, N. Nisizawa, J. Fujimoto, W. Seitz, M. Lederer, and D. Kopf, "Continuum generation in novel photonic crystal fiber for ultrahigh resolution optical coherence tomography at 800 nm and 1300 nm," Opt. Express **14**, 1145–1160 (2006).
13. A. Apolonski, B. Povazay, A. Unterhuber, W. Drexler, W. J. Wadsworth, J. C. Knight, and P. St. J. Russell, "Spectral shaping of supercontinuum in a cobweb photonic-crystal fiber with sub-20-fs pulses," J. Opt. Soc. Am. B **19**, 2165–2170 (2002).
14. M. H. Frosz, P. Falk, and O. Bang, "The role of the second zero-dispersion wavelength in generation of supercontinua and bright-bright soliton-pairs across the zero-dispersion wavelength," Opt. Express **13**, 6181-6192 (2005).
15. H. Zhang, S. Yu, J. Zhang, and W. Gu, "Effect of frequency chirp on supercontinuum generation in photonic crystal fibers with two zero-dispersion wavelengths," Opt. Express **15**, 1147-1154 (2007).

16. R. L. Fork, O. E. Martinez, and J. P. Gordon, "Negative dispersion using pair of prisms," Opt. Lett. 9, 150-152 (1984).
17. H. Wang and A.M. Rollins, "Optimization of dual-band continuum light source for ultrahigh-resolution optical coherence tomography," Appl. Opt. **46**, 1787-1794 (2007).
18. M. Pezolet and D Georgescauld, "Raman Spectroscopy of Nerve Fibers. A study of membrane lipids under steady state conditions," Biophys. J. **47**, 367–372 (1985).
19. K. P. Knutsen, J. C. Johnson, A. E. Miller, P. B. Petersen, and R. J. Saykally, "High spectral resolution CARS spectroscopy using chirped pulses," Chem. Phys. Lett. **387**, 436-441 (2004).
20. E.H.K. Stelzer, "The Intermediate Optical System in Confocal Microscopes," in The handbook of biological confocal microscopy, J. Pawley, ed. (IMR Press: Madison. 1989).
21. H. Wang, Y. Fu, P. Zickmund, Riyi Shi and Ji-Xin Cheng, "Coherent anti-Stokes Raman scattering imaging of axonal myelin in live spinal tissues," Biophys. J. **89**, 581–591 (2005).
22. H. Kano and H. Hamaguchi, "In-vivo multi-nonlinear optical imaging of a living cell using a supercontinuum light source generated from a photonic crystal fiber," Opt. Express **14**, 2798 – 2804 (2006).
23. J. A. Palero, V. O. Boer, J. C. Vijverberg, H. C. Gerritsen, and H. J. C. M. Sterenborg, "Short-wavelength two photon excitation fluorescence microscopy of tryptophan with a photonic crystal fiber based light source," Opt. Express 13, 5363-5368 (2005).

1. Introduction

Coherent anti-Stokes Raman scattering (CARS) microscopy has been demonstrated to be a powerful tool for non-invasive, chemical imaging of biological systems [1-7]. This technique obviates the need for labeling the sample because it relies on molecular vibrations for contrast. When the difference in the frequencies of the pump and Stokes fields incident on the sample is in resonance with the sample molecular vibration frequency, a strong CARS signal is emitted. Due to the coherent nature of the CARS signal and nonlinear dependence on the excitation intensity, CARS microscopy permits relatively fast data acquisition times and has inherent 3-dimensional sectioning capability.

Despite its well acknowledged power and utility, CARS microscopy is not yet a widely adopted, commercially available biomedical imaging tool. One of the primary reasons for this is that it is technologically complex and involves investing in expensive light sources for generating the pump and Stokes beams. Examples of such expensive, yet close to ideal light sources range from two synchronized picosecond lasers [1] to the current state-of-the-art synchronously pumped OPO system [2]. A fiber based approach involving a single broadband laser source and photonic crystal fiber (PCF) [4-6] to generate both pump and Stokes pulses for CARS, has been developed recently with the view to reducing costs. In particular, broadband, multiplex CARS spectroscopy has been demonstrated using the supercontinuum (SC) generated in a photonic crystal fiber (PCF) with a single zero dispersion wavelength (ZDW) [5, 6]. An alternate scheme for CARS microspectroscopy was proposed recently [7], in which a picosecond fiber laser generated the pump pulse while a PCF with two widely separated ZDWs, was used as a frequency tunable Stokes source. It is notable that these efforts [4-7] involving PCF for the Stokes pulse have not been successful at generating CARS images with short data acquisition times for studying dynamic living systems. The reason for this is that the SC generated in a PCF with one ZDW involves soliton fission and exhibits significant noise amplification [8-10] at low frequencies that are important for imaging. In contrast, SC generation in a PCF with two closely lying ZDWs results from a combination of self-phase modulation and phase matched four-wave mixing and not soliton fission [11]. Consequently, the noise amplification through modulation instabilities is suppressed, resulting in very well-behaved, low noise amplitude and phase of the SC. Such a PCF was recently employed for ultrahigh resolution optical coherence tomography at 800 nm and 1300 nm [12, 17].

We present in this paper, our results involving the use of a PCF with two closely lying ZDWs for generating the low noise Stokes pulse and its application in CARS microscopy when combined with a femtosecond pump pulse. The current prototype CARS microscope provides a low cost alternative for imaging lipid-rich structures in biological specimens with short data acquisition times. The SC output of the PCF was experimentally characterized as a function of the average input power, pump wavelength, pulse duration and polarization of the input pulse. The possibility of extending the CARS imaging for molecular vibration frequencies below 2400 cm^{-1} by spectral shaping of the Stokes pulse, was also explored.

2. PCF with two closely lying ZDWs for Stokes pulse

The PCF (NL-1.4-775-945, Crystal Fibre A/S, Denmark) used for generating the Stokes pulse has a parabolic dispersion profile similar to the one used by Hilligsoe and colleagues [11], and has two closely lying ZDWs at 775nm and 945nm. It is however 12.5 cm long and is housed inside a hermetically sealed package (Femtowhite, Crystal Fibre A/S) that improves ease of light coupling and enhances long term power stability. The pitch of the fiber is 0.98 μm and it has a relative hole size of 0.54. The fiber core diameter is 1.5 μm with a corresponding effective area of ~1.3 μm^2 and a high nonlinear coefficient γ of 0.15 $W^{-1}m^{-1}$. The numerical aperture of the fiber is 0.49 at 800 nm and the fiber is single mode but not polarization maintaining.

Light from a tunable Ti:sapphire laser (Tsunami, Spectra-Physics, Mountain View, CA) producing ~ 65 fs pulses at 80 MHz repetition rate was split into two arms: pump and Stokes arms as shown in Fig. 4, Section 3. A Faraday isolator was inserted in the beam path immediately after the laser, for avoiding back reflection into the laser. This however stretched the pulse (dispersion of ~ 6600 fs^2), so a custom-built prism compressor consisting of two prisms was added in the Stokes arm. This enabled pulse compression and the ability to control duration of the input pulse launched into the PCF. Due to the non-perfect alignment of the prism compressor, the pulse after compression, had residual amounts of spatio-temporal distortions. This resulted in the measured pulse duration of ~ 100 fs (instead of ~ 65 fs) out of the prism compressor. An intensity autocorrelator (FR-103XL, Femtochrome Research Inc., Berkeley, CA) was used for the measurement of the pulse duration.

Light was coupled into the PCF with a coupling efficiency of ~ 40 - 50 % by means of an aspheric lens (Thorlabs, Newton, NJ) having a focal length of 4.5 mm. The measured spectral output of the PCF as a function of the average pump power coupled into the core of the PCF is shown in Fig. 1. The excitation wavelength of 810 nm (~ 100 fs pulse duration) lies within the anomalous dispersion region indicated by the vertical lines. For this measurement, light from the PCF was collected by butt-coupling a multimode fiber at the output end of the PCF and was analyzed using an optical spectrum analyzer (OSA). Fig. 1 shows that when output power is greater than 55 mW, the spectral density is mainly located in two peaks centered in the visible and infra-red (IR) regions accompanied by almost total depletion inside the anomalous dispersion region. The ratio of intensities between the two peaks was found to depend on the efficiency of collection of the light output from the PCF into the multimode fiber into the OSA. With increasing power, the outer edges of the SC shift outward in agreement with observations reported earlier [11]. It was also found that the spectral intensity at 1040 nm increased. This new observation is particularly important since this region centered at 1040 nm with a bandwidth of ~ 53 nm was used as the Stokes pulse for CARS imaging of lipids. When spatially and temporally overlapped with the pump pulse at 810 nm (12346 cm^{-1}) the difference between the pump and Stokes frequency bands was in the range of ~2484 cm^{-1} – 2965 cm^{-1}. The Raman vibrational frequency of the C-H bonds in lipids at 2840 cm^{-1} lies in this range as discussed in Section 3 below. Average input power of 300mW at 810 nm was typically used to excite the SC for the CARS microscopy experiment. This corresponds to average power of ~140 mW or peak power of ~ 18 kW for a pulse of ~100 fs duration propagating inside the core of the PCF. Under this condition, average power measured in the Stokes pulse was ~ 10 mW.

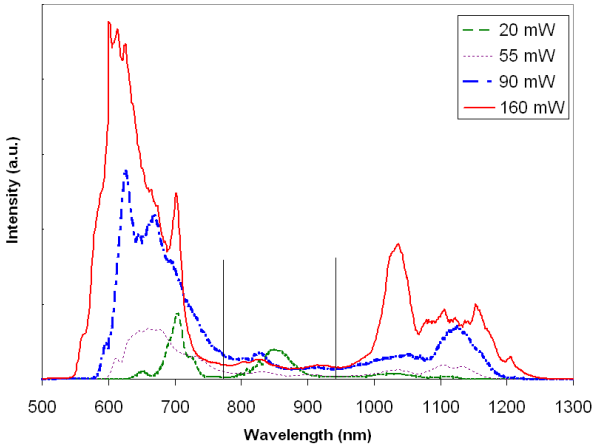

Fig 1. (Color online) Measured spectral output of the PCF as a function of average power coupled into the core. The vertical straight lines indicate the position of the two ZDWs. Excitation pulse is at 810 nm and is ~ 100 fs wide.

The significance of spectral shaping of the SC output of the PCF by changing input pulse parameters has been pointed out in the literature [13, 10]. The possibility of controlling spectral shape of the SC for CARS microscopy by tuning the input pulse wavelength is considered here for the first time. The excitation wavelength was tuned inside the anomalous dispersion region in steps of 5 nm from 810 nm to 915 nm, while keeping the pulse duration, average input power and coupling efficiency constant.

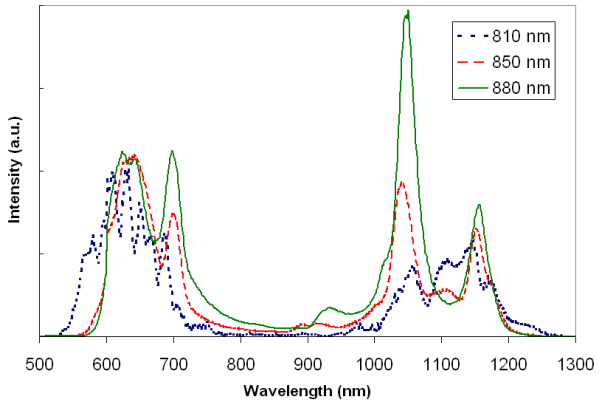

Fig. 2. (Color online) Dependence of SC on pump wavelength. Output power in the PCF is constant at 140 mW and pulse duration is ~ 100 fs.

Figure 2 illustrates the raw experimental data at representative wavelengths of 810 nm, 850 nm and 880 nm. Note that the spectral intensity changes at different excitation wavelengths are not absolute since the coupling of output power from the PCF into the collection fiber changed in between data sets. It is evident from Fig. 2 that the double peaked spectrum is maintained when the input pulse wavelength is increased. However there is a significant increase in the energy content of the IR peak, especially at ~ 1040 nm when pump wavelength is at 880 nm. This experimentally confirms for the first time the predictions of results reported earlier [11] for the dependence of SC output on pump wavelength, which were based only on simulations. When average input power of ~ 300 mW is used, the average output power measured in a bandwidth of ~ 53 nm centered at 1040 nm is ~ 20 mW at 850 nm and 23 mW at 880 nm as opposed to 10 mW at 810 nm. Note that the frequency difference between the Stokes band around 1040 nm and pump pulse at 850 nm and 880 nm, approximately equals the Raman shifts of 2100 cm^{-1} and 1650 cm^{-1} respectively. This result is particularly favorable for CARS microscopy, since this would enable imaging of aggregates of deuterated lipids (at 2100 cm^{-1}) and proteins (1650 cm^{-1}) corresponding to vibration frequencies of the C-D and amide I vibration bands, respectively.

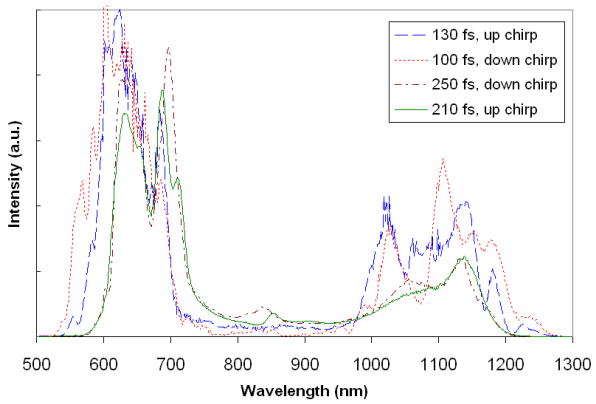

Fig. 3. (Color online) Dependence of SC on frequency chirped (indicated as up and down chirp) pulses. Pump wavelength is at 810 nm and output power of the PCF is 140 mW.

The SC output did not change significantly when the input pulse duration was varied. This experimentally confirms the theoretical results reported earlier for such dependence [11], which were based primarily on simulation. However as shown in Fig. 3 and in contrast to simulation results in Ref. 15, our experimental results indicate that there is no significant difference in the spectral output of the PCF when the pump pulse is positively (up chirp) or negatively (down chirp) chirped. The chirp values were estimated using a standard formula [16] and varied by changing the distance between the two prisms in the prism compressor. A pulse with duration of ~100 fs launched at the input of the PCF was found to acquire a positive chirp [11] and resulted in a measured pulse duration of ~185 fs after propagation through the PCF. A half wave plate positioned in front of the focusing lens allowed control of the polarization of the input pulse injected into the PCF. A slight redistribution of spectral intensity occurred within 45 degrees for every 10 degree of rotation in polarization. The polarization was adjusted for obtaining maximum power in the Stokes band for the CARS microscopy experiments. This dependence on polarization can be attributed to the appreciable amount of birefringence induced in the PCF due to slight irregularities in the diameter, position, pitch and shape of the air holes inside the cladding of the PCF [17]. The output from the PCF was found to be slightly polarized as well.

The process of SC generation in this PCF with two closely lying ZDWs has been explained by Hilligsoe and colleagues [11] as follows. Self-phase modulation is the dominant broadening mechanism and provides seed wavelengths for four-wave mixing which leads to efficient depletion of spectral intensity between the two ZDWs. Additional non-degenerate four wave mixing also contributes to extending the depleted region between the main peaks beyond the region between the ZDWs [11]. The role of four-wave mixing in the spectral broadening was questioned by Frosz et al in a subsequent paper [14] where they demonstrated the role of generation of dispersive waves followed by soliton self frequency shift (SSFS) when the separation between the ZDWs is large enough [14]. Additional work on the fundamental mechanisms of SC generation in such fibers is necessary to fully understand the discrepancies in these studies. However, since the anomalous dispersion region is very narrow (165 nm) in the PCF considered in this work, we believe that the theory of soliton generation does not apply [14] and that a combination of self-phase modulation and four-wave mixing moves most of the power out of the anomalous dispersion region. In the absence of soliton fission in the PCF with two closely lying ZDWs, the SC contains much less noise compared to SC from conventional PCFs with 1 ZDW.

Noise characteristics of SC generated in a PCF with 1 ZDW have been extensively studied in the literature [8-10]. The significant amplitude noise, well in excess of shot noise, has been shown to be comprised of two components: a broadband or white-noise component, and a low-frequency component. The low-frequency component of the amplitude noise results from amplification of the technical noise (i.e., all noise excluding shot noise) on the input Ti:sapphire laser pulse, and can be reduced through the use of a highly stabilized pump laser [8]. In contrast, the substantial white-noise component of the SC results predominantly from the amplification of the quantum shot noise on the input laser pulse and thus represents a fundamental limit to the SC stability [9]. The amplification of the input pulse shot noise has a strong dependence on pulse energy, pulse duration and wavelength. Its physical origin lies in the extreme sensitivity of the spectral broadening mechanism involving the process of soliton fission in particular, to input pulse noise [10]. The noise in the SC in a PCF with 1 ZDW was experimentally measured by Corwin et al. [8, 9]. The spectrally filtered, 8 nm bandwidth of the SC was directed to either an IR or a visible photodetector. The resulting electrical signal was fed into an electrical spectrum analyzer, where the RF noise power above the detector noise floor was measured. The typical RF noise power in the raw data was found to be ~ 45 dB below the signal power level. The relative intensity noise (RIN) deduced from such a measurement corresponded to pulse-to-pulse amplitude fluctuations of 7 % - 50 % depending on the values for the input pulse energy and chirp.

A noise measurement similar in procedure to that described above was performed by Hilligsoe et al. [11] for a PCF with two closely lying ZDWs. For every 2 nm bandwidth of the SC in the range of 600 nm to 700 nm, the signal power at 76 MHz was compared to the maximum noise feature in the spectrum. The spectra were however seen to be flat and without noise over the entire frequency range. An upper limit on the noise level was established to be at least 60 dB below the signal power at all wavelengths. This lower noise level in the SC compared to that in the PCF with 1 ZDW is consistent with the fact that the SC generation process in PCF with two ZDWs does not involve soliton fission and hence no amplification of shot noise comes into play. This result has important implications for laser scanning microscopy and in particular, CARS microscopy. In most applications involving imaging of biological samples, the low signal levels dictate that pixel dwell time is typically ≥ 1 μs. This implies that any fluctuations in the intensity of the excitation light in the low frequency region (≤ 1 MHz) will be detrimental to image quality. The effect of the light source fluctuations can be overcome to a limited extent by

increasing the pixel dwell time or by averaging over many frames. However this is not a practical approach for applications involving imaging of dynamic processes in live biological samples. The quieter light source involving the PCF with two closely lying ZDWs is thus ideal for CARS microscopy with short data acquisition times as proven in Section 4 below.

3. CARS microscopy setup

A schematic of the experimental setup of our CARS microscope is shown in Fig. 4. Light from a Ti:sapphire laser producing ~ 65 fs pulses at 80 MHz repetition rate was split into two arms marked as pump and Stokes in Fig. 4. A Faraday isolator (Electro-Optics Technology, Inc., Traverse City, MI) was included immediately at the output to reduce back reflections into the laser. The pump arm (degenerate with the probe) proceeds to the sample via a variable delay line. The pump pulse acquires a temporal chirp of ~300 fs after passing through the Faraday isolator. Its measured bandwidth was ~12 nm (~180 cm^{-1}). In principle this would imply low spectral resolution, since typical sample Raman line widths in the "fingerprint" region are ~ 10 - 15 cm^{-1} [1]. This would reduce the resonant to non-resonant CARS signal for imaging in such bands [1]. However in the case of lipid rich samples, such as myelin or adipocyte cells, the effective band width of the band of Raman vibrational frequencies in the CH vibrational region (2,800–3000 cm^{-1}) is large (~130 cm^{-1}) [3, 18]. This wide spectral shape is indicative of the chemical composition which includes many vibrational bands, including the aliphatic CH_2 and the vinyl CH stretches [3]. Thus, in spite of the large pump pulse bandwidth, we were able to obtain very large resonant to non-resonant CARS signal (20:1) as evident from the images in Section 4 below. In order to extend the CARS imaging to the fingerprint region, we will resort to chirped CARS or spectrally compressed chirped CARS microscopy for reducing the spectral width of the pump pulse [6, 19].

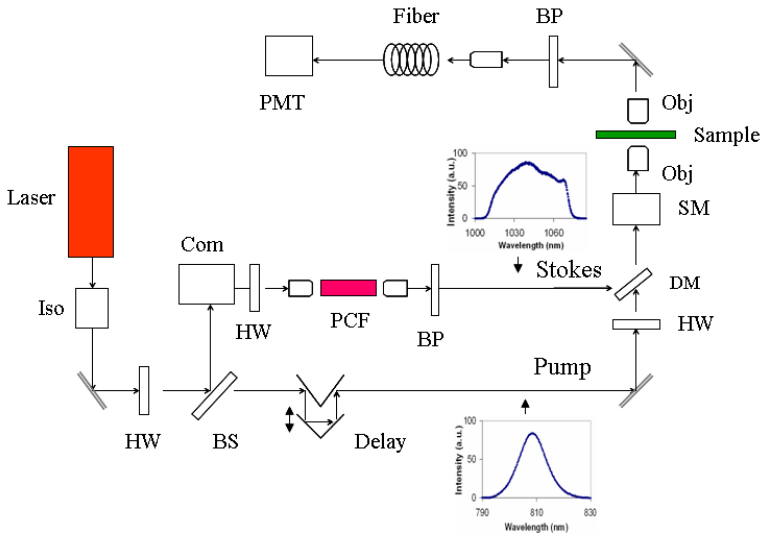

Fig. 4. (Color online) Schematic of the CARS microscope setup. PCF- Photonic Crystal Fiber with two ZDWs; Iso – Faraday Isolator; DM- Dichroic mirror; Com - Prism compressor; SM – Scanning mirror assembly; HW – Half wave plate; BP – Band Pass filter; BS – Beam Splitter; Obj – Objective; PMT – Photo Multiplier Tube; Fiber – multimode fiber to guide the CARS signal into the PMT.

The second arm (Stokes) consists of a pulse compressor and the PCF with two closely lying ZDWs as described in Section 2 above. Recompression of pulses was performed by a prism compressor before the pulse was injected into the PCF. This compensated for the dispersion due to the Faraday isolator. The SC output from the PCF was recollimated and filtered (Chroma Technologies, Brattleboro, VT) to produce the Stokes pulse centered at ~ 1040 nm with a bandwidth of ~ 53 nm. This particular frequency band was chosen so that the difference between the pump and Stokes frequencies corresponds to the Raman vibrational frequency (~ 2800 to 3000 cm^{-1}) of the C-H bonds associated with lipid-rich structures such as myelin. The input pulse at 810 nm, 300 mW average power and pulse duration of 100 fs when launched into the PCF generated about 10 mW of average power in the Stokes pulse after bandpass filtering. The measured spectra corresponding to the pump and Stokes pulses are shown in the insets in Fig. 4. The pump and Stokes beams were combined and spatio-temporally overlapped inside the sample using a

dichroic mirror and a home built laser scanning microscope system. This system utilizes an XY pair of galvanometer mounted mirrors and relay lenses in the standard optical configuration of a laser scanning microscope [20]. The Zeiss Plan Neofluar (40x, 1.3 NA) oil immersion microscope objective used to focus the pump and Stokes light has about 15% transmission at these wavelengths. This resulted in a measured average power at the sample of ~ 15 mW (0.2 nJ pulse energy) for the pump beam and ~ 0.5 mW (0.006 nJ) for the Stokes beam. The forward-directed CARS signal was collected by an Olympus 40x, 0.8 NA water immersion, microscope objective and was filtered by a 700nm short pass filter (Chroma Technologies). This light was coupled into a multimode fiber and detected by a photomultiplier tube.

4. CARS imaging results

As mentioned above, positive dispersion in the Faraday isolator temporally stretches the laser pulse so that the pump pulse duration is ~ 300 fs. In the Stokes arm, an input pulse that is ~ 100 fs wide acquires a slightly positive chirp after emerging from the PCF such that the Stokes pulse duration is ~ 185 fs. This configuration involving the overlap of a temporally narrow, broad band Stokes pulse with a temporally wide, narrower band pump pulse is similar to the configuration of chirped pulse CARS [19]. When the time delay between the pump and Stokes pulse is varied, different frequencies from the pump bandwidth are involved in the CARS generation process, resulting in a shift of the center wavelength in the CARS spectrum. For CARS imaging, the pump and Stokes pulses were temporally overlapped by finding time zero using the delay line. CARS signal from the oil used for oil immersion objective was optimized by tuning the optical alignment in the beam paths. The ratio of the resonant CARS signal obtained from oil to the non-resonant CARS signal obtained from glass is > 55:1.

Some proof of principle CARS images taken in the forward direction from various types of samples are presented in Fig. 5. The forward CARS image of isolated unstained live dorsal root axons from rat obtained in about 5.5 seconds is shown in Fig. 5(a). Bright parallel bands seen in the image correspond to large resonant CARS signal from myelin that surrounds the axons which are ~ 10 μm in diameter. Although the axial resolution in the image can be further improved, interesting features such as the node of Ranvier and a Schmidt-Lanterman incisure [21] indicated by a line arrow and a block arrow, respectively, can be still be seen along the myelin in the bottom half of this image. Fig. 5(b) shows the unaveraged CARS image of lipid droplets seen as bright circular spots inside unlabeled 3T3 L1 cultured adipocyte cells. The single frame collection time for the 256x256 pixels image was ~ 5.5 seconds. Figs. 5 (c and d) are forward CARS images of sebacious gland (c) and fat-producing adipocyte cells (d) about 20-30 μm in size, taken at different thicknesses at a depth of at least 100 μm inside the tissue of a mouse ear. Fig. 5(e) is an image of the same adipocyte cells as in (d), but with the Stokes signal blocked. A weak signal probably dominated by two photon excitation fluorescence from endogenous fluorophores in tissue surrounding the fat cells, is evident in the image. This also confirms that the signal in Fig. 5 (d) is mainly due to CARS. The note worthy features in all of these CARS images are that the pixel dwell time is very short at ~ 84 μs per pixel and that the signal originating from lipid rich regions is typically found to be a factor of 10 – 20 greater than background levels.

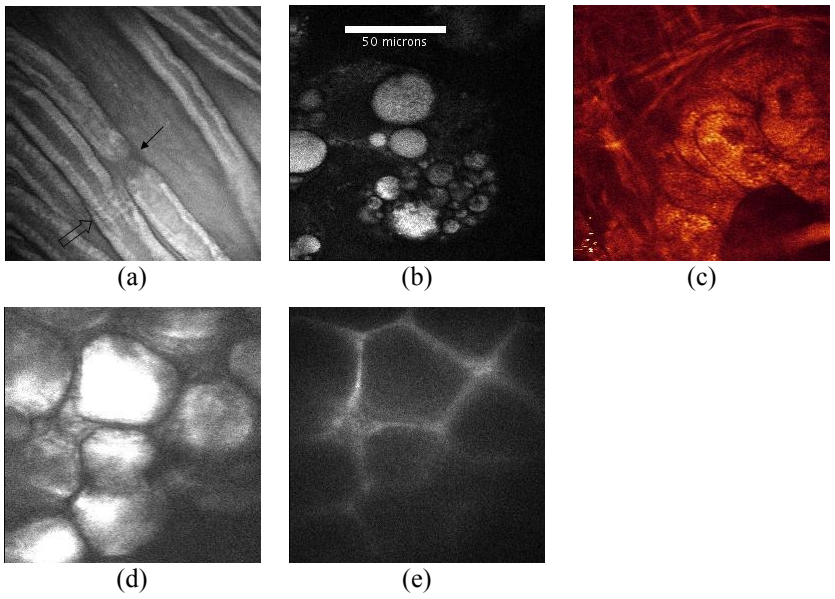

Fig. 5. Proof-of-principle forward - CARS images at Raman shift of 2840 cm^{-1} from (a) isolated unstained live rat dorsal root axons (b) lipid droplets in unlabeled 3T3 L1 adipocyte cell culture (c) sebaceous gland (in pseudo colour) in a mouse ear at a depth of ~ 40 μm and (d) adipocyte cells at a depth of 100 μm in a mouse ear imaged in the forward mode through several hundred microns of tissue. (e) same as in (d) but with Stokes beam blocked.

5. Discussion and conclusion

A practical implementation of a cost effective, low noise source for CARS microscopy with short data acquisition times, is demonstrated in this paper. It is based on using a single femtosecond Ti:sapphire laser source and makes use of a PCF with two closely lying ZDWs to produce the Stokes pulse for CARS microscopy. Unlike the PCF with 1 ZDW or two widely separated ZDWs employed in earlier work [4–7], the SC generated in the PCF with two closely lying ZDWs does not involve soliton fission and is hence inherently more stable. The special dispersion profile of this type of PCF enables generation of very stable, low noise Stokes pulses, resulting in high contrast CARS images with short acquisition times of 84 μs per pixel. In contrast, the SC generated in a PCF with one ZDW exhibits higher noise content [8,9] at low frequencies that are important for CARS imaging.

The particular parameters such as wavelength, average power, pulse duration and polarization for input light pulse launched into the PCF, were determined with the aim of generating optimum Stokes pulses for CARS microscopy. We showed that it is possible to control the spectral shape of the SC by tuning the pump wavelength of the input pulse and that the energy content of the Stokes pulse filtered out of the IR part of the SC increased with increase in pump wavelength. Due to the single source based design of our CARS microscope, increasing the pump wavelength up to ~ 915 nm enables access to Raman shifts in the "fingerprint" region below 1800 cm^{-1}, up to about 1200 cm^{-1}.

Although not shown here, application of this PCF with two closely lying ZDWs for CARS multiplex spectroscopy [4 – 7, 19] is relatively straightforward. For example, the spectrally narrow pump pulse can be generated by means of spectral compression of a chirped pulse [6]. In that case, the whole IR band of the SC interacts with the spectrally narrow pump pulse to generate multiplex CARS spectra.

Proof-of-principle CARS images at ~ 2840 cm^{-1} Raman shift, obtained with our CARS setup demonstrated high signal to background levels. Signal originating from lipid rich regions was typically found to be a factor of 10 – 20 greater than background levels. The non resonant background excited due to the broad bandwidth pump does not limit CARS imaging of lipid rich biological materials as demonstrated in this report. This is due in part to the fact that the Raman active CH vibrational region in lipid-rich structures has a large effective band width of ~130 cm^{-1} [3, 18].

Another application involving this PCF with two closely lying ZDWs will be very useful to explore in conjunction with CARS microscopy. The IR or visible part of the SC spectrum can be used as a low noise source for

two-photon excitation fluorescence (TPEF) of exogenous fluorophores such as green fluorescence protein [22] or several endogenous fluorophores such as elastin, NADH and aromatic amino acids like tryptophan, tyrosine and phenylalanine [23]. This can be combined with CARS microscopy as well as other nonlinear optical techniques such as second harmonic generation (SHG) and sum frequency generation (SFG) for multi-nonlinear optical imaging [21, 22]. In conclusion, the high-contrast low noise CARS imaging capability demonstrated in this paper could be fairly readily adapted to most currently installed two-photon excited fluorescence microscopy systems, resulting in major cost savings. Such an instrument could extend the two-photon fluorescence excitation capabilities of conventional systems to include simultaneous label-free, non-bleaching and chemically selective CARS imaging of fixed and live biological samples.

C. Portable miniaturized fiber deliverd Exoscope

Novelty:

We demonstrated for the first time, a portable multimodal coherent anti-Stokes Raman scattering microscope (exoscope) for minimally invasive in-vivo imaging of tissues. We did a series of TPEF images of a stained mouse lung tissue sample, a SHG image of a KDP crystal sample, and CARS imaging of a mouse myelin nerve sample. There are a number of challenges that were addressed in the design of the exoscope:

- Miniaturized optics: Designing small-diameter bulk optics to achieve high NA with as little chromatic aberrations as possible for widely-spaced wavelengths was non-trivial in such a constrained mounting volume.
- Photon collection: An integral element in this nonlinear exoscope is the fibre delivery of single-mode, low noise, femtosecond pump and Stokes beams to the sample. Using large mode area PCF with a custom optical filter was an ideal solution.
- MEMS mirror: A miniaturized MEMS mirror capable of high frame rates was used thus enabling us to produce high quality images from living samples.

In article 3.5.4 (journal) and 3.5.5 (conference), we demonstrate a novel, miniaturized and multimodal CARS microscope based on MEMS scanning mirrors and custom miniature optics. By producing high resolution and distortion-free CARS, TPEF and SHG images in forward direction from different samples and by using designed optics; we successfully demonstrate the proof of concept of a bench-top miniaturized CARS microscope. In these two articles, the microscope was not fully integrated, the excitation light was delivered in free space and the generated signal was collected in the forward direction only.

In Article 3.5.6 (conference) and 3.5.7 (journal), we demonstrate, a fully- integrated, portable, multimodal, fiber delivered coherent anti-Stokes Raman scattering microscope (exoscope) for minimally invasive in-vivo imaging of biological tissues. A single Ti:sapphire femtosecond pulsed laser is used as the light source to produce CARS, TPEF and SHG images of biological and chemical samples. Excitation lights were delivered to the exoscope body via a connectorized LMA 20 PCF cord. The generated CARS signal was collected in the epi direction using a

multimodal fiber optics cord. The high resolution and distortion-free images were obtained successfully from various biological samples, particularly in the backward direction (epi).

Contributions:

My contributions in Articles 3.5.4 and 3.5.5 were the design of the optical paths to deliver the pump and Stokes beams to the exoscope, performing multimodal imaging with Dr. Murugkar, and testing the optical head of the exoscope.

Dr. Murugkar was the lead on the project, Mr. Smith did the MEMS segment, tested the electronics of the exoscope, and helped Dr. Murugkar assemble the exoscope. Mr. Srivastava and Mr. Moica wrote the software for data acquisition and imaging. Since this was a joint project with Dr. Stys group at the University of Calgary, Dr. Stys and Mr. Brideau were involved in the exoscope concept and requirements. In articles 3.5.6 and 3.5.7 , Brett and I worked jointly on characterizing and testing the portable miniaturized exoscope.

3.5.4. Miniaturized multimodal CARS microscope based on MEMS scanning and a single laser source

Sangeeta Murugkar,[1,*] Brett Smith,[1] Prateek Srivastava,[2] Adrian Moica,[3] Majid Naji,[1] Craig Brideau,[4] Peter K. Stys,[4] and Hanan Anis[1]

[1]*School of Information Technology and Engineering (SITE), University of Ottawa 800 King Edward, P.O. Box 450, Stn A, Ottawa, Ontario, K1N 6N5, Canada*
[2]*RatworX Inc., 47 Wycliffe Street, Ottawa, Ontario, K2G 5L9, Canada*
[3]*1761 Matthews Avenue, Ottawa, Ontario, K2C0X5, Canada*
[4]*Department of Clinical Neurosciences, Hotchkiss Brain Institute, University of Calgary, AB, T2N 4N1, Canada*

Abstract: We demonstrate a novel miniaturized multimodal coherent anti-Stokes Raman scattering (CARS) microscope based on microelectromechanical systems (MEMS) scanning mirrors and custom miniature optics. A single Ti:sapphire femtosecond pulsed laser is used as the light source to produce the CARS, two photon excitation fluorescence (TPEF) and second harmonic generation (SHG) images using this miniaturized microscope. The high resolution and distortion-free images obtained from various samples such as a USAF target, fluorescent and polystyrene microspheres and biological tissue successfully demonstrate proof of concept, and pave the path towards future integration of parts into a handheld multimodal CARS probe for non- or minimally-invasive in vivo imaging.

OCIS codes: (170.3880) Medical and biological imaging; (180.4315) Nonlinear microscopy; (190.4180) Multiphoton processes; (230.4685) Optical microelectromechanical devices

References and links

1. C. L. Evans, and X. S. Xie, "Coherent anti-stokes Raman scattering microscopy: chemical imaging for biology and medicine," Annu Rev Anal Chem (Palo Alto Calif) **1**(1), 883–909 (2008).
2. X. L. Nan, J. X. Cheng, and X. S. Xie, "Vibrational imaging of lipid droplets in live fibroblast cells with coherent anti-Stokes Raman scattering microscopy," J. Lipid Res. **44**(11), 2202–2208 (2003).
3. T. B. Huff, Y. Shi, Y. Fu, H. Wang, and J. X. Cheng, "Multimodal nonlinear optical microscopy and applications to central nervous system," IEEE J. Sel. Top. Quantum Electron. **14**(1), 4–9 (2008).
4. T. T. Le, C. W. Rehrer, T. B. Huff, M. B. Nichols, I. G. Camarillo, and J. X. Cheng, "Nonlinear optical imaging to evaluate the impact of obesity on mammary gland and tumor stroma," Mol. Imaging **6**(3), 205–211 (2007).
5. T. T. Le, I. M. Langohr, M. J. Locker, M. Sturek, and J. X. Cheng, "Label-free molecular imaging of atherosclerotic lesions using multimodal nonlinear optical microscopy," J. Biomed. Opt. **12**(5), 054007 (2007).
6. S. Murugkar, C. L. Evans, X. S. Xie, and H. Anis, "Chemically specific imaging of cryptosporidium oocysts using coherent anti-Stokes Raman scattering (CARS) microscopy," J. Microsc. **233**(2), 244–250 (2009).
7. H. Chen, H. Wang, M. N. Slipchenko, Y. Jung, Y. Shi, J. Zhu, K. K. Buhman, and J. X. Cheng, "A multimodal platform for nonlinear optical microscopy and microspectroscopy," Opt. Express **17**(3), 1282–1290 (2009).
8. F. Helmchen, M. S. Fee, D. W. Tank, and W. Denk, "A miniature head-mounted two-photon microscope. high- resolution brain imaging in freely moving animals," Neuron **31**(6), 903–912 (2001).
9. H. Bao, J. Allen, R. Pattie, R. Vance, and M. Gu, "Fast handheld two-photon fluorescence microendoscope with a 475 μm x 475 μm field of view for in vivo imaging," Opt. Lett. **33**(12), 1333–1335 (2008).
10. C. J. Engelbrecht, R. S. Johnston, E. J. Seibel, and F. Helmchen, "Ultra-compact fiber-optic two-photon microscope for functional fluorescence imaging in vivo," Opt. Express **16**(8), 5556–5564 (2008)
11. W. Piyawattanametha, E. D. Cocker, L. D. Burns, R. P. Barretto, J. C. Jung, H. Ra, O. Solgaard, and M. J. Schnitzer, "In vivo brain imaging using a portable 2.9 g two-photon microscope based on a microelectromechanical systems scanning mirror," Opt. Lett. **34**(15), 2309–2311 (2009).
12. J. T. C. Liu, M. J. Mandella, N. O. Loewke, H. Haeberle, H. Ra, W. Piyawattanametha, O. Solgaard, G. S. Kino, and C. H. Contag, "Micromirror-scanned dual-axis confocal microscope utilizing a gradient-index relay lens for image guidance during brain surgery," J. Biomed. Opt. **15**(2), 026029 (2010).

13. H. Bao, A. Boussioutas, R. Jeremy, S. Russell, and M. Gu, "Second harmonic generation imaging via nonlinear endomicroscopy," Opt. Express 18(2), 1255–1260 (2010).
14. F. Légaré, C. L. Evans, F. Ganikhanov, and X. S. Xie, "Towards CARS Endoscopy," Opt. Express 14(10), 4427–4432 (2006).
15. H. Wang, T. B. Huff, Y. Fu, K. Y. Jia, and J. X. Cheng, "Increasing the imaging depth of coherent anti-Stokes Raman scattering microscopy with a miniature microscope objective," Opt. Lett. **32**, 2212 – 2214 (2007).
16. I. Veilleux, M. Doucet, P. Coté, S. Verreault, M. Fortin, P. Paradis, S. Leclair, R. S. Da Costa, B. C. Wilson, E. Seibel, O. Mermut and J. Cormier, " Design and modeling of a prototype fiber scanning CARS endoscope," Proc. SPIE, **7558**, 75580D1 - 12 (2010).
17. B.G. Saar, R.S. Johnston, M. Roeffaers, E.J. Seibel and X.S. Xie, "CARS endoscopy," presented at SPIE Photonics West, San Francisco, California, USA, 23 - 28 Jan. 2010.
18. S. Murugkar, C. Brideau, A. Ridsdale, M. Naji, P. K. Stys, and H. Anis, "Coherent anti-Stokes Raman scattering microscopy using photonic crystal fiber with two closely lying zero dispersion wavelengths," Opt. Express, **15**,14028 – 14037 (2007).
19. L. Fu and M. Gu, "Fibre-optic nonlinear optical microscopy and endoscopy", J. Microscopy, **226**, 195–206 (2007).
20. T. M. Liu, M. C. Chan, I. H. Chen, S. H. Chia, and C. K. Sun, "Miniaturized multiphoton microscope with a 24Hz frame-rate," Opt. Express **16**, 10501 - 10506 (2008).
21. C. L. Hoy, N. J. Durr, P. Chen, W. Piyawattanametha, H. Ra, O. Solgaard, and A. Ben-Yakar, "Miniaturized probe for femtosecond laser microsurgery and two-photon imaging," Opt. Express **16**, 9996–10005 (2008).
22. S. Tang, W. Jung, D. McCormick, T. Xie, J. Su, Y. Ahn, B. J. Tromberg and Z. Chen, "Design and implementation of fiber-based multiphoton endoscopy with microelectromechanical systems scanning," J. Biomed. Opt. **14**, 034005 (2009).
23. M. Scholles, A. Bräuer, K. Frommhagen, Ch. Gerwig, H. Lakner, H. Schenk, and M. Schwarzenberg, "Ultracompact laser projection systems based on two-dimensional resonant microscanning mirrors," J. Micro/ Nanolith. MEMS MOEMS, **7**, 021001 (2008).
24. M. Scholles, K. Frommhagen, Ch. Gerwig, J. Knobbe, H. Lakner, D. Schlebusch, M. Schwarzenberg, and U. Vogel, "Recent advancements in system design for miniaturized MEMS-based laser projectors," Proc. SPIE **6911**, 69110U (2008).
25. K. C. Maitland, H. J. Shin, H. Ra, D. Lee, O. Solgaard and R. Richards-Kortum, "Single fiber confocal microscope with a two-axis gimbaled MEMS scanner for cellular imaging," Opt. Express **14**, 8604 – 8612 (2006).
26. E. Spiess, F. Bestvater, A. Heckel-Pompey, K. Toth, M. Hacker, G. Stobrowa, T. Feurer, C. Wotzlaw, U. Berchner-Pfannschmidt, T. Porwol and H. Acker, "Two-photon excitation and emission spectra of the green fluorescent protein variants ECFP, EGFP and EYFP," J. Microscopy, **217**, 200–204 (2005).
27. A. Chong, J. Buckley, W. Renninger and F. Wise, "All-normal-dispersion femtosecond fiber laser," Opt. Express **14**, 10095 (2006).

1. Introduction

CARS microscopy has evolved over the past decade as a powerful label-free imaging modality based on intrinsic vibrational contrast [1]. A wide variety of important applications involving CARS microscopy have been demonstrated. These range from imaging lipid droplet biology [2], imaging axonal myelin in spinal cord injuries and demyelinating diseases [3], identifying obesity related risks in cancer [4] and atherosclerosis [5] and the rapid detection of pathogens [6]. Moreover, it has been clearly shown that there is a tremendous benefit in combining CARS with other imaging modalities such as TPEF and SHG in a multimodal imaging and spectroscopy platform to obtain a complete picture of the health of the biological tissue [3-5, 7]. However, in order to truly extend the benefits of multimodal CARS microscopy to human health, development of a multimodal CARS probe in the form of an endoscope or miniaturized hand held microscope is essential. In fact, significant progress has been made in the development of TPEF and SHG imaging endoscopes and miniaturized microscopes for in vivo imaging applications [8-13]. For CARS microscopy which involves the pump and Stokes beams for excitation of the nonlinear optical signal, progress towards fiber based endoscopy has been quite slow [14-16]. The key challenges have been (i) the efficient delivery of the ultrafast pump and Stokes light using optical fibers (ii) efficient fiber based collection of the CARS signal (iii) miniaturization of laser scanning mechanisms and (iv) efficient design of chromatic aberration corrected miniature optics for achieving high resolution CARS images. Past research efforts [15,16] have focused mostly on overcoming the challenges of fiber based light delivery and collection. In particular, laser scanning and focusing at the sample to generate a CARS image was achieved using standard macro-optics, such as a galvanometric scanner and a microscope objective. A miniaturized objective lens [17] was demonstrated for deeper penetration in CARS imaging, but was used with a standard microscope objective and a galvanometric scanner. Only recently, progress was reported related to the design and modeling [18] and implementation [19] of a fiber scanning based CARS endoscope.

While miniature microscopes and hand held probes based on TPEF [8-11], fluorescence confocal microscopy [12] and SHG [13] have been fabricated earlier, there is no report of a miniaturized CARS microscope to the best of our knowledge. In this paper, we demonstrate for the first time, a miniaturized multimodal CARS microscope based on MEMS scanning mirrors and custom miniature optics. Moreover, a single femtosecond pulsed laser is used as the light source to produce the CARS, TPEF and SHG images. A scheme first demonstrated by our group [20], using the supercontinuum generated in a nonlinear photonic crystal fiber (PCF) as the Stokes beam and part of the

femtosecond pulse laser as the pump beam, is employed for CARS imaging. The high resolution and distortion-free images obtained from various samples such as a USAF target, fluorescent and polystyrene microspheres and biological tissue successfully demonstrate proof of concept, and pave the path towards future integration of parts into a handheld multimodal CARS probe for non- or minimally-invasive in vivo imaging. The use of a single femtosecond laser as the light source for the miniature multimodal CARS microscope holds further promise for making the whole setup more compact for future clinical use. We describe below, details of the design as well as the experimental setup to test the performance of our MEMS-based miniature multimodal CARS microscope.

2. Materials and Methods

2.1 Experimental setup

The light source for multimodal nonlinear optical excitation is based on a single Ti:sapphire femtosecond laser (Tsunami, Spectra-Physics, Mountain View, CA) producing ~ 65 fs pulses at 80 MHz repetition rate and tunable between 720 nm - 1000 nm. This light is split into pump and Stokes arms as shown in Fig. 1. As described in detail in our earlier work [20], about 300 mW of this light at ~ 800 nm is directed into a commercial photonic crystal fiber (PCF) module (NKT Photonics, FemtoWhite CARS) for creating the Stokes beam. The remainder (~ 400 mW) comprises the pump beam used for CARS, TPEF and SHG imaging. The supercontinuum output from the PCF is band pass filtered (Chroma Technology) so that it consists of wavelengths between 1014 nm - 1067 nm. The pump beam is sent through a computer controlled delay stage and then recombined with the Stokes beam at the dichroic mirror. The diameter of the pump and Stokes beams is reduced using a pair of plano-convex lenses so that they do not overfill the MEMS mirror of diameter 500 µm. Light reflected at 45 degrees by the MEMS mirror is incident on the miniature optics held inside a stainless steel barrel on a vertical rail. The sample is mounted on a three axis automated stage so that it can be placed in the focal plane of the incident pump and Stokes beams. Nonlinear optical signal from the sample is collected by a long working distance, air objective (Mitutoyo, 20x, 0.42NA) in the forward direction. This is filtered by a 680 nm short pass filter (Chroma Technology) to remove the excitation light. Appropriate band pass filters are used to separate the SHG, TPEF, and CARS signals as described in Section 3.2. This light is coupled into a large (1 mm diameter) core multimode fiber (Thorlabs) and detected by a photomultiplier tube (PMT) (Hamamatsu, H7422-40) for image generation.

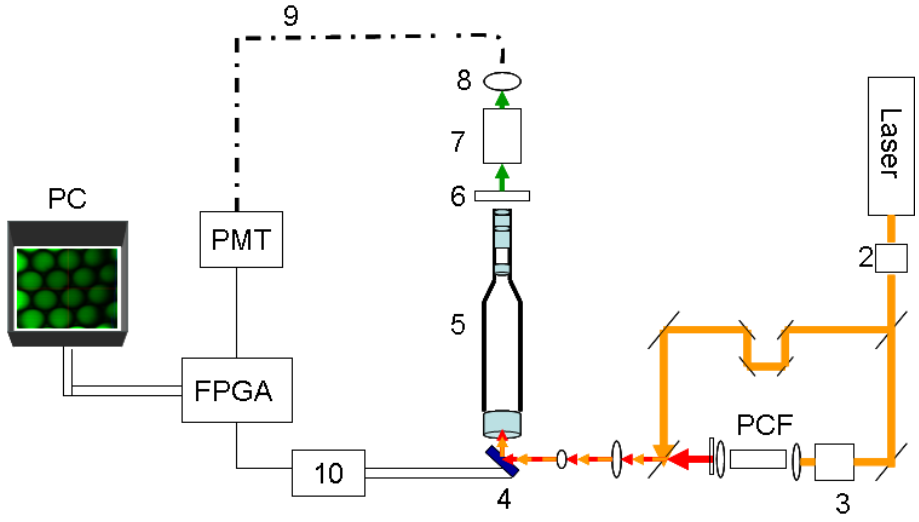

Fig. 1 Bench top miniaturized multimodal CARS microscope. Details of components are as follows: (2) Faraday isolator (3) Prism compressor (4) MEMS mirror (5) Miniature optics inside stainless steel tube (barrel) (6) Sample for imaging (7) microscope air objective (20x) for collecting nonlinear optical signal from sample (8) Lens for coupling light into collection fiber (9) Multimode fiber (10) Voltage Amplifier circuit to amplify electrical signal, for driving the MEMS mirror, provided by the Field Programmable Gate Array (FPGA).

2.2 Miniature optics

The miniature optics were designed with the intention of integrating them at a later stage inside a portable miniature microscope for in vivo imaging of the rat spinal cord. This imposed the requirement that its distal end would have a

tip whose outer diameter is no more than 3 mm. This meant that the optics had to be designed with a diameter of less than 2 mm such that it would still provide an NA of ~ 0.6, working distance of ~ 400 µm and enable sub-micron resolution imaging. Traditionally, gradient index (GRIN) lenses with relatively high numerical apertures (NA) of 0.5- 0.6 have been preferred in multi-photon microendoscopy applications, mainly because of their low cost and nearly diffraction-limited image quality [21]. However from our optical design analysis, it became clear that the two excitation wavelengths at 800 nm (pump beam) and 1040 nm (Stokes beam) separated by ~ 200 nm for CARS imaging of lipids, poses a significant challenge in terms of compensating the longitudinal chromatic aberration in the GRIN lenses. Hence we opted for designing a conventional miniaturized front end objective that would perform to the required specification. This is indeed very challenging since a large numerical aperture is required from small diameter optics. The final design consists of multiple lenses that are ~ 1.8 mm in diameter and have varying prescriptions. Two different glass types, SF4 and FK51 are chosen to compensate for the chromatic aberration at 800 nm and 1040 nm. The effective NA of the front end objective is 0.6 and the designed field of view is 100 x 100 µm with a working distance of 400 µm. Relay lenses are included in the optical design in order to image the MEMS mirror on the back aperture of the miniature objective with a magnification of 5x. Appropriate antireflection coatings are applied on all optics to maximize throughput of excitation and emission light. All of the miniature optics are assembled (BMV Optical, Ottawa, Canada) inside a stainless steel tube (barrel) which is about 4.1 cm as shown in Fig. 2. A thin glass window seals off the distal end of the barrel thus permitting water immersion.

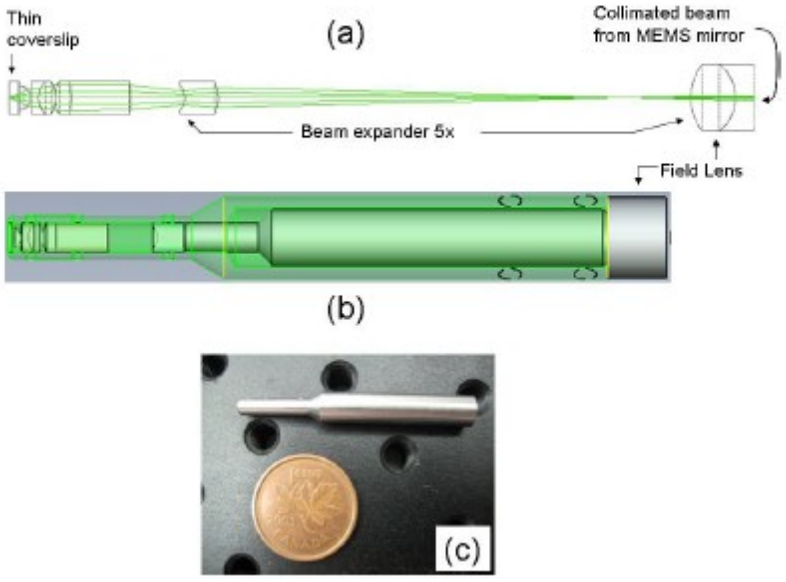

Fig. 2. (a) Ray-trace diagram of the optical beam as it enters from the right after the MEMS mirror and is relayed to the miniature focusing optics on the left, through a 5x beam expander assembly including the field lens. (b) Computer-aided-design of the barrel. (c) Photograph of the fully packaged barrel. A penny is included for size comparison

2.3 MEMS scanning and image reconstruction

Miniaturized laser scanning in fluorescence based endoscopes and miniaturized microscopes is achieved by means of cantilever fiber-scanners [8-10], as well as MEMS scanning mirrors [11, 12, 22-24]. MEMS scanners operating at resonant frequencies offer the advantages of adjustable and fast frame rates and allow batch fabrication.

In our microscope, a two dimensional scanning MEMS mirror (Fraunhofer IPMS, Germany) with a diameter of 500 µm is employed for beam scanning and image generation. The device consists of a circular silicon plate in gimbal mounting suspended by a total of four torsional spring bars [25]. The reflectivity of the mirror plate is enhanced by a thin layer of aluminum and was measured to be ~ 80 % at 800 nm. Independent resonant oscillation of the mirror plate (fast axis) and the frame (slow axis) itself, is set up by applying a high voltage to the comb electrodes adjacent to the mirror and frame. A Field Programmable Gate Array (FPGA) (Altera DE2) board running a 50 MHz system clock is programmed to sweep from higher frequencies to lower frequencies with a sweep time of 5 s, until it stops at the resonant frequency for each axis. A custom-built voltage amplifier circuit amplifies the

rectangular waveform output from the FPGA to drive the MEMS oscillations along the fast and slow axes. When high voltage is applied to both axes, a Lissajous pattern is scanned, with a filling factor determined by the particular ratio of the slow and fast resonant frequencies. An optical scan angle of +/-17 degrees along both axes is obtained by applying 40 V and 70 V, at the resonant frequencies of 1.336 KHz and 16.99 KHz to the slow and fast axis, respectively. In order to avoid overfilling the back of the barrel in the optical geometry of the bench top setup the scan angle was reduced by setting the resonant frequencies to higher values of 1.429 KHz and 17.225 KHz for the slow and fast axis respectively.

The nonlinear optical signal from the sample is collected in the forward direction as shown in Fig. 1 and sent to the PMT followed by an amplifier-discriminator unit (Ortec 9327). TTL pulses from the discriminator are sent to the FPGA where they are synchronized with respect to the FPGA clock. The time difference between subsequent events is encoded and sent to the PC via a custom-made board that uses the FT2232H chip. A program running on the PC receives these data and saves them to disk. An image reconstruction program simulates the trajectory of the laser and creates a mapping table. It uses the stored data files in the PC and transforms the scanned vector data in a frame period into a 512 × 512 pixel image. The phase delay between the driving electrical signal and the mechanical response of the MEMS mirror is adjusted in order to remove ghost images in the final 512 x 512 pixel image.

We would like to now comment on the frame rates that are achievable with our multimodal miniature microscope. The goal is to achieve a self repeating Lissajous scan pattern of the optical beam that fulfills the conditions that i) every pixel in the 512 x 512 pixel image is hit at least once and ii) the spatial coverage is very uniform across the FOV. We first experimentally measure the resonance curves for the slow and fast axes at 40 V and 70 V, respectively. From this data, we determine the resonant frequencies for the desired optical scan amplitude. These slow and fast axis resonant frequencies are then expressed in terms of the number of system clock cycles (ticks), ns and nf, respectively, where the system clock of the FPGA is at a much higher frequency of 50 MHz. The resulting Lissajous pattern will self repeat after n ticks where n is the least common multiple of ns and nf. Thus the frame repeat rate is given by (50 MHz) / n. It should be clear that different choices of ns and nf, or in other words, the slow and fast axis resonant frequencies, will give different frame repeat rate. Our choice of the slow and fast axis resonant frequencies of 1.429 KHz and 17.225 KHz, respectively provided a good spatial coverage over a 512 x 512 pixel image. The resulting frame rate of 4 Hz is sufficient for our current requirement of imaging stationary samples. This frame rate was identical for all imaging modalities in our microscope. We collected a fixed amount of data (10MB, roughly 9 million nonlinear optical events) per image file which included multiple frames. The brighter images had more nonlinear optical events per frame, and therefore the time required to acquire this data was less.

3. Results

3.1 Microscope characterization using standard samples

The resolving power of the microscope was investigated by acquiring transmission images of a USAF resolution test target (Edmund Optics). The femtosecond pulsed laser tuned to 720 nm, followed the pump beam path as shown in Fig.1. A water drop was placed on top of the tip of the barrel and the USAF target glass slide was placed facing down, touching this water drop such that the smallest features on the target were centered on the focused beam spot with a reduced average power of 1.5 mW. The reconstructed image is shown in Fig. 3a. The smallest element 6 in the 7th group is at the left side of the image. It has a line spacing of 228 line pairs/mm, corresponding to a line width of approximately 2.2 μm. There is no distortion in the shape of the individual lines in the image except for a conical distortion in which the right side of the image is slighty rotated counter clockwise. This is a known artifact due to the 45 degree angle between the slow axis of the MEMS mirror and the incident light beam [26] and can be corrected in future image post processing.

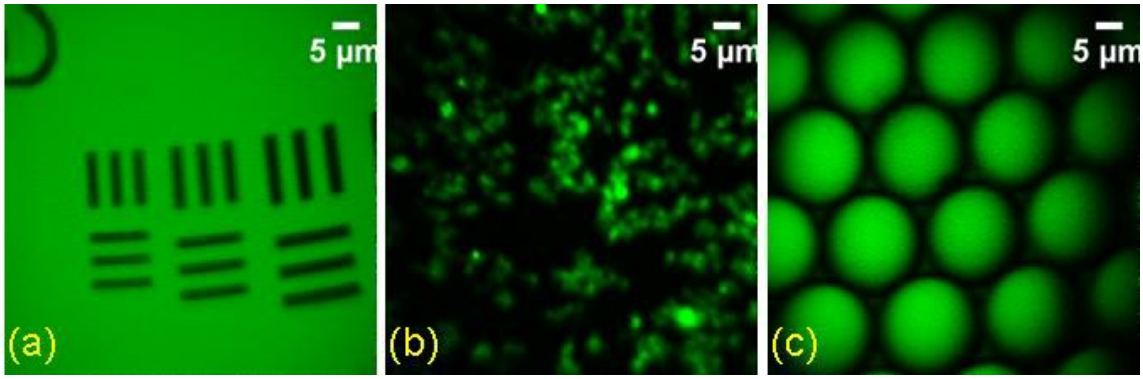

Fig 3. (a) Transmission image in 720 nm light of the smallest bars in Group 7, element 6 on a USAF1951 target obtained with the miniature multimodal microscope. Part of the number '6' can be seen in the top left side corner of the image. (b) TPEF image of a sample of 1 µm fluorescent microspheres on a thin #1 coverslip (c) CARS image of 20 µm polystyrene beads

We next performed TPEF microscopy on a sample of diluted solution of 1 µm fluorescent microspheres (Polysciences Inc., PA, USA). Light from the femtosecond laser at 800 nm was reflected off the MEMS with close to 80% reflectivity and ~ 64% of this light was transmitted through the optics inside the barrel, such that an average power of ~28 mW is focused at the sample. The reconstructed TPEF image is shown in Fig 3 (b). Most of the 1 µm spheres are seen to coalesce together, however a few individual spheres can be clearly resolved.

For CARS imaging experiments, a small drop of diluted solution of 20 µm and 4.5 µm polystyrene beads on a # 1 cover slip was used. The pump beam at 800 nm and the Stokes beam containing the near IR filtered output at 1057 nm are focused into the volume of beads, so that the aromatic CH vibration in polystyrene at 3045 cm^{-1} Raman shift gets resonantly excited. Fig. 3 (c) is the CARS image of the 20 µm spheres obtained with the miniature microscope when the average power at the sample was ~28 mW in the pump beam and ~ 0.8 mW in the Stokes beam. From this image it is seen that the FOV is ~ 70 x 70 µm. The slightly decreasing intensity to the right of the FOV in Fig 3 (c) is because of slight beam clipping owing to the non-perfect alignment of the barrel with respect to the MEMS mirror on the vertical rail. The axial resolution of the miniature microscope was experimentally measured by CARS imaging of 4.5 µm polystyrene beads (Polysciences Inc.) in steps of 1 µm along the "z" optical axis. The maximum intensity values of the line profiles in the z stack were plotted as a function of z step. A full width at half-maximum value of the Gaussian curve fitted to this plot resulted in an axial resolution of 12.74 µm for the miniature CARS microscope. This is larger than the design value of 3 µm and is mainly attributed to slight optical misalignment in the beam paths of the bench top microscope system.

3.2 Multimodal imaging of biological tissue

We next demonstrate multimodal ex vivo imaging of biological tissue samples with the miniature microscope. A 0.5 mm thin section of a fixed dorsal root from a YFP mouse (Jackson Laboratory, Bar Harbor, Maine) was mounted on a slide, covered with a thin cover slip and imaged facing down for TPEF and CARS, as described above. In this sample, the axons selectively express yellow fluorescent protein (peak emission ≈ 530 nm) whereas the lipid rich myelin surrounding the axons is label-free. The frequency difference between the pump and Stokes light sets up a coherent vibration of the CH bonds at 2845 cm^{-1} Raman shift in the lipid molecules of myelin. A 65 nm bandpass filter centered at 645 nm (Chroma Technology) is used in the collection beam path to selectively pass only the CARS signal. Proof of principle forward CARS image of unlabeled myelin surrounding the axons is seen in Fig 4a. The bright strands of lipid-rich myelin, marked by an arrow, can be clearly distinguished in Fig 4a. When the Stokes beam was blocked, no appreciable signal was detected. This confirms that the contribution due to YFP emission at 645 nm is negligible and that the image in Fig. 4(a) is primarily due to CARS emission.

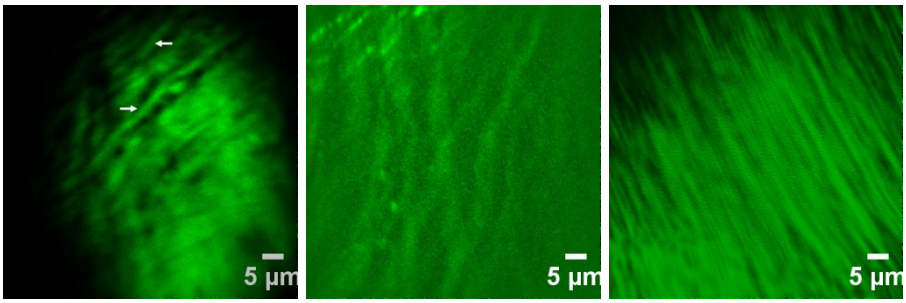

(a) (b) (c)

Fig. 4 Multimodal imaging using miniature CARS microscope (a) forward - CARS image at a Raman shift of 2845 cm^{-1} from label free myelin surrounding YFP labeled axons in fixed dorsal roots of mouse. (b) TPEF image of YFP labeled axons at excitation wavelength of 870 nm. (c) SHG image from unlabeled rat tail collagen.

The excitation wavelength for optimal two photon absorption in YFP is known to be ~ 970 nm [28]. However, our laser could only be tuned to ~ 870 nm where mode locking was still possible. The TPEF image of the same sample of fixed YFP mouse dorsal root as in Fig. 4a was obtained at 870 nm and is shown in Fig. 4b. Although the signal to noise ratio is poor, the YFP labeled axons in Fig 4b can be identified. The laser was tuned back to 800 nm for SHG imaging and a short pass filter (Chroma Technology, VT, USA) was used in the collection beam path to selectively pass only wavelengths below 450 nm. Fig. 4c illustrates the SHG image obtained from a 0.5 mm thin section of fixed rat tail collagen. The wavy type-I collagen fibers are well resolved in the image.

4. Discussion and conclusion

We have demonstrated a novel miniature multimodal microscope capable of performing CARS, TPEF and SHG imaging. The excitation light is scanned in a Lissajous pattern by means of a two dimensional scanning MEMS mirror that is 500 µm in diameter and is focused on the sample by a miniaturized probe containing miniature relay optics and a multiple lens objective that is 1.8 mm in diameter. The miniature objective corrected for chromatic aberration is able to generate a strong CARS signal corresponding to the vibrations of the CH bonds at 2845 cm^{-1} and 3045 cm^{-1} Raman shifts. Proof of principle images of fluorescent and polystyrene beads as well as biological tissue obtained with our setup demonstrate very high resolution and the shapes of features remain consistent throughout the FOV.

Our current setup serves as a test bench for a future portable, handheld prototype of a miniature multimodal CARS microscope for in vivo imaging. In fact, integration of the components is underway in which the excitation light is delivered by a large mode area PCF [16] and the nonlinear optical signal from the sample is collected by the same miniature optics in the epi-direction, separated from the excitation light by a miniature dichroic mirror and collected by means of a large core multimode fiber. A frame rate of 4 Hz is obtained for the particular values of resonant frequencies chosen for the slow and fast axes in this paper. For imaging dynamic phenomena, or for positioning the sample in the FOV, we plan to generate video frames. The video frame rate will be achieved by using the "sliding" Lissajous pattern technique as described in Ref. 12. This technique uses the fact that unlike raster scan, the Lissajous pattern scans the whole FOV several times in each frame, and by marking the start of a frame at a different "sliding" spot, faster video rate can be achieved without compromising the spatial coverage. For situations where not enough nonlinear optical events are present, the image will be enhanced by brightening the image and/or reducing the image size (256x256 instead of 512x512).

The axial resolution for CARS imaging is expected to improve and get closer to the design specification of 3 µm due to better optical alignment and collinearity of the fiber delivered pump and Stokes beams in this prototype. It is also notable that the light source for our miniature multimodal CARS microscope is based upon a single femtosecond Ti:sapphire laser and the use of a PCF for Stokes generation. A femtosecond fiber laser such as in Ref. [29] could be used to replace the tabletop Ti:sapphire laser making the entire setup compact and amenable to translation to the bedside.

Acknowledgements

This work was funded by the CIHR – NSERC grant # 87490. We would like to gratefully acknowledge Roger Montcalm, SITE, University of Ottawa for loaning the FPGA (Altera DE2) board. We would like to thank Ian Powell for help in designing the bench-top setup, and Dr. Ileana Micu and Thomas Kannanayakal for preparing the tissue samples.

3.5.5. Development of a micromirror-scanned multimodal CARS miniaturized microscope for the in vivo study of spinal cord disorders

Sangeeta Murugkar*[a], Brett Smith[a], Majid Naji[a], Craig Brideau[b], Peter Stys[b] and Hanan Anis[a]
[a] School of Information Technology and Engineering (SITE), University of Ottawa
800 King Edward, P.O. Box 450, Stn A, Ottawa, Ontario, K1N 6N5 , Canada
[b]Department of Clinical Neurosciences, Hotchkiss Brain Institute,
University of Calgary, AB, T2N 4N1, Canada

ABSTRACT

We discuss the design and implementation of a novel multimodal coherent anti-Stokes Raman scattering (CARS) miniaturized microscope for imaging of injured and recovering spinal cords in a single living animal. We demonstrate for the first time, the use of a biaxial microelectromechanical system (MEMS) mirror for scanning and diffraction limited multiple lens miniaturized objective for exciting a CARS signal. The miniaturized microscope design includes light delivery using a large mode area photonic crystal fiber (PCF), and multimode fiber for collection of the nonlinear optical signal. The basic design concept, major engineering challenges, solutions, and preliminary results are presented. We demonstrate CARS and two photon excitation fluorescence microscopy in a benchtop setup with the miniaturized optics and MEMS scanning. The light source is based on a single femtosecond laser (pump beam) and a supercontinuum generated in a nonlinear PCF (Stokes beam). This is coupled using free space optics onto the surface of a resonantly driven two dimensional scanning MEMS mirror that scans the excitation light in a Lissajous pattern. The novel design of the miniaturized microscope is expected to provide significant new information on the pathogenesis of demyelinating diseases such as Multiple Sclerosis and Spinal Cord Injury.

Keywords: Coherent anti-Stokes Raman scattering, multiphoton imaging, microelectromechanical scanning mirrors, miniature multimodal microscope.

INTRODUCTION

CARS microscopy has evolved over the past decade as a powerful label-free imaging modality based on intrinsic vibrational contrast [1]. In particular, CARS imaging based on a single femtosecond laser source is very well-suited to image the high lipid densities in myelin, the fatty tissue surrounding axons in nerve bundles in the spinal cord [2]. Disorders of the spinal cord such as spinal cord injury (SCI) and Multiple Sclerosis (MS) are devastating conditions leaving patients with severe lifelong disabilities. While animal models of both SCI and MS are well developed, readout of tissue changes in the same animal as a function of time and experimental treatment is limited. There is a clear need for relatively non-invasive methods of examining spinal tissue in living animals over time with microscopic resolution. A multimodal nonlinear miniaturized microscope or endoscope combining CARS, two photon excitation fluorescence (TPEF) and second-harmonic generation (SHG) microscopy would be extremely valuable for this purpose. While there have been recent advances in developing miniature microscopes for confocal fluorescence imaging [3] and multiphoton endoscopes [4] for TPEF and SHG microscopy, limited progress has been made in developing such a probe for CARS microscopy. The key challenges have been (i) the efficient delivery of the ultrafast pump and Stokes light using optical fibers (ii) efficient fiber based collection of the CARS signal (iii) miniaturization of laser scanning mechanisms and (iv) efficient design of chromatic aberration corrected miniature optics for achieving high resolution CARS images. This paper describes our progress in the design and development of a fiber optic-based, micromirror-scanned, miniaturized multimodal CARS microscope for the in vivo study of spinal cord disorders. The overall design concept is described followed by recent development of a bench top version of the multimodal CARS miniscope.

DESIGN CONCEPT

Overall design

The spinal cord in rodents (rats/ mice) is ~ 5 mm deep below the skin of the animal and is ~ 3 – 4 mm wide in rat. Since the depth of the spinal cord is not within the optical penetration depth for in-vivo CARS imaging, our strategy is to implant a stainless steel guide tube (13 mm deep and 4 mm wide) by means of minimally invasive surgery that involves exposing the dorsal spinal cord at the thoracic level via a laminectomy. The implanted tube will rest just above the white matter of the spinal cord as shown in Fig 1. Our miniaturized multimodal CARS microscope is thus an "exoscope" since it is external to the body rather than internal to a bodily canal or a hollow organ as in the case of an endoscope. The outer diameter of the tip of the exoscope probe is restricted to ~ 3 mm for this particular application. The light source for multimodal excitation is based on a single femtosecond laser (Tsunami, 100 fs, 80 MHz rep rate, 800 nm) and a photonic crystal fiber (PCF) for the Stokes beam as we reported earlier [2]. The main components in the exoscope design are i) large mode area PCF for delivery of femtosecond pump and Stokes pulses ii) MEMS mirrors for scanning the light beams on the tissue iii) custom miniature optics for focusing the light beams and iv) multimode large core fiber for collecting nonlinear optical signal generated in the tissue.

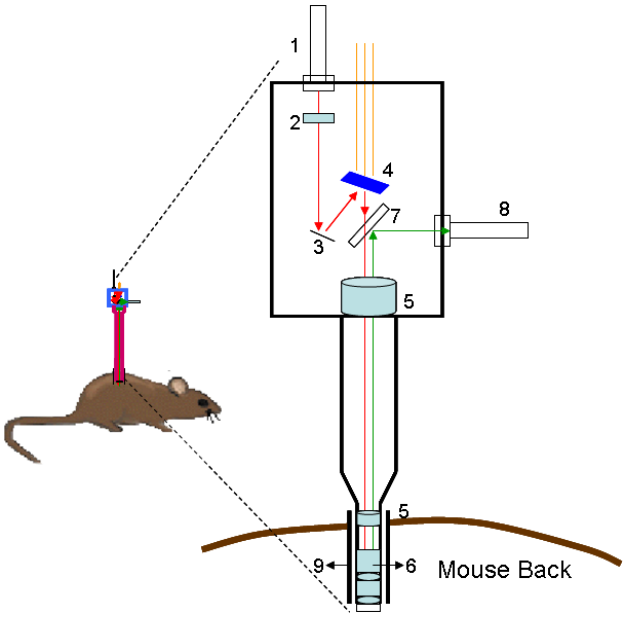

Fig 1 Schematic of the design concept of CARS exoscope includes 1) LMA-20 as delivery fiber for pump and Stokes excitation light 2) Collimating lens 3) mirror 4) MEMS mirror 5) Relay optics 6) Front end objective 7) Dichroic Beamsplitter 8) 1mm core multimode fiber for collecting light emitted from nerve tissue 9) Optical port installed in the back of the mouse. In our terminology, the rectangular box is called the "body" while the thinner funnel shaped tube is called the "barrel".

Fiber based light delivery and collection

An important consideration in choosing the delivery fiber for the femtosecond pump and Stokes pulses is the use of a large mode area fiber core in order to suppress nonlinearities in the fiber that would result in unwanted spectral broadening of the pulses. A large mode area PCF, LMA20 (NKT Photonics) was chosen for this reason. It was recently reported that a strong four wave mixing signal is generated inside the fiber core [5] under similar excitation conditions. This will not affect the integrity of the CARS signal in our case, since the excitation and collection paths are separated by a dichroic mirror as shown in Fig. 1. The pump and Stokes pulses at 810 nm and 1040 nm respectively, are negatively prechirped by means of a grating or prism compressor, before coupling into the LMA20 to compensate for pulse dispersion inside the fiber. The collection path for the CARS, TPEF and SHG signal generated in the sample tissue is collinear with the excitation path until it is separated by the dichroic beamsplitter as shown in Fig 1. A large core (1mm diameter) multimode fiber (Thorlabs) collects the emitted light which is filtered and delivered to a photomultiplier tube (Hamamatsu H7422-40).

Miniature Optics

Excitation light delivered by the LMA20 is collimated by means of a simple plano-convex lens with a focal length of 4 mm. A mirror reflects the collimated beam with a spot size of 350 μm onto the surface of a small (diameter of 500 μm) circular MEMS mirror whose properties are described in more detail in section 2.4 below. The desired exoscope specifications are that the lateral (axial) resolution is ≤ 1 μm (≤ 3 μm), for a field of view of 100 μm x 100 μm and the working distance ≥ 400 μm. The signal to be collected from the animal tissue would be at ~650 nm (CARS), 500 nm (TPEF) and 400 nm (SHG). These specifications were used as a guide for the optical design of the rest of the optics in the exoscope probe.

Traditionally, gradient index (GRIN) lenses with relatively high numerical apertures (NA) of 0.5 - 0.6 have been preferred in multi-photon microendoscopy applications [6]. This is because of their nearly diffraction-limited image quality, their low cost for off-the-shelf components, their possible miniaturization down to diameters of 0.25 mm, and their simple geometry with plane optical surfaces permitting ease of integration in fiber based endoscopes. However from our optical design analysis, it became clear that the two excitation wavelengths separated by ~ 200 nm in CARS, poses a significant challenge in terms of compensating the longitudinal chromatic aberration in the GRIN lenses. Hence we opted for designing a conventional miniaturized front end objective lens that would perform to the required specification. This is indeed very challenging since a large numerical aperture is required from small diameter optics. The final design consists of multiple lenses that are ~1.8 mm in diameter and have varying prescriptions. Two different glass types, SF4 and FK51 are chosen to compensate for the chromatic aberration at 800 nm and 1040 nm. The effective NA of the front end objective is 0.6 and the field of view is 100 x 100 micron with a working distance of 400 μm. Relay lenses are included in the design in order to image the MEMS mirror on the back aperture of the front end objective with a magnification of 5x.

MEMS based scanning

A two dimensional scanning MEMS mirror (Fraunhofer Institut Photonische Mikrosysteme, Germany) with a diameter of 500 μm is employed for image generation. The device consists of a circular silicon plate in gimbal mounting suspended by a total of four torsional spring bars [7]. The die chip is ~ 2.2 mm x 2.9 mm in size. Independent resonant oscillation of the mirror plate (fast axis) and the frame (slow axis) itself, is set up by applying a high voltage to the comb electrodes adjacent to the mirror and frame. The reflectivity of the mirror plate is enhanced by a thin layer of aluminum. The resonant frequencies of the slow and fast axes are 1.29 kHz and 17 kHz respectively. An optical scan angle of +/-17 degrees along both axes is obtained by applying 50 V (slow axis) and 70 V (fast axis).

MINIATURE OPTICS FABRICATION

Fabrication and assembly

Fig. 2 (a) is a ray-trace diagram of the optical beam as it propagates through the miniature optics and focuses on the sample just past the coverslip, while Fig 2 (b) depicts the computer-aided design of the construction of the stainless steel tube (barrel) into which all of the miniature optics are assembled (BMV Optical, Ottawa, Canada). The fully packaged barrel is ~4.1 cm long and is shown in Fig. 2 (c). A thin glass window seals off the distal end of the barrel thus permitting water immersion.

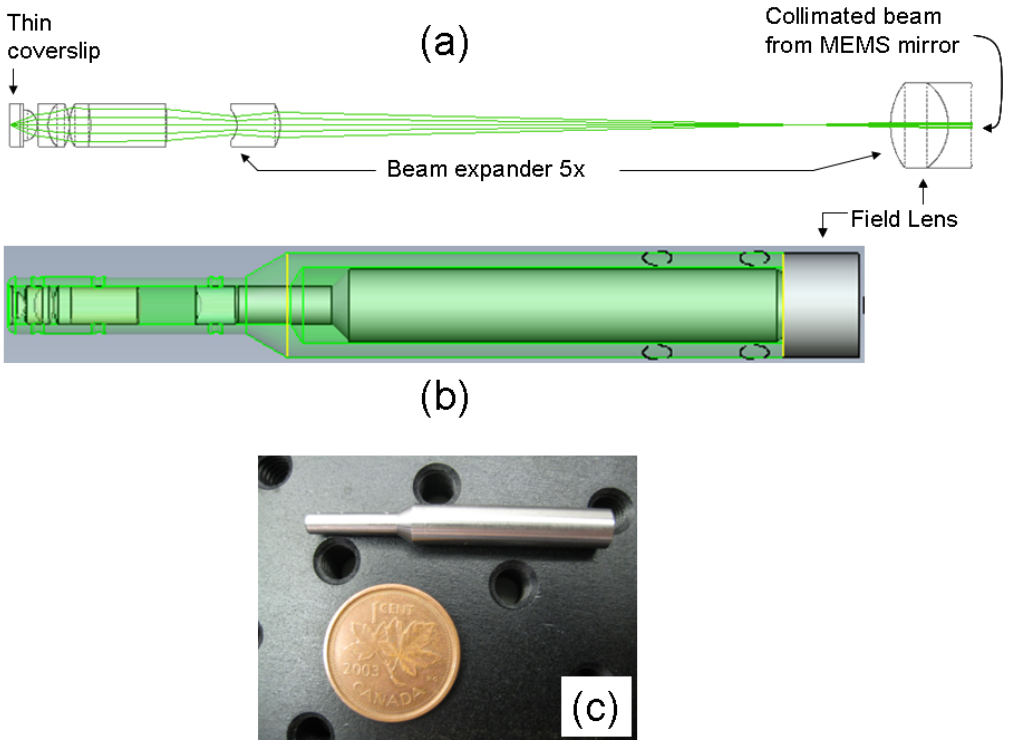

Fig. 2a) Fig. 2 (a) Ray-trace diagram of the optical beam as it enters from the right after the MEMS mirror and is relayed to the miniature focusing optics on the left, through a 5x beam expander assembly including the field lens. (b) Computer-aided-design of the barrel. (c) Photograph of the fully packaged barrel. A penny is included for size comparison.

MINIATURE MICROSCOPE TESTING

Our strategy leading up to the development of a portable miniature epi-CARS/ TPEF/ SHG imaging device involving a MEMS scanner, is to develop and demonstrate new capabilities in individual stages where performance can be experimentally verified. Our testing methodology thus comprises of i) testing the MEMS mirror, ii) testing a benchtop version of the exoscope with the MEMS mirror and the barrel alone and iii) testing the full exoscope after integrated assembly of the body and barrel.

MEMS testing

A custom-built voltage amplifier circuit amplifies the rectangular waveform output from the FPGA(Altera DE2 board) to drive the MEMS oscillations along the fast and slow axes. When high voltage is applied to both axes, a Lissajous pattern is scanned at the sample. We first experimentally measured the resonance curves for the slow and fast axes at 40 V and 70 V, respectively. From this data, we determine the resonant frequencies for the desired optical scan amplitude of +/- 17 degrees. We further fine tune this choice of the slow and fast axis resonant frequencies to provide a full and uniform coverage over a 512 x 512 pixel image. A frame repeat rate of 4 Hz is obtained based on the values of resonant frequencies of 1.336 kHz and 16.99 kHz chosen corresponding to the slow and fast axis, respectively.

Bench top miniature multimodal CARS microscope

We recently reported for the first time our results involving a bench top multimodal miniature CARS microscope [8]. The experimental setup is described in detail in Ref 8 and is illustrated in Fig. 3 below.

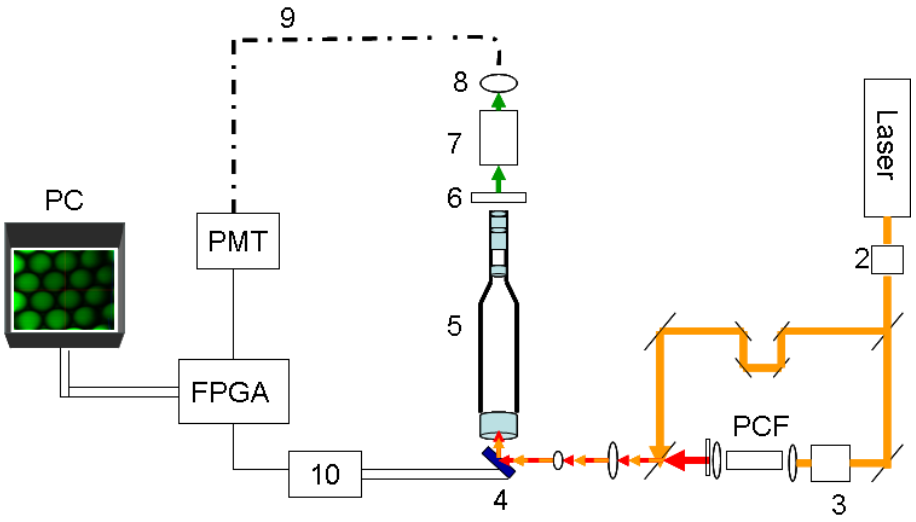

Fig. 3 Bench top miniaturized multimodal CARS microscope. Details of components are as follows: (2) Faraday isolator (3) Prism compressor (4) MEMS mirror (5) Miniature optics inside stainless steel tube (barrel) (6) Sample for imaging (7) microscope air objective (20x) for collecting nonlinear optical signal from sample (8) Lens for coupling light into collection fiber (9) Multimode fiber (10) Voltage Amplifier circuit to amplify electrical signal, for driving the MEMS mirror, provided by the Field Programmable Gate Array (FPGA).

We have successfully demonstrated multimodal ex-vivo imaging of biological tissue samples with the miniature microscope using this bench-top setup. Proof of concept CARS, TPEF and SHG images are shown in Fig. 4. The lateral resolution for the miniature CARS microscope is 1.3 µm and is in good agreement with the design value of 1 µm. The axial resolution was measured to be 12.74 µm. This is larger than the design value of 3 µm and is mainly attributed to residual chromatic aberration inside the miniature objective as well as slight optical misalignment in the beam paths of the bench top microscope system.

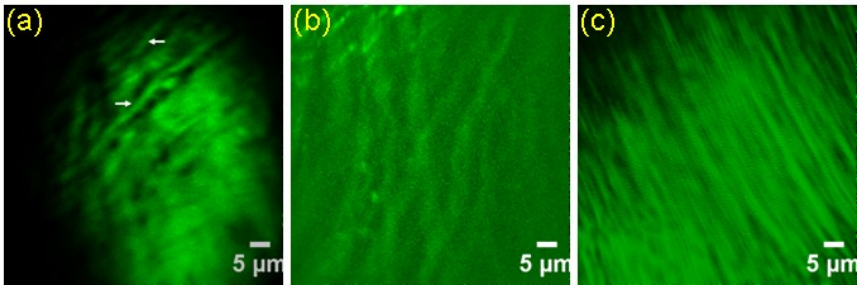

Fig. 4 Multimodal imaging using miniature CARS microscope: the average power at the sample was ~28 mW in the pump beam and ~ 0.8 mW in the Stokes beam. (a) forward - CARS image at a Raman shift of 2845 cm-1 from label free myelin (indicated by arrows) surrounding YFP labeled axons in fixed dorsal roots of mouse. (b) TPEF image of YFP labeled axons at excitation wavelength of 870 nm. (c) SHG image from unlabeled rat tail collagen.

Further integration of the body and barrel into a full exoscope is ongoing. The ability of the exoscope to perform CARS, TPEF and SHG imaging in the epi direction will be tested shortly.

CONCLUSIONS

This paper describes our progress in developing a fiber optic, MEMS-scanning based multimodal miniature microscope for nonlinear optical imaging of the spinal cord in live rat/ mice. The novel design of the multimodal exoscope includes i) a MEMS scanner ii) miniature objective probe and iii) a single femtosecond laser source for generating CARS, TPEF and SHG images. We have demonstrated the functionality of the miniature optics and the MEMS scanning by obtaining proof of concept images of biological samples ex vivo in a bench top set up, in the forward direction. It is well-known that back-scattered forward-CARS signal is the main source of epi-CARS signal detected from thick tissue [9]. Our device is designed for imaging such highly scattering biological tissue and hence demonstrating the functionality of our device for F-CARS imaging is an important milestone towards development of the full exoscope.

We are undertaking the complex task of integration of the MEMS mirror and alignment of miniature optics inside the body, at the present time. The testing of the integrated multimodal exoscope will involve fiber based delivery (and collection) of excitation (and generated nonlinear) light. This will be implemented in the near future. The multimodal miniature, fiber based CARS exoscope will enable serial examinations of the status of the myelin sheath, axons and supporting cells in spinal cord and peripheral nerve over time in the same animal. This imaging modality is expected to provide significant new information on the pathogenesis of demyelinating diseases such as Multiple Sclerosis and Spinal Cord Injury.

ACKNOWLEDGEMENTS

This work was funded by the CIHR – NSERC grant # 87490. We would like to gratefully acknowledge Roger Montcalm, SITE, University of Ottawa for loaning the FPGA (Altera DE2) board. We would like to thank Dr. Ian Powell for help in designing the bench-top setup, and Dr. Ileana Micu and Thomas Kannanayakal for preparing the tissue samples. We would like to thank Prateek Srivastava of RatworX Inc. and Adrian Moica for their technical support in FPGA based control of the MEMS scanners.

REFERENCES

1. Evans, C. L. and Xie, X. S., "Coherent anti-Stokes Raman scattering microscopy: chemical imaging for biology and medicine," Annu. Rev. Anal. Chem. 1, 883-909 (2008).
2. Murugkar, S., Brideau, C., Ridsdale, A., Naji, M., Stys, P. K. and Anis, H. et al., "Coherent anti-Stokes Raman scattering microscopy using photonic crystal fiber with two closely lying zero dispersion wavelengths," Opt. Express, vol. 15 (21), 14028 – 14037 (2007).
3. Liu, J. T. C., Mandella, M. J., Loewke, N. O., Haeberle, H., Ra, Hyejun, Piyawattanametha, W., Solgaard, O., Kino, G. S and Contag, C.H., "Micromirror-scanned dual-axis confocal microscope utilizing a gradient-index relay lens for image guidance during brain surgery," J. Biomedical Optics, vol. 15 (2), 26029-26035 (2010).
4. Tang, S., Jung W., McCormick, D., Xie, T, Su, J., Ahn, Y., Tromberg, B. J. and Chen, Z., "Design and implementation of fiber-based multiphoton endoscopy with microelectromechanical systems scanning," Journal of Biomedical Optics, vol. 14(3), 034005 (2009).
5. Balu, M., Liu, G., Chen, Z., Tromberg, B. and Potma, E. O.,"Fiber delivered probe for efficient CARS imaging of tissues", Opt. Express, vol. 18 (3), 2380 – 2388 (2010).
6. Fu, L. and Gu, M., "Fibre-optic nonlinear optical microscopy and endoscopy", Journal of Microscopy, vol. 226 (3), 195–206 (2007).
7. Scholles, M. , Frommhagen, K., Gerwig, Ch., Knobbe, J., Lakner, H., Schlebusch, D., Schwarzenberg, M., and Vogel, U., "Ultracompact laser projection systems based on two-dimensional resonant microscanning mirrors," J. Micro/ Nanolith. MEMS MOEMS, vol. 7 (2), 021001 (2008).
8. Murugkar, S., Smith, B., Srivastava, P., Moica, A., Naji, M., Brideau, C., Stys, P. K., and Anis, H., "Miniaturized multimodal CARS microscope based on MEMS scanning and a single laser source," Opt. Express, Vol. 18, Issue 23, pp. 23796-23804 (2010).
9. Evans, C. L., Potma, E. O., Puoris'haag, M., Cote, D., Lin, C., and Xie, X. S., "Chemical imaging of tissue in vivo with video-rate coherent anti-Stokes Raman scattering (CARS) microscopy," Proc. Natl. Acad. Sci. USA 102, 16807-16812 (2005).

3.5.6. A novel multimodal CARS miniaturized microscope

Brett Smith*, Majid Naji*, Sangeeta Murugkar*, Craig Brideau**, Peter Stys** and Hanan Anis*

*School of information Technology and Engineering (SITE), University of Ottawa, Ottawa, Ontario, K1N 6N5
** Department of Clinical Neurosciences, Hotchkiss Brain Institute, University of Calgary, AB, T2N 4N1, Canada

Abstract

We demonstrate the operation of a novel portable, fibre delivery miniaturized multimodal microscope (exoscope) for coherent anti-Stokes Raman scattering and two-photon excitation fluorescence imaging using a single Ti:sapphire femtosecond pulsed laser. This microscope features a large mode area photonic crystal fibre for light delivery, as well as biaxial scanning microelectromechanical system mirrors and custom miniaturized optics corrected for chromatic aberration. We demonstrate imaging of polystyrene beads, two photon excitation fluorescence beads in both forward and backward (epi) directions. This miniaturized exoscope will enable in-vivo imaging.

Key words: Coherent anti-Stokes Raman scattering, two-photon excitation fluorescence imaging, microelectromechanical scanning mirrors, large mode area core photonics crystal fibre, miniaturized multimodal microscope.

1. Introduction

CARS microscopy has evolved over the past decade as a powerful label-free imaging modality based on intrinsic vibrational contrast [1]. A wide variety of important applications involving CARS microscopy have been demonstrated. These range from imaging lipid droplet biology [2], imaging axonal myelin in spinal cord injuries and demyelinating diseases [3], identifying obesity related risks in cancer [4] and atherosclerosis [5] and the rapid detection of pathogens [6]. Moreover, it has been clearly shown that there is a tremendous benefit in combining CARS with other imaging modalities such as TPEF and SHG in a multimodal imaging and spectroscopy platform to obtain a complete picture of the health of the biological tissue [3–5, 7]. However, in order to truly extend the benefits of multimodal CARS microscopy to human health, development of a multimodal CARS probe in the form of an endoscope or miniaturized hand held microscope is essential. In fact, significant progress has been made in the development of TPEF and SHG imaging endoscopes and miniaturized microscopes for in vivo imaging applications [8–13]. For CARS microscopy which involves a pump and Stokes beam for excitation of the nonlinear optical signal, progress towards fiber based endoscopy has been quite slow [14–16].

In this paper we demonstrate a novel portable hand-held fibre-delivered multimodal CARS microscope based on our previously reported bench-top miniaturized microscope design [17, 18]. In this paper, we integrate the miniaturized optics, the MEMS mirror and using a large mode area photonic crystal fibre (LMA20) for delivering the Stokes and pump beams to the sample as well as multimode fiber for signal collection. The use of a portable hand-held miniature multimodal microscope in conjunction with a single femtosecond laser as the light source paves the way for possible future clinical use.

2. Methodology

2.1: Multimodal CARS Exoscope setup

Fig.1 shows the multimodal CARS exoscope setup that consists of a Ti:Sapphire laser (1) that generates 76 fs pulses at 800 nm with ~80 MHz repetition rate. A Faraday isolator (2) was used to prevent laser back reflection. A half wave plate (3) followed by a beam splitter (4) was used to control the laser power distribution. A prism compressor (5) was used to control the pulse width and chirp of the fs laser pulses in the Stokes arm. By using an X40 (6)

Newport microscope objective lens the laser beam was coupled to a 2ZDW PCF fibre (7) (Crystal Fibre, NL-1.4-775-945). The generated supercontinuum (SC) was collimated by an aspheric lens (8), f = 5mm (Thorlabs, Newton, NJ), and then filtered by a band pass filter (9) with 1040 nm central wavelength and 60 nm FWHM (Chroma technologies, Brattleboro VT).
In the pump arm, the 800 nm femtosecond laser beam was negatively chirped, using a grating compressor (10). Both beams (Stokes and pump) were spatially overlapped using a short pass dichroic mirror (11) and then by using a low numerical aperture (NA) and magnification microscope objective lens (12) (Newport, X5 NA = 0.05), both beams were coupled to a large mode area core photonics crystal fibre (13) (Crystal fibre, LMA20). The LMA20 was then mechanically coupled to the exoscope body (14) and subsequently the light was passed through the exoscope's optical head: the barrel (water immersion, working distance= 400 µm, NA = 0.6) . The generated CARS signal was collected either in forward direction by using an 40X (15), NA=0.8 water immersionOlympus objective lens or in the backward direction using the exoscope's optical head and then coupled to a silica multimode fibre (16), passing a 660 nm short band pass filter (17) and then coupled to the photomultiplier tube (18) (PMT, Hamamatsu H7422P-40). The generated signal was amplified and passed through a discriminator and Field Programmable Gate Array (19) (FPGA) and sent to a computer for image reconstruction.

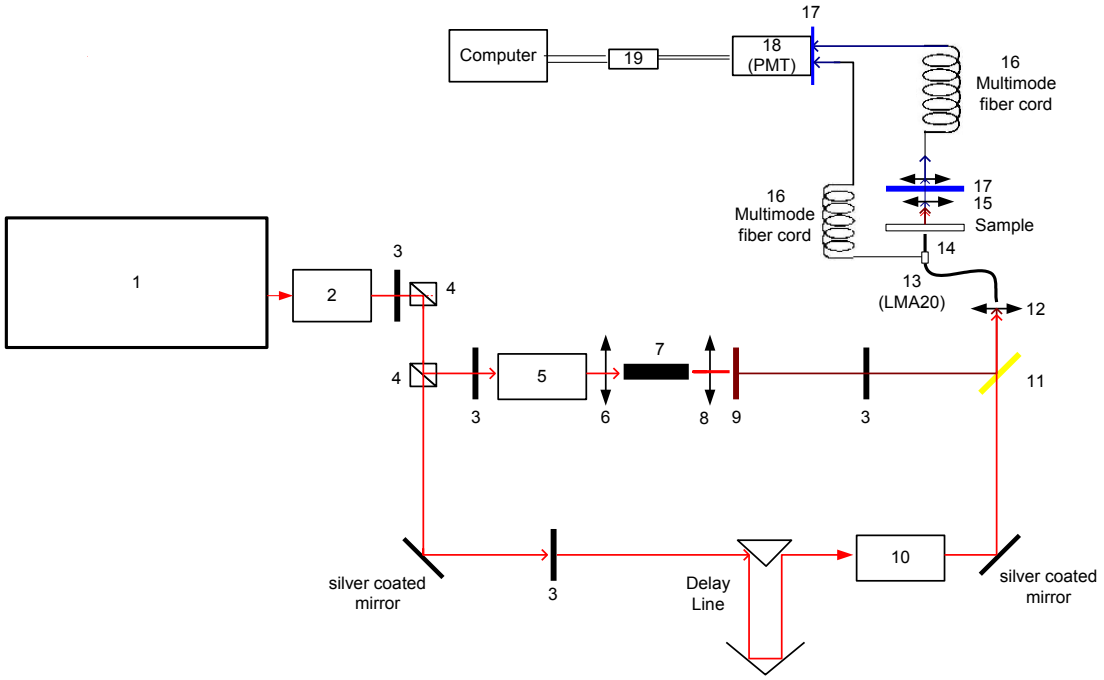

Figure 1: Exoscope setup.

A large mode area photonic crystal fibre (LMA20) was used to deliver both pump and Stokes beams. The LMA20 operates in the single mode regime for both the pump and Stokes and has relatively low loss for both wavelengths. Moreover, as it is a large mode area fibre, the nonlinear effects in the fibre are significantly decreased. Dispersion compensation of both the pump and stokes would ensure maximum nonlinear signal generation at the sample. Since both beams would undergo different pulse broadening effects, two discrete pre-compensators should be used. Unfortunately the power levels of the Stokes beam available does not allow for such a high loss component. However, the available pump power is high, and temporal compensation resulting in a 100 fs pulse at the sample was possible. As the CARS signal intensity is proportional to the square of pump intensity, compensation for the Stokes beam was not critical and a reasonable CARS signal was still attainable.

Fig. 2 shows the details of the exoscope's body: The excitation beams out of LMA20 were incident upon a collimation lens (1) followed by a folding mirror (2). This additional reflection was necessary as the scanning mechanism itself is reflection-based and the design required that the input and output beams be parallel. The excitation light was then incident upon the MEMS scanning mirror (3) (Fraunhofer Institut Photonische

Mikrosysteme, Germany). The MEMS mirror is a key component that enabled the miniaturization of the probe. The electrostatically driven mirror's independent axes were scanned at mechanical frequencies of ~2kHz and ~16kHz resulting in a Lissajous scanned pattern. The beams then passed through the dichroic beam splitter (4) (BMV Optical Technologies, Nepean, Ontario). When the probe is used to collect light in the epi direction, the dichroic beam splitter provides discrete paths for the excitation and emission wavelengths. This is accomplished by means of highly customized multi-layered coatings. This component will also eliminate any unwanted four wave mixing generated within the delivery fibre. A 5X beam expansion telescope is the first element located in the barrel (5). This is to ensure the filling of the back aperture of the upcoming focusing optics. After passing through the remainder of the optics and finally focusing at the sample, an area of 100 μm by 100 μm is scanned at a working distance of greater than 400 μm. The generated blue-shifted photons are then collected in the forward or epi direction. If the desired collection direction is backward (epi), the photons pass through the barrel and are reflected off of the dichroic and focused into the multimode collection fibre. If the collection direction is forward, standard microscope objectives and filters can be used.

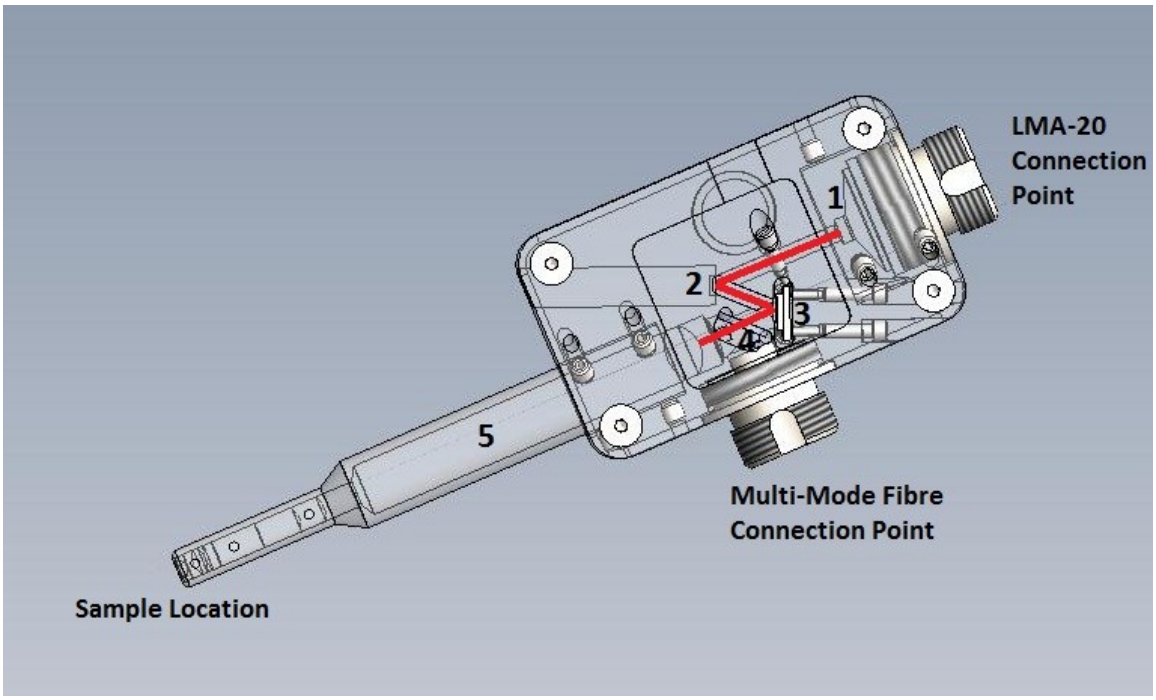

Figure 2: Mechanical drawing of the exoscope body.

The barrel is ~4.1 cm long and 5.5 mm (outer diameter) at the proximal end and 3.0 mm (outer diameter) at the distal end to allow in-vivo spinal cord or other tissue imaging.

3. Exoscope testing and demonstration:

Our exoscope testing method consisted of three stages: I) testing the MEMS mirror, II) testing a benchtop version of the exoscope with the MEMS mirror and barrel only, performing imaging in forward direction and III) testing the full exoscope after integrating exoscope body and barrel using a delivery fibre, and acquiring photons in the forward and backward direction. References [17] and [18] reported the details of the tests completed in steps I and II while we focus here on step III.

3.1: Exoscope assembly

After performing tests on components individually including the MEMS mirror, the collimation lens, the folding mirror and dichroic beam splitter, these components were all mounted inside the exoscope body. When proper

placement and function of all of these components were confirmed, the independently tested barrel was then added and precisely aligned.

The femtosecond laser pulse was pre-compensated (negative chirp) so that the pulse width of the pump beam out of LMA20 was 100 fs. By using a United States Air Force (USAF) (Edmund Optics) target, the resolving power of the exoscope in the forward direction was determined. As is shown in Fig. 3a the 2.2 µm features of the smallest element in the smallest group are distinct. The sharp edges of the calibration bars are seen in the intensity profile plotted in Fig. 3d.
By using spin coated TPEF sensitive 1µm diameter fluorescent microspheres (Polysciences Inc., PA, USA), lateral resolution of the exoscope in the epi direction was investigated at 800 nm. By plotting the intensity profile (Fig. 3e) of an individual bead from Fig. 3b and fitting a Gaussian curve to the plot and taking an average value of the full width half maximum (FWHM), the lateral resolution was determined to be less than 1 µm (~0.8 µm). This fits well within the 1 µm design value. When compared to the images obtained from the benchtop free space delivered probe [17], a clear improvement in the resolving power is seen.
Finally the epi and forward CARS capabilities of the exoscope were demonstrated. The epi axial resolution of exoscope was measured by using spin coated 2 µm and 750 nm polystyrene beads. While the 2 µm beads seen in Fig. 2c were individually resolvable we were not able to observe single 750 nm beads. This was not an alarming result as the probe was not designed to resolve features of size less than 1 µm. The 2 µm beads were used for axial resolution measurements by taking images separated by 1 µm along the vertical z-axis. The peak value of the intensity profile of a single bead was taken for each image in the z-stack and these values plotted, shown in Fig. 3f. The FWHM of the plot was taken, and the axial resolution was determined to be 8 µm. Using the best focused image from the z stack, a lateral resolution of 1.06 µm was found. The axial resolution is still larger than the designed value of 3 µm, but this is most likely due to residual chromatic aberrations inside the miniature objective [19]. The axial resolution value obtained is an improvement on the bench top free space design [17], due to the internal integration of the scanner and associated optics.

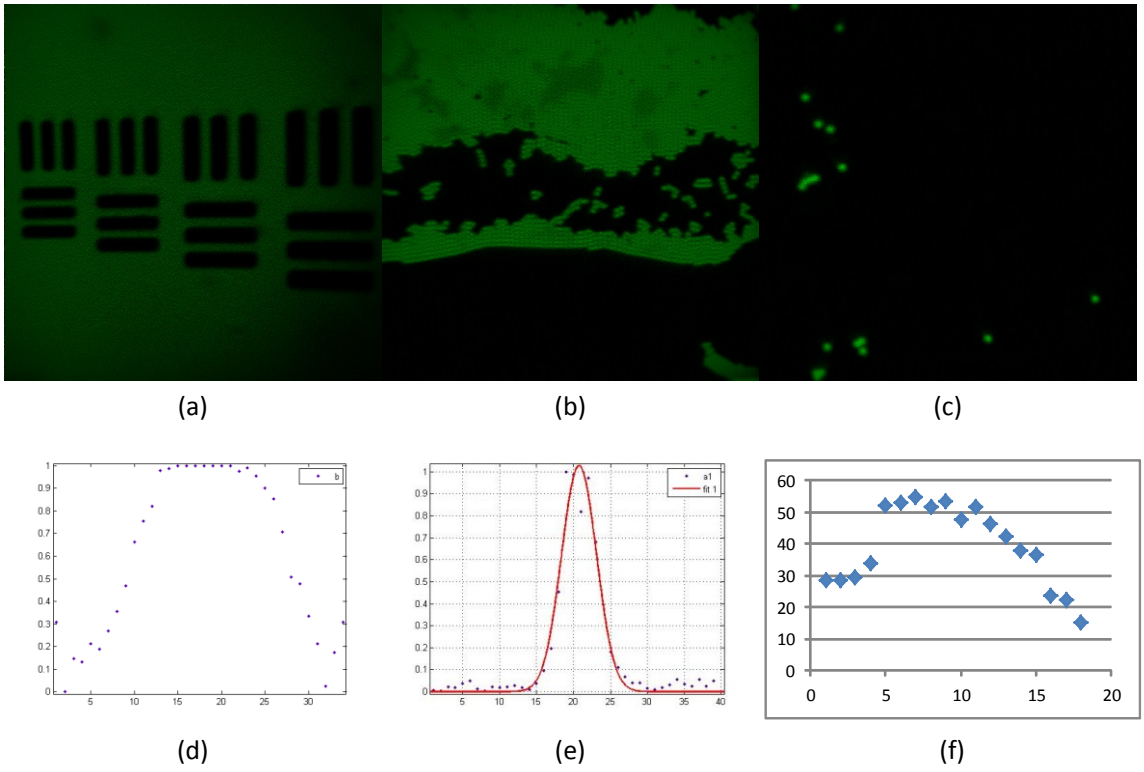

Figure 3: (a) USAF Target (b) 1um TPEF Beads (c) 2um PS Beads (d) USAF Target Intensity Profile (e) 1µm TPEF Beads Lateral Intensity Profile (f) 2 µm PS Beads Axial Profile. The average powers of the pump and Stokes at the sample were ~16 mW and 0.75 mW respectively.

As can be seen in the images from Fig. 3, there was not a significant background signal despite the presence of a weak four-wave mixing (FWM) signal out of the delivery fibre. This should have caused a detectable non resonant background noise in our CARS exoscope, but since the excitation and collection paths are physically distinct the dichroic mirror inside of exoscope body successfully transmitted only the resonant nonlinear signal. The unwanted four-wave mixing inside of the LMA20 fibre did not affect the integrity of the CARS signal in our case.

4. Conclusion

This paper presents our progress in developing a portable hand-held multimodal miniaturized microscope using a single femtosecond laser source, a photonic crystal fiber for delivery and MEMS mirror for scanning. We have demonstrated the functionality of the completed miniaturized exoscope by obtaining proof of concept images of TPEF beads, as well as polystyrene beads in the both forward and epi directions. These simple images are the first steps towards ex-vivo (and ultimately in-vivo) biological imaging. The use of a portable hand-held miniature multimodal microscope in conjunction with a single femtosecond laser as the light source paves the way for possible future clinical use. A femtosecond fiber laser such as in Ref. [20] could be used to replace the tabletop Ti:sapphire laser making the entire setup compact and amenable to translation to the clinic

.

6. Acknowledgement

This work was funded by the CIHR – NSERC grant # 87490.

References

[1] C. L. Evans, and X. S. Xie, "Coherent anti-stokes Raman scattering microscopy: chemical imaging for biology and medicine," Annu Rev Anal Chem (Palo Alto Calif) 1(1), 883–909 (2008).
[2] X. L. Nan, J. X. Cheng, and X. S. Xie, "Vibrational imaging of lipid droplets in live fibroblast cells with coherent anti-Stokes Raman scattering microscopy," J. Lipid Res. 44(11), 2202–2208 (2003).
[3] T. B. Huff, Y. Shi, Y. Fu, H. Wang, and J. X. Cheng, "Multimodal nonlinear optical microscopy and applications to central nervous system," IEEE J. Sel. Top. Quantum Electron. 14(1), 4–9 (2008).
[4] T. T. Le, C. W. Rehrer, T. B. Huff, M. B. Nichols, I. G. Camarillo, and J. X. Cheng, "Nonlinear optical imaging to evaluate the impact of obesity on mammary gland and tumor stroma," Mol. Imaging 6(3), 205–211 (2007).
[5] T. T. Le, I. M. Langohr, M. J. Locker, M. Sturek, and J. X. Cheng, "Label-free molecular imaging of atherosclerotic lesions using multimodal nonlinear optical microscopy," J. Biomed. Opt. 12(5), 054007 (2007).
[6] S. Murugkar, C. L. Evans, X. S. Xie, and H. Anis, "Chemically specific imaging of cryptosporidium oocysts using coherent anti-Stokes Raman scattering (CARS) microscopy," J. Microsc. 233(2), 244–250 (2009).
[7] H. Chen, H. Wang, M. N. Slipchenko, Y. Jung, Y. Shi, J. Zhu, K. K. Buhman, and J. X. Cheng, "A multimodal platform for nonlinear optical microscopy and microspectroscopy," Opt. Express 17(3), 1282–1290 (2009).
[8] F. Helmchen, M. S. Fee, D. W. Tank, and W. Denk, "A miniature head-mounted two-photon microscope. high-resolution brain imaging in freely moving animals," Neuron 31(6), 903–912 (2001).
[9] H. Bao, J. Allen, R. Pattie, R. Vance, and M. Gu, "Fast handheld two-photon fluorescence microendoscope with a 475 μm x 475 μm field of view for in vivo imaging," Opt. Lett. 33(12), 1333–1335 (2008).
[10] C. J. Engelbrecht, R. S. Johnston, E. J. Seibel, and F. Helmchen, "Ultra-compact fiber-optic two-photon microscope for functional fluorescence imaging in vivo," Opt. Express 16(8), 5556–5564 (2008).
[11] W. Piyawattanametha, E. D. Cocker, L. D. Burns, R. P. Barretto, J. C. Jung, H. Ra, O. Solgaard, and M. J. Schnitzer, "In vivo brain imaging using a portable 2.9 g two-photon microscope based on a microelectromechanical systems scanning mirror," Opt. Lett. 34(15), 2309–2311 (2009).
[12] J. T. C. Liu, M. J. Mandella, N. O. Loewke, H. Haeberle, H. Ra, W. Piyawattanametha, O. Solgaard, G. S. Kino, and C. H. Contag, "Micromirror-scanned dual-axis confocal microscope utilizing a gradient-index relay lens for image guidance during brain surgery," J. Biomed. Opt. 15(2), 026029 (2010).
[13] H. Bao, A. Boussioutas, R. Jeremy, S. Russell, and M. Gu, "Second harmonic generation imaging via nonlinear endomicroscopy," Opt. Express 18(2), 1255–1260 (2010).
[14] F. Légaré, C. L. Evans, F. Ganikhanov, and X. S. Xie, "Towards CARS Endoscopy," Opt. Express 14(10), 4427–4432 (2006).

[15] H. Wang, T. B. Huff, and J. X. Cheng, "Coherent anti-Stokes Raman scattering imaging with a laser source delivered by a photonic crystal fiber," Opt. Lett. 31(10), 1417–1419 (2006).
[16] M. Balu, G. Liu, Z. Chen, B. J. Tromberg, and E. O. Potma, "Fiber delivered probe for efficient CARS imaging of tissues," Opt. Express 18(3), 2380–2388 (2010).
[17] Sangeeta Murugkar , Brett Smith , Majid Naji , Craig Brideau , Peter Stys and Hanan Anis " Development of a micromirror-scanned multimodal CARS miniaturized microscope for the in vivo study of spinal cord disorders", Proc. of SPIE Vol. 7903, 79031D , 2011
[18] Sangeeta Murugkar et al, "Miniaturized multimodal CARS microscope based on MEMS scanning and a single laser source", Opt. Express, Vol.18, Issue 23, P.23796, Oct. 2010
[19] H. Wang, T. B. Huff, Y. Fu, K. Y. Jia, and J. X. Cheng, "Increasing the imaging depth of coherent anti-Stokes Raman scattering microscopy with a miniature microscope objective," Opt. Lett. 32(15), 2212–2214 (2007).
[20] A. Chong, J. Buckley, W. Renninger, and F. Wise, "All-normal-dispersion femtosecond fiber laser," Opt. Express 14(21), 10095–10100 (2006).

3.5.7. Portable, miniaturized, fibre delivered, multimodal CARS exoscope

Brett Smith,[1]* Majid Naji,[1] Sangeeta Murugkar,[2] Emilio Alarcon,[3] Craig Brideau,[4] Peter Stys,[4] and Hanan Anis[1]

[1]School of Electrical Engineering and Computer Science (EECS), University of Ottawa, 800 King Edward, P.O. Box 450 Stn A, Ottawa, Ontario, K1N 6N5, Canada
[2]Department of Physics, University of Ottawa, 150 Louis Pasteur, Ottawa ON Canada, K1N 6N5, Canada
[3]Department of Chemistry, University of Ottawa, 10 Marie Curie, Ottawa ON Canada, K1N 6N5, Canada
[4]Department of Clinical Neurosciences, Hotchkiss Brain Institute, University of Calgary, AB, T2N 4N1, Canada

Abstract: We demonstrate for the first time, a portable multimodal coherent anti-Stokes Raman scattering microscope (exoscope) for minimally invasive in-vivo imaging of tissues. This device is based around a micro-electromechanical system scanning mirror and miniaturized optics with light delivery accomplished by a photonic crystal fibre. A single Ti:sapphire femtosecond pulsed laser is used as the light source to produce CARS, two photon excitation fluorescence and second harmonic generation images. The high resolution and distortion-free images obtained from various resolution and bio-samples, particularly in backward direction (epi) successfully demonstrate proof of concept, and pave the path towards future non or minimally-invasive in vivo imaging.

OCIS codes: (170.3880) Medical and biological imaging; (180.4315) Nonlinear microscopy; (020.4180) Multiphoton processes; (230.4685) Optical microelectromechanical devices.

References and links

1. C. L. Evans and X. S. Xie, "Coherent anti-Stokes Raman scattering microscopy: chemical imaging for biology and medicine," Annu Rev Anal Chem (Palo Alto Calif) **1**(1), 883–909 (2008).
2. T. T. Le, T. B. Huff, and J. X. Cheng, "Coherent anti-Stokes Raman scattering imaging of lipids in cancer metastasis," BMC Cancer 9:42 (2009). BMC Cancer **9**(1), 42 (2009), doi:10.1186/1471–2407–9-42.
3. E. Kang, H. Wang, I. K. Kwon, J. Robinson, K. Park, and J. X. Cheng, "In situ visualization of paclitaxel distribution and release by coherent anti-Stokes Raman scattering microscopy," Anal. Chem. **78**(23), 8036–8043 (2006).
4. X. Nan, J. X. Cheng, and X. S. Xie, "Vibrational imaging of lipid droplets in live fibroblast cells with coherent anti-Stokes Raman scattering microscopy," J. Lipid Res. **44**(11), 2202–2208 (2003).
5. Y. Fu, T. B. Huff, H. W. Wang, H. Wang, and J. X. Cheng, "Ex vivo and in vivo imaging of myelin fibers in mouse brain by coherent anti-Stokes Raman scattering microscopy," Opt. Express **16**(24), 19396–19409 (2008).
6. Y. Fu, H. Wang, T. B. Huff, R. Shi, and J. X. Cheng, "Coherent anti-Stokes Raman scattering imaging of myelin degradation reveals a calcium-dependent pathway in lyso-PtdCho-induced demyelination," J. Neurosci. Res. **85**(13), 2870–2881 (2007).
7. H. A. Rinia, M. Bonn, E. M. Vartiainen, C. B. Schaffer, and M. Müller, "Spectroscopic analysis of the oxygenation state of hemoglobin using coherent anti-Stokes Raman scattering," J. Biomed. Opt. **11**(5), 050502-1– 050502-3 (2006).
8. +T. T. Le, I. M. Langohr, M. J. Locker, M. Sturek and J. X. Cheng, "Label-free molecular imaging of atherosclerotic lesions using multimodal nonlinear optical microscopy," J. of Biomedical Opt. **12** (5), 054007–1–054007–10 (2007).
9. Y. M. Wu, H. C. Chen, W. T. Chang, J. W. Jhan, H. L. Lin, and I. Liau, "Quantitative assessment of hepatic fat of intact liver tissues with coherent anti-Stokes Raman scattering microscopy," Anal. Chem. **81**(4), 1496–1504 (2009).
10. H. G. Breunig, M. Weinigel, R. Bückle, M. Kellner-Höfer, J. Lademann, M. E. Darvin, W. Sterry, and K. König, "Clinical coherent anti-Stokes Raman scattering and multiphoton tomography of human skin with a femtosecond laser and photonic crystal fiber," Laser Phys. Lett. **10**(2), 1–5 (2013).
11. A. Uchugonova, M. Lessel, S. Nietzsche, C. Zeitz, K. Jacobs, C. Lemke, and K. König, "Nanosurgery of cells and chromosomes using near-infrared twelve-femtosecond laser pulses," J. Biomed. Opt. **17**(10), 101502 (2012).

12. H. Chen, H. Wang, M. N. Slipchenko, Y. Jung, Y. Shi, J. Zhu, K. K. Buhman, and J. X. Cheng, "A multimodal platform for nonlinear optical microscopy and microspectroscopy," Opt. Express **17**(3), 1282–1290 (2009).
13. F. Helmchen, M. S. Fee, D. W. Tank, and W. Denk, "A miniature head-mounted two-photon microscope. high-resolution brain imaging in freely moving animals," Neuron **31**(6), 903–912 (2001).
14. H. Bao, J. Allen, R. Pattie, R. Vance, and M. Gu, "Fast handheld two-photon fluorescence microendoscope with a 475 microm x 475 microm field of view for in vivo imaging," Opt. Lett. **33**(12), 1333–1335 (2008).
15. C. J. Engelbrecht, R. S. Johnston, E. J. Seibel, and F. Helmchen, "Ultra-compact fiber-optic two-photon microscope for functional fluorescence imaging in vivo," Opt. Express **16**(8), 5556–5564 (2008).
16. W. Piyawattanametha, E. D. Cocker, L. D. Burns, R. P. Barretto, J. C. Jung, H. Ra, O. Solgaard, and M. J. Schnitzer, "In vivo brain imaging using a portable 2.9 g two-photon microscope based on a microelectromechanical systems scanning mirror," Opt. Lett. **34**(15), 2309–2311 (2009).
17. J. T. C. Liu, M. J. Mandella, N. O. Loewke, H. Haeberle, H. Ra, W. Piyawattanametha, O. Solgaard, G. S. Kino, and C. H. Contag, "Micromirror-scanned dual-axis confocal microscope utilizing a gradient-index relay lens for image guidance during brain surgery," J. Biomed. Opt. **15**(2), 026029 (2010).
18. H. Bao, A. Boussioutas, R. Jeremy, S. Russell, and M. Gu, "Second harmonic generation imaging via nonlinear endomicroscopy," Opt. Express **18**(2), 1255–1260 (2010).
19. F. Légaré, C. L. Evans, F. Ganikhanov, and X. S. Xie, "Towards CARS Endoscopy," Opt. Express **14**(10), 4427–4432 (2006).
20. F. Knorr, D. R. Yankelevich, J. Liu, S. Wachsmann-Hogiu, and L. Marcu, "Two-photon excited fluorescence lifetime measurements through a double-clad photonic crystal fiber for tissue micro-endoscopy," J Biophotonics **5**(1), 14–19 (2012).
21. D. R. Rivera, C. M. Brown, D. G. Ouzounov, I. Pavlova, D. Kobat, W. W. Webb, and C. Xu, "Compact and flexible raster scanning multiphoton endoscope capable of imaging unstained tissue," Proc. Natl. Acad. Sci. U.S.A. **108**(43), 17598–17603 (2011).
22. M. Weinigel, H. G. Breunig, P. Fischer, M. Kellner-Höfer, R. Bückle, and K. König, "Compact clinical high-NA multiphoton endoscopy," Proc. SPIE **8217**, 821706, 821706-8 (2012), doi:10.1117/12.908755.
23. H. Wang, T. B. Huff, and J. X. Cheng, "Coherent anti-Stokes Raman scattering imaging with a laser source delivered by a photonic crystal fiber," Opt. Lett. **31**(10), 1417–1419 (2006).
24. M. Balu, G. Liu, Z. Chen, B. J. Tromberg, and E. O. Potma, "Fiber delivered probe for efficient CARS imaging of tissues," Opt. Express **18**(3), 2380–2388 (2010).
25. P. S. Hsu, A. K. Patnaik, J. R. Gord, T. R. Meyer, W. D. Kulatilaka, and S. Roy, "Investigation of optical fibers for coherent anti-Stokes Raman scattering (CARS) spectroscopy in reacting flows," Exp. Fluids **49**(4), 969–984 (2010).
26. P. S. Hsu, W. D. Kulatilaka, J. R. Gord and S. Roy, "Single-shot thermometry using fiber-based picosecond coherent anti-Stokes Raman scattering (CARS) spectroscopy," J. Raman Spectro. DOI 10.1002/jrs.4280 (2013).
27. Z. Wang, L. Gao, P. Luo, Y. Yang, A. A. Hammoudi, K. K. Wong, and S. T. C. Wong, "Use of multimode optical fibers for fiber-based coherent anti-Stokes Raman scattering microendoscopy imaging," Opt. Express **19**(9), 7960–7970 (2011).
28. B. G. Saar, R. S. Johnston, C. W. Freudiger, X. S. Xie, and E. J. Seibel, "Coherent Raman scanning fiber endoscopy," Opt. Lett. **36**(13), 2396–2398 (2011).
29. S. Murugkar, B. Smith, P. Srivastava, A. Moica, M. Naji, C. Brideau, P. K. Stys, and H. Anis, "Miniaturized multimodal CARS microscope based on MEMS scanning and a single laser source," Opt. Express **18**(23), 23796–23804 (2010).
30. A. F. Pegoraro, A. Ridsdale, D. J. Moffatt, J. P. Pezacki, B. K. Thomas, L. Fu, L. Dong, M. E. Fermann, and A. Stolow, "All-fiber CARS microscopy of live cells," Opt. Express **17**(23), 20700–20706 (2009).
31. S. Murugkar, C. Brideau, A. Ridsdale, M. Naji, P. K. Stys, and H. Anis, "Coherent anti-Stokes Raman scattering microscopy using photonic crystal fiber with two closely lying zero dispersion wavelengths," Opt. Express **15**(21), 14028–14037 (2007).
32. A. F. Pegoraro, A. D. Slepkov, A. Risdale, D. J. Moffatt and A. Stolow, "Hyperspectral multimodal CARS microscopy in the fingerprint region," J. Biophot. doi: 10.1002/jbio.201200171 (2012).
33. K. J. Bock, H. E. Kotb, M. A. Abdelaim, and H. Anis, "Increasing energy in an ytterbium femtosecond fiber laser with a longer gain medium and lower doping," Proc. SPIE **8237**, 823731-1–823731-7 (2012), doi:10.1117/12.908886.

1. Introduction

As a label-free imaging modality coherent anti-Stokes Raman scattering (CARS) has proven over the last decade to be a crucial diagnostic tool within the vibrational spectroscopic imaging domain [1]. While CARS microscopy has been demonstrated in preliminary research performed in many fields including cancer identification [2], drug therapy selection [3], biological lipid droplet imaging [4], myelinated axon structure [5], spinal cord injuries and demyelination [6], determining the oxygenation state of blood within individual vessels [7], arterial atherosclerosis detection [8], determination of hepatic fat content of liver tissue [9], its expense, due to high equipment costs, and the need for highly qualified personnel for operation has limited its propagation into mainstream medicine. Based on this broad list of applications, it is apparent that the functionality of CARS is unique, and its proliferation into mainstream medicine could most certainly benefit from the development of a cost-effective, miniaturized and portable, imaging platform [10, 11].

The CARS process is based on the fundamentals of Raman scattered photons. However, Raman scattering is inherently weak; typical photon conversion efficiencies for Raman are lower than 1 in every 10^{18} [1]. CARS exploits the generation of inelastically scattered photons by stimulating this typically spontaneous event. This is

accomplished through the interaction of three input photons: a pump (e.g. at 800 nm), a Stokes (e.g. at 1030 nm) and a probe (e.g. at 800 nm) that together generate the anti-Stokes photons (since the pump and the probe are the same beam in degenerate CARS, they will be referred to as simply the pump). The difference between the pump and Stokes wavelengths can be tuned to resonantly excite and stimulate the emission of anti-Stokes photons, allowing the CARS process to monitor the presence of specific molecular bond energies. In the case of the previously mentioned wavelengths, the CH-rich lipid region is strongly excited in a resonant manner.

When CARS is combined with other nonlinear imaging and spectroscopic techniques such as two photon excitation fluorescence (TPEF) and second harmonic generation (SHG), the utility of the acquired images greatly increases; considerable chemical information can be extracted from biological tissues [5, 8, 12]. Imaging these tissues ex vivo is useful but in order to make nonlinear imaging amenable to clinical use, endoscopic variants of current microscopes must be developed. Currently, extensive research has been performed on integrating fibre-delivered SHG and TPEF probes [13-22] but fibre-delivered CARS endoscopic research hasn't been as prolific [22-24]. The difficulty with CARS as an imaging modality is that it is absolutely critical that the pump and Stokes beams overlap both temporally and spatially at the sample. Without this temporal and spatial overlap, there is no vibrational resonance created within the bonds of the molecule being probed, as the pump and Stokes photons cannot interact in tandem with the molecule. This fact causes many complications. First, a pair of ultrashort pulses separated by more than 200 nm must retain high peak powers and temporally overlap at the sample, overcoming dispersions induced by the delivery fibre. Second, size-constrained focusing optics that have little chromatic aberrations to ensure spatial overlap of both pump and Stokes beams at the sample, while maintaining high CARS resolution must be implemented. Lastly, the fibre delivery of a pair of ultrashort pulses can produce unwanted nonresonant effects including four-wave mixing (FWM) within a delivery fibre which can overwhelm any sample-generated CARS signals.

The vast majority of endoscopic CARS research has centred on the delivery of femtosecond and picosecond light. Significant work characterizing delivery fibres has been performed analyzing temporal and spectral characteristics, beam quality, damage thresholds and efficiencies of various fibres types, including single-mode fibres, fibre bundles and PCFs [19, 24, 25, 26]. Fibre based investigations have also been performed reducing unwanted four-wave mixing that is generated within the delivery fibres, through means of polarization control [27]. This work represents significant milestones in CARS endoscopy, although macro optics, or galvanometric scanners are used. While there has been recent research into piezo tube fibre scanning probes in conjunction with gradient index (GRIN) lenses for CARS and stimulated Raman scattering [28], the high costs associated with the development of a custom GRIN lens led to the use of a MEMS scanner. The high driving frequencies of a micro-electromechanical system (MEMS) mirror still allows for video rate imaging. To the best of our knowledge, we have developed the first MEMS scanner based portable CARS miniaturized microscope with the unique capability of collecting CARS, SHG, and TPEF photons in the epi direction, with the entire exoscope demonstrated in Fig. 1(a). Our previously published work [29] was based on a bench-top setup that neither included fibre delivery, nor the integration of the MEMS scanner into a miniaturized portable platform. In this paper, we demonstrate for the first time, an optical probe that not only allows capture of nonlinearly generated photons in the epi direction through an exoscope-connected multi-mode fibre, but in addition offers device portability. Moreover, the laser source for this exoscope is based on a single femtosecond laser, which reduces the required footprint for the entire system. Integrating this microscope with an entirely fibre based CARS system [30] would further improve the robustness and compactness of the device, allowing real-time bedside, nonlinear imaging and patient diagnostics.

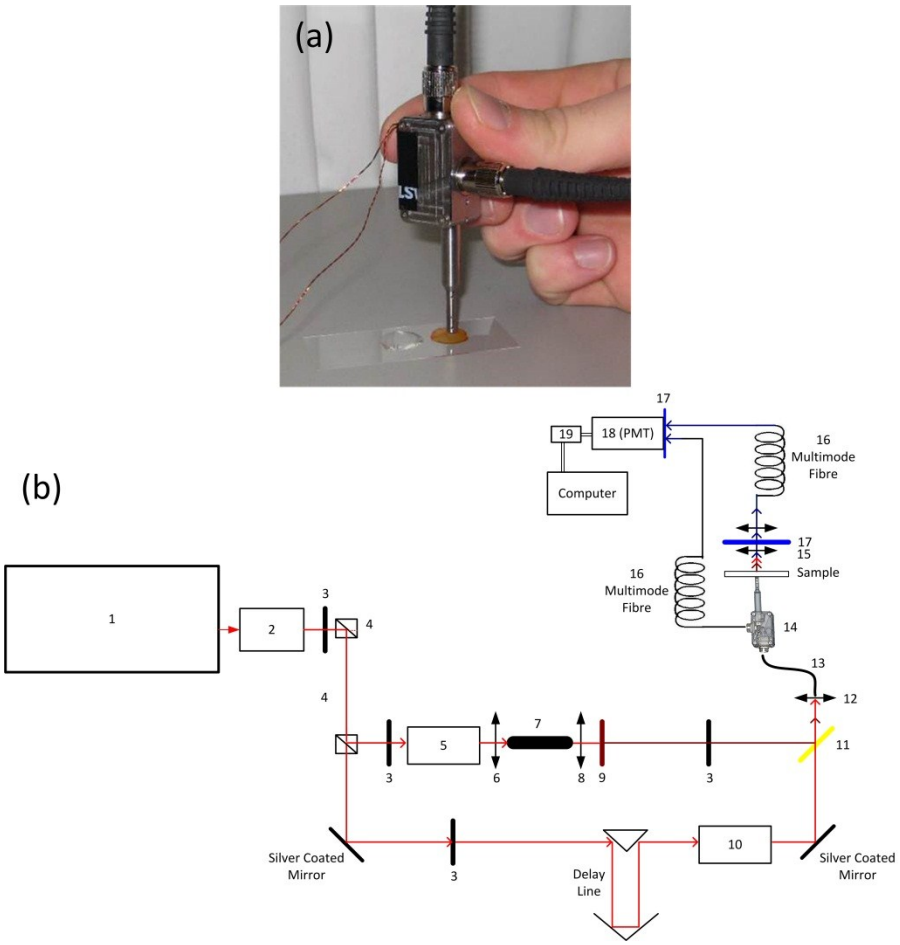

Fig. 1(a) Portability demonstration of the exoscope (b) Schematic of the experimental setup for the multimodal CARS imaging using the exoscope in (a). Various components are as follows: (1) Titanium sapphire laser source (2) Isolator (3) Half wave plate (4) Polarizing beam splitters (5) Prism compressor (6) 40X microscope objective lens (7) Supercontinuum generation PCF (8) Aspheric 5 mm focal length lens (9) 1040 nm central wavelength band-pass filter (10) Grating compressor (11) Short pass dichroic mirror (12) 5X microscope objective lens (13) LMA 20 PCF (14) Exoscope (15) 40X water immersion lens (16) Multimode collection fibre (17) Short-pass Filter (18) Hamamatsu PMT (19) Discriminator and field programmable gate array.

1. Materials and methods

2.1 Experimental setup

Our CARS system is based on a single Ti:sapphire femtosecond laser Fig. 1(b1) (Tsunami, Spectra-Physics, USA). The source is tuneable (between 700-1000 nm) and produces a transform limited ~70fs pulse train at an 80 MHz repetition rate. This light is split into pump and Stokes arms.

As described in detail in our earlier work [29, 31], 250 mW of this light at ~800 nm is directed into a FemtoWhite photonic crystal fibre (PCF) (NKT Photonics, Denmark) for creating the Stokes beam. The remainder (~600 mW) is the pump beam used for CARS, TPEF and SHG imaging. The supercontinuum output from the PCF Fig. 1(b7) is band-pass filtered Fig. 1(b9) (D1040/60 M, Chroma Technology, USA) so that it consists of wavelengths between 1014-1067 nm. The pump beam is sent through a computer-controlled delay stage to maintain temporal overlap of pump beam, as well as a grating compressor to compensate for the dispersion of the delivery fibre. The pump is then recombined with the Stokes beam at a dichroic mirror Fig. 1(b11). The spatially overlapped beams are coupled to the delivery fibre Fig. 1(b13) (LMA-20, NKT Photonics) by a 5x 0.09 numerical aperture (NA) microscope objective lens Fig. 1(b12). The fibre-coupled light is delivered to the vertically mounted exoscope Fig. 1(b14). The sample is mounted onto a three axis computer controllable stage. The generated signals can be collected in the forward direction by a 40x, 0.8 NA water immersion microscope objective Fig. 1(b15) (Olympus, Japan) or in the epi direction by the optical head of the exoscope. It was observed that upon exit, the excitation

beams had a slight off axis tilt, measured to be ~8º. This was compensated by tilting the exoscope body itself to maintain a level imaging plane. The implications of this tilt for the imaging performance of the exoscope are discussed in the following sections.

In both forward and epi configurations, light is collected by a large core (1.0 mm) multi-mode fibre Fig. 1(b16) (Thorlabs, USA). For epi collection, the fibre is mounted on the body of the exoscope while for forward collection the fibre is mounted above the exoscope. Before entering the photomultiplier tube (PMT) Fig. 1(b18), a 680 nm short pass filter Fig. 1(b17) (ET680SP-2P8, Chroma Technology) is used to remove the excitation light. Additional filters appropriate to the imaging modality can be introduced in the signal collection path as needed.

2.2 Miniaturized optics

The miniature objective lens was designed to enable in-vivo imaging of rat spinal cord. This required that the distal end of the exoscope must not have an outer diameter greater than 3.0 mm. Based on this prerequisite, the internal optics of the exoscope could have a maximum diameter of 2.0 mm while still maintaining a high NA of 0.6 and a long enough working distance of 400 µm while still attaining sub-micron resolution. The reasoning behind the choice to design a miniaturized set of optics is discussed in our previous work [29].

Designing small-diameter bulk optics to achieve high NA with as little chromatic aberrations as possible for widely-spaced wavelengths was non-trivial in such a constrained mounting volume. The chosen design includes several lenses with varying focal lengths ranging from 3.0 mm diameter BK7 glass for input light collimation down to a combination of SF4 and FK51 glass of 1.8 mm diameter for a 5x post-MEMS beam diameter expansion to fill the back aperture of the focusing optics. All of these optical elements are coated with broadband anti-reflection coatings with a reflection of less than 1% over 652-1036 nm on both air/glass surfaces. This low reflection per surface is made possible by a custom four layer deposition of alternating hafnium oxide and silicon dioxide (BMV Optical Technologies, Canada). This entire optical system is capped off with a 100 µm glass window to protect the optics and allow for water/specimen immersion. Simulations indicate that the optical system will give a diffraction-limited focus for both wavelengths. The ray diagram of the system is shown in Fig. 2a.

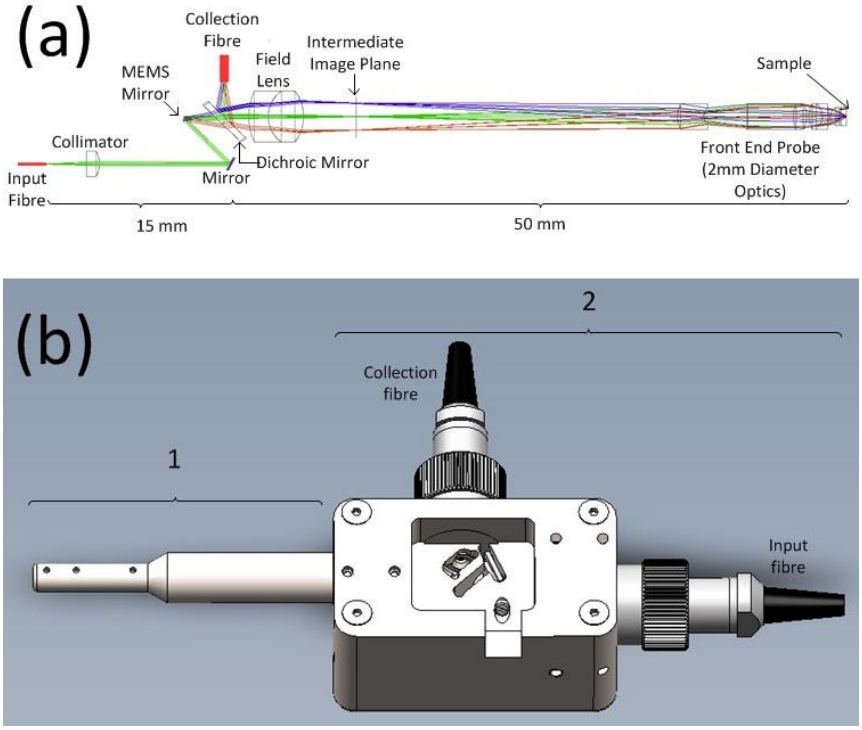

Fig. 2(a). Optical ray diagram of the exoscope featuring the lenses and scanning mechanism. (b). Computer-aided design SolidWorks image of the miniaturized multimodal CARS exoscope model including (1) the barrel of the exoscope (2) the body of the exoscope.

All of these optical components are mounted into a two-piece unit. The first section labeled as (1) in Fig. 2(b) has been characterized in the forward signal collection direction using a benchtop mounted MEMS mirror [29]. This portion is a tapered cylinder where the beam expander, chromatic correction and focusing lenses are contained. It is 41 mm long, 5.5 mm (outer diameter) at the proximal end and 3.0 mm (outer diameter) at the distal end.

The recently attached second piece (body) labeled as (2) in Fig. 2(b) houses the dichroic mirror, MEMS mirror, collimating lens and fibre mounting receptacles. As we are using a mirror to scan the beam, the beam path could not be entirely straight; a folding mirror had to be introduced. This, in conjunction with the need for physical fibre mounts, necessitated a larger housing for the body. The dimensions of this piece are 31 mm by 18.4 mm which also contains the set of four precision alignment screws to aid in the positioning and angle of the MEMS mirror and to ensure efficient light throughput.

In addition to the miniaturized lenses, a dichroic mirror is used to provide a discrete path into the collection fibre for the sample emission wavelengths. A reflection of greater than 95% over a wavelength range of 400-700 nm and transmission of greater than 99% from 800-1036 nm is accomplished by a highly customized 105 layer design of alternating Ta_2O_5 and SiO_2, with a total thickness of 88,495 Å (BMV Optical Technologies).

2.3 MEMS mirror

In order to create a minimally invasive, portable scanning CARS exoscope, a laser scanning system that is extremely small, robust, and produces high frame rates is crucial. Without a high frame rate scanner, the ability to produce high quality images from living samples would not be practical due to the continuous displacement of the specimen being imaged. A 2D, gimballed scanning mirror fulfilling these requirements was obtained from the Institut Photonische Mikrosystem (Germany). Both axes of the 500 µm mirror are driven as close as possible to their natural resonance frequency to maximize the mirror's scan angle and desired field of view. The slow and fast axis electrical driving frequency is ~4.0 KHz and ~32 KHz respectively. The electrical driving square wave has an amplitude of 50 V for the slow axis and 70 V for the fast axis. This corresponds to a sinusoidal mechanical oscillation frequency of ~2.0 kHz for the slow axis and ~16 kHz for the fast axis. When combined these parameters result in a mechanical oscillation of +/-8.5 degrees and a corresponding Lissajous pattern scanning a ~70x70 µm field of view.

2.4 Photonic crystal fibre delivery

An integral element in this nonlinear exoscope is the fibre delivery of single-mode, low noise, femtosecond pump and Stokes beams. Standard fused silica single-mode fibre cannot be used to deliver femtosecond pulses to the sample for CARS imaging due to the inherent high nonlinear signal generation and spectral broadening effects associated with the small mode area of standard fibres. PCFs circumvent these issues for ultrashort pulses [24] as they have customizable dispersive properties, and single mode operation for a broad range of wavelengths. Moreover, the large mode area makes them ideal for ultrashort pulse delivery, as the energy density of the wave is kept as low as possible. Pre-compression is still performed prior to the fibre to compensate for the dispersion that is encountered within the PCF to maintain a high peak power pulse at the sample.

A 1 metre long, large mode area PCF (LMA-20, NKT Photonics) fibre was used for the delivery of the two excitation wavelengths while a multi-mode fibre was used for signal collection. Using independent fibres for the delivery and collection allowed us to isolate and eliminate the four-wave mixing components in the fibre, through the insertion of a dichroic mirror between the delivery, and collection fibres. Using LMA-20 fibre allows single mode operation for a wide spectral band from 600 nm to greater than 1.0µm which includes both pump and Stokes wavelengths.

The low dispersion characteristic of LMA-20 fibre has allowed other groups [24, 28] to obtain CARS signal while using picosecond sources. Without compensation, and an input pulse of ~300 fs, an output pulse width of 1.331 ps was measured. An even stronger CARS signal could be obtained if the peak powers at the sample were maximized by using femtosecond pulses. This was accomplished by using a grating compressor setup for the pump arm at the input to the LMA-20 fibre, delivering a near-transform-limited pulse to the exoscope. Based on the LMA-20 output pulse width, the total dispersion of all the normally dispersive elements in the pump beam path was calculated. A negative 45521 fs^2 chirp was introduced to the pump beam, which, after fine tuning of the grating compressor geometry, resulted in a measured ~90 fs pulse width out of the LMA-20. This was accomplished while maintaining a Gaussian beam profile (M^2=1.34). The pulse width out of the exoscope itself was measured to be ~150 fs. Comparisons of the spectrum and autocorrelation traces of the pump and Stokes before and after the LMA-20 and exoscope did not show any abnormal spectral or temporal anomalies. The LMA-20 did introduce a polarization shift of 11º, although the ellipticity remained relatively unchanged. The difference between the input and the output ellipticity was determined to be less than 0.004. Bending loss measurements were also performed on

the LMA-20, and very little additional losses were experienced at radii greater than 15cm. The maximum bending radius used in these experiments was never less than 20cm, maintaining high coupling efficiency.

The final issue with utilizing a large mode area PCF for the propagation of two broadband pulses, is the generation of in-fibre non-resonant FWM at the CARS frequency [24]. This signal was observed exiting the LMA-20, with the spectrum of this signal depicted in Fig. 3. However, this non-resonant signal completely extinguished by the internal dichroic mirror and was not observed coming out of the exoscope, or the separate collection fibre.

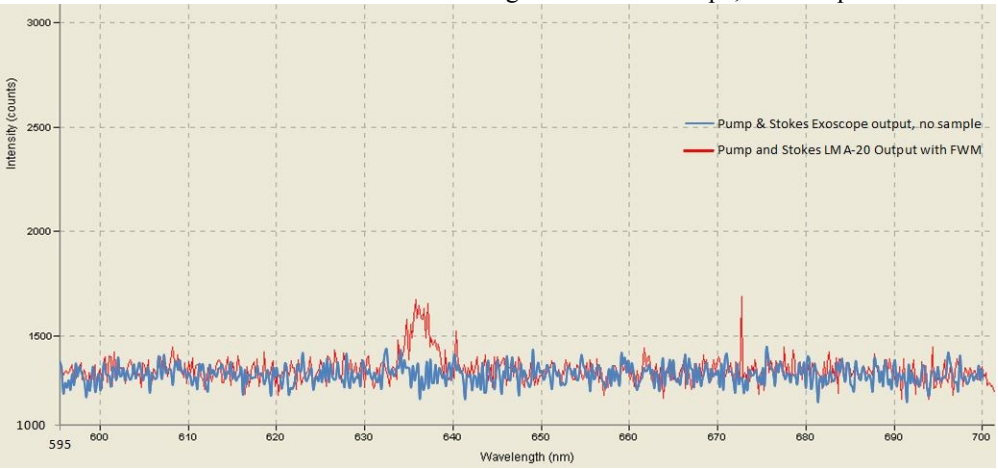

Fig. 3. Non-resonant FWM spectrum out of the LMA-20 VS the output spectrum of the exoscope (both with temporal overlap of pump and Stokes). The lack of the FWM signal at ~635 nm demonstrates the effectiveness of the internal dichroic mirror.

2. Results

3.1 Resolution measurements

A United States Air Force 1951 (USAF) (Edmund Optics, USA) target was used to determine the resolving power and to calibrate the exoscope in the forward direction. The negative pre-chirped 800 nm pump beam from the titanium sapphire laser was coupled to the LMA-20 fibre and then to the exoscope. A water drop was placed on the tip of the exoscope, and the glass USAF target was placed with the marking side down (as the microscope is inverted) and making contact with the water. The smallest features of the resolution target were brought into focus for transmission imaging. The average power at the sample was 16 mW, which was attenuated after the target by a 680 nm short-pass filter (ET680SP-2P8, OD5, Chroma Technology), to avoid saturating the PMT. The smallest features (group 7, element 6) are very well resolved at the left side of Fig. 4.

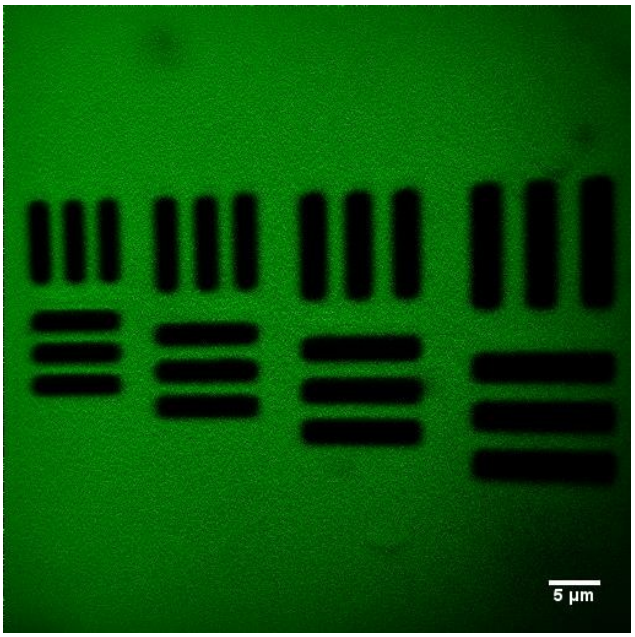

Fig. 4. Transmission image of the USAF target captured in the forward direction: The line spacing of this element is 228 line pairs per mm, which results in a 2.18 µm separation distance between lines and a calibration value of 0.118 µm per pixel.

Following the USAF target calibration, the performance of the exoscope was further examined by determining the axial and lateral resolutions. TPEF sensitive 1.0 µm diameter fluorescent microspheres (Polysciences Inc., USA) were spin coated onto a #1 cover slip. 800 nm light from the femtosecond laser was negatively chirped for dispersion pre-compensation, coupled to the LMA-20 fibre, and delivered to the exoscope, with an average power of 15 mW at the sample. The transmission efficiency through the exoscope was measured as 47%. Fig. 5(a) shows the TPEF signal from the microspheres in the epi direction.

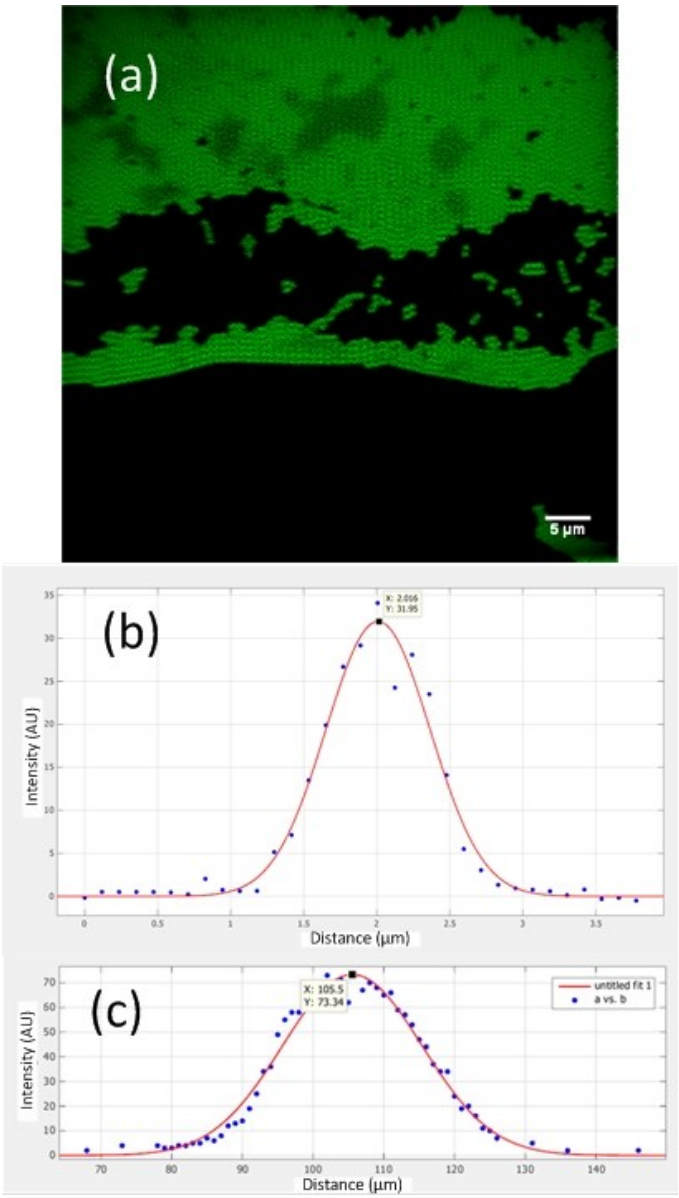

Fig. 5(a) TPEF excitation of 1.0 µm Fluorescebrite microspheres in the epi direction. (b) Lateral intensity profile of a single 1.0 µm Fluorescebrite microsphere. (c) Axial profile the same bead.

For a bead located 14.7 µm from the image centre, the intensity profile was plotted. A Gaussian curve was fit to the profile, shown in Fig. 5(b), and an observed bead size was found to be 0.94 µm full width at half maximum (FWHM), which is an improvement compared to the measured ~1.3 µm demonstrated in the free-space delivered version [29].The exoscope design goal was to achieve a lateral resolution better than 1.0 µm at the sample, and this measurement demonstrates that the exoscope has at least 1.0 µm resolution for single wavelength illumination. 500 nm TPEF sensitive beads were also imaged, but they could not be resolved. Axial resolution measurements were also performed with these 1.0µm TPEF beads, resulting in a value of 24 µm, with the profile demonstrated in Fig. 5(c). This is much larger than the anticipated design value of 3.0 µm and is mainly attributed to the aberration caused inside the miniature objective due to the slight off-axis propagation of the excitation beam as mentioned in Section 2.1.

The final TPEF calibration measurement was undertaken to characterize the inherent chromatic aberrations of the exoscope. Ultra rainbow fluorescent particles (Polysciences Inc.) that are TPEF sensitive for a broad wavelength range were used. The polychromatic sensitivity is due to the affixation of multiple fluorochromes, allowing efficient excitation for both pump and Stokes wavelengths. As there was not enough peak power in the 1040 nm Stokes beam

to generate a TPEF signal, the Ti:sapphire laser was tuned to 960 nm which is as close to the Stokes wavelength as could be attained while maintaining mode locking. 1.0mW of 800 nm light and 2.5 mW of 960 nm light were independently used to image these polyfluorescent beads, with the specific bead imaged located 16 μm from the image centre. To determine the lateral chromatic aberrations, the z axis was scanned until the beads were in focus. The centres of the beads were located by analyzing the intensity profile in both the X and Y directions. The lateral offset caused by chromatic aberrations was found to be 0.1 μm in the X direction, and 0.73 μm in the Y direction. This relatively large Y- offset could be a result of the tilt in the optical output of the exoscope. The difference in the z focus was used to discern the strength of the axial chromatic aberrations, which ended up shifting the focus of the 960 nm light with respect to the 800 nm light by 1.3 μm. It is important to note that the axial and lateral resolutions are not constant throughout the field of view (for all resolution measurements). It was determined that the resolutions decreased as a function of distance from the centre of the field of view.

Now beginning with CARS experiments, we used a selection of polystyrene (PS) microspheres with diameters of 20 μm, 4.5 μm, 2.0 μm and 1.0 μm. These beads were spin coated onto #1 coverslips. The aromatic CH bonds in these beads have a strong peak at 3070 cm^{-1}, which is suitable for excitation with the available pump and Stokes wavelengths. The CARS signal of the polystyrene beads was generated by focusing the temporally and spatially overlapped pump (800 nm) and Stokes (1014-1067 nm) beams on the sample. The generated CARS signal was collected by the exoscope and detected in the epi direction. Temporal overlap is achieved by maximizing the CARS signal in the forward direction from a bulk oil sample, while fine-tuning the delay between the pump and the Stokes beams.

CARS lateral and axial resolution measurements were performed in the epi direction, on a 2.0 μm PS bead sample, shown in Fig. 6. The FWHM of the intensity profile of a single 2.0 μm bead located 23.3 μm from the centre of the field of view was determined to be 2.02 μm. The 1.0 μm PS beads were not resolvable. For the axial resolution measurement, a stack of images was collected with 1.0μm steps along the optical axis (z). For the entire data set, a line profile of the bead's intensity was taken. These values were then plotted against their corresponding z position and a Gaussian curve was fit. The FWHM of this curve which corresponds to the axial resolution of the miniaturized CARS microscope was determined to be 13 μm, similar to the 12.74 μm value reported in the free-space iteration [29]. Although this is much larger than the anticipated and designed value of 3.0 μm, it still allows for some 3D sectioning ability. The aberrations caused by the off-axis propagation of the pump and Stokes excitation beams are mainly responsible for this relatively large axial resolution for CARS. For these PS beads, multiple axial and lateral resolution measurements were performed, to better understand the relationship of the resolution to the radial distance from the centre of the field of view. It was determined that beads located near the edges of the field of view have a decreased lateral and axial resolution by upwards of 0.3 μm, and 3.0 μm respectively.

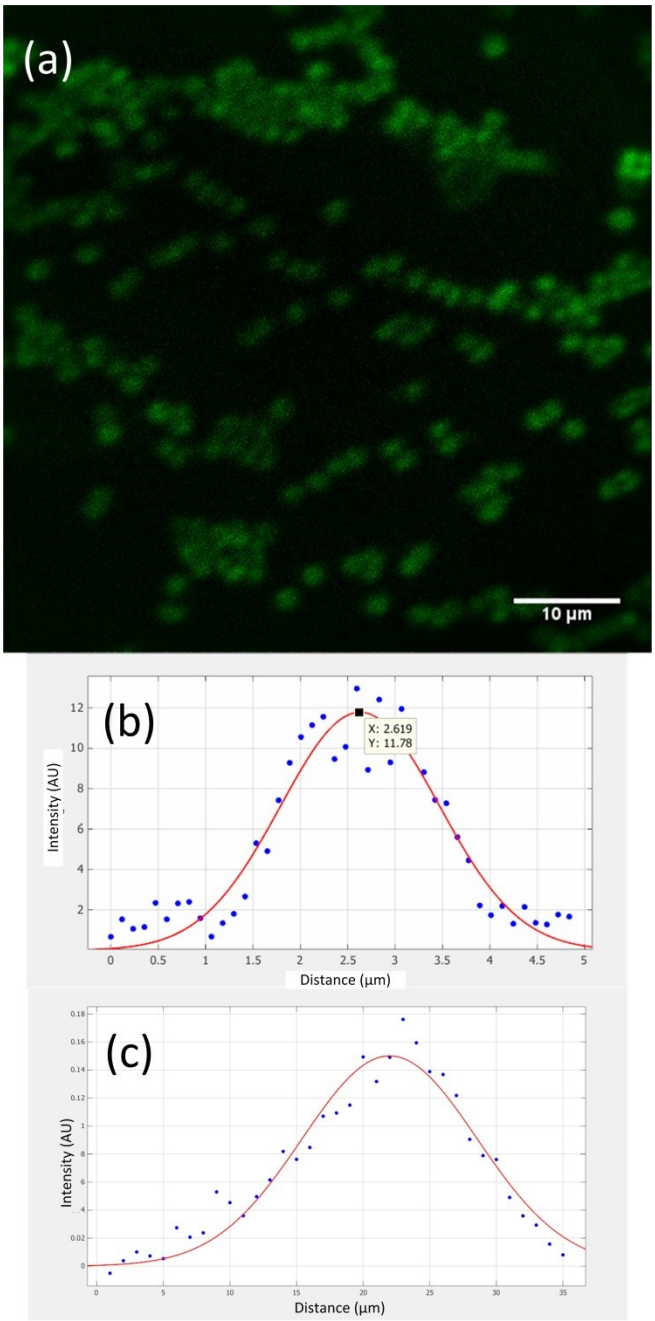

Fig. 6(a) CARS-excited 2.0 µm polystyrene microspheres in the epi direction. (b) Lateral profile curve (c) Axial profile curve.

3.2 Structural and biological multimodal imaging

Beginning with the mouse lung tissue, a section was placed between a standard microscope slide, and a #1 coverslip. The slide was placed on the microscope stand, coverslip down, with a water drop bridging the gap between the exoscope tip and the coverslip. The pre-chirped 800 nm beam was delivered to the exoscope via the LMA-20 fibre, and 18 mW of power was scanned on the sample. The generated TPEF signal was collected in the epi direction and the excitation wavelengths were filtered out using a short pass filter (ET680SP-2P8, Chroma Technology). The fluorescein, which had propagated throughout the mouse's vasculature, can be seen in Fig. 7(a) with the vasculature rich alveolar walls visible surrounding the alveolar cavities.

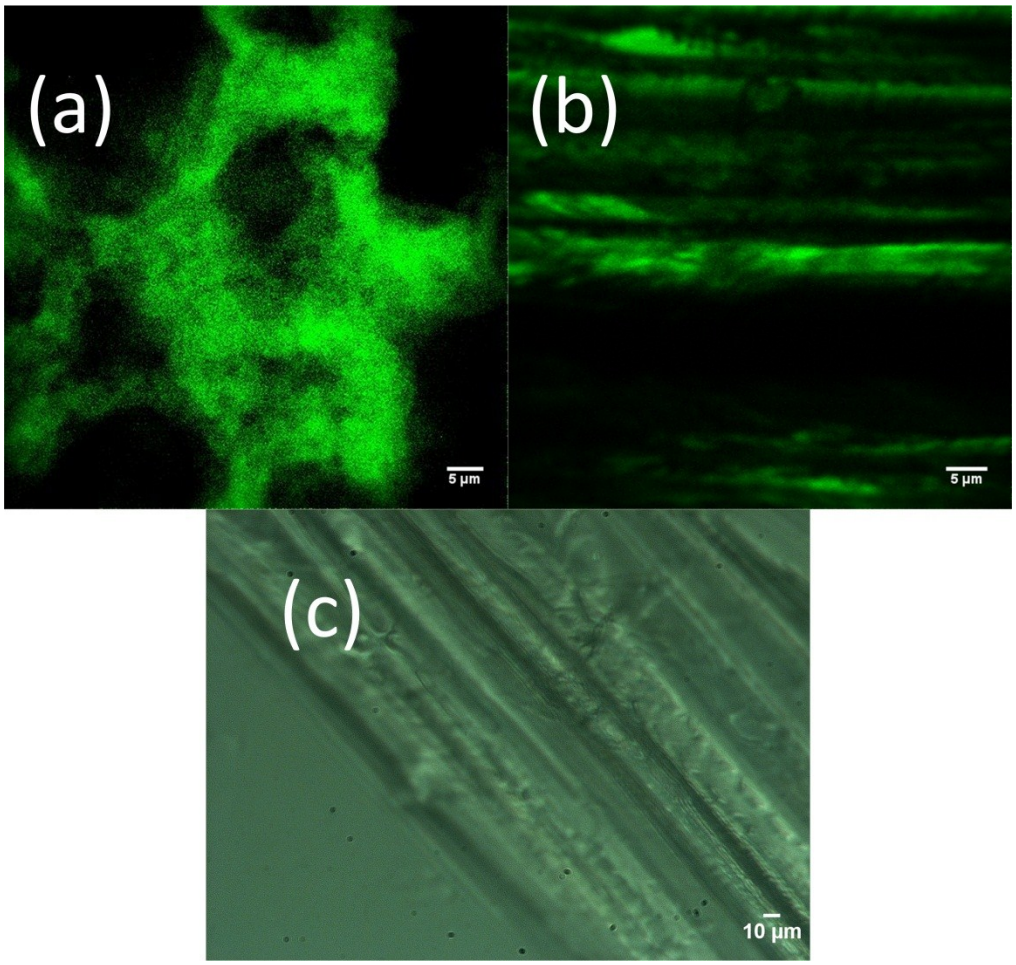

Fig. 7(a) Epi - Fluorescein stained mouse lung tissue. (b) Epi - SHG image of KDP crystal. (c) For comparison: White light transmission microscopic image of KDP crystal at 100X magnification.

In order to determine the full multimodality of the exoscope, an SHG signal must also be collected, and imaged. To accomplish this task, a sample of potassium dihydrogen phosphate (KDP) crystal was exposed to 3.5 mW of 800 nm laser light. An additional short pass filter (Z485SP, Chroma Technology) was included to allow only the SHG signal to pass while the generated photons were still being captured in the epi direction. The longitudinal structure of the KDP crystal captured in Fig. 7(b) demonstrates the ability to observe a strong backscattered SHG signal in the epi direction. A transmission image of the same sample is shown for reference in Fig. 7(c).

Finally the exoscope was used to demonstrate its biological epi-CARS imaging capabilities. Unstained, unfixed, fresh mouse sciatic nerves, rich in C-H bonds were mounted on #1 coverslips. The vibrational mode of the C-H bonds at ~2840 cm^{-1} contained within the myelin and surrounding fat cells is resonantly excited by the frequency difference between the pump and the Stokes wavelengths, with powers of 12.5 mW (~0.156 nJ) and 1.2 mW (~0.015 nJ) respectively. The pump and Stokes wavelengths are extinguished with a 65 nm band pass filter with central peak at 645 nm (ET645/65 M, OD7, Chroma Technology) while allowing the epi-collected photons to reach the PMT. This unlabeled sample is pictured in Fig. 8(a) with the myelin surrounding the central axons clearly visible. To confirm the signal is indeed from the CARS process, the Stokes beam is blocked in Fig. 8(b). The images demonstrated in Fig. 8(c) and Fig. 8(d) are of fat cells surrounding the sciatic nerve, with both pump and Stokes present, and then with the Stokes beam blocked respectively.

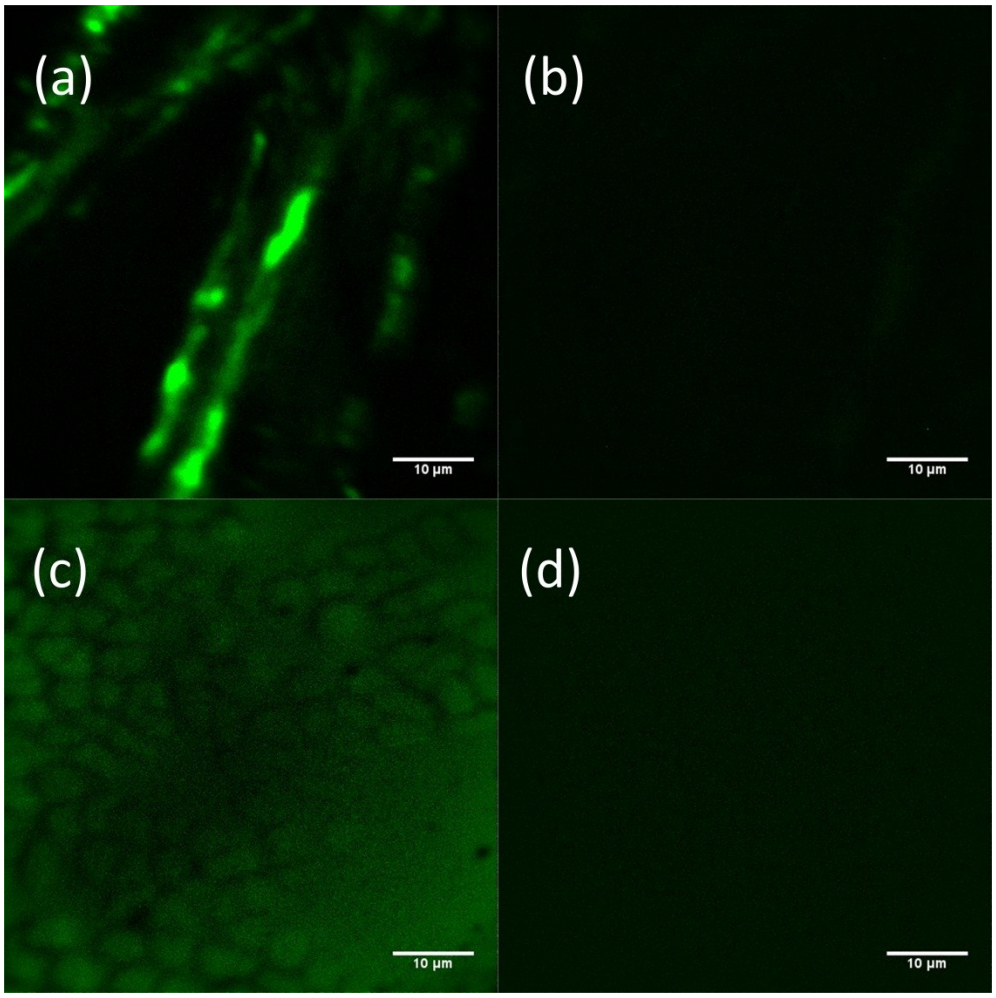

Fig. 8(a) Epi – CARS image from unlabeled mouse sciatic nerve, showing a few axons in the field of view. (b) Epi image of the same region demonstrated in (a), with the Stokes beam blocked. (c) Epi-CARS image of fat cells surrounding the sciatic nerve. (d) Epi image of the same region demonstrated in (c) with the Stokes beam blocked.

3. Discussion and conclusion

We have successfully demonstrated a portable, miniaturized, fibre delivered, multimodal CARS imaging device. The device was made possible by the inclusion of many specialized parts, including a MEMS scanning mirror, with a 500 µm diameter reflective surface being driven at very high frequencies, a custom built dichroic mirror, a large mode area fibre and a custom built miniaturized objective lens. Due to the portability, the applications in which this exoscope can be applied to clinical situations are numerous. The demonstrated TPEF, SHG and CARS capabilities could potentially allow serial monitoring of morphological and chemical changes in vivo, in the same animal. Applications of this in vivo imaging can range from cancer identification, drug therapy selection, detection of spinal cord injuries and demyelination to arterial atherosclerosis, all potentially enabled by the use of this device. Specific medical applications of this exoscope include, but are not limited to detecting squamous cell carcinoma [10], performing nanosurgery [11], and studying myelination [5].

The design, lens manufacture, and assembly of the exoscope provided a significant hurdle. A slight misalignment in one of the nine different glasses would have caused catastrophic aberrations in the exoscope barrel. Spatial overlap of both pump and Stokes beams would have been impossible, rendering the exoscope useless for CARS imaging. Substantial attention, effort, and time ensured that each component was manufactured to specifications, and installed precisely according to the design.

The end result of this effort was an optical system that completely blocked unwanted fibre-generated non-resonant FWM, successfully separated the excitation light from the emitted light while maintaining a 3.0 mm probe diameter at the distal end. Unfortunately, all design specifications were not as successfully met. The chromatic

aberrations caused substantial lateral and axial offsets limiting the three-dimensional sectionability, although these aberrations were not severe enough to inhibit the generation of CARS photons. Further improvements to the exoscope manufacture and assembly will most certainly benefit the lateral and axial offsets, and increase system performance.

Together, all of these components resulted in the successful resonant excitation of CH bonds at 2845 cm^{-1} and 3070 cm^{-1} Raman shifts, generating a strong CARS signal, whether it is from oil, beads or biological tissue. While the fundamentals of a multimodal nonlinear exoscope have been successfully verified, there were some issues in this first prototype that caused the quality of the images demonstrated to be less than ideal. The optical path of the excitation beams out of the exoscope's barrel was off axis, with an observable tilt of 8º. This slight tilt in the optical path was impossible to correct for, even during the initial integration of the body and barrel. It is expected that better control of the longitudinal and lateral position of the input fibre tip with respect to the collimating lens, as well as finer control of the angular placement of the MEMS mirror, will enable elimination of this off-axis tilt. It is most likely that this tilt is responsible for the majority of the aberrations and for the resulting degradation of the axial resolution measurements. The lack of available Stokes beam power also negatively contributed to the quality of the images reported. A system with ample Stokes power would have a more intense CARS signal, and consequently, images with a higher signal to noise ratio.

The lateral resolution measurements taken confirm that the focus is near diffraction limited for TPEF measurements, as designed. The lateral resolution measurements are larger for CARS, and this can be attributed to the chromatic aberrations, reducing the overlap in the X-Y plane. The discrepancy between the chromatic aberration in the X and Y directions can be attributed to the off axis propagation of the beams due to the optical tilt that was reported. The axial resolution measurements, however, were larger than anticipated. This could be due to a number of reasons, most likely caused by various types of aberrations experienced within the miniaturized optics. The decrease seen in the axial resolution for the two wavelength CARS process is due to the mismatch in the chromatic overlap of the two beams. The larger axial resolution of the TPEF signal can be attributed to the previously mentioned aberrations caused by the off-axis propagation of the pump beam, extending the axial focal volume.

Further improvements on the manufacturing processes of exoscope will reduce the optical aberrations of the system in the next prototype. This will increase pump and Stokes beam overlap, reduce the elongated active focal volume, increasing the image quality and resolution capabilities. Signal collection will be improved by using a more sensitive PMT, as well as locating more suitable samples. As the goal of this project was to image lipids using CARS imaging, a broadband pump and Stokes was suitable to excite the strong vibration resonances of the CH bonds in the lipid molecules as demonstrated here. A technique such as spectral focusing based CARS microscopy using a single femtosecond laser and PCF-generated supercontinuum [31], will enable extension of the application range of the exoscope to the Raman fingerprint region of ~ 800 – 1800 cm^{-1}[32]. Integration with a femtosecond fibre laser [33] is also being considered to reduce the footprint of the entire setup, bringing multimodal nonlinear imaging closer to a clinical application.

4. Acknowledgments

This work was made possible by the support of CIHR – NSERC grant 87490. We would like to thank Dr. Tito Scaiano and his students Chiara Fasciani and Madeline Simpson, as well as Dr. M. Parsanejad for the preparation of various biological samples and Dr. Ileana Micu and Thomas Kannanayakal for sample preparation consultation.

D. fs-laser pulse compressing

Novelty:

For the first time, we did the compression and shaping of the ultra-short pulses of an optical parametric amplifier at 1300 nm, to 20 fs, using gas filled hollow core fiber. This was a joint project between Dr. Anis at the University of Ottawa, and Dr. Lagare at the Institute National de la Recherche Scientifique (INRS), in Montreal, Quebec.

Contributions:

To conduct the measurements, I assembled, modified and tested the hollow core gas filled pulse compressor setup in the Advanced Laser Laboratories (ALLS) at INRS.

My contributions to this article were installing the experimental setup, doing the experiments and measurements, analysing data and spectrums and writing the experimental results report. Dr. Lagare suggested the idea of using the hollow core approach based on a similar setup at NRC, supervised the experimental procedure and wrote the entire article.

3.5.8.Pulse compression and shaping of broadband optical parametric amplifier laser source

François Légaré,[1,*] Madji Naji,[2] Philippe Lassonde,[1] Daniel Comtois,[1] Vincent Crozatier,[3] Thomas Oksenhendler,[3] Hanan Anis,[2] and Jean-Claude Kieffer[1]

[1]*Institut National de la Recherche Scientifique, Centre Énergie Matériaux et Télécommunications, 1650 Boulevard Lionel-Boulet, Varennes, QC J3X1S2, Canada*

[2]*School of Information Technology and Engineering (SITE), University of Ottawa, 800 King Edward, P.O. Box 450, Station A, Ottawa, ON K1N 6N5, Canada*

[3]*Fastlite, Bât 403, École Polytechnique, 91128 Palaiseau, France*

Received August 25, 2008; revised October 17, 2008; accepted October 17, 2008; posted October 22, 2008 (Doc. ID 100601); published November 24, 2008

We report pulse compression and shaping of a 100 Hz broadband optical parametric amplifier (OPA) laser source generated by self-phase modulation in a hollow-core fiber. The amplitude and phase of the broadband OPA laser pulses are controlled using an acousto optic programmable dispersive filter (AOPDF). Using the AOPDF, we demonstrate compression, characterization, and amplitude/phase control of 1300 nm 20 fs laser pulses with energies up to 10 J. This novel source is suitable for seeding successive OPA amplification stages and for time-resolved spectroscopy. © 2008 Optical Society of America

OCIS codes: 320.5520, 140.7090, 190.4970.

Generation of millijoule carrier-envelope phase stabilized sub-5 fs titanium–sapphire 800 nm laser pulses has been the key technological breakthrough for the generation of isolated attosecond laser pulses [1–4]. Using 1.5-cycle 800 nm driving laser pulses, an 80 as pulse duration has been recently demonstrated [5]. It is recognized that the key approach to further decrease the duration of attosecond pulses is to use a driving laser field at a longer wavelength [4]. This can be easily understood by the three-step model introduced by Corkum in 1993 [6]. Recently, the technology of carrier-envelope phase stabilized few-cycle laser pulses has been extended in the infrared spectral range using different approaches; 20 fs at 2 m using an optical parametric chirped-pulse amplifier [7], 17 fs at 2.1 m using pulse compression in an optical filament [8], and 17 fs at 1.5 m using difference frequency generation of few-cycle 800 nm laser pulses followed by optical parametric amplification [9].

Pulse compression of 800 nm Ti–Sa laser pulses by self-phase modulation through propagation into a hollow-core fiber has been introduced by Nisoli *et al.* in 1996 [10]. At 800 nm, dispersion compensation can easily be achieved using chirped mirrors [11–13]. With such technology, sub-4 fs Ti–Sa laser pulses have recently been generated [5]. A similar approach has been used in the visible spectral range [14,15]. In the infrared, sub-10 fs 1.1 m submicrojoule laser pulses have been produced using a noncollinear optical parametric amplifier (OPA) [16]. The possibility of using the hollow-core fiber approach is attractive since higher energy per pulse (submillijoule) will be available. In this Letter, we show spectral broadening of OPA laser pulses (1300 nm, signal wavelength) using the hollow-core fiber approach. Using an acousto-optic programmable dispersive filter (AOPDF) [17], we demonstrate pulse compression, characterization, and shaping of laser pulses with an 200 nm spectral bandwidth with energies up to 10 *J* and a 20 fs pulse duration.

The experiment was conducted at the advanced laser light source (ALLS) using the 100 Hz, 100 mJ, 25 fs, Ti–Sa laser system (Thales Laser). Laser pulses of 7 mJ at 800 nm were directed to an OPA, TOPAS-HE, Light Conversion and frequency-shifted to 1300 nm signal pulses. A typical signal pulse energy is 1.3 mJ with an energy fluctuation of about 4% rms. The OPA signal pulse energy is controlled using an achromatic half-waveplate and a Glan–Calcite polarizer. The signal laser beam is coupled into the hollow-core fiber compressor using an $f=750$ mm plano-convex lens. The fiber diameter is 400 m and its length is 100 cm. This configuration favors the coupling into the fundamental EH_{11} spatial mode, which has the highest transmission and whose spatial profile is a zeroth-order Bessel function of the first kind [10]. The fiber is attached at one end to a closed gas cell and supported on an aluminum V-groove [18]. Argon gas flowed through the fiber from the cell at 1.2 atm of pressure and leaked into air at the exit. The typical transmission efficiency was near 30% due to the poor spatial quality of the OPA laser beam. At the output, the laser beam was collimated with an $f=300$ mm concave silver mirror. With this configuration, the beam diameter was set to 3 mm as the input size of the AOPDF.

Typical spectra after the fiber as a function of the output pulse energy are shown in Fig. 1. At a low output energy 30 J, the spectra is unchanged compared to the input one. At higher output energies (150 and 225 J), we observed spectral broadening and amplitude modulations related to the process of self-phase modulation. At a 150 J output energy, the spectral bandwidth extended over 200 nm while at 225 J the spectral bandwidth became 300 nm. Assuming a Fourier-transform-limited pulse duration for the spectra presented in Fig. 1, the

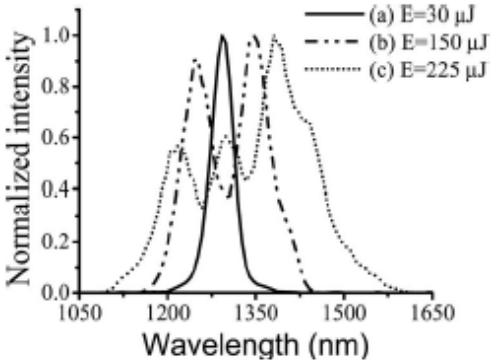

Fig. 1. Normalized spectra after propagation into the hollow-core fiber as a function of output energy. (a) 30, (b) 150, and (c) 225 μJ. Assuming a Fourier-transform-limited pulse duration, the durations (FWHM of temporal intensity) are 43, 20, and 11.5 fs.

durations (FWHM of temporal intensity) are (a) 43, (b) 20, and (c) 11.5 fs.

In our experiments, pulse compression and shaping was performed using an AOPDF (Dazzler, WB45-1150-1600, Fastlite, France) located after the hollow-core fiber. The AOPDF is configured for the spectral range between 1150 and 1600 nm. The AOPDF used a TeO_2 crystal with 45 mm in length. To prevent damage to the AOPDF, input energy was limited to 20 μJ. At the output of the AOPDF, there are two beams spatially separated, the purely transmitted beam and the diffracted one being shaped. For ~200 nm of bandwidth [see Fig. 1(b)], we achieved 50% of the energy in the diffracted beam. Pulse compression is performed using a system comprising a 50 μm thickness B-barium borate (BBO) crystal, focusing optics (off-axis parabolic silver mirror, f = 100 mm), a spectrometer, and closed-loop feedback software controlling the AOPDF. In this procedure, the AOPDF is used to add a well-defined sequence of pure second-order phase. The second-harmonic generation (SHG) spectra is recorded for a well-defined sequence of $\phi^{(2)}(\mathrm{fs}^2)$. The software generates the chirp sequence and uses the SHG spectra function of $\phi^{(2)}(\mathrm{fs}^2)$ to retrieve the high-order components of the spectral phase [$\phi^{(2)}(\mathrm{fs}^2)$, $\phi^{(3)}(\mathrm{fs}^3)$, $\phi^{(4)}(\mathrm{fs}^4)$ and higher orders]. This is possible due to the AOPDF capability of a highly accurate control on the spectral phase. This optimization is performed in multishot measurements and therefore suffers from pulse-to-pulse energy fluctuations. Consequently, a higher laser repetition rate is expected to significantly improve the quality of the measurements.

We also used the AOPDF for pulse characterization after compression. With the AOPDF, we can produce pulse replica at variable delays that are locked in regard to the carrier frequency. In the spectral domain, this corresponds to the following filter: $H(\omega)=1+\exp(i(\omega-\omega_0)\tau+\phi_0)$, with the delay being τ, ω_0 being the carrier frequency, and ϕ_0 being a phase shift. By measuring the baseband interferometric autocorrelation traces at $\phi_0=0,(\pi/4),(\pi/2),(3\pi/4),\pi$, one can retrieve the interferometric autocorrelation trace [19]. The energy fluctuation at the end of the hollow-core fiber prevents us from reconstructing the interferometric trace. This baseband interferometric autocorrelation basically removes the oscillation part. The shape of those traces is smooth allowing the measurement of only few points per traces, which is compatible with a 100 Hz repetition rate. In Fig. 2, we show the experimental autocorrelation $\phi_0=0,\pi$ traces for the spectra obtained in Figs. 1(a) and 1(b), i.e., Fourier transform limited pulse duration of 43 and 20 fs. We measured the $\phi_0=0,\pi$ traces since their shapes are characteristic of the envelope of the interferometric autocorrelation. Such a type of measurements has never been reported in literature. This is possible due to the AOPDF capability to apply a highly accurate spectral phase.

In Fig. 2(b), for the laser pulses with an ~200 nm spectra, we observed two types of oscillations. The low frequency modulations observed in the $\phi_0=0,\pi$ traces are directly linked to the amplitude modulations observed in the spectral domain [see Fig. 1(b)]. The high frequency modulations, also observed in Fig. 2(a), are related to the 4% rms energy fluctuation of the laser system. The dotted curves represent the calculation of the $\phi_0=0,\pi$ traces assuming Fourier transform limited pulses. The agreement between our measurements and the assumption of a constant spectral phase confirms that we have compressed the OPA laser pulses down to a 20 fs duration (FWHM of temporal intensity).

For compression, the AOPDF has been uniquely used for adding spectral phase, but it can also control the spectral amplitude. For time-resolved spectroscopy, broadband laser pulses are highly interesting since multiple colors are available [20]. To demonstrate the ability of our laser source to perform time-resolved experiments, we shaped the amplitude and the phase of the laser pulses characterized in Fig. 2(b), corresponding to the ~200 nm spectra of Fig. 1(b). First, we applied amplitude filters such that we produced three laser pulses. The first amplitude filter selects the complete broadband spectra. The second and the third filters, with 50 nm of bandwidth at FWHM, are applied at 1250 nm and 1350 nm. The shape of these amplitude filters as a function of fre-

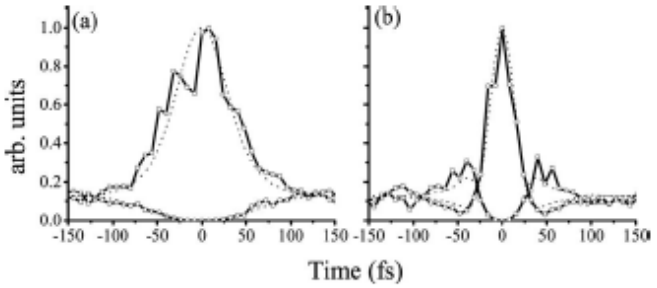

Fig. 2. Autocorrelation traces of the compressed laser pulses generated with the AOPDF; square $\phi_0=0$, circle $\phi_0=\pi$. The dotted curves are the $\phi_0=0,\pi$ autocorrelation traces assuming a Fourier-transform-limited pulse duration. (a) Corresponding spectra are presented in Fig. 1(a), Fourier-transform-limited pulse duration of 43 fs. (b) Corresponding spectra are presented in Fig. 1(b), Fourier-transform-limited pulse duration of 20 fs.

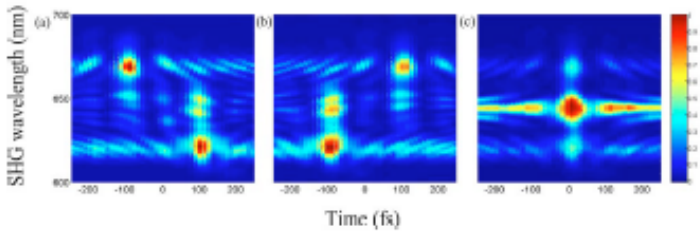

Fig. 3. (Color online) SHG spectra as a function of τ_2 for three different values of τ_1: (a) 200, (b) −200, and (c) 0 fs.

quency is a sixth-order superGaussian. Second, the delay (τ_1) between those two laser pulses (1250 and 1350 nm) was fixed by applying a linear spectral phase. Third, we scanned the temporal delay (τ_2) between the broadband pulse and the two filtered pulses from −250 to 250 fs. In Fig. 3, we are showing the SHG spectra as a function of τ_2 for three different τ_1: 200, −200, and 0 fs. For τ_1 equal to −200 and 200 fs, the SHG spectra as a function of τ_2 contain two distinct peaks that are located in two different spectral regions, while the SHG spectra at τ_1 equals to 0 fs reflect the sum frequency of the three laser pulses.

Using self-phase modulation by propagation into a hollow-core fiber combined with an AOPDF pulse shaper, we have demonstrated generation, compression, characterization, and shaping of 20 fs OPA laser pulses. We also demonstrated how this novel laser source can be used for time-resolved spectroscopy. Currently, we are limited to ~200 nm bandwidth due to limitations in the dispersion capability imposed by the AOPDF. We have not been able to compress the ~300 nm broadband spectra presented in Fig. 1(c). Efficient acousto-optic coupling over ~300 nm bandwidth would require a longer TeO_2 crystal or a double-pass configuration. This will increase the effective length of the AOPDF. With the double-pass configuration, we expect to generate sub-12 fs OPA laser pulses. Double-pass configuration requires resetting the amplitude and phase calibration of the AOPDF pulse shaper. For scaling up the energy to the millijoule level, it will be possible to use this novel laser source for seeding successive OPA amplification stages, similar to Vozzi *et al.* [9], but with complete control over the amplitude and the phase of the broadband spectra.

The authors acknowledge the support of the Canada Foundation for Innovation, the Canadian Institute for Photonic Innovations, The Natural Sciences and Engineering Research Council of Canada, and the Fonds Québécois de la Recherche sur la Nature et les Technologies.

References

1. R. Kienberger, E. Goulielmakis, M. Uiberacker, A. Baltuska, V. Yakovlev, F. Bammer, A. Scrinzi, Th. Westerwalbesloh, U. Kleineberg, U. Heinzmann, M. Drescher, and F. Krausz, Nature **427**, 817 (2004).
2. I. J. Sola, E. Mével, L. Elouga, E. Constant, V. Strelkov, L. Poletto, P. Villoresi, E. Benedetti, J.-P. Caumes, S. Stagira, C. Vozzi, G. Sansone, and M. Nisoli, Nat. Phys. **2**, 319 (2006).
3. G. Sansone, E. Benedetti, F. Calegari, C. Vozzi, L. Avaldi, R. Flammini, L. Poletto, P. Villoresi, C. Altucci, R. Vellota, S. Stagira, S. De Silvestri, and M. Nisoli, Science **314**, 443 (2006).
4. P. B. Corkum and F. Krausz, Nat. Phys. **3**, 381 (2007).
5. E. Goulielmakis, M. Schultze, M. Hofstetter, V. S. Yakovlev, J. Gagnon, M. Uiberacker, A. L. Aquila, E. M. Gullikson, D. T. Attwood, R. Kienberger, F. Krausz, and U. Kleineberg, Science **320**, 1614 (2008).
6. P. B. Corkum, Phys. Rev. Lett. **71**, 1994 (1993).
7. T. Fuji, N. Ishii, C. Y. Teisset, X. Gu, Th. Metzger, A. Baltuska, N. Forget, D. Kaplan, A. Galvanauskas, and F. Krausz, Opt. Lett. **31**, 1103 (2006).
8. C. P. Hauri, R. B. Lopez-Martens, C. I. Blaga, K. D. Schultz, J. Cryan, R. Chirla, P. Colosimo, G. Doumy, A. M. March, C. Roedig, E. Sistrunk, J. Tate, J. Wheeler, L. F. DiMauro, and E. P. Power, Opt. Lett. **32**, 868 (2007).
9. C. Vozzi, F. Calegari, E. Benedetti, S. Gasilov, G. Sansone, G. Cerullo, M. Nisoli, S. De Silvestri, and S. Stagira, Opt. Lett. **32**, 2957 (2007).
10. M. Nisoli, S. De Silvestri, and O. Svelto, Appl. Phys. Lett. **68**, 2793 (1996).
11. A. Stingl, M. Lenzner, Ch. Spielmann, F. Krausz, and R. Szipöcs, Opt. Lett. **20**, 602 (1995).
12. M. Nisoli, S. De Silvestri, O. Svelto, R. Szipöcs, K. Ferencz, Ch. Spielmann, S. Sartania, and F. Krausz, Opt. Lett. **22**, 522 (1997).
13. S. Sartania, Z. Cheng, M. Lenzner, G. Tempea, Ch. Spielmann, F. Krausz, and K. Ferencz, Opt. Lett. **22**, 1562 (1997).
14. O. Dühr, E. T. J. Nibbering, G. Korn, G. Tempea, and F. Krausz, Opt. Lett. **24**, 34 (1999).
15. G. Cerullo, M. Nisoli, S. Stagira, S. De Silvestri, G. Tempea, F. Krausz, and K. Ferencz, Opt. Lett. **24**, 1529 (1999).
16. A. Shirakawa, I. Sakane, and T. Kobayashi, Opt. Lett. **23**, 1292 (1998).
17. F. Verluise, V. Laude, Z. Cheng, Ch. Spielmann, and P. Tournois, Opt. Lett. **25**, 575 (2000).
18. F. Légaré, I. V. Litvinyuk, P. W. Dooley, F. Queré, A. D. Bandrauk, D. M. Villeneuve, and P. B. Corkum, Phys. Rev. Lett. **91**, 093002 (2003).
19. K. Naganuma, K. Mogi, and H. Yamada, IEEE J. Quantum Electron. **25**, 1225 (1989).
20. T. Takaya, H.-O. Hamaguchi, H. Kuroda, and K. Iwata, Chem. Phys. Lett. **399**, 210 (2004).

Chapter 4

4.1. Conclusions

In this thesis, I investigated two different methods to enhance a Raman signal.

The first method, presented in Chapter 2, demonstrated a novel Raman spectroscopy platform created by non-selectively filling a short length of HC-PCF; this enhanced the generated Raman signal of an analyte by an order of 40. The simplicity of this method to achieve reasonable Raman signal enhancement, combined with the high degree of overlap between the propagating mode and the analyte and the small sample volume required, make it a promising candidate for sensitive, low-power identification of biological specimens. Combining this method with a surface enhanced Raman scattering effect, by embedding gold/silver nanoparticles inside the fiber core, resulted in significantly higher Raman signal enhancement. This facilitates the use of Raman in biomedical applications with very low concentrations of the analyte in question.

The second Raman enhancement method, using the CARS approach, was presented in Chapter 3. A single fs laser CARS microscope was built and developed by using 2 closely lying ZDWs PCF. Due to its high contrast, low noise signal, the microscope could be applied to label-free, non-bleaching and chemically selective fast CARS imaging of fixed and live biological samples for numerous medical and clinical applications. By not requiring an extra light source, this approach reduces the complexity and size, and achieves major cost savings.

A 2 far-lying ZDWs fiber was used to enable polarization of CARS and CARS imaging/spectroscopy in the fingerprint region, rather than the standard 2 closely-lying ZDWs fiber. And the conditions in which a PCF with two far-lying ZDWs can be used to perform high quality and stable polarization CARS imaging of lipid rich density biological samples were investigated. I demonstrated a comparable high quality CARS signal from the fiber with two far-lying ZDWs when the coupled laser's pulse duration was at approximately 100 fs, with a slightly positive chirp, and minimum possible average power (around 100 mW), as well as a polarization direction parallel to the slow axis of the PCF. The low fs laser power requirement for the two far-lying ZDWs (100mW versus 300 mW) means this fiber can be used with low power sources, such as femtosecond fiber lasers, to perform single fs laser CARS microscopy/endoscopy in both CH bond and fingerprint region.

A miniaturized, fiber delivered handhold multimodal CARS endoscope, which reduced the size of the existing CARS microscope and enabled it to perform in-vivo CARS imaging, was developed and tested. It is shown that by using a large mode area core PCF combined with a custom built dichroic mirror we can avoid beam distortions and completely block unwanted fibre-generated non-resonant FWM signals, to deliver just pump and the Stokes beams at the sample. Using a MEMS scanning mirror with a 500 μm diameter reflective to scan the pump and Stokes beams, enabled us to perform ex-vivo multimodal CARS imaging. We demonstrated the functionality and applicability of the completed miniaturized exoscope by obtaining proof of concept images of biological and chemical samples of TPEF, SHG and CARS, in both the forward and epi directions.

4-2. Future outlook

The work that presented in this thesis is mainly a demonstration of the proof of concept of potential applications of a fully miniaturized broadband multimodal CARS endoscope/exoscope. For future improvement and future application of a more developed CARS imaging endoscope, my outlook is divided to short-medium and long term future plan as follows:

Short and medium term:

- Improving the manufacturing processes of the existing exoscope/endoscope. By doing more precise beam and endoscope component alignment, fix all endoscope components (preventing any displacement after) and measuring and characterizing all optical aberrations of the whole system, the optical aberrations of the exoscope can be reduced. This will increase the pump and Stokes beam overlap, allowing us to reduce the active focal volume (further improving the axial resolution), and increasing the image quality and resolution capabilities.
- Using two far ZDWs PCF instead of two closely ZDWs PCF: By adjusting the input fs laser pulse, coupled to a 2 far-lying ZDWs fiber we can generate a low noise and stable SC as good as the SC out of an standard 2 closely-lying ZDWs fiber, with enough spectral density in the region between 800 nm - 1100 nm. This enable us to do high quality, fast acquisition time CARS imaging in the C-H bond region as well as the finger print region if it is combined with the spectral focusing method to reduce the non-resonant CARS background signal .

- Using a portable and less expensive fs fiber laser: By using the current bulky fs laser sources, it is not possible to reach to the goal of having a miniaturized portable CARS endoscope for clinical on-bed applications. However, by using a portable, well developed fs fiber laser combined with the existing miniaturized endoscope this dream will be more achievable.

By combining the modified version of the existing exoscope/endoscope with a portable all-fiber femtosecond laser, using two far-lying ZDWs fiber and spectral focusing method, we could have an all fiber, portable, miniaturized, robust and user-friendly multimodal CARS exoscope /endoscope. This endoscope can conduct CARS imaging in both the C-H bond and fingerprint regions (doing broadband CARS), as well as TPEF and SHG imaging. The size and portability of such an endoscope/exoscope, as well as its broad range of potential imaging modalities, will give us the capability to do many more applications, like in-vivo bone density imaging measurements or nanosurgery brining multimodal nonlinear imaging endoscopy closer to a clinical applications..

Long term

- A developed miniaturized portable multimodal CARS imaging exoscope would be extremely valuable for, minimally invasive characterization of the bone material and structure.

  Bone is a very dynamic living tissue in our body. Bone composition undergoes constant remodelling and changing through our life. Bone is the second most commonly transplanted tissue in human medicine. Therefore, the exact characterization of the bone material and structure is of crucial importance. For instance, characterizing / imaging of the cellulose scaffolds are of particular of the interest, to enable cell invasion and attachment, and the subsequent formation of new bone, in bone genesis tissue engineering applications like spinal fusion. The Fourier transform infrared (FTIR) imaging is used recently to characterize the bone matrix. However, the FTIR has a low spectral and spatial resolution and cannot be used in an aqueous medium. In addition, FTIR systems are bulky and not portable for most of the on-bedside clinical applications. The spectral and spatial resolution of the CARS is more than FTIR, which will enable us to have a higher resolution image and more precise model. In addition, CARS is not sensitive to the aqueous medium, does not need any special sample preparation and

therefore can be easily used for a minimally invasive in vivo clinical applications. Such imaging tool will have an excellent ability to do 3-D imaging and analysing of the bone and bone graft materials using CARS, SHG and TPEF methods.

- Doing more miniaturization of the CARS endoscope, will open new doors to the clinical applications of the CARS endoscopy especially in the nanosurgery and minimally invasive medical monitoring/imaging applications like endoscopy of inside of the human artery for diagnosing the atherosclerosis. This new imaging diagnostic method will be more precise with more detail information method compared to the current existing approaches.

Appendix A

Theory of Raman signal enhancement, by increasing the interaction length of excitation light and analyte

As discussed, the main drawback of the Raman is the weak Raman signal. In a linear conventional method, this can be solved by:

1) Increasing the laser intensity (excitation light), leading to increased intensity of the Raman scattered signal;

2) improving the quality of the transverse beam profile inside of impaling the sample, to get a single mode, one point focused Gaussian beam with a very small spot size and high intensity; and,

3) Increasing the laser beam interaction length with the analyte in the medium.

With respect to increasing the intensity of the laser, despite the availability of powerful, inexpensive diode laser sources for Raman spectroscopy, there are many limitations with the biological approaches. The biological samples are very sensitive to the excitation light intensity, and are easily damaged by increasing the intensity. The figure of merit, used to quantify the Raman signal enhancement, is defined by (2-8). For a Gaussian laser beam focused inside an analyte (Figure 3-9), using a conventional optical setup we have [31]:

$$L_{\text{int}} = 2\,Z_{\text{R}} \tag{A-1}$$

and

$$A_{eff} = \pi\, w_0^2 \tag{A-2}$$

where Z_R is the Rayleigh length, w_0 is half the beam at the focus, and λ is the wavelength of the laser light in the vacuum.

We also have:

$$Z_R = \frac{\pi\, w_0^2}{\lambda} \tag{A-3}$$

By substituting (A-1), (A-2) and (A-3) in (2-8), we find M~2 for a Gaussian beam, regardless of the optical focusing system. In other words, when the Gaussian beam focuses more tightly at the medium (i.e. with higher laser intensity or smaller A_{eff}), the interaction length L_{int} decreases, and when the interaction length increases the effective cross-sectional area increases.

By using conventional mirrors, and multi-reflecting the focused laser beam in a cavity containing analyte, it is possible to enhance the figure of merit by couple of times, but no more.

As mentioned, the spontaneous Raman signal can be much more enhanced by coupling and confining the laser light in a capillary or hollow core silica/Teflon fiber, if the refractive index of the analyte is more than the refractive index of silica/Teflon (~1.4/ 1.29) [13,14,32]. Consider a capillary with a refractive index of n_{sil}, a length of "L(m)", and a bore radius of "a", filled with an analyte with a refractive index of n_a, ($n_a > n_{sil}$). The excitation light will be trapped, and travel inside the filled analyte core of the fiber if the normal incident is smaller or equal to the critical angle θ_c (Figure 1). Thus, we have:

$$\theta_c = cos^{-1}\left(\frac{n_{sil}}{n_a}\right) = \sqrt{\frac{2(n_a - n_{sil})}{n_a}} \tag{A-4}$$

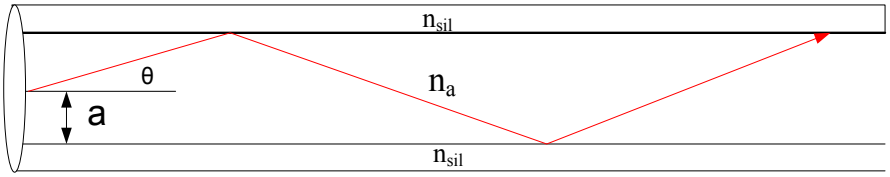

Figure A-1: Liquid core optical fiber

If the excitation light is focused to the end of fiber, the Raman signal intensification after traveling "dx" in the fiber core will be [13]:

$$dI_R = G_R I dz - \alpha I_R dz \tag{A-5}$$

where $G_R = g_R \pi \theta_c^2$, g_R is the Raman scattering cross section, $\pi\theta_c^2$ is the solid angle, I is the intensity of the excitation light coupled to the fiber, I_R is the scattered Raman intensity, and α' is the loss coefficient of the core of the analyte filled fiber at the frequency of the Raman scattering. If we assume a same "α'" at the excitation frequency, the travelling excitation light intensity inside the fiber will be:

$$I = I_0\, e^{-\alpha' z} \tag{A-6}$$

where I_0 is the initial intensity of the excitation light at z = 0, and z is the travelling distance of the excitation light inside of the fiber.

By substituting (A-6) in (A-5), and solving the final equation, we have:

$$I_R = G_R I_0 L e^{-\alpha' L} \tag{A-7}$$

Which can be written as:

$$I_R = I_{R0} L e^{-\alpha' L} \tag{A-8}$$

As (A-8) shows, the generated Raman intensity is increased by increasing the fiber length, while it is attenuated because of the core medium loss. Therefore, at the beginning the Raman signal is increased linearly, but after travelling a certain distance it starts to decrease, due to overcoming the loss exponential term. The optimum enhancement length will be driven by differentiating the equation (A-7):

$$\frac{dI_R}{dL} = -\alpha G_R I_0 L e^{-\alpha' L} + G_R I_0 e^{-\alpha' L} = 0 \tag{A-9}$$

Thus, the optimum length will be:

$$L_{opt} = \frac{1}{\alpha'} \tag{A-10}$$

By combining (A-8) and (2-8), we get:

$$M_{fiber} = \frac{L_{int}\lambda}{A_{eff}} = \frac{\lambda L e^{-\alpha' L}}{\pi w_{eff}^2} \tag{A-11}$$

where w_{eff} w_{eff} is the effective mode radius of the traveling excitation light inside the fiber core. By comparing the M for a focused Gaussian beam inside analyte with the M_{fiber}, the enhancement factor for using a core-filled analyte hallow core fiber will be:

$$\text{Enhancement factor} = \frac{M_{fiber}}{M_{Gaus}} = \frac{\lambda L e^{-\alpha L}}{2\pi w_{eff}^2} \tag{A-12}$$

For example, in an ideal case for L=0.1 (m), w_{eff} = 10 μm single mode transmission condition, and λ=1 μm and negligible loss, the enhancement factor will be around 160 times.

In practice, the enhancement factor will be less than the theoretical value, due to:

(a) Loss in the coupling of the excitation light to the fiber;

(b) More loss inside the fiber (material and waveguide loss as well as leakage of optical field from the core);

(c) No single mode transmission condition; and,

(d) α not being the same at the excitation and Raman frequencies.

Therefore, by using a short length hollow core fiber or capillaries, the Raman signal of a transparent analyte can be enhanced about hundreds of times. In addition, due to the very small

hole diameter of the fiber, the Raman spectroscopy analysis can be done with an extremely small amount of sample. However, the refractive index selective rule ($n_{sil} > n_c$) limits this technique to just a few analytes with high refractive indices. This limitation is more severe for aqueous based biological analytes. This confinement can be partially solved by using HC-PCF.

Appendix B

Raman signal enhancement using HC-PCF and SERS effect

After enhancing the Raman signal using HC-PCF, we were looking forward to do more Raman signal enhancement by combining the HC-PCF method with surface enhance Raman scattering, using silver nanoparticles.

Contribution

This paper was joint research between Dr. V. Tiwari, Altaf Khetani and myself.

This work was led by Dr. Tiwari (a new post doc. in our research group at that time) with collaboration of Altaf and I. The result was published in the proceeding of the IEEE sensor 2009 as follow:

Vidhu Tiwari, Altaf Khetani, Majid Naji, Hanan Anis, "Study of surface enhance Raman scattering with PCF", IEEE Sensors, 2009, 978-1-4244-5335-1, New Zealand.

Study of Surface Enhanced Raman Scattering (SERS) within Hollow Core Photonic Crystal Fiber

Vidhu S. Tiwari, Altaf Khetani, Majid Naji, Hanan Anis

Department of Electrical Engineering
School of Information Technology and Engineering, University of Ottawa
Ottawa, ON K1N 6N5, Canada

***Abstract*—The presented work aims to realize the surface enhanced Raman scattering (SERS) signal of rhodamine 6G (Rh 6G) molecule by non-selectively filling all the holes of hollow core photonic crystal fiber (HC-PCF) while exploiting the bandgap property of HC-PCF. As a consequence, strong mode field overlap with the analyte solution is achieved resulting in an amplified Raman signal with just a few milliwatts (~2mW) of sample energy within the fiber core. The actual contribution of enhancement by HC-PCF has been deconvolved from that of nanoparticles in the overall Raman signal enhancement of Rh 6G. Finally, we report the enhancement factor of Raman signal of Rh 6G, filled within the different lengths of HC-PCF.**

I. INTRODUCTION

The combination of SERS and photonic crystal fiber has offered a strong platform for sensitive molecular fingerprinting of chemical and biological species of interest [1-5]. Recently, several groups have studied the SERS signal of molecules within the hollow core photonic crystal fiber (HC-PCF) by non-selectively filling the fiber with analyte solution [2, 3]. Some of the reports also features the challenge involved in filling core and cladding holes of HC-PCF [4]. However, these studies merely use HC-PCF as a sample container and do not exploit the photonic bandgap property of HC-PCF. As a consequence, modal field is barely confined to the sample filled core region leading to higher fiber transmission loss and poor quality spectral response.

The novelty of our work lies in interfacing SERS with HC-PCF while exploiting the photonic band gap property in a non-selectively filled HC-PCF with Rh 6G and silver nano particles. The presented work builds upon our previous work of non-selectively filling HC-PCF with ethanol [6]. Inclusion of nano particles in the core and cladding region resulted in amplifying the Raman signal of Rh 6G to several orders of magnitude. On the other hand, hollow core photonic crystal fiber further enhances the Raman signal by supporting a strong modal field overlap with the sample solution along the entire length of HC-PCF via photonic band gap property. The contribution of SERS and HC-PCF towards the enhancement of Raman signal of Rh 6G were individually calculated, which hasn't been accounted in the previous reports.

Prior to filling the sample solution in HC-PCF, refractive index measurement were performed on sample solution as well as its constituents to ensure that the transmission band of sample filled HC-PCF lies in the close proximity of the excitation wavelength. Finally, different lengths of HC-PCF were filled with the sample solution to provide higher interaction of laser light with the sample; thereby studying the detection sensitivity with different length of HC-PCF to be utilized for future biosensor development work.

II. METHODS

A. Experimental setup

Figure 1 shows the schematic of experimental set-up with 785-nm single mode laser (Innovative photonic Sol.) as an excitation source having a max. output power of 100 mW. The laser beam was coupled to a filled Rh 6G and silver nano particles (~$5*10^{-4}$ M) HC-PCF (HC-1550, Thorlabs Inc.) by means of X40 microscope objective lens. The output beam was allowed to pass through a long-pass filter (IRIDIAN PN-ZX000445) which was centered around 785-nm for rejecting the scattered laser light. The SERS signal was collected in transmission mode by a multimode fiber bundle and fed to a Kaiser f/1.8 spectrograph with a TE-cooled Andor camera and monitored on computer. The SERS spectrum of Rh 6G and nanoparticles solution was first recorded in quartz cuvette (pathlength~1cm) followed by non-selectively filling the same solution to a 6cm of HC-PCF. For the sake of comparison, sample power in bulk (cuvette) solution was kept same as that in micro-litre (HC-PCF) solution.

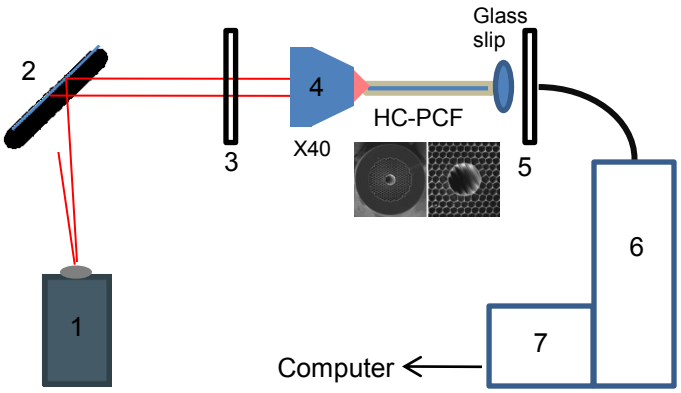

Fig.1. Schematic of the experimental set up.1: laser; 2: mirror; 3:band pass filter; 4:microscope objective lens; 5:long pass filter; 6:spectrograph; 7:camera

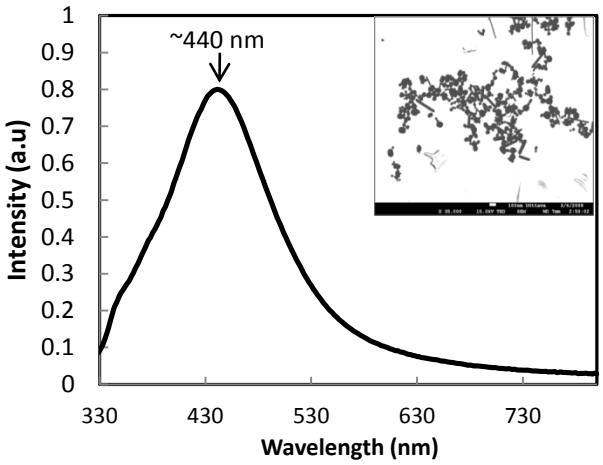

Fig. 2. Absorption spectrum of silver nano particles. Inset shows the SEM image of silver nano sphere particles with small amount of nanorods..

B. Nano particle Synthesis

Rhodamine 6G, silver nitrate, sodium citrate were purchased from Sigma Aldrich. Silver spheres 60 ±10 nm in diameter were prepared according to conventional citrate reduction method as reported by Lee and Meisel [7]. Eighteen milligrams of $AgNO_3$ diluted in 100 ml of deionized water and resulting solution was heated under magnetic stirring until it began to boil. Then 2 ml of 1% of sodium citrate solution in water was quickly added to the vigorously stirred $AgNO_3$ solution. The heating was continued until color changed to yellow and then to dark brown green. The solution was removed from heating and stirred until it has cooled to room temperature. Silver spheres show only one principal plasmon band ~ 440 nm as shown in Fig. 2. The majority of silver nano particles are spheres but there are small percentages of silver nano rods as shown in the SEM image (inset of Fig. 2) which are responsible for the red- shift of absorption peak of silver sphere from 410 to 440 nm.

C. Choice of HC-PCF

The guiding property of the HC-PCF changes depending on the refractive index of the sample. In this case, the guiding principle is still due to bandgap effect but the transmission band supported by the fiber is shifted. The shift in wavelength can be determined from the equation given by Russell *et al* [8], by changing the refractive index n_1 relative to the refractive index of liquid n_{liq} and the shifted wavelength is given by

$$\lambda' = \lambda_0 \left[\frac{1 - \left(\frac{n_{liq}}{n_{sil}}\right)^2}{1 - \left(\frac{n_{air}}{n_{sil}}\right)^2} \right]^{1/2}$$

where λ_0 is the wavelength at which the bandgap originally occurs, and λ' is the wavelength of the shifted bandgap. Also, n_{air} and n_{sil} are refractive index of air and silica respectively. Therefore depending on the excitation wavelength, one needs to find fiber which would guide this wavelength when filled.

D. Non-selective HC-PCF filling and refractive index measurement

All the holes of HC-PCF fiber were filled non-selectively with sample solution of Rh 6G and silver nano particles in the volume ratio of 1:1. To achieve this, an HC-PCF was inserted in syringe needle whose other end was sealed with a glass slip. The cavity enclosed between syringe needle and glass slip served as a reservoir for sample solution, which was sucked along the length of HC-PCF by capillary action. The reservoir ensures that the liquid is continuously supplied within the fiber channels to replenish any evaporated liquid.

Refractive index of sample solution and their constituents were measured by Metricon Model 2010/M Prism Coupler at wavelengths ~633-nm and ~1312-nm respectively. These values of refractive index were averaged to get an approximate value around the excitation wavelength (785 nm) for each set of sample and shown in Table 1. The sample solution of Rh 6 and silver nano particles with Rh 6G concentration ~ $5*10^{-4}$ M shifted the photonic band gap of HC-PCF from 1550-nm for air to 812-nm .

Sample	Refractive Index (n_{liq})			Shifted Wavelength (nm)
	633 nm	1312 nm	Average	
Rh 6G	1.3307	1.3085	1.3196	887
Silver Nano (Ag)	1.3306	1.3201	1.32535	868
Rh 6G & Ag	1.3525	1.3306	1.34155	812

TABLE I. REFRACTIVE INDEX VALUES

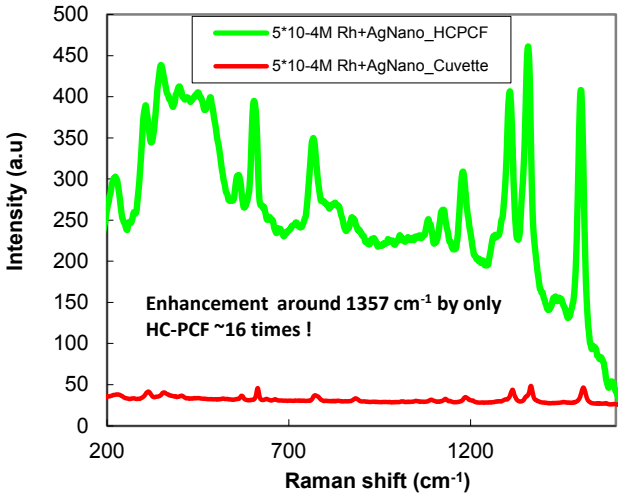

Fig. 3 SERS spectrum of Rh 6G and silver nanoparticles showing only HC-PCF enhancement

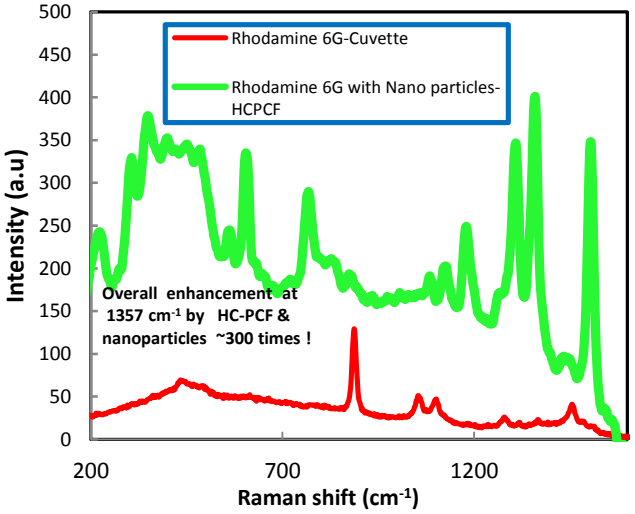

Fig. 4 SERS spectrum of Rh 6G and silver nanoparticles showing overall enhancement by both HC-PCF and nanoparticles.

which is in close proximity to the excitation wavelength (785-nm). Our calculation further suggest that shifted photonic band wavelength lies in the range of 760-865 nm which overlaps well with region of Raman wavelength of interest including the excitation wavelength. Thus, non-selective filling of HC-PCF by sample solution still confines the modal field within the core region and allows the utilization of photonic band gap property-a feature intrinsic to the nature of HC-PCF.

III. RESULTS & DISCUSSION

A. SERS in HC-PCF

The SERS spectrum of Rh 6G and nanoparticles solution was first recorded in quartz cuvette (pathlength~1cm) followed by non-selectively filling the same solution to a 6cm of HC-PCF. For comparison, sample power in bulk (cuvette) solution was kept same as that in micro-litre (HC-PCF) solution. While comparing the SERS spectrum of same sample solution (Rh 6G and silver nano particles) in both these cases, one can draw conclusion about the effective contribution of HC-PCF towards enhancing Raman signal of Rh 6G. Figure 3 indicates the actual role played by HC-PCF fiber (~16 times for SERS peak at 1357 cm^{-1}) in the overall enhancement of Raman signal of Rh 6G. Our data also indicates the contribution of nanoparticles in amplifying SERS signal at 1357 cm^{-1} in HC-PCF by a factor of ~20 (not shown here).This was estimated by filling pure Rh 6G in HC-PCF and subsequently filling the solution of Rh 6G and silver nano particles in HC-PCF under similar experimental conditions, thus out weighing the contribution of HC-PCF towards the enhancement of Raman signal of Rh 6G. Figure 4 shows the overall Raman signal enhancement (~300 times) of Rh 6G around 1357 cm^{-1} and takes into account the contribution of nanoparticles and HC-PCF. The enhancement factor represented here is ratio of SERS peak intensity at a certain wavelength to that of normal Raman peak of Rh 6G. Other Raman peaks of Rh 6G around 612, 1314, 1508 cm^{-1} etc also show varying degree of enhancements but maximum enhancement ~(300 times) was observed in case of peak around 1357 cm^{-1}. Figure 4 clearly shows Raman peaks ~886, 1100 cm^{-1}, which are of ethanol (solvent for Rh 6G), and not considered in calculation. The Rhodamine 6G was used as SERS test sample and the concentration of presented study is more oriented towards investigating the response of HC-PCF as Raman signal enhancer. Therefore, a detailed assignment of various Raman bands of Rh 6G with respect to various modes of vibration is not discussed here and can be found elsewhere[9].

B. SERS in different length of HC-PCF

In the last part of our investigation, different lengths of HC-PCF were filled with Rh 6G and nanoparticles solution to study the effect of varying the light interaction length with sample on the overall enhancement factor of SERS signal around 1357cm^{-1}. The major challenge associated with this task was to maintain same power of light and ensuring homogeneous distribution of sample solution within different lengths of HC-PCF. Figure 5 shows gradual

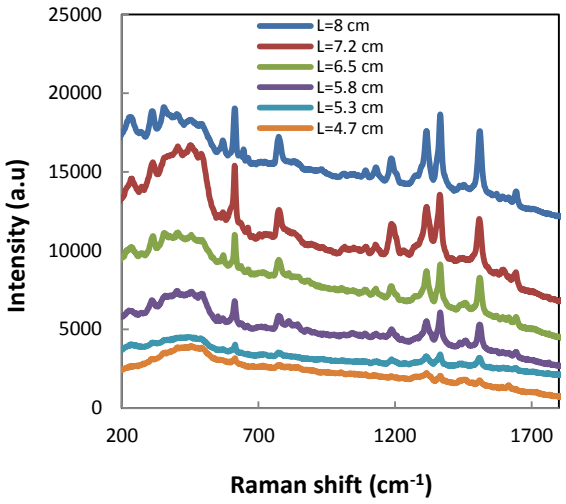

Fig. 5 SERS spectrum of Rh 6G showing variation in the Raman peak intensity with HC-PCF length

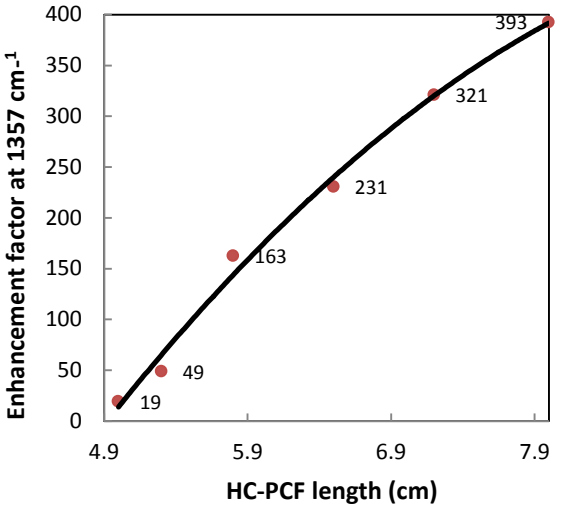

Fig. 6 Variation of enhancement factor of Raman peak at 1357 cm^{-1} with HC-PCF length

increase in SERS peak intensity of Rh 6G with increase of HC-PCF length in the range of 4.7 to 8 cm. The peak intensity around 1357 cm^{-1} was calculated in each case, and compared with one calculated with pure Rh 6G in bulk (cuvette) solution to obtain a calibration curve as shown in Fig.6.

Based on these results, one can note following: The enhancement factor is directly proportional to sample volume in the core region, which is ultimately related to the HC-PCF length. The enhancement factor linearly increases within the range of 4.7 to 6.5 cm, and tends to saturate for higher values of HC-PCF length. It signifies uniform distribution of nano particles with respect to HC-PCF core volume and a complete coverage of HC-PCF micro-structured core and cladding within this range. The nano particle solution may not be evenly distributed within higher length (l> 6.5 cm) of HC-PCF owing to various factors like viscosity, evaporation, scattering due to aggregation, resulting in saturation of SERS peaks of Rh 6G.

IV. CONCLUSION

We have demonstrated surface enhanced Raman scattering in a non-selectively filled HC-PCF with rhodamine 6G and silver nano particles sample solution while preserving the photonic band gap property in HC-PCF. Our results indicate individual contributions of nano particles (~20 times) and HC-PCF (~16 times) towards the overall enhancement of Raman signal of Rh 6G. Additionally, we have determined the enhancement factor with different lengths of HC-PCF. This further indicates that the length of HC-PCF can be tailored to design sensitive optical sensor for monitoring bio chemical species of interest.

REFERENCES

N. Skivesen et al."Photonic-crystal waveguide biosensor," *Opt. Express*, vol.15, pp. 3169-3176, 2007.

Claire Gu et al. "Hollow core photonic crystal fiber surface-enhanced Raman probe," *Appl. Phys. Lett*., vol. 89, pp.204101-1-204101-3, 2006.

F.M. Cox, A. Argyros, M.C.J. Large and S. Kalluri, " Surface enhanced Raman scattering in a hollow core micrstructured optical fiber," *Opt. Express*, vol. 15, pp. 13675-13681, 2007.

X. Zhi-Guo et al., " Photonic crystal fibre sensors based on silver nanoparticle colloid," *Chin. Phys. Lett*., vol 25, pp. 4473-4475, 2008.

S.O. Konorov, C.J. Addison, H.G. Schulze, R.F.B. Turner, and M.W. Blades, "Hollow-core photonic crystal fiber-optic probes for Raman spectroscopy," *Opt. Lett*., vol. 31, pp. 1911-1913, 2006.

M. Naji, A. Khetani, N. Lagali, R. Munger and H. Anis, " A novel method of using hollow-core photonic crystal fiber as a Raman biosensor," *Proc. of SPIE*, vol. 6865, pp. 68650E-1, 2008.

P. C. Lee, and D. Meisel, "Adsorption and surface-enhanced Raman of dyes on silver and gold sols," *J. Phys. Chem*., vol. 86, pp. 3391-3395, 1982.

G. Antonopoulos, F. Benabid, T. A. Birks, D. M. Bird, J. C. Knight and P. St. J. Russell, "Experimental demonstration of the frequency shift of bandgaps in photonic crystal fibers due to refractive index scaling", *Opt. Express*, vol. 14, pp.3000-3006, 2006.

V. S. Tiwari**,** T. Oleg, G. K. Darbha, W. Hardy, J.P. Singh, and P. C. Ray , "Non-Resonance SERS effects of silver colloids with different shapes," *Chem. Phys Lett.,vol.* 446, pp. 77-82, 2007.

Bibliography and References

[1] R. McCreery, “Raman Spectroscopy for chemical analysis”, John Wiley(2000).

[2] http://www.diabetes.ca/diabetes-and-you/what/prevalence/

[3]http://www.qualityprofiles.org/leadership_series/diabetes/diabetes_effective

_management.asp

[4] P.D Raymond, M.J Ray, SN Callen and NA Marsh, “Heparin monitoring during cardiac surgery, Part 1: validation of whole-blood heparin concentration and activated clotting time”, Perfusion, 18: 269 -276 (2003).

[5] P. J. Santrach, “Devices for Monitoring Heparin and Protamine in the Operating Room”, Seminars in Cardiothoracic and Vascular Anesthesia, Vol 7, No 4, pp 379-385(2003).

[6]D. H. Athax, A. Gaigalas and V. Reipa, “Structural Analysis of Heparin by Raman Spectroscopy,” J. of Pharm. Sci. , Vol. 85, No.1 (1996).

[7] A. Khetani, V. S. Tiwari, A. Harb, and H. Anis, “Monitoring of heparin concentration in serum by Raman spectroscopy within hollow core photonic crystal fiber”, Opt. Exp., Vol. 19, Issue 16, pp. 15244-15254(2011).

[8] M. Naji, A. Katani, N. Legali, R. Munger, H. Anis , “A novel method of using HC-PCF as a Raman biosensor,” Proc. of the SPIE, 6865, 68650E (2008).

[9] A. Khetani, M. Naji, N. Lagali, H. Anis, R. Munger, “Methods for using Photonics Crystal Fiber as a Raman Biosensor”, USA patent US7738097

[10] V. S. Tiwari, A. Khetani, M. Naji and H. Anis, “Study of surface enhanced Raman scattering (SERS) within hollow core photonic crystal fiber,” procceding of IEEE SENSORS Conference (2009).

[11] http://hyperphysics.phy-astr.gsu.edu

[12] F. Benabid, J. C. Knight, G. Antonopoulos, P. St. J. Russell , “Stimulated Raman Scattering in Hydrogen-Filled Hollow-Core Photonic Crystal Fiber” , Sci. , Vol. 298, 399 (2002).

[13] G. E. Walrafen and J. Stone, “Intensification of Spontaneous Raman Spectra by use of Liquid Core Optical Fibers”, Appl. Spect., Volume 26, Number 6 (1972).

[14] R. Altkorn, I. Koev, R. P. Van Duyne, and M. Litorja, “Low-loss liquid-core optical fiber for low-refractive-index liquids: fabrication, characterization, and application in Raman spectroscopy”, Appl. Opt., Vol. 36, No. 34, 1 December (1997).

[15] Philip Russell, “Photonic Crystal Fibers”, Sci. 299, 358 (2003).

[16]D. Pristinski and H. Du, “Solid-core photonic crystal fiber as a Raman spectroscopy platform with a silica core as an internal reference”, Opt. Lett., Vol. 31, No. 22, Nov. 15 (2006).

[17] K. Nielsen, Da. Noordegraaf , T. Sørensen, A. Bjarklev and T. P Hansen, “Selective filling of photonic crystal fibers”, J. Opt. A: Pure Appl. Opt. 7, L13 (2005).

[18] L. Xiao, W. Jin, M. Demokan, H. Ho, Y. Hoo, C. Zhao, "Fabrication of selective injection microstructured optical fibers with a conventional fusion splicer," Opt. Exp. 13, 9014-9022 (2005).

[19] P. Kambhampati, C.M. Child, M.C. Foster, and A. Campion, “On the chemical mechanism of surface enhanced Raman scattering: experiment and theory,” J. Chem. Phys. 108, 5013 (1998).

[20] M. Fleischmann, P. J. Hendra, and A. J. McQuillan,“Raman spectra of pyridine adsorbed at a silver electrode, ”Chem. Phys. Lett., 26, 163(1974).

[21] D. L. Jeanmaire and R. P. Van Duyne, “Surface Raman pectroelectrochemistry: Part I. Heterocyclic, aromatic, and aliphatic amines adsorbed on the anodized silver electrode”. J. Electroanal. Chem. 84, 1-20 (1977).

[22] K. Kneipp, H. Kneipp, I. Itzkan, R. R Dasari and M. S Feld, “Surface-enhanced Raman scattering and biophysics ”, J. Phys,: Condens. Matter, 14, R597–R624 (2002).

[23] I. Nabiev, I. Chourpa and M. Manfait, “Applications of Raman and Surface-Enhanced Raman Scattering Spectroscopy in Medicine ”, J. of Raman Spect., Vol. 25, 13-23(1994).

[24] Y. Zhang, C. Shi, C. Gu, L. Seballos, and J. Z. Zhang,“ Liquid core photonic crystal fiber sensor based on surface enhanced Raman scattering”, Appl. Phys. Lett. 90, 193504, (2007).

[25] X. Yang, C. Shi, Re. Newhouse, J. Z. Zhang and C. Gu. “Hollow-Core Photonic Crystal Fibers for Surface-Enhanced Raman Scattering Probes”, Int. J. of Opt., Article ID 754610, (2011).

[26] “Selective filling of liquids into Photonic Crystal Fibers”, http://www.mpl.mpg.de/en/russell/news-old/talks-and-seminars/talks-and-seminars-details/article/selective-filling-of-liquids-into-photonic-crystal-fibers.html?no_cache=1

[27] L. Xiao, W. Jin, M. Demokan, H. Ho, Y. Hoo, C. Zhao, "Fabrication of selective injection microstructured optical fibers with a conventional fusion splicer," Opt. Exp. 13, 9014-9022 (2005).

[28] A. Ketani, “Photonics Crystal Fiber As A Biosensor”, Master of Applied Science (M.A.Sc) thesis, Universiy of Ottawa (2009).

[29] G. Antonopoulos, F. Benabid, T. A. Birks, D. M. Bird, J. C. Knight and P. St. J. Russell “Experimental demonstration of the frequency shift of bandgaps in photonic crystal fibers due to refractive index scaling”, Opt. Exp., Vol. 14 No.7 (2006).

[30] Raman Spectra of Ethanol , http://openi.nlm.nih.gov/

[31] B. E. A. Saleh, M. C.Teich, “Fundamentals of Photonics,” Wiley-Interscience; second edition (2007).

[32] R. Altkorn, M. Malinsky, R. Vanduyne and I. Koev, "Intensity Considerations in Liquid Core Optical Fiber Raman Spectroscopy", Appl. Spect., Vol. 55, No. 4 (2001).

[33] J. Cheng and X. S. Xie, "Coherent Anti-Stokes Raman Scattering Microscopy: Instrumentation, Theory, and Applications", J. Phys. Chem., 108, 827-840, B (2004).

[34] F. Ganikhanov, S. Carrasco, X. S. Xie, M. Katz, W. Seitz and D. Kopf, "Broadly tunable dual-wavelength light source for coherent anti-Stokes Raman scattering microscopy", Opt. Lett. 31, 1292-1294, (2006).

[35] http://en.wikipedia.org/wiki/Multiple_sclerosis

[36] MS Society of Canada, http://mssociety.ca/en/information/

[37] E.O. Potma and X. S. Xie , "CARS Microscopy For Biology and Medicine", Opt, and Phot. News, p40, Nov. (2004).

[39] M. Naji, S. Murugkar, K. R. Khan, H. Anis, "Coherent anti-Stokes Raman scattering microscopy using photonic crystal fibers," Proceedings of the SPIE, Volume 7569, pp. 75692S-75692S-6, (2010).

[40] NKT, "NL-PM-750, Nonlinear Photonic Crystal Fiber," http://www.nktphotonics.com/files/files/NL-PM-750–090612.pdf.

[41] M. Naji, S. Murugkar, and H. Anis, "Determining optimum operating conditions of the polarization-maintaining fiber with two far-lying zero dispersion wavelengths for CARS microscopy", Opt. Exp., vol 22, No 9, 5 (2014).

[42] "Newport Announces CARS Optimized Supercontinuum Generation Fiber Device for Use with 800 nm Femtosecond Lasers," http://www.newport.com/Newport-Announces-CARS-Optimized-Supercontinuum-G/988836/1033/annoucement.aspx.

[43] S. Murugkar , B. Smith , M. Naji , C. Brideau , P. Stys and H. Anisa, "Development of a micromirror-scanned multimodal CARS miniaturized microscope for the in vivo study of spinal cord disorders., Photonics west, Proc. of SPIE Vol. 7903 79031D-1, (2011).

[44] R. F. 8egley, A. B. Harveyt, and R. L. Byer,"Coherent anti-Stokes Raman spectroscopy", Appl. Phys. Lett., Vol. 25, No.7, 1 Oct. (1974).

[46] T. Kee and M. T. Cicerone, "Simple approach to one-laser, broadband coherent anti-Stokes Raman scattering microscopy", Opt. Lett. 29, 2701 – 2703 (2004).

[47] Application Note 36, "Coherent Anti-Stokes Raman Scattering Microspectrometer", Technology and Applications Center Newport Corporation , assets.newport.com/webDocuments-EN/images/AppNote36-CARS.pdf

[48] M. D. Duncan, J. Reintjes, and T. J. Manuccia, "Scanning coherent anti-Stokes Raman microscope", Opt. Lett., Vol. 7, No. 8, Aug. (1982).

[49] A. Zumbusch, G. R. Holtom, and X. Sunney Xie, “Three-Dimensional Vibrational Imaging by Coherent Anti-Stokes Raman Scattering”, Phys. Rev. Lett., Vol. 82, No. 20, 17 May (1999).

[50] H. N. Paulsen, K. M. Hilligsøe, J. Thøgersen, S. R. Keiding and J. J. Larsen, “Coherent anti-Stokes Raman scattering microscopy with a photonic crystal fiber based light source,” Optics lett. Vol. 28, No. 13 (2003).

[51] K. L. Corwin, N. R. Newbury, J. M. Dudley, S. Coen, S. A. Diddams, K. Weber, and R. S. Windeler “Fundamental Noise Limitations to Supercontinuum Generation in Microstructure Fiber,” Phys. Rev. Lett., 90, 113904 (2003)

[52] H. Kano and H. Hamaguchi, “Vibrationally resonant imaging of a single living cell by supercontinuum-based multiplex coherent anti-Stokes Raman scattering microspectroscopy,”Opt. Exp., 13, 1322 (2005).

[53] K. Hilligsoe, T. Andersen, H. Paulsen, C. Nielsen, K. Molmer, S. Keiding, R. Kristiansen, K. Hansen and J. Larsen, “Supercontinuum generation in a photonic crystal fiber with two zero dispersion wavelengths,” Opt. Exp., 12, 1045 - 1054 (2004).

[54] S. Murugkar, C. Brideau, A. Ridsdale, M. Naji, P.K. Stys, H Anis ,“Coherent anti-Stokes Raman scattering microscopy using PCF with two closely laying zero dispersion wavelength”, Opt. Exp., 15, Issue 21, Oct. (2007).

[55] B.v. Vacano, L. Meyer and M. Motzkus, “Rapid polymer blend imaging with quantitative broadband multiplex CARS microscopy,” J. Raman Spectro. 38: 916–926 , (2007).

[56] A. F. Pegoraro, A. Ridsdale, D. J. Moffatt, Y. Jia, J. P. Pezacki, and A. Stolow , “Optimally chirped multimodal CARS microscopy based on a single Ti:sapphire oscillator,” Opt. Exp.,Vol. 17, Issue 4, pp. 2984-2996 (2009).

[57] A. F. Pegoraro, A. D. Slepkov, A. Ridsdale, D. J. Moffatt, and A. Stolow, “Hyperspectral multimodal CARS microscopy in the fingerprint region,” J. Biophotonics 7(1-2), 49–58 (2014).

[58] F. Légaré, C. L. Evans, F. Ganikhanov, and X. S. Xie, “Towards CARS endoscopy,” Opt. Exp.,14(10), 4427–4432 (2006).

[59] Z. Wang, L. Gao, P. Luo, Y. Yang, A. A. Hammoudi, K. K. Wong and S. T. C. Wong, “Use of multimode optical fibers for fiber-based coherent anti-Stokes Raman scattering microendoscopy imaging,” Opt. Exp., 19 (9), 7960-7970 (2011).

[60] B. G. Saar, R. S. Johnston, C. W. Freudiger, X. S. Xie, and E. J. Seibel, “Coherent Raman scanning fiber endoscopy,” Opt. Lett., 36(13), 2396–2398 (2011).

[61] B. Smith, M. Naji, S. Murugkar, E. Alarcon, C. Brideau, P. Stys, and H. Anis, “Portable, miniaturized, fibre delivered, multimodal CARS exoscope,” Opt. Exp. 21(14), 17161–17175 (2013).

[62] R. R. Alfano and S. L. Shapiro, "Emission in the region 4000 to 7000 Å via four-photon coupling in glass" Physical Review Letters 24, 584 (1970).

[63] R. R. Alfano and S. L. Shapiro, "Observation of self-phase modulation and small-scale filaments in crystals and glasses" Physical Review Letters 24, 592 (1970).

[64] J. T. Manassah, P.P. Ho, A. Katz, and R. R. Alfano, "Ultrafast supercontinuum laser source," Photonics Spectra,18, 53-59, (1984).

[66] A. V. Husalou and J. Herrmann, "Supercontinuum generation of higher-order solitons by fission in photonics crystal fibers," Phys. Rev. Lett. 87(20), 203901, (2001).

[67] J. Herrmann, U. Griebner, N. Zhavoronkov, A. Husakou, D. Nickel, J. C. Knight, W. J. Wadsworth, P. St. J. Russell, and G. Korn, "Experimental evidence for supercontinuum generation by fission of higher-order solitons in photonic fibers," Phys. Rev. Lett. 88(17), 173901(2002).

[68] J. M. Dudley, G. Genty, and S. Coen, "Supercontinuum generation in photonic crystal fiber," Rev. Mod. Phys. 78(4), 1135–1184(2006).

[69] P.S.J. Russell, "Photonic-Crystal Fibers," J. Lightwave Tech., Vol. 24, No. 12, Dec. (2006).

[70] D.A. Akimov, A.A. Ivanov, M.V. Alfimov, A.M. Zheltikov, "Photonic-crystal fiber sources for nonlinear spectroscopy," Vib. Spect. 42, 33–40 (2006).

[71] I. Hartl, X. D. Li, C. Chudoba, R. K. Ghanta, T. H. Ko, J. G. Fujimoto, J. K. Ranka, and R. S. Windeler, "Ultrahigh-resolution optical coherence tomography using continuum generation in an air–silica microstructure optical fiber," Opt. Lett. 26, 608, (2001).

[72] G. P. Agrawal, Nonlinear Fiber Optics 5th edition, Academic Press (2013).

[73] A. K. Sarma and P. Kumar, "Modulation Instability of ultrashort pulses in quadratic nonlinear media beyond the slowly varying envelope approximation" App..Phys. B Vol. 106, p.289 (2012).

[74] A. Demircan, U. Bandelow, "Analysis of the interplay between soliton fission and modulation instability in supercontinuum generation," Applied Physics B, Volume 86, Issue 1, pp 31-39, January (2007).